Theses and Dissertations

Theses, Dissertations, and Senior Projects

January 2012

Heat Transfer, Transition, And Aerodynamic Loss In A Linear Vane Cascade At Low Reynolds Numbers In High Speed Flows

Matthew Phillip Mihelish

Follow this and additional works at: https://commons.und.edu/theses

www.manaraa.com

HEAT TRANSFER, TRANSITION, AND AERODYNAMIC LOSS IN A LINEAR
VANE CASCADE AT LOW REYNOLDS NUMBERS IN HIGH SPEED FLOWS

by

Matthew P. Mihelish
Bachelor of Science, University of Idaho, 2009

A Thesis

Submitted to the Graduate Faculty

of the

University of North Dakota

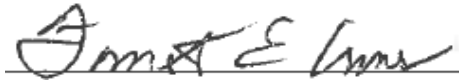in partial fulfillment of the requirements

for the degree of

Master of Science
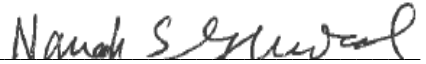
Grand Forks, North Dakota
May
2012

This thesis, submitted by Matthew P. Mihelish in partial fulfillment of the requirements for the Degree of Master of Science from the University of North Dakota, has been read by the Faculty Advisory Committee under whom the work has been done, and is herby approved.

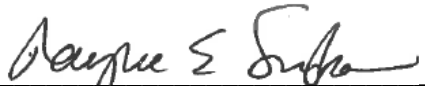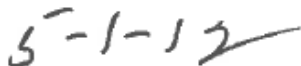Forrest Ames, Ph.D.
Chairperson

Nanak Grewal, Ph.D.

Gautham Krishnamoorthy, Ph.D.

This thesis is being submitted by the appointed advisory committee as having met all of the requirements of the Graduate School at the University of North Dakota and is hereby approved.

Wayne Swisher, Ph.D.
Dean of the Graduate School

May 1, 2012

ii

PERMISSION

Title   Heat Transfer, Transition, and Aerodynamic Loss in a Linear Vane
             Cascade at Low Reynolds Numbers in High Speed Flows

Department   Mechanical Engineering

Degree   Master of Science

        In presenting this thesis in partial fulfillment of the requirements for a graduate
degree from the University of North Dakota, I agree that the library of this University
shall make it freely available for inspection. I further agree that permission for extensive
copying for scholarly purposes may be granted by the professor who supervised my
thesis work or, in his absence, by the chairperson of the department or the dean of the
Graduate School. It is understood that any copying or publication or any other use of this
thesis or part thereof for financial gain shall not be allowed without my written
permission. It is also understood that due recognition shall be given to me and to the
University of North Dakota in any scholarly use which may be made of any material in
my thesis.

                                            Matthew P. Mihelish
                                            May 1, 2012

TABLE OF CONTENTS

LIST OF FIGURES

vi

LIST OF TABLES

NOMENCLATURE

English Letter Symbols

AC	aero-combustor turbulence
Beta	turning angle, ($\circ$), also β
C	vane true chord length, m
Cax	axial chord length, m
Cp	pressure coefficient
D	diameter, m
FLT	FLUENT solution
h	convective heat transfer coefficient, $W/(m^2K)$
I	electrical current, amps
K	acceleration parameter
k	thermal conductivity, $W/(m\ K)$
LT	low turublence
Lu	energy scale, $Lu = 1.5\ |u'|_3/\ \varepsilon$
M	million
Ma,ex	vane cascade exit Mach number
M_{surf}	local Mach number at the surface
Nu	Nusselt number
Omega	total pressure loss coefficient, $[P_{Tin}-P_{Tex}]/[P_{Tin}-P_{Sex}]$

P	pressure, Pa
Pr	Prandtl number
q"	heat flux, kJ per unit time per unit area
R	resistance, ohms
Re	Reynolds Number
Re_C	Reynolds number based on true chord and exit conditions
S	vane surface arc length measured from stagnation point, m
St	Stanton number
T	temperature, K
TC	thermocouple
Tu	turbulence intensity, $Tu = |u'|/U_\infty$
U_∞	freestream velocity, m/s
Vex	vane cascade exit velocity, m/s
Y	cross-span axis for traversing system
Z	cross-passage axis for traversing system

Greek Letter Symbols

β	turning angle, (°), also Beta
γ	ratio of specific heats
Δ	amount of change in a quantity, also Delta
$\delta*$	displacement thickness
ε	emissivity
θ	yaw angle, (°)
μ	absolute viscosity, Pa*s

xviii

ν	kinematic viscosity, m^2/s
ρ	fluid density, mass per unit of volume, kg/m^3
σ	Stefan-Boltzmann constant, $W/(m^2 K^4)$
Ω	total pressure loss coefficient, $[P_{Tin}-P_{Tex}]/[P_{Tin}-P_{sex}]$
φ	pitch angle, (°)

Subscripts

cor	refers to corrected values
ex	refers to conditions at the cascades exit plane
gen	refers to heat flux generated
in	refers to conditions at the cascades inlet plane
rad	refers to radiation energy
s	refers to static conditions
T	refers to total or stagnation conditions
x	refers to some distance across a surface
0	reference condition
∞	evaluated in the freestream

ACKNOWLEDGMENTS

This thesis would not have been possible without the support of many people. I would like to express my gratitude towards my advisor, Dr. Ames who was extremely helpful and offered invaluable assistance, support, and guidance. I would also like to thank the University of North Dakota and the Mechanical Engineering Department for providing me an excellent education as well as facilities and patience, while I completed my wind tunnel testing. I would also like to thank NASA EPSCoR and Rolls-Royce for providing financial support, which made my work in pursuing a Master of Science degree in mechanical engineering possible.

Special thanks to all my fellow graduate friends, especially Preethi Gandavarapu, Prasanta Dey, Nafiz Chowdhury, Mitch Busche, and Leolein Moualeu for sharing knowledge and invaluable assistance.

Additionally, I would like to sincerely thank Gary Dubuque and Jay Evenstad for providing their altruistic assistance and profligacy of technical knowledge and Teri Salwey for her invaluable help.

Finally, I would like thank my family for the necessary support and guidance's during my time at the University of North Dakota. I would also like to thank God for providing me this opportunity, the many great friendships, and experiences I had while in North Dakota.

ABSTRACT

Low pressure turbine research is essential for improving the efficiency of the modern gas turbine engine. At high altitude cruise conditions, the low pressure turbine experiences low Reynolds number flow, which produces a laminar boundary layer on airfoil surfaces. The integrity of the laminar boundary layer is highly susceptible to flow disturbances resulting from blade wakes and freestream turbulence. This susceptibility often leads to enhanced profile and secondary losses, which reduces turbine efficiency. Previous research conducted on low pressure turbine flow conditions, has investigated heat transfer, boundary layer separation bubbles, and secondary flows subjected to varying levels of freestream turbulence. This research is often conducted with low velocity wind tunnels, which are unable to produce engine relevant Mach numbers. Facilities that are able to produce engine relevant velocities are restricted to high Reynolds numbers and face difficulties acquiring well resolved flow data from restricted run times. Due to the limited abilities of current ground test facilities, new methodologies and facilities are needed to produce detailed heat transfer and flow loss data pertinent to the low pressure turbine operating conditions.

The Mechanical Engineering Department at the University of North Dakota has designed and developed a new facility able to conduct low Reynolds number research at engine relevant velocities, which is applicable to low pressure turbines. The facility is comprised of a sealed, closed loop wind tunnel, which operates at steady state conditions.

xxi

The facility is able to create flow conditions with a Reynolds number between 50,000 and 1,000,000 at Mach numbers up to 0.9.

The work of this thesis documents, in detail, the low Reynolds number transonic facility and the research conducted within it. The research includes vane surface heat transfer and pressure distributions along with exit surveys acquired using a five-hole cone probe documenting total pressure loss, secondary velocity vectors, turning angle, and loss distributions over a range of Reynolds numbers between 90,000 and 720,000 at Mach numbers between 0.7 and 0.9 under low and aero-combustor turbulence conditions.

The experimental results of this research indicate as Reynolds number decreases, secondary losses increase. In addition, for a given Reynolds number, secondary losses decrease as Mach number increases. Secondary loss structures such as the passage/horseshoe vortex weaken with enhanced turbulence but overall losses increase. Heat transfer measurements show a scaling factor on Stanton number as Reynolds number increases, which is augmented under aero-combustor turbulence.

CHAPTER I

INTRODUCTION

The study of low pressure turbine engines is highly relevant in today's jet engine industry due to the demand for more efficient engines [1],[2]. Engines on commercial and military jets operate in variable atmospheric conditions from taxiing, takeoff, cruise, and descent which must be considered in the engine design. The designs must take into account changes in airflow turning angle, secondary losses, separation transition, and heat transfer to name a few. Fluctuations in an engine's core flow occur due to the changes in operating conditions such as the engines rotation per minute (RPM), inlet air temperature and pressure. The inlet turbine temperature and pressure can vary significantly from a sea level takeoff to a cruise altitude of 12 km. Generally, the high pressure turbine operates in high Reynolds number flow but transitions to a lower Reynolds number in the low pressure turbine as the pressure drops. Due to the laminar characteristics of the boundary layer, adverse pressure gradients tend to cause flow separation within the low pressure turbine. Instabilities within the boundary layer are influenced by many mechanically produced components such as passing blade wakes or freestream turbulence from the combustor. Understanding transition at low Reynolds numbers is crucial for researchers and engineers to better characterize boundary layer instabilities and transition length. Therefore, the difficulty of predicting low Reynolds number flows requires a significant amount of research focused on improving a comprehensive view of the aerodynamics in low pressure turbines.

1

Boundary layer disruption has an effect on the heat transfer characteristics which may not have been anticipated for the overall design. Generally, the high pressure turbine experiences high Reynolds number flow; however, cruising altitudes for unmanned aerial vehicles (UAV's) are nearly 20 km, making low Reynolds number flow possible in the high pressure turbines. Some of the highest temperatures within a gas turbine engine are located in the high pressure turbine which depends on exotic cooling schemes to prevent components from overheating and failing. Ensuring proper functionality of the high pressure turbine depends on low Reynolds number flow characterization which results in improved efficiency, lower fuel consumption, and lower operating cost.

There are many laboratory facilities which study low Reynolds number flow at large scales but low speeds. These types of facilities are common. Facilities that examine turbine flows at high speeds use higher pressures which then generate much higher Reynolds numbers. Higher speed facilities typically operate in a transient mode which causes significant difficulties developing well resolved aerodynamic data. The Mechanical Engineering Department at the University of North Dakota has developed a high speed low pressure closed loop wind tunnel facility in order to study low Reynolds number flows at engine relevant Mach numbers at steady state conditions.

The work of this thesis focuses on the details of the operation and capabilities of a new transonic test facility and the aerodynamic and heat transfer performance of a gas turbine vane. The instrumented vane was tested in a large scale transonic linear vane cascade facility at chord Reynolds numbers of 90,000, 180,000, 360,000, and 720,000 over Mach numbers of 0.7, 0.8, 0.9 based on true chord exit conditions. Two different freestream turbulence levels were investigated during the tests. Aerodynamic losses are

compared for varying Reynolds number, inlet turbulence, and Mach number. Mass averaged total pressure loss data were acquired with exit surveys at ¼ axial chord downstream of the trailing edge of the test vane. Vane static pressure along with inlet and exit static pressure referenced to inlet total pressure were also acquired during the tests. Temperature measurements around the heat transfer test vane were also recorded at adiabatic conditions and while a constant heat flux was applied at each test condition conducted.

The aerodynamic loss and heat transfer data recorded in this study represents the initial tests conducted with the transonic facility. The construction of the transonic facility at the University of North Dakota was undertaken to enhance the Mechanical Engineering Department's research capabilities and competitive edge in the gas turbine industry. The study, which utilized this facility, is part of an ongoing investigation of low Reynolds flow phenomenon using vane geometries from Rolls Royce of North America. This study will provide turbine blade designers and computational fluid dynamics (CFD) researchers with additional information in ascertaining relevant predictions of secondary losses and heat transfer at low Reynolds number flow.

3

CHAPTER II

LITERATURE REVIEW

Currently, the unpredicted losses in low pressure turbines operating at cruise altitudes has initiated new interest in understanding transition and flow separation at low Reynolds numbers [3]. There are several methods for evaluating the unpredicted losses at high altitude flight in the low pressure turbines. Low velocity wind tunnels are used to reproduce low Reynolds number conditions and capture flow losses. Blow-down facilities are utilized to generate engine relevant velocities in the low pressure turbines where flow losses are also observed. In this chapter, archival literature will be reviewed on the nature of aerodynamic losses, the facilities used to study low Reynolds number, and engine relevant velocity flows. Literature will also be presented on pressure probes utilized by many of these facilities to acquire aerodynamic losses data.

Aerodynamic Losses

The understanding of air flow characteristics through turbomachinery is continually being developed and a comprehensive understanding of aerodynamic losses is essential for more efficient gas turbine design. A tractable review of aerodynamic losses is provided by Denton [4] where he defines categorically, losses in turbine vanes attributed to profile, end-wall, and leakage losses. Denton explains the magnitudes of these losses are dependent on the type of machine and the geometry of blades such as aspect ratio and tip clearances. He continues by explaining that in many machines, these loss components are comparable in magnitude and account for ⅓ of the total loss.

4

Overall, any reduction in the efficiency of a turbomachine would be considered a loss; however, the scope of this study will only encompass profile and secondary flow losses.

Profile Losses

Profile losses are a combination of the viscous effects and separated flow of the boundary layer on vanes and blades. According to Glassman [5], viscous effects and separation are the main source for profile losses. Trailing edge flow separation is also attributed to profile loss and often assumed to be two dimensional, which makes two dimension cascade testing relevant [4]. High intensity large scale turbulence cascade testing was conducted by Ames and Plesniak [6] who found about 50 to 60% of total losses could be attributed to vane boundary layers, with 30 to 40% of the total loss attributed to separation at the trailing edge of the vane. The significant loss at the trailing edge is due to separation at the trailing edge. The authors attributed elevated freestream turbulence to significantly influencing wake growth, causing wakes to be broader and have smaller peak velocity deficits. These characteristics are due to turbulent mixing causing the wakes to spread faster than at lower turbulence levels. A high inlet turbulence investigation with 4% grid generated turbulence was conducted by Gregory-Smith and Cleak [7] who found a slight increase in profile loss as a result. They attributed this increase to the boundary layer on the suction surface transitioning earlier, which can be seen in the suppression of the laminar separation bubble.

Secondary Flow Losses

Endwall losses, also known as "secondary flow losses" are three dimensional flow patterns resulting from the development of boundary layers on the endwalls of an airfoil cascade. The strength of the secondary losses is gained through the upstream boundary

5

layer and the amount of turning in a blade or vane row [4]. Due to the significant

efficiency lost in secondary flows, extensive research and resources have been devoted to

further understanding this flow phenomenon. A comprehensive description of the physics

of secondary losses is given by Gregory-Smith [8] who details vortex formation within a

vane cascade. He explains, flow at the mid-span of a vane is considered "primary flow"

which is two dimensional, and flow near the endwalls is considered "secondary flow" due

to a span-wise velocity gradient of the boundary layer. As the primary and secondary

flows are turned by either blades or vanes, a transverse velocity gradient is formed. The

velocity gradient between the pressure and suction side of the airfoils for the primary and

secondary flows is defined by Equation 2.1.further explained by Figure 1.

$$\frac{dp}{dR} = \frac{\rho V^2}{R} = \frac{\rho v^2}{r} \tag{2.1}$$
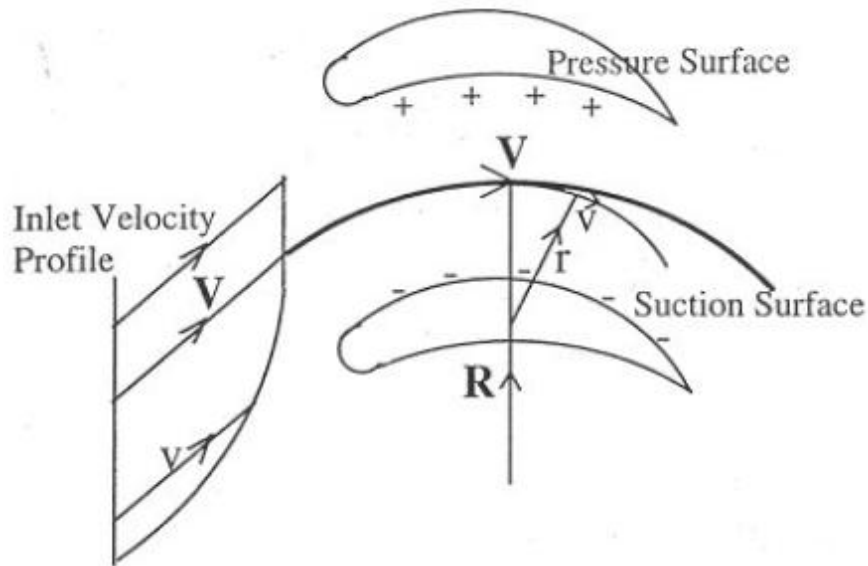
Figure 1. Turning of primary and secondary flow within an airfoil cascade [8].

The relatively slower moving secondary flow has a smaller radius of turning, which

moves toward the suction side, while the primary flow moves towards the pressure side

with a larger turning radius. A backflow occurs to maintain flow continuity due to the

6

tighter radius of turning which induces vortical flow. The vortical flow develops into a passage vortex at the airfoils exit.

A comprehensive review of secondary losses was compiled by Sieverding [9], which details the classical model of secondary flow. Sieverding described three basic vortices responsible for secondary flow losses, which are the passage, horseshoe, and corner vortex. The passage vortex is secondary circulation, which occurs due to the distortion of the inlet boundary layer as it passes through a curved passage. Sieverding describes the notorious horseshoe vortex as the rolling up of the endwall boundary layer in front of a cylinder and takes its name from its shape as it passes on both sides of a vane. Eckerle and Langston [10] explain the horseshoe vortex formation is to due high energy flow within the boundary layer moving away from the stagnation region of a cylinder as seen in Figure 2. This flow tends to moves downward to lower energy fluid underneath. As the high energy fluid comes within close proximity of the endwall, it travels upstream forming a saddle point which separates from the surface. As the flow translates from the plane of symmetry, a vortex is formed and travels around the cylinder.
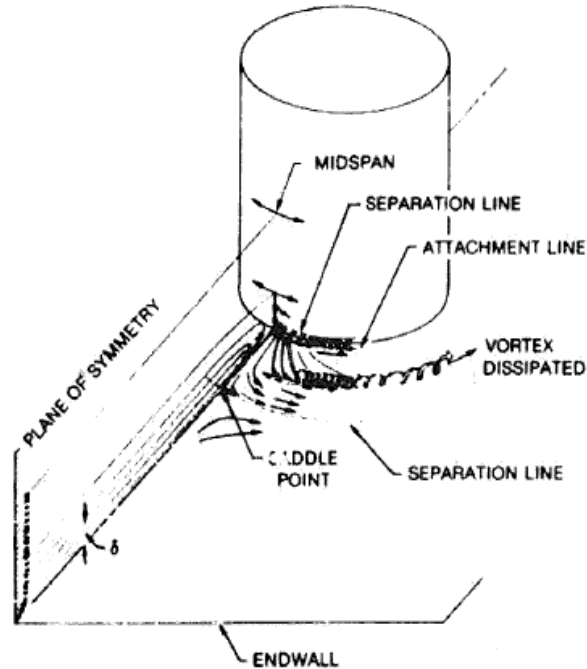
Figure 2. Horseshoe vortex formation around a cylinder [10].

Sieverding provides accounts of Klein [11] and Langston [12] who were the pioneers in the initial work of describing how the passage and horseshoe vortex interact. Klein was the first to describe a "stagnation vortex" and later provided a models represented by Figure 3a. This model depicts the horseshoe and passage vortex counter rotate to each other. Langston later developed a model seen in Figure 3b, which had two differences from Klein's model. The first described the pressure side horseshoe vortex as having the same orientation as the passage vortex and merged to become one. Langston then determined the suction side of the horseshoe vortex rotated opposite of the passage vortex, they continued into the suction side corner, which Klein [11] had previously concluded gradually dissipated. These results were similar to those found by Marchal and Sieverding [13] who used a light sheet technique to visualize sectional views of the flow in selected planes of blade passages. They confirmed with Langston that the pressure side horseshoe vortex and the passage vortex merged to form a single vortex.

8
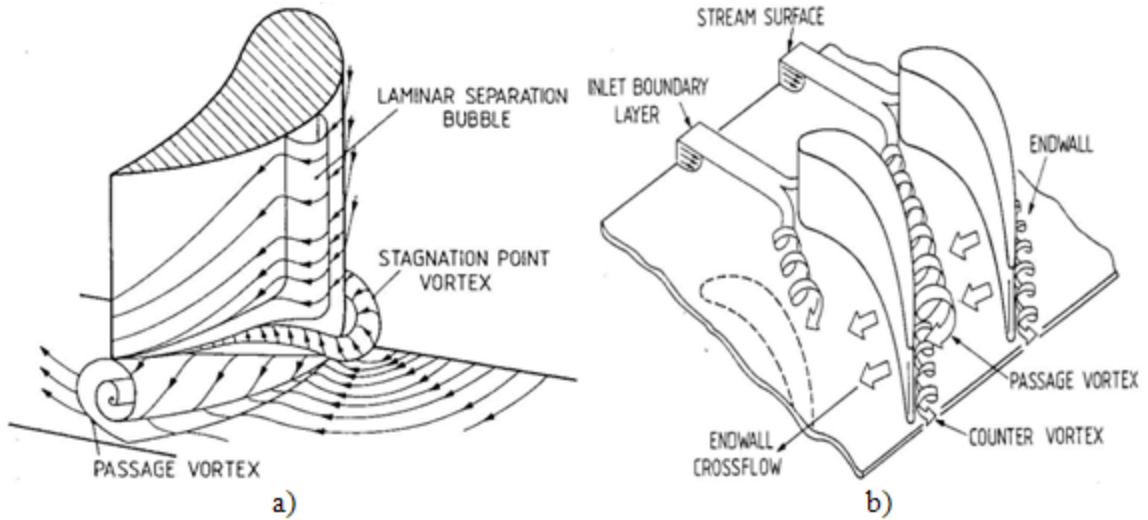
Figure 3. Klein's model a) and Langston's model b) describing the stagnation and passage vortex orientation to one another [11, 12].

Their smoke visualizations showed a counter-rotating suction side horseshoe vortex in the trailing edge plane at the mid-span side passage vortex, rather than in the corner as Langston showed. Research conducted by Goldstein and Spores [14], based on mass transfer results, indicated the suction leg of the horseshoe vortex stays above the passage vortex and travels with it. A graphical depiction of Goldstein and Spore secondary flow model is provided in Figure 4, which will be later referenced in CHAPTER VI.
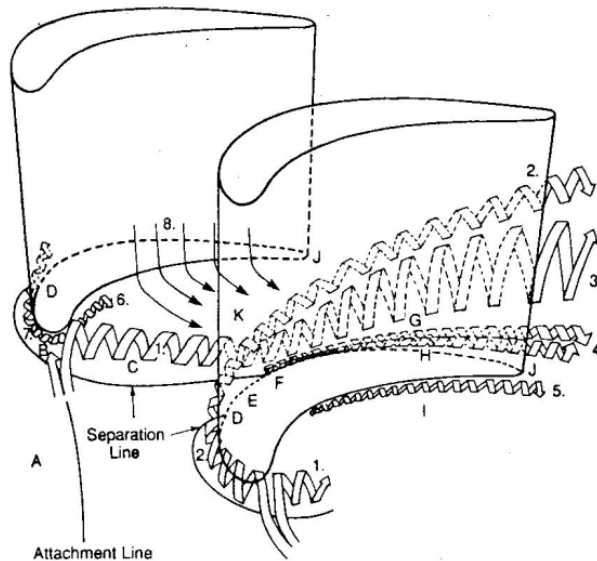
Figure 4. Goldstein and Spores secondary flow model [14].

Sieverding describes a corner vortex as rotating in an opposite sense to the passage vortex and is located in the suction side and wall corner. According to Sieverding, it is small and hard to visualize but can be found in spanwise angle distributions behind highly loaded cascades. Chung and Simon [15] were also able to locate and measure the corner vortex with an oil and lampblack technique. Their experimental results also agree with Sieverding and conclude the formation of the corner vortex is the result of two boundary layers that are wrapped up by the motion of the passage vortex.

Work on secondary losses by other researchers such as Sharma and Butler [16] proposed a modified model seen in Figure 5. The author's model depicts the counter vortex wrapping around the passage vortex, which was determined by other researcher and their own experimental observations. This model was then used to formulate a semi-empirical model for determining losses in a turbine. Their work led to findings which described how the inlet boundary layer losses are transferred through the cascade without causing any further losses and was independent of passage turning. Therefore, the saddle point separation boundary layer essentially separates it from the effects of turning.

10
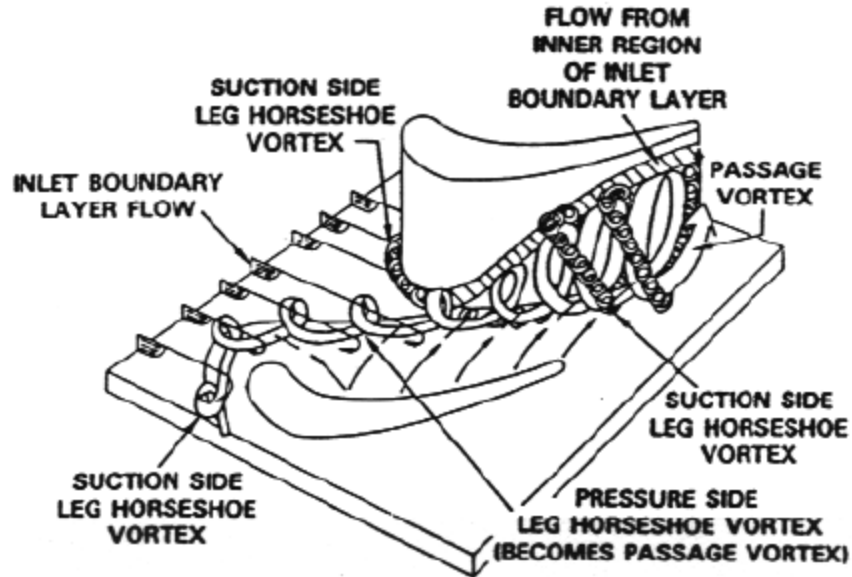
Figure 5. Sharma and Butler's secondary flow loss model [16, 17].

Additional work conducted by Wang, Olson, Goldstein, and Eckert [18] utilized smoke and laser light sheets to create a highly detailed model of vortical motion near an endwall. Their technique provided improved visualization, which depicted addition vortices and movement characteristics. A very intense vortex called a wall vortex was found on the suction wall which originated from the leading edge stagnation point and is swept up on the suction wall by the passage vortex. This new vortex has been found to have significant impact on mass transfer considering its relatively small size. Wang et al. also found the path and size of the passage vortex is affected by the turbulence level. Other researchers such as Ames, Johnson, and Fiala [19] have found effects on secondary flow patterns due to high freestream turbulence levels. The researchers determined from experimental results, a weak discernible secondary loss core and broader wakes at high turbulence. Their results concluded an augmentation of total pressure losses due to high turbulence attributed to enhanced mixing.

11

The negative impact secondary losses have on turbomachinery has been characterized by Gregory-Smith [8]. These impacts are described by a variation in flow exit angle causing a change in output work of the turbine, extra losses in the vane or blade row, enhanced heat transfer and film cooling, and increased unsteadiness possibly affecting the mechanical design of the blades. He proceeds to enforce the fact that severely non-uniform flow at the exit of one blade or vane row would have a detrimental increase in losses downstream. Gregory-Smith states, that up to half of the loss in a high pressure turbine stage with a low aspect ratio can be attribute to secondary losses.

Extensive research has been conducted to diminish secondary losses and increase efficiency. Shih and Lin [20] performed research with leading-edge airfoil fillets to prevent secondary losses. The fillets increase the extent of the stagnation region down near the endwalls and past the geometric leading edge. The relocated stagnation zone is then positioned against a flatter region of the airfoil, which results in a thicker boundary layer. By increasing boundary layer thickness, velocity gradients are reduced, resulting in a reduction of secondary losses. Similar results were also found by Zess and Thole [21] who were able to completely restrict the formation of the horseshoe vortex with a leading edge fillet seen in Figure 6. Their experimentation concluded the prevention of the horseshoe vortex and delayed formation of the passage vortex can be attributed to the inlet boundary layer accelerating up the filleted leading edge. These conclusions, resulting from filleted leading edges, were confirmed by Han and Goldstein [22] and also by Saur, Muller, and Vogeler [23] who used a bulb shape geometry at the leading edge.

12
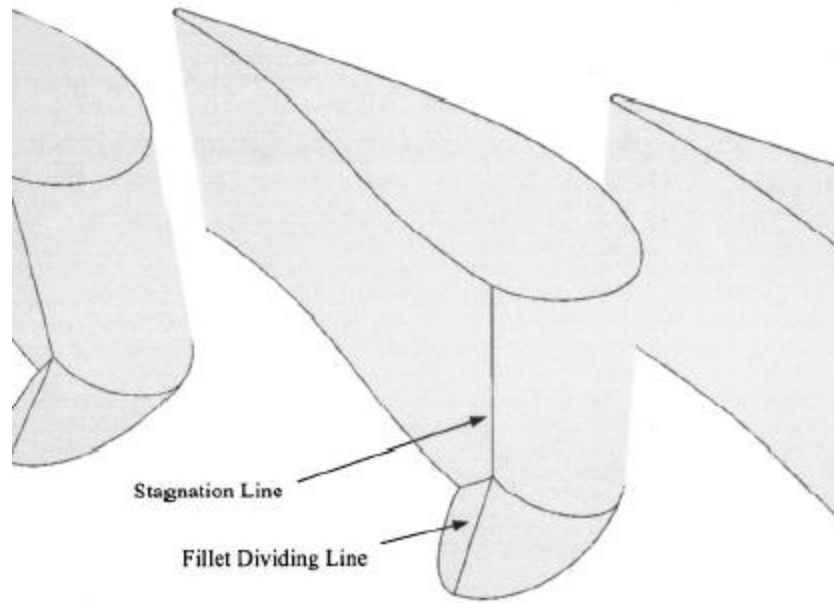
Figure 6. Airfoil leading edge fillet [21].

Contoured endwalls is another method used for decreasing secondary flow losses. Researchers such as Knezevici, Sjolander, and Praisner [24] performed experiments with non-axisymmetric contoured endwalls and found a reduction in secondary losses. According to these authors this is due the reduction in pitch-wise cross-passage flow near the endwall and spanwise flow reduction resulting in a weaker passage vortex. The roll-up of secondary flow is delayed due to the weaker passage vortex mitigating the amount of fluid convected into the vortex. Further studies by Burd and Simon [25] have also confirmed through experimentation, with one contoured and one flat endwall, a reduction of total pressure loss resulting in a decrease in secondary loss.

Wind Tunnel Test Facilities

The performance of aviation gas turbine engines at cruise is not well understood due to the restricted capabilities of ground test facilities. Much of what is not well known is the performance of the low pressure turbine and factors such as blade loading, endwall losses, wake passing effects and boundary layer separation, and transition [26]. Ground

13

test facilities must be able to reproduce conditions seen at cruise altitude to be effective in producing meaningful experimental data which can be used to further understand low pressure flows. Rivir [3] explains that a low pressure turbine operates at a chord Reynolds number of 10^6 at takeoff but falls down to 10^5 at cruise conditions. With this drop in Reynolds number Sharma, Ni, and Tanrikut [17] found the loss coefficient nearly doubles from a Reynolds number of 300,000 to 50,000. Turbulence conditions must also be accurately recreated, which according to Simon and Kaszeta [27] can be around 10% in the low pressure turbine.

<div align="center">Low Reynolds Number Flow Test Facilities</div>

Currently, there is a broad spectrum of facilities that perform aerodynamic testing at cruise relevant Reynolds numbers and turbulent conditions. Though these facilities are unable to recreate engine relevant Mach numbers, their work is pivotal for understanding the flow physics at cruise conditions. Such work was conducted by Schobeiri, Ozturk, and Ashpis [28] who performed research at the NASA Glen Research Center with an open flow subsonic linear cascade facility. This facility was used to perform aerodynamic testing at Reynolds number between 50,000 to 125,000 with a wake generator. Vane surface pressure measurements along with hotwire boundary layer measurements were acquired with and without the wake generator operating. The authors found the wake turbulence was able to enhance momentum and energy into the boundary layer which reduced the separation zone on the vane suction side. The suction side separation zone has also been studied by Satta, Simoni, and Ubaldi [29] who used a three vane, high-lift low pressure profile open flow linear cascade. The authors conducted testing at a Reynolds number of 70,000, and found a large laminar separation bubble on the suction

14

side. Their data conclude the separation bubble was reduced when wakes were present; this was due to the increased mixing causing the boundary layer to reattach. Other LPT aerodynamic work with open loop subsonic wind tunnels has been performed by McAuliffe and Sjoland [30] who sought to influence separation with active flow control. Their open flow cascade used for testing is seen in Figure 7, which is similar to many of the test cascades used for low Reynolds number research. McAuliffe and Sjolander performed testing at Reynolds numbers of 25,000 and 50,000 at freestream turbulence levels of 0.4 and 4%. Their work utilized a test vane with flow slot, which air was pumped through in an attempt to inject momentum into boundary layer and prevent separation. The authors found the flow injection to prevent flow separation and reduce profile loss at both Reynolds numbers but only for the low turbulence condition of 0.4%. At the higher turbulence level, the injected flow caused earlier separation and increased profile loss.
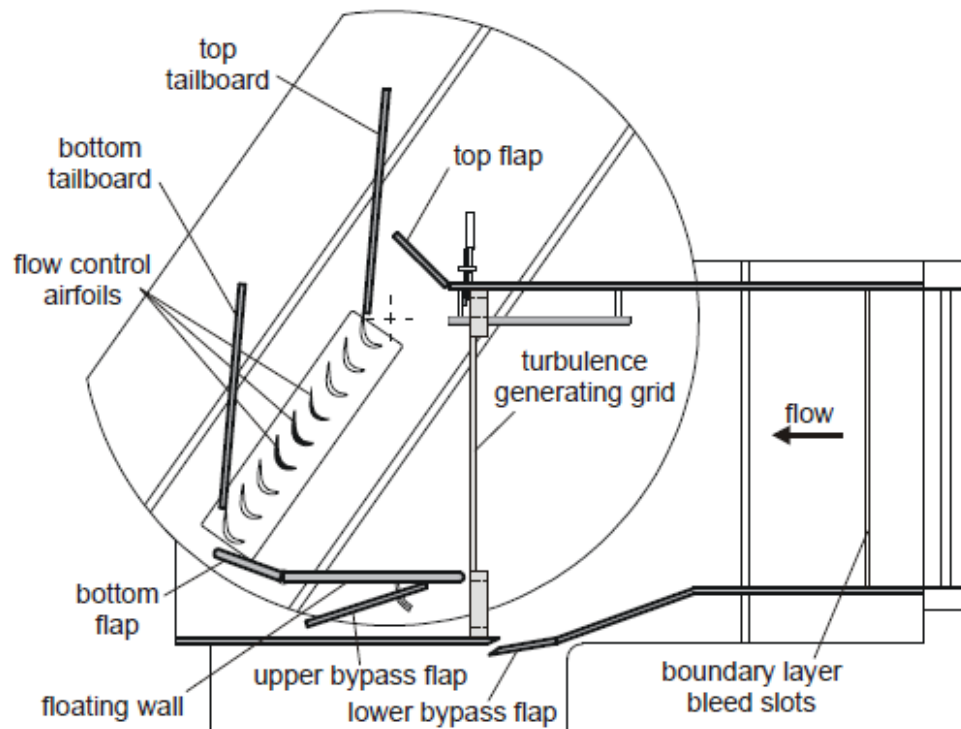
Figure 7. Subsonic open flow cascade used for low Reynolds number research [30].

Close looped facilities have also been used for conducting low Reynolds number research. The closed loop wind tunnel seen in Figure 8 was used by Van Treuren, Simon, and von Koller [2] at the United States Air Force Academy. Testing was conducted at Reynolds numbers between 25,000 and 50,000 with grid generated freestream turbulence intensities of 1 to 9%. A loss coefficient pitot rake was used to measure flow loss, and vane surface pressure measurements were also acquired. Due to the minor velocities used for testing, the pressure sensitivity of the instruments used had an approximated 32% error. This high error demonstrates the difficulties researchers have with low Reynolds number research under low velocity flow conditions. The author's experimental results indicated a steady separation on the vane suction region at low turbulence, which was eliminated with higher turbulence. Their work also studied the influence of attaching micro vortex generators on the test vane's surface to prevent separation by energizing the boundary layer. The results showed augmented transition at high turbulence provided little noticeable improvement due to transitioning already occurring, but the vortex generators provided the necessary mixing to reestablish attachment at low freestream turbulence.
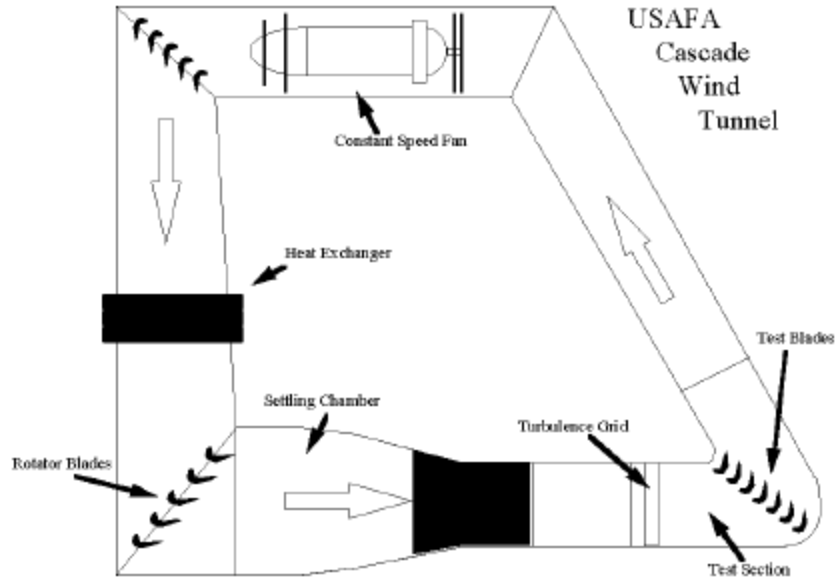
Figure 8. Closed loop subsonic linear cascade facility at the United States Air Force Academy [2].

Volino and Hultgren [31] also conducted testing in a closed loop facility at the NASA Glen Research Center. Their testing specifically analyzed the transition of boundary layers at Reynolds numbers between 50,000 to 300,000 over a flat plate which was subjected to a stream-wise pressure gradient corresponding to the suction side of the "Pak-B" vane profile. The instrumentation utilized a single hotwire traversed by stepper motors. Volino and Hultgren found Reynolds number and freestream turbulence levels do not affect boundary layer separation unless they are strong enough to cause transition before separation. They concluded transition begins at the shear layer but moves to the near wall region and causes the boundary layer to reattach. Similar testing was conducted by Shyne, Sohn, and De Witt [26] who studied Reynolds numbers between 100,000 and 250,000 with various freestream turbulence intensities. Smoke-wire visualization, hot film gauges, and static pressure instrumentation were used during this study. The author's observations showed short separation bubbles forming with the laminar portion being steady, while the region downstream from transition was unsteady. Their results

17

coincided with the generally accepted conclusion that separation bubble length and height decrease as freestream turbulence increases.

High Speed Flow Test Facilities

The study of engine relevant Mach number flow is performed in transonic linear cascade wind tunnels, which utilize a variety of methodologies to achieve desired velocities. The most common type of transonic wind tunnel is of a blow-down type, which depend on high pressure and large volume tanks to achieve desired flow conditions. Though the transonic facilities are able to achieve engine relevant Mach numbers, many of them are unable to reproduce low Reynolds number flow. Also, blow-down facilities are only able to achieve high velocity for short durations lasting only seconds, making data measurements difficult to acquire.

A blow-down facility seen in Figure 9 is used by Jouini, Sjoland, and Moustapha [32] to study mid-span aerodynamic performance of vanes at transonic Mach numbers. The testing was conducted over a range of Mach numbers of 0.5 to 1.2 and for Reynolds numbers from 400,000 to 1,000,000. Vane surface pressure measurements were acquired with a 48-port Sanivalve system and a miniature fast-response Kulite pressure transducer. Exit velocity surveys were performed using a 3-hole probe. The authors' results showed significant profile losses above a Mach number of 0.85 and Reynolds numbers below 600,000. This type of loss trend was also experienced by Mee, Baines, and Oldfield [33] who used a blow-down transonic wind tunnel. Their conditions encompassed Mach numbers between 0.7 to 1.1, while Reynolds numbers were around 1,000,000. Vane surface pressure measurements were taken along with Schileren photographs which showed shock wave formations. Their results concluded boundary layer formation loss

18

dominates at low Mach numbers but becomes a small component at higher Mach numbers. The authors concluded recompression shocks striking the suction surface boundary layer do not lead to an augmentation of boundary layer loss. With shock formation in transonic wind tunnels researchers such as Rona, Paciorri, and Geron [34] have utilized methods to prevent recompression shocks from influencing results. The authors studied the influence of walls within transonic cascades using the University of Leicester blow-down transonic wind tunnel. Utilizing CFD calculations the researchers were able to design endwalls to mitigate shock reflection. The tests were captured with Schlieren visualization and analyzed. The results indicated substantial decrease in shock reflection, providing the researchers confirmation that their CFD model adequately predicted flow conditions.

19
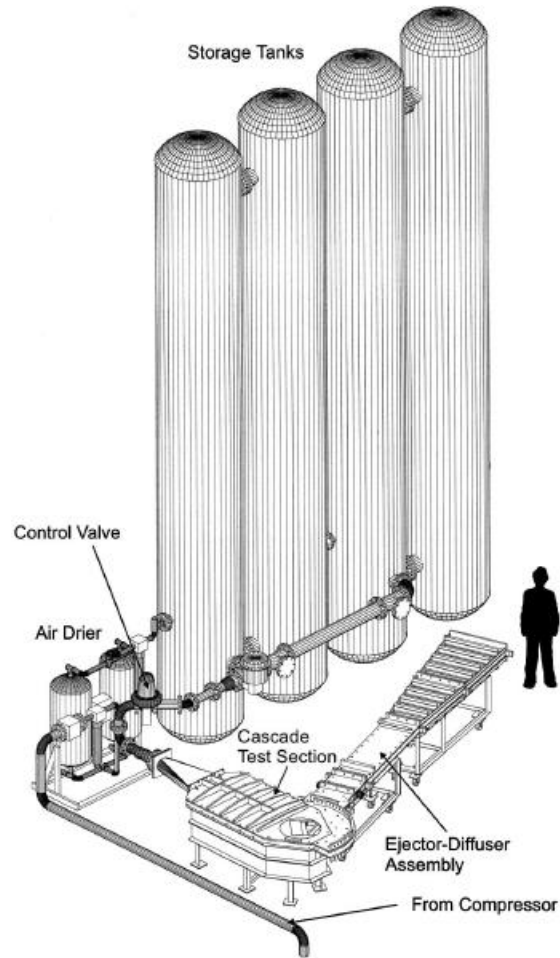
Figure 9. Carelton University blow-down wind tunnel [32].

A variation to the blow-down type facility is a reversal of its concept seen in Figure 10, which uses a large vacuum tank and atmospheric pressure as the driving force. The facility located at the Royal Military College of Canada was used by Woodson, Asghar, and Allan [35] to examine the flow quality through a transonic cascade. The facility was designed to operate at choked conditions with an exit Mach number of 1.05. Inlet and outlet static pressures were recorded to determine the periodicity of the flow conditions. Schlieren flow visualizations were used to record shock formation. The results indicate the transonic cascade produced periodic flow, which was determined

20

from symmetric inlet and outlet static measurements. The Schlieren flow visualization showed repeating shock formations in each passage, indicating periodic passage flow.
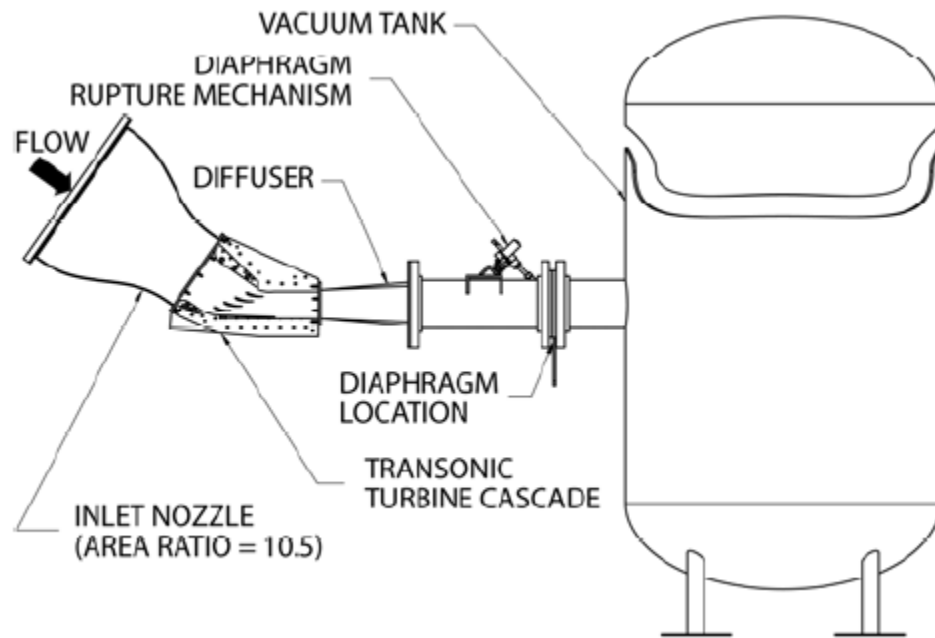
Figure 10. The Royal Military College transonic linear cascade wind tunnel [35].

Another transonic facility located at the NASA Lewis Research Center in Cleveland, Ohio provides high speed flow from combustion air. This facility was described by Verhoff and Camperchioli and Lopez [36] as being used to perform aerodynamic and heat transfer tests to validate aero-thermodynamic code. The facility has the capability of reaching an exit Mach number of 1.3 and also the ability to adjust incidence angle between -30° and +15°. The data acquisition system has the ability to measure 1,750 channels a second, with analog channels for thermocouples, pressure transducers, and the inlet angle position reporter. Another facet is the ability to remove the test section sidewall boundary layer with a bleed manifold system. The authors describe the current results of this facility as being excellent and they have great expectations for its future due to its versatility.

21

Though many transonic facilities are unable to produce low Reynolds number flow, there are several which can. The transonic blow-down facility featured by Povey, Oldfield, and Haselbach [37] at the University of Oxford is able to produce low Reynolds number flow by using a miniature scale cascade. This design feature simply reduces the scale of vane, which in turn has lower Reynolds numbers for a given Mach number. The small size allows results in lower mass flow rates, resulting in run times greater than three minutes, which is 60 times longer than some blow-down facilities. The extended run time also allows exit velocity surveys and highly resolved digital Schlieren flow visualizations. Another facility able to control Reynolds number is detailed by Gostelow and Watson [38], which is a variable density transonic wind tunnel at the Whittle Laboratory in Cambridge, England. The facility is a close-circuit design which is driven by a 1.5 MW compressor. It is capable of producing sustained air speeds up to Mach 1.35 with the ability to adjust Reynolds number between 100,000 to 2,000,000. The facility instrumentation includes the Schlieren visualizations, traversing exit probe, and scanning of pressure transducer signals. Experimental work conducted by Hodson [39] at the facility demonstrates how its unique flow conditions can be used to study boundary layer transition and separation near the leading edge of a blade. His work utilized hot film instrumentation, at the mid-span of the vane near the leading edge to acquire heat transfer measurements. Hodson also acquired surface vane pressures along with hotwire anemometry measurements to study boundary layer transition. The results indicated velocity overspeed at the leading edge of the suction surface, which then decelerated resulting in separation of the laminar boundary layer. He then found relaminarization of the boundary layer as it accelerated at peak suction of the blade. The results represent an

22

important venue of research that industry is seeking to improve efficiency for low pressure turbines.

Linear Cascade Heat Transfer

Increasing the power generation and efficiency of gas turbine engines has resulted in higher operating temperatures. The drastic increase in efficiency was clear when the first gas turbine powered locomotive in 1941 had an efficiency of 18.4% and in 1992 a simple-cycle industrial gas turbine engine had an efficiency of 40% [40]. The increase of temperatures is in direct relation to gas turbine efficiency, which has increased from 1500 K to 1750 K in the span of a decade [14]. Producing lower levels of NO_x has also affected temperature variations within engines by generating flatter temperature profiles leaving combustion systems. Due to the gas turbine industries' drive to produce ever increasingly efficient, powerful, and cleaner emissions, the appetence to understand heat transfer within gas turbine engines has followed suit.

The influence of the freestream turbulence intensity and the Reynolds number has been the general focus of heat transfer research on vanes and blades. Such research was conducted by Ames [41], who performed vane heat transfer tests over exit Reynolds numbers based on chord lengths of 500,000 and 800,000. Four levels of turbulence conditions were used at each Reynolds number for low (1.1%), moderate (7.8%), and high (8.3 and 12.0%) turbulence. Ames' results indicate an important influence on heat transfer as turbulence increased. His data show the turbulence length scale, Lu, has a drastic influence on the stagnation region and pressure surface heat transfer. Ames provided a good engineering approximation developed by Ames and Moffat [42] for stagnation region heat transfer with high freestream turbulence in Equation 2.2.

23

$$Nu/Re_D^{1/2} = 0.95 + 0.038\, Tu\, Re_D^{5/12}(Lu/D)^{-1/3} \qquad (2.2)$$

Ames concluded that the dependence of heat transfer augmentation on the Reynolds number was estimated to be scaled by the ⅓ power for the pressure surface. The power relation was shown by the decline of the heat transfer coefficient by 70% from the stagnation region to the rest of the pressure surface.

Vane surface heat transfer research in regards to compressible flow was performed by Ames, Zhang, and Smart [43]. The test conditions consisted of a linear cascade with exit Mach numbers of 0.60 and 0.75 at turbulence levels between 2 and 12%. Results indicated agreement with increasing turbulence levels affecting the pressure and stagnation heat transfer. The correlation proposed by Ames and Moffat [42] also produced an agreeable prediction of heat transfer augmentation in the stagnation region. Ames and Moffat's findings were also confirmed by Nasir, Carullo, and Ng [44] who used large scale freestream turbulence to enhance heat transfer. Their testing conditions consisted of exit Mach numbers of 0.55, 0.75, and 1.01 with turbulence levels between 2 and 16%. The results indicated higher augmentation heat transfer levels on the pressure surface than suction surface for all Mach numbers tested. The high freestream turbulence enhanced the transition on the suction surface at Mach 0.55 and 0.75 cases, but no effect was seen at Mach 1.01. These results also showed an increase of heat transfer levels and earlier boundary layer transition on the suction side as the Reynolds number increased.

A comprehensive review of the heat transfer for nine different vane and blade geometries was performed by Boyle, Ames, and Giel [45] to evaluate predictive codes. The data for the different heat transfer tests was compiled to provide a means to evaluate predictive heat transfer codes. The codes utilized were AMLE, AMS, SKVF, and SK.

The AMLE model had the smallest deviation from the experimental values for the vane profiles. Further analysis of the results indicated the sensitivity of each model to turbulence intensity. The SKVF model proved to be least influenced by turbulence intensity while the SK model was highly influenced.

Due to changing combustion methodologies, mid-span heat impingement on vanes and blades has reduced, while heat loads have increased on endwalls [46]. Endwall heat transfer is highly influenced by secondary flows, which Ames, Barbot, and Wang confirmed experimentally. Their experiments were conducted over a range of Reynolds number between 500,000 and 2,000,000 with turbulence levels between 0.7% and 14%. Utilizing liquid crystal thermography, endwall heat transfer levels were found to be the highest downstream from the vane's trailing edge due to a velocity deficit. Corner vortices are also thought to influence heat transfer at the aft portion of the vane as well. The authors also found heat transfer to be 10 to 20% higher at most endwall locations for the highest turbulence cases, which smooth isotherms geometric orientation. A prime feature of these tests was the high heat transfer rates at the leading edge of the vanes and the wake regions due to the wake. Similar results of the augmented leading edge and the wake region heat transfer found by Ames, Barbot, and Wang [46], were confirmed by Goldstein and Spores [14] who used a naphthalene mass transfer method.

Five-Hole Probes

Five-hole cone probes are used in a variety of turbomachinery applications and have many geometric configurations, some of which can be seen in Figure 11 [47]. These five-hole probes are commonly used in linear vane cascades, where exit velocity surveys are measured at an area plane perpendicular to the flow direction. Pyramid and cone

25

probe configurations are commonly used in linear vane cascades and are utilized by researchers such as Ames, Johnson, and Fiala [19] and Dominy and Hodson [47]. The forward facing pyramid probe can be configured with four tubes grouped at ninety degree increments around a central tube. The outer ends are cut to a desired angle to form the four sided pyramid geometry (Figure 11a). The perpendicular pyramid probe generally consists of a solid four sided pyramid with holes drilled normal to the faces seen in Figure 11b. The cone probe seen in Figure 11c and 11d have a solid tip with either forward facing or perpendicular holes drilled normal to the surface. Other five-hole probes commonly used are the hemispherical probe and the pitch pipe probes. Hemispherical probes simply have a spherical radius at the tip with pressure holes drilled normal to the surface. The pitch-pipe probe is configured with five tubes grouped on a single horizontal plane, with each tip but one, cut at the same angle, but oriented 90° apart from one another to measure total, pitch, and yaw flow pressures.

a) Forward facing pyramid   b) Perpendicular pyramid

c) Forward facing cone   d) Perpendicular cone

e) Hemispherical   f) Pitch-pipe
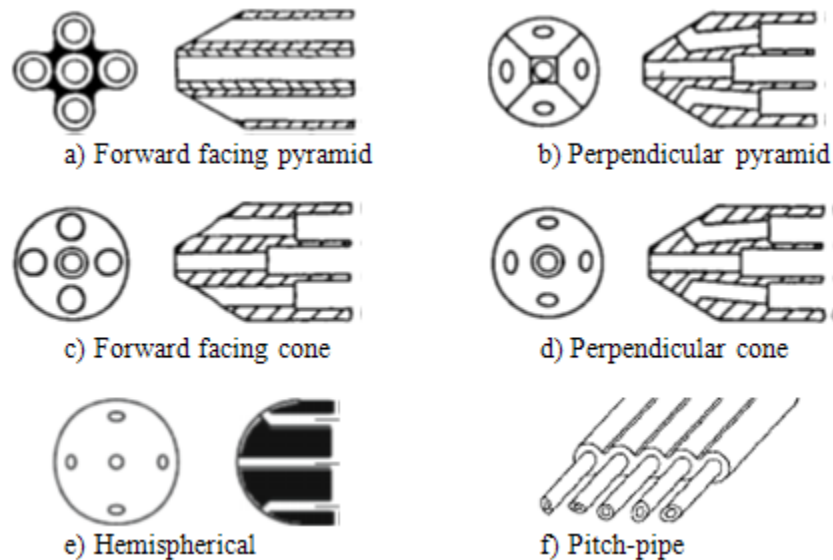
Figure 11. Schematic of various geometries of five-hole probes used for exit flow field survey measurements in aerodynamic research.

The size of a five-hole probe is generally desired to be small enough to provide a clear spatial resolution of the velocity field but not be significantly influenced by Reynolds number [47]. Adcock and Smith [48] experienced Reynolds number effects with a pyramid probe being used below a Reynolds number of 100,000. While using conical probes, Wallen [49] found similar Reynolds number sensitivities, which produced errors the in measurement of stagnation and static pressures. Probe sensitivity to Reynolds number is clearly evident in the literature and should be considered when choosing probe geometry for low and high Reynolds numbers.

Attaining close probe proximity to endwalls is crucial for measuring secondary losses and bleed boundary conditions. When proximity is limited due to the diameter of the probe, a pitch-pipe design is usually used. Schoeneberger and Greber [50] began using a new design for a pitch-pipe probe, which reduced the effective probe diameter by a factor of five. His improved probe enabled more data points to be measured within the vicinity of the wall, where a standard circular probe could not measure. Schoenenberger found pitch-pipe probes are ideal for rectilinear surveys where gradients in the freestream velocity are significant or where there is appetence for boundary layer measurements.

Hole geometry and location, also have an effect on a probes ability to measure accurate pressures. Perpendicular holes have smaller areas than forward facing holes, which results in an improvement of dynamic pressure sensitivity according to Dominy and Hodson [47]. These results were confirmed by Fransson and Sari [51], who found that cone probes with pressure tapings drilled normal to the probe surface hold better characteristics than holes parallel to the flow direction. Pressure holes located farther from the tip are less likely to be affected by leading edge separation but have a reduction

27

in sensitivity [47]. Bryer [52] found pyramid-head probes have several advantages over conical or hemispherical probes because of their flat surfaces. This advantage is due to the lower pressure gradient across their surfaces resulting in reduced sensitivity to orifice location with Reynolds number and compressibility effects.

According to Dominy and Hodson [47], the pyramid and cone angle also influence pressure measurements due to how the degree of separation is related to angle. The authors found for measurements below a Reynolds number of 20,000 a probe angle of 90° should be used, but for Reynolds numbers between 20,000 and 40,000, a 60° probe should be used. Therefore, the greater the cone angle, the lower a Reynolds number can be before separation effects will be noticed.

High velocity flows and freestream turbulence should also be considered in the geometry of a five-hole probe. Higher velocities would have some compressibility effects, which could influence flow patterns. Bow shocks emanating from the probe tip could also influence pressure downstream. Turbulence levels could augment or diminish separation bubbles and have an adverse effect on probe sensitivity [47].

Due to the uniqueness of each probe, interpreting pressures encountered requires the probes to be calibrated over a range of flow conditions pertinent to actual measurement conditions. Two methods commonly used to calibrate five-hole probes are a nulling or a non-nulling technique. The nulling technique requires a sophisticated traversing system and an extensive data acquisition time, since the probe must be pitched and yawed at each measurement location until the four outer pressures are equal [53]. The non-nulling technique is performed by exposing the probe to a known flow and varying the yaw and the pitch over a range of angles, which exceed expected flow angles.

28

Due to the extensive time and equipment required for either calibration technique, advanced numerical and computational fluid dynamic (CFD) methods have been used to extend the range in Mach and Reynolds number for these calibrations. Morrison, Pappu, and Schobeiri [54] have used CFD and Taylor-Maccoll differential equations to extend the predicted Mach coefficient (above Mach=3.0) for the five-hole cone probe placed on the first Ares I-X rocket. Other researches such as Huffman, Poti, and Rabe [55] and Gonsalez and Arrington [56], have created mathematical models of cone probes in hopes that analytically generating calibration coefficients for Mach numbers, other than those found during calibration. Huffman verified his theoretical model with actual wind tunnel conditions over a range of flow angles and Mach numbers up to 0.9. Although, there were some variations in theoretical to measured coefficients, Huffman believes the mathematical model can be employed as a preliminary design tool.

CHAPTER III

EXPERIMENTAL APPROACH—AERODYNAMICS

The following chapter details the experimental setup for the vane surface Mach number distribution and the vane aerodynamic loss survey tests. A description of the test facility will be given along with a description of the vane cascade used to perform the tests. A brief description will be given on the 5-hole cone probe along with the traversing system used to measure the aerodynamic loss data. An in-depth comprehensive description is given in CHAPTER IV on the cone probe, which details the calibration process and results of the 5-hole cone probe. The vane cascade was tested at low turbulence and high turbulence generated by a mock aero-derivative combustor. The low and high turbulence cases were tested over Mach numbers of 0.7, 0.8, and 0.9 at Reynolds numbers of 90,000, 180,000, 360,000, and 720,000 based on true chord exit conditions.

Compressible Flow Wind Tunnel Facility

The University of North Dakota's compressible flow wind tunnel facility seen in Figure 12, includes a 10X18 RGS Roots blower driven by a 56 kilowatt (KW) electric motor, vacuum pump, flow conditioning unit, a linear vane cascade test section, a custom traversing system, transonic diffuser, and fin and tube heat exchanger.
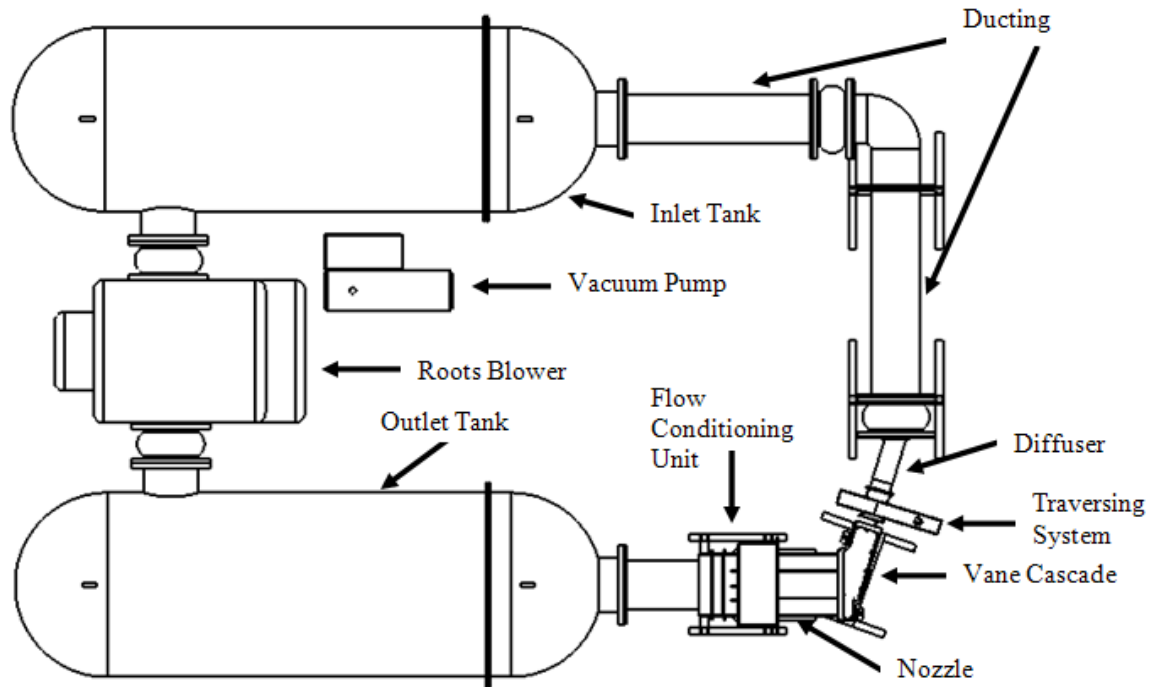
Figure 12. Cascade configuration of compressible flow wind tunnel.

The closed loop transonic facility allows independent control of the Reynolds number and the Mach number. Producing low Reynolds number flow in the high speed facility requires sub-atmospheric pressures within the wind tunnel. Sub-atmospheric pressures are achieved with a vacuum pump seen if Figure 13. The rugged 63B vacuum pump is capable of a continuous 0.5 Torr vacuum, at a volumetric flow rate of 1.27 m^3/min. The vacuum within the tunnel is adjusted with a custom control system, which enables the variation of the pressure within the tunnel to achieve a range of Reynolds numbers between 50,000 to 1,000,000. The pressure controls on the vacuum pump consists of a 3.12 cm ball valve as a course adjustment, and a 1.27 cm needle valve with a C_v of 0.73, as the fine adjustment. An air filter with a polyester element capable of filtering particulate 5 microns in size was integrated into the vacuum system. The filter is required due to the intake of outside air into the vacuum piping, which balances the pressure inside the tunnel to the amount being withdrawn by the vacuum pump.

31

The Mach number within the wind tunnel is controlled using a large Roots blower capable of a volumetric flow rate of 105 m^3/min. The Roots blower, seen in Figure 13, is driven by a 56 KW electric motor that is controlled by a three phase, 60 Hz Yaskawa P7 drive. The output power, voltage, current, and frequency can be monitored by the Yaskawa control panel LCD display, which provides the means of mapping the functionality and the capabilities of the facility. A custom remote control was constructed to enhance operator efficiency, which provided control over motor RPM at either the computer station or the vacuum pump controls.

Figure 13. Heat exchanger and vacuum pump systems used during wind tunnel operation.

The airflow movement through the wind tunnel begins by being pumped through the Roots blower and then into an outlet tank seen in Figure 14a. The 1.92 m^3 tank has been insulated with polyimide foam, which possesses high thermal and acoustic performance properties. The foam was covered with a white navy cloth to enhance its resistance to degradation by air movement. The insulated tank provides a means to

32

dampen oscillatory pressure fluctuations from the pump and aids in unifying

temperatures to steady state condition.
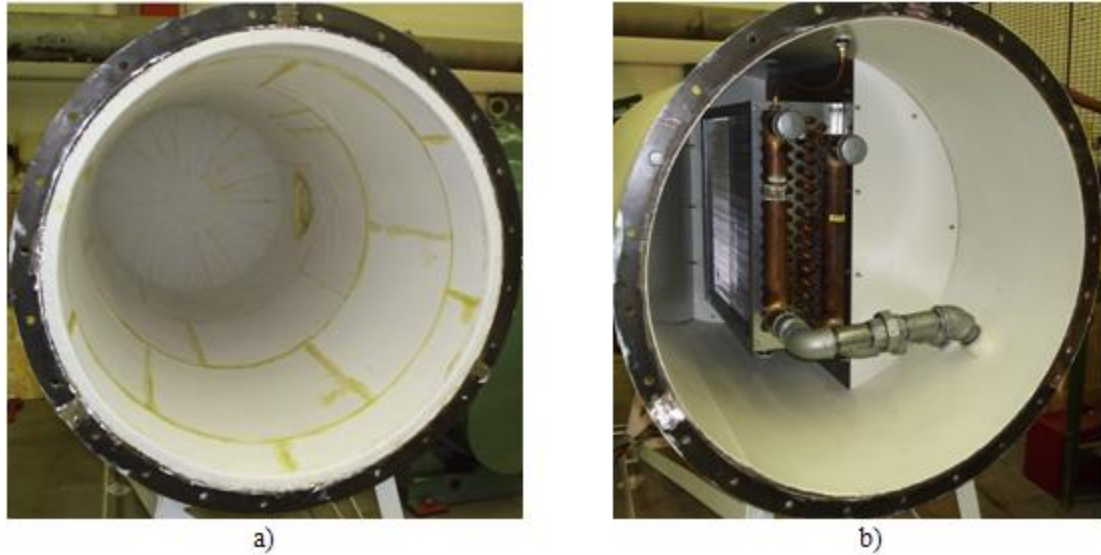
Figure 14. Insulated outlet tank (a) and inlet tank (b) which contains a fin and tube heat exchanger.

After passing through the outlet tank, the airflow enters a circular to square pipe

duct, which leads into the flow conditioner. The flow conditioner unifies velocity

distribution in the flow field as it passes through two offset perforated aluminum plates

with an open area of 0.056 m^2 and then two fine meshed stainless steel screens. The

conditioned flow then travels through either a smooth 4 to 1 area ratio nozzle or mock

aero-combustor turbulence generator and then funnels into a cascade with four vanes and

3.3 passages seen in Figure 18. The traversing system is located aft of the cascade

followed by a diffuser to recover static pressure, which extends the Reynolds number

range of the facility.

The custom designed traversing system seen in Figure 15, controls the position of

the five-hole cone probe on a Y-Z exit plane. The design incorporates two high

temperature NEMA 17 stepper motors, which articulate power screws to produce linear

33

motion in the Y and Z sliding mechanisms. The probe is held by a mounting bracket attached to the Y-slide, which provides up and down motion. The Y-slide is mounted onto the Z-slide, which provides the probe side to side motion enabling the exit plane to be traversed. High temperature Hall effect limit switches are used on the Y-slide and monetary limit switches are utilized on the Z-slide to prevent damage to the probe if traversed beyond intended range. The traversing system is housed inside a steel enclosure to provide an airtight seal to all components. Velmex VXM controllers provide power to the stepper motors through a hermetic connecter, which has integrated Teflon coated wire to withstand the high operating temperatures. High temperature silicone tubing connects the five-hole cone probe pressure tubes to a conduit running through the housing wall. The conduit contains five, 1.588 mm brass tubes, which transfer pressures sensed by the probe to miniature piezo-electric pressure sensors located outside the wind tunnel.

Figure 15. The five-hole cone probe traversing system used for exit velocity surveys during aerodynamic secondary loss testing.

Once the air has passed through the transonic diffuser it travels through return ducting and into a 1.92 m^3 inlet tank seen in Figure 14b. The inlet tank has an air to water fin and tube heat exchanger, which is supplied by a steady flow of cooling water from the facilities water supply. The cooling water flow rate to the heat exchanger is monitored by a 36 gallon per minute (GPM) rotameter and regulated with a one inch gate valve. The flow rate is adjusted to maintain constant air temperature in the tunnel for testing requiring steady state conditions. Figure 13 is an image of the heat exchanger and piping system used to cool the wind tunnel and Roots blower. The Roots blower is equipped with a shell and tube heat exchanger, which is used to cool the blower's lubricating oil supply. The water flow rate is indicated by an 11 GPM rotameter and can be adjusted with a half inch gate valve.

<div align="center">Turbulence Generator</div>

Two freestream turbulence intensities were used during aerodynamic testing. Low freestream turbulence was generated by the 4 to 1 area ratio nozzle, while the high freestream turbulence was generated by a mock aero-derivative combustor. The mock aero-derivative combustor is seen below in Figure 16 and Figure 17. The mock aero-derivative combustor was designed to create high intensity turbulence seen in industrial gas turbine engine combustors. As the air flow enters the mock combustor, it passes through two rows of four slots in the back panel and through two rows of eight holes in each side panel. The slots and holes create air jets similar to the recirculation and dilution zones of modern industrial gas turbine combustors. The air flow exits the mock combustor through a 2.35 to 1 area ratio nozzle.

35

The mean turbulence levels for the straight nozzle and mock aero-derivative combustor have not been measured. However, based on experimental work performed by Ames, Fiala, and Johnson [19] in an incompressible flow facility with similar nozzle and mock combustor geometry, a scaling factor was used to estimate values of mean turbulence intensity. The straight nozzle was estimated to have a mean turbulence intensity of 1%. The mock aero-derivative combustor was estimated to have a mean turbulence intensity of 11.5% with an energy scale (Lu) of 2.1 cm.
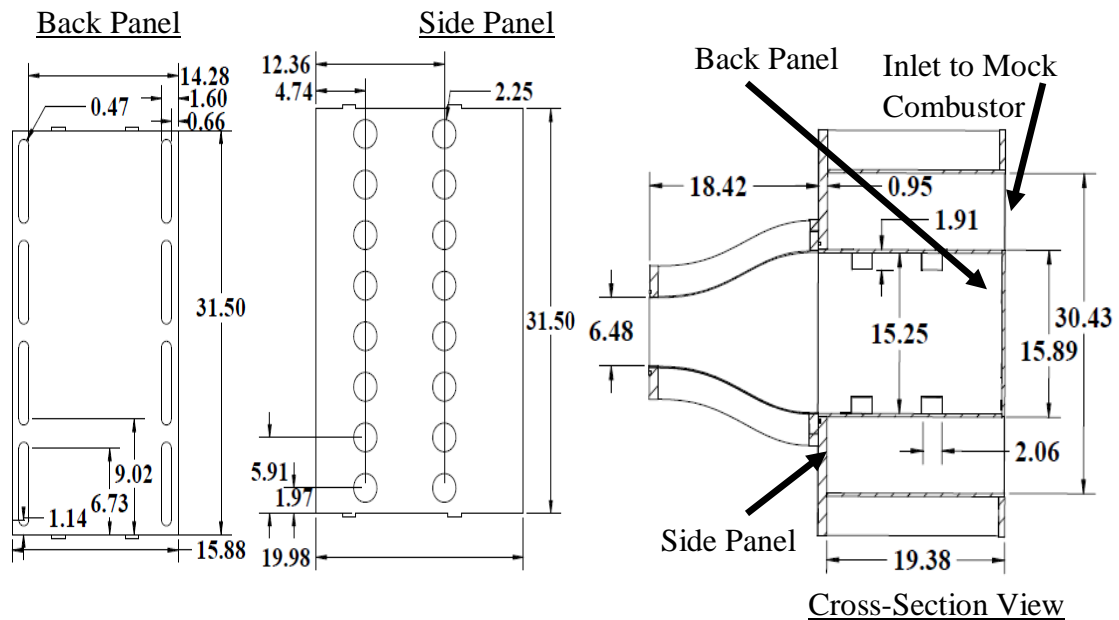
Figure 16. Diagram of aero-derivative combustor turbulence generator.

Figure 17. Images of the mock aero-derivative combustor turbulence generator.

Cascade Test Section

The linear cascade test section seen schematically and pictorially in Figure 18, was designed to represent 2-D first stage turbine vanes in a mid-size gas turbine engine. The core of the design incorporates 3.3 passages with four vanes. Bleed air flow passages are located on the pressure side of vane one and suction side of vane four, which aid in creating a uniform inlet flow. The bleed flow circumvents the cascade and is reintroduced into the duct network at the diffuser's exit. The geometry of the bleed air passages along with the curvature of the tailboard were designed in accordance to FLUENT streamline calculations. The location of the tailboard can be adjusted to ensure that periodicity of the exit flow is established.

To evaluate the inlet flow conditions, a row of thirty-two static pressure taps are located ¼ axial chord forward of the vanes. A row of twenty-nine static pressure taps were used to monitor exit conditions and are located ¼ axial chord from the vanes' trailing edge. The inlet static pressure taps are monitored and indicate flow uniformity, which can be influenced by the bleed airflow rate. The bleed air flow rate can be adjusted

37

with gate valves seen in Figure 18, to balance inlet flow conditions. The cascade is equipped with a polycarbonate view window on the top plate and tailboard. The profile of the vane, along with tapped mounting holes is incorporated into the top window to allow interchangeability of an instrumented vane. The inlet dynamic pressure is acquired by two kiel probes located ¼ axial chord upstream from the lead edge of the vanes. Two total temperature thermocouple probes are also positioned in line with the kiel probes, positioned approximately 5 cm apart. The kiel and thermocouple probes are positioned at the mid-flow passage between each vane in order to avoid disturbing flow upstream of the vanes and acquire mid-span conditions.

The instrumented experimental vane is cast from a high temperature epoxy, while the other three are constructed from aluminum. The 2.8 scale vane has a true chord of 12.10 cm and an axial chord of 5.92 cm. The vane leading edge has a diameter of 1.56 cm with a trailing edge diameter of 0.25 cm. The vanes are spaced 9.77 cm in the Y position with a span of 6.48 cm. The vanes have an exit angle of 73°.
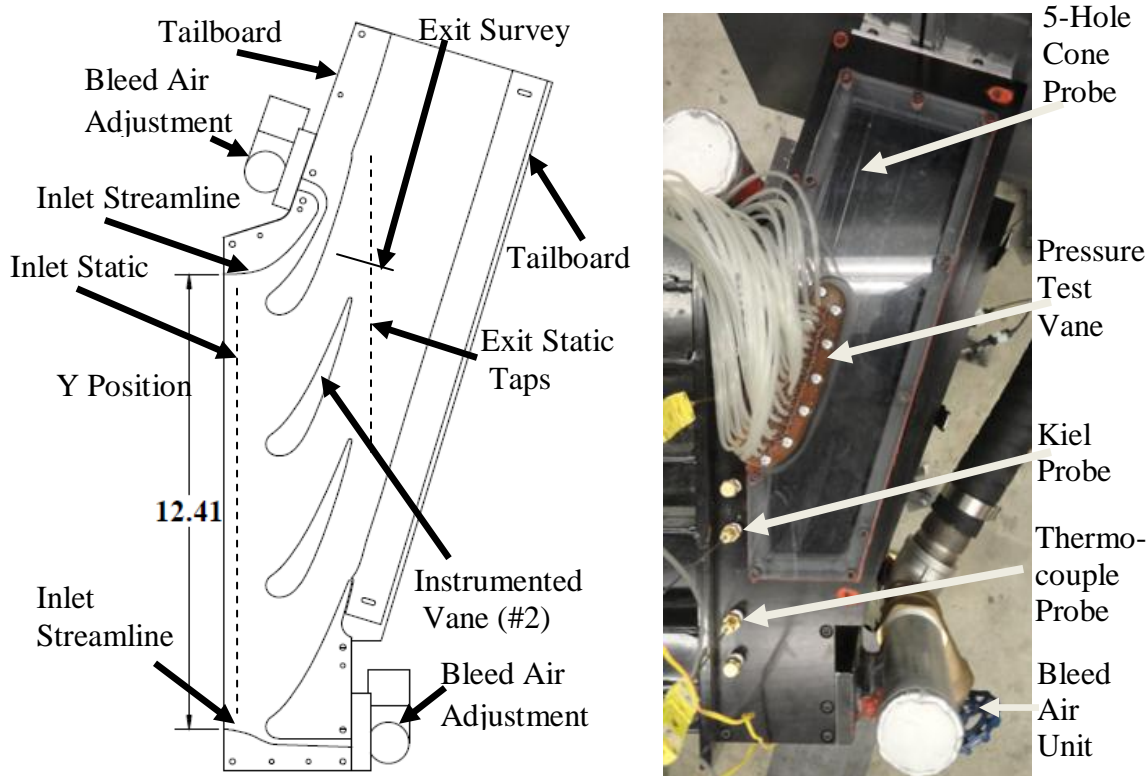
Figure 18. Schematic and photograph of the compressible flow cascade.

The aerodynamic experimental study was conducted over a range of Reynolds numbers of 90,000, 180, 000, 360, 000, and 720,000 at a Mach number of 0.7, 0.8, and 0.9, which are based on the vanes true chord exit conditions. This range of Reynolds numbers and Mach numbers is consistent with current interest of low Reynolds number flow in aviation gas turbine conditions.

<div align="center">Test Vane and Pressure Distributions</div>

The instrumented vane used to measure the static pressure distribution was cast in an aluminum mold seen in Figure 19. The vane was cast from a JEFFCO high temperature epoxy resin 1337 and hardener 3137. An underlying frame comprised of forty 0.159 cm brass tubes, held into position by two spars, was cast into the vane. The frame provided instrumentation access channels approximately 0.159 cm under the vane's surface, which extended over the span of the vane. Pressure taps could then be

39

drilled normal to the surface intersecting the tubing or the tubing could act as a conduit for thermocouple wiring. Within 24 hours of casting, the vane was thermally-cycled, which enhanced its strength characteristics when exposed to elevated temperatures.

Figure 19. Aluminum mold used to cast the vane geometry from high temperature epoxy.

The thermal cycle process was performed by covering the vane, still encased in the mold, with a one inch thick polyisocyanurate foam board box. The box provided adequate insulation to maintain constant temperature as the vane mold was heated with an electric element. The thermal cycle required three hours of heating and cooling the mold at prescribed intervals. Once the mold had reached 175 °C, it was left to cool to the ambient room temperature. Details of the thermal cycle process are tabulated in Appendix A.

www.manaraa.com
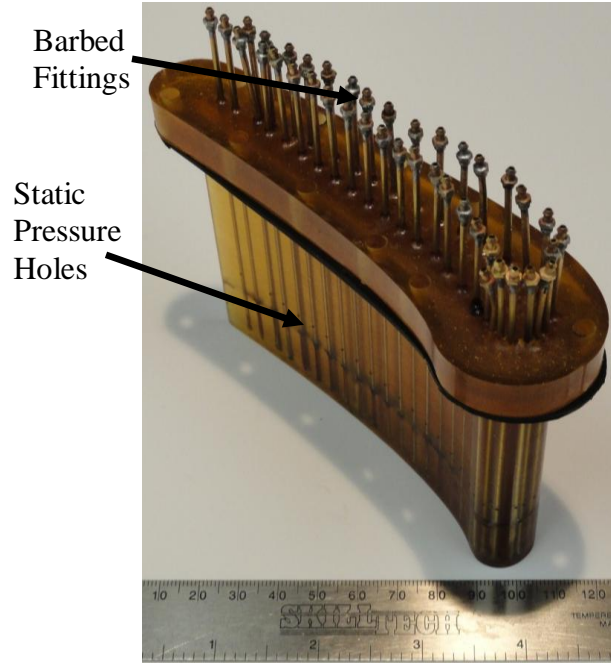
Figure 20. Instrumented vane used for circumferential static pressure measurements.

The 2.8 times scaled instrumented test vane used for measuring the circumferential surface pressure at the mid-chord can be seen in Figure 20. The surface pressure was measured at forty locations around the vane, which are detailed in Figure 21. The surface pressure holes have a diameter of 0.762 mm and were drilled at the mid-span of the vane normal to the surface, which intersected the 0.159 cm brass tubes. Miniature barbed fittings were soldered onto the ends of the tubing that provided an adequate attachment fitting for a 0.159 cm inner diameter Tygon tube.

41
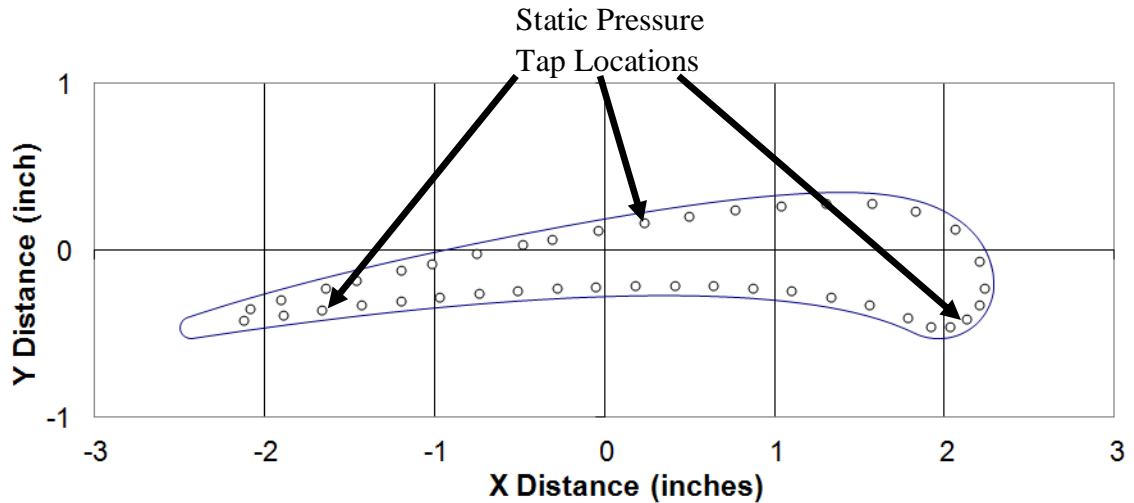
Figure 21. Locations of the static pressure tap tubing inside the pressure vane.

Exit Surveys

Exit velocity surveys were performed to measure total pressure loss, turning angle, and secondary velocities using a five-hole cone probe. The probe traversed an exit plane of the transonic cascade using a custom fabricated traversing apparatus. The T-shaped, 4.76 mm diameter probe used for the exit surveys can be seen by itself in Figure 18 and Figure 22, where it is positioned within the cascade.
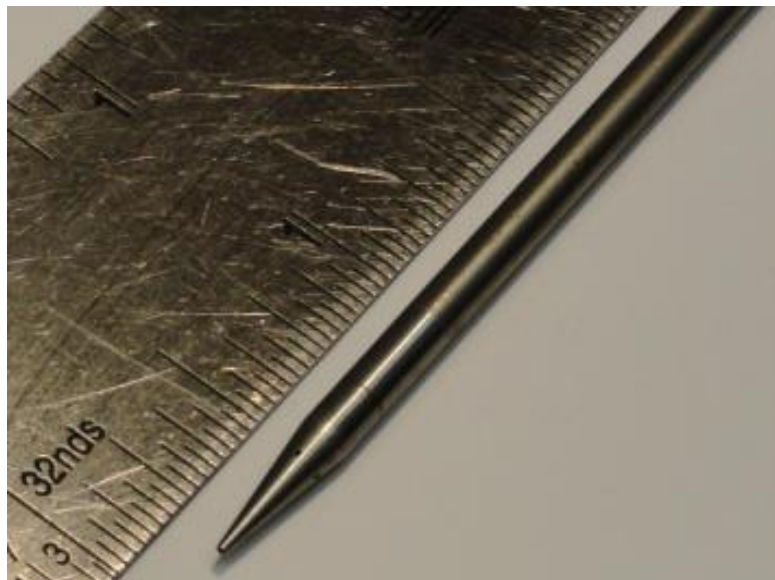
Figure 22. Pressure sensing end of the five-hole cone probe used for exit velocity surveys.

42

The five-hole cone probe was calibrated for the yaw direction over a range of Reynolds number of 50,000, 100,000, 200,000, 400,000, and 800,000 at a series of Mach numbers of 0.5, 0.6, 0.7, 0.8, and 0.9. The calibration correlated total pressure recovery of the center port, angle sensitivity between the pitch and yaw paired ports, and an averaged port pressure compared to local static pressure as a function of angle. The probe was calibrated within custom designed equipment, which was integrated into the wind tunnel. The probe was connected to five miniature differential piezo-electric pressure sensors. The four ports positioned 90° apart were referenced to the center pressure port, while the center port was referenced to the inlet total pressure.
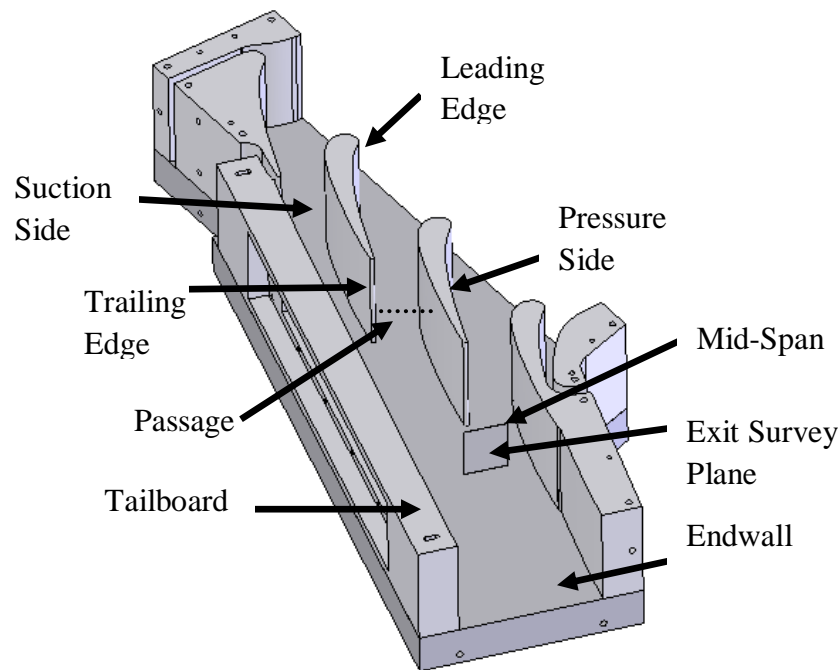
Figure 23. Detailed schematic of the exit survey plane location within the cascade in relation to the test vane.

The traversing apparatus moved the probe over a plane normal to the exit of the cascade set as 73° to the inlet of the cascade. A visual example seen in Figure 23 provides a clear view of the exit plane and how it is oriented in relation to the vanes within the cascade. The exit survey plane is located ¼ axial chord from the vane's trailing edge. The

43

planes width is defined by the distance between mid-passages, equaling 2.79 cm. The probe was traversed 0.438 cm from the endwall to the mid-span of the vane, equaling 3.23 cm from the endwall. The width and height of the exit plane was divided into 21 points, totaling 441 locations where measurements were taken with the probe for each survey. Points located closer to the endwall and the center of the cross-passage were grouped tighter together to enhance endwall boundary layer and secondary flow visualization.

Pressure Data Acquisition

The data acquisition was performed with a Gateway 2000, model E-3000 computer. The computer utilized an IEEE 488 bus card, which controlled and read voltages from a HP 3497A data acquisition unit. A 48 port DI/O board integrated into the computer controlled a 48 channel electro-mechanical relay board, which operated the 48 pressure solenoids seen in Figure 24. There were four Rosemount pressure transducer used to measure experimental pressures with a quoted accuracy of ±0.1 percent. The first transducer was calibrated to read 0 to 103.4 kPa absolute, the second 0 to 3.73 kPa differential, the third 0 to 34.34 kPa differential, while the remaining was configured for 0 to 206.85 kPa differential. The solenoids and pressure transducers are connected with 0.159 cm Tygon tubing. The 48 solenoids were divided up with four exclusively connected to the high pressure side of the transducers, while the remaining 44 were connected to the low pressure side of each transducer.

44
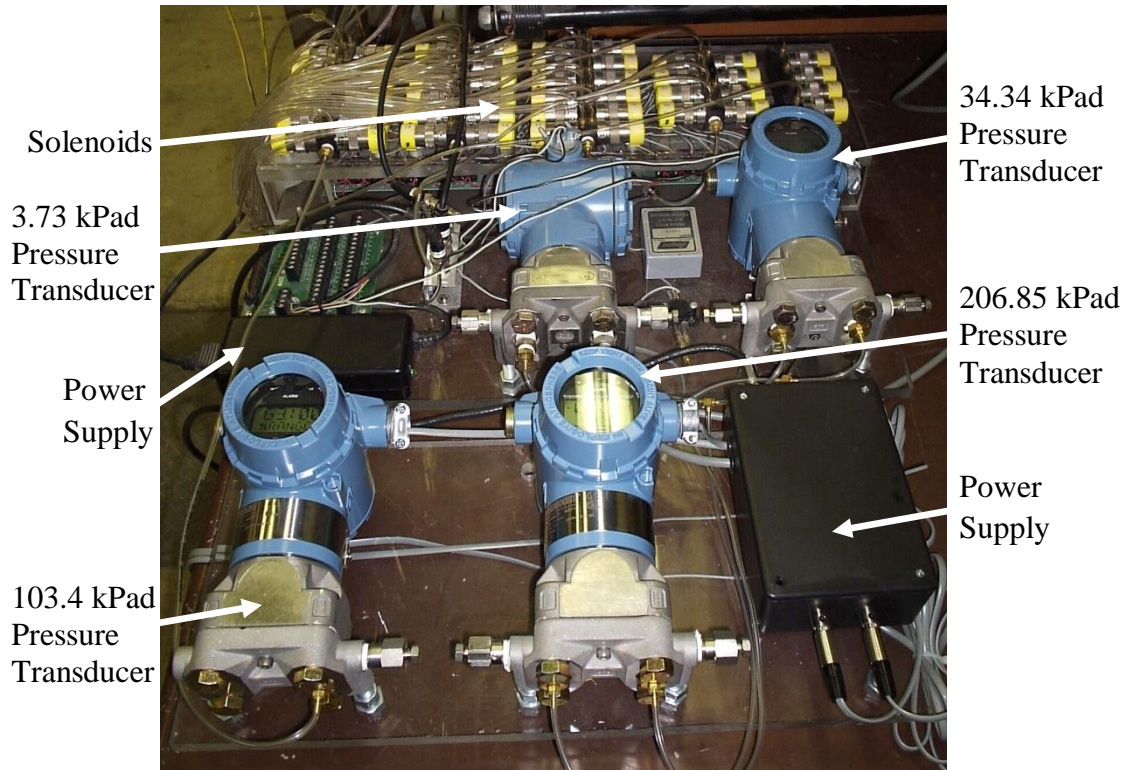
Figure 24. Data acquisition sensors used to measure absolute and differential pressures.

The vane surface, inlet, and exit static pressures were referenced with a total pressure kiel probe. The differential pressures were determined by reading both 3.73 and 34.34 kPa differential pressure transducers and choosing the appropriate sensor. The pressure measurements were averaged from 10 readings. The exit survey pressure measurements were taken with five miniature differential piezo-electric pressure sensors. Exit survey conditions between Reynolds numbers of 90,000 to 360,000 were measured with the 14,931 Pa sensors and a Reynolds number of 720,000 were recorded with the 34,475 Pa sensors. Each exit survey measurement was taken 20 times and averaged, to reduce error that may occur due to unsteadiness in the flow. A detailed description of the miniature sensors can be found in CHAPTER IV: PROBE CALIBRATION.

A data acquisition program was written in QUICK BASIC to systematically perform the aerodynamic testing. The program allowed the user to select a procedure

from the menu screen, which then executed a sub-routine without any further input. The options available to the user included monitoring wind tunnel conditions, scanning cascade inlet and exit conditions, vane surface pressures, and performing an exit survey. Once an option was selected, the program performed a series of procedures ranging from pressure settling times, opening appropriate solenoids, reading voltages, aerodynamic calculations, and outputting the data to a .prn file. The code for this program became vary malleable enabling variability, which helped complete the necessary testing. This program was later updated for heat transfer tests and will be further discussed in CHAPTER V.

Data Analysis

Inlet and Exit Conditions

The inlet and exit static pressures were measured at each Reynolds and Mach number for low and high turbulence cases. Inlet and exit Mach number were determined by referencing the local static pressure and the total kiel probe pressure at the inlet of the cascade.

The inlet static pressures was measured at 32 pressure taps spanning the inlet of the cascade and were located ¼ axial chord upstream from the vane's leading edge. The distribution of local inlet Mach number was monitored for each condition to ensure appropriate uniform inlet velocity. The inlet velocity distribution was adjusted by opening or closing the bleed air valves until velocity uniformity was achieved. The local Mach number across the inlet of the cascade for a Reynolds number of 360,000 is seen in Figure 25. The low inlet Mach number regions of Figure 25 indicate an area in front of a

46

vane, while the higher Mach number regions indicate the mid-passages between each

vane.
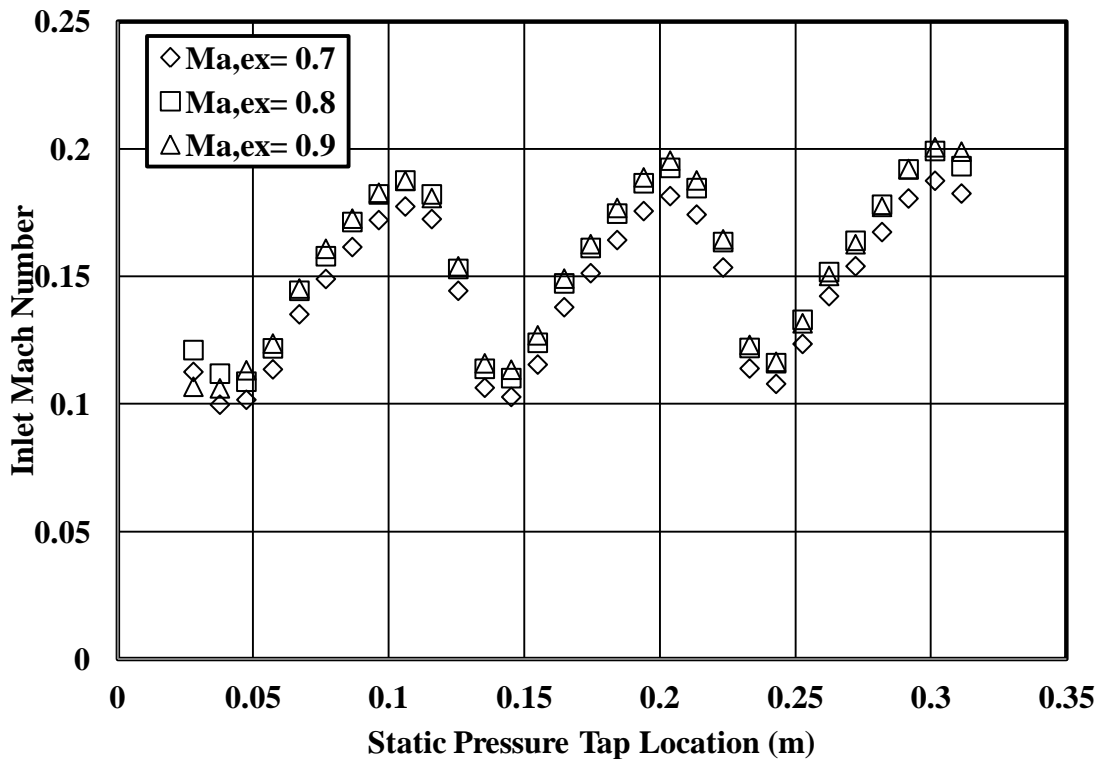
Figure 25. Inlet Mach number survey with a Reynolds number of 360,000 over a span of exit Mach number of 0.7, 0.8, and 0 .9.

The exit static pressures were measured at 29 pressure taps spanning the cascades

exit and were located ¼ axial chord from the vane's trailing edge. The exit Mach number

distribution seen in Figure 26 was used to choose the appropriate static pressure tap to

determine an exit Mach number. The exit static tap was chosen by taking an average of

the entire exit static pressure for the highest peak distribution. Generally, the location

remained the same and only deviated by one static tap location for lower Reynolds

numbers. The exit velocity distribution could be adjusted by changing the tailboard

location.

47
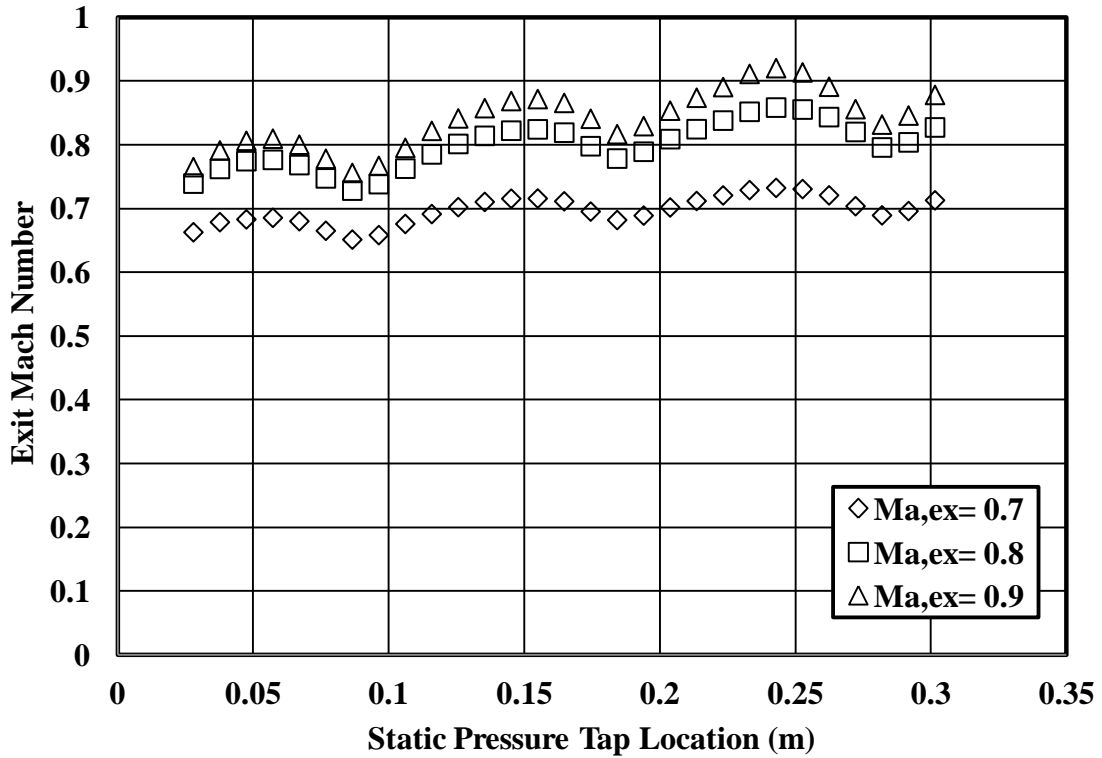
Figure 26. Exit Mach number survey with a Reynolds number of 360,000 over a span of exit Mach number of 0.7, 0.8, and 0.9.

The suction side tailboard location used for the aerodynamic testing was set for turbulent condition, at an exit Reynolds number of 400,000. This location was determined from the streamline location from FLUENT calculations and an approximate boundary layer displacement thickness. The displacement thickness of a turbulent boundary layer over a flat plate was calculated with Equation 3.1, which was taken from Ames' Computational Fluid Dynamics lecture [57],

$$\frac{\delta^*}{x} = \frac{0.0463}{Re_{ex}^{\frac{1}{5}}} \tag{3.1}$$

where δ^* is the boundary layer displacement thickness, x is the length of the tailboard, and Re_{ex} is the Reynolds number based on the exit conditions of the cascade.

48

Vane Pressure Distributions

The local vane circumferential pressure distributions were analyzed to provide a plot of the surface Mach number at each flow condition. The surface pressure was referenced to total inlet pressure where a Mach number was calculated using Equation 3.2 which was taken from the book Gas Dynamics by John and Keith [58],

$$Ma_{,sur} = \sqrt{\left(\left(\frac{P_T}{P_{sur}}\right)^{\frac{\gamma-1}{\gamma}} - 1\right)\frac{2}{\gamma-1}} \qquad (3.2)$$

where P_T is the inlet total pressure, P_{sur} is the local pressure on the vane surface, and γ is the ratio of specific heats. The surface Mach number was plotted as a function of the ratio of surface arc distance to the true chord length, with 0 being the stagnation point on the leading edge of the vane. The negative distance represents the pressure side of the vane, while the positive distance is the suction side. The Mach number for the low and high turbulence conditions will be examined in detail. Comparisons over the range of Reynolds and Mach numbers will used to evaluate possible adverse pressure gradients that may cause flow separation on the vane surface. FLUENT calculations for several conditions will be compared against the surface measurements to further enhance understanding of the results.

Exit Surveys

The exit velocity pressure measurements taken at each Reynolds and Mach number for low and mock aero-derivative turbulence conditions was analyzed to

49

determine a mass averaged total pressure loss coefficient Ω (Omega) and turning angle β (Beta). The total pressure loss coefficient is defined by Equation 3.3,

$$\Omega = \frac{P_{T,in} - P_{T,ex}}{P_{T,in} - P_{s,ex}} \qquad (3.3)$$

where $P_{T,in}$ is the inlet total pressure, $P_{T,ex}$ is the total pressure measured by the center port on the five-hole cone probe, and $P_{s,ex}$ is the exit static pressure. The mass averaged total pressure loss coefficient is determined by taking a cross-passage average of the product of the local total pressure loss coefficient and the mass flow rate per area at each measurement point. The turning angle β (Beta) seen in Figure 27, is the directional change in the flow due to the presence of the vane. The cross-passage averaged turning angle is calculated by determining the mass flow rate per area measured at each point and averaging its product with the locally sensed yaw angle across the passage. The cross-passage averaged total pressure loss coefficient and cross-passage averaged turning angle, were plotted against the cross span distance. Contour plots were generated from each measurement point, which describe the local total pressure loss coefficient with secondary flow vectors detailing the flow field. The secondary velocity vectors were determined by correlating flow conditions sensed during the probe calibration to the flow conditions at the vanes exit. Coefficients determined from the probe calibration were used to determine yaw and pitch angles, where velocity vectors could be calculated based on exit velocity. An example of the total pressure loss coefficient contour plot is provided in Figure 28, which aids in explaining the presentation of the results. A visual explanation for the plots pertaining to the total pressure loss coefficient and turning angle related to the cross span distance are found in Figure 29 and Figure 30. Figure 27 also

50

shows a detailed location of the exit survey plane the probe traversed to acquire

measurements for the total pressure loss and turning angle.
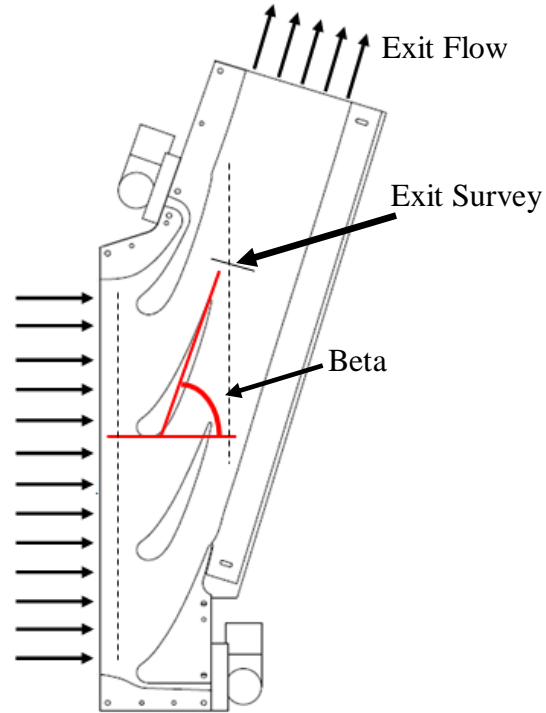
Figure 27. Definition of turning angle, β Beta.
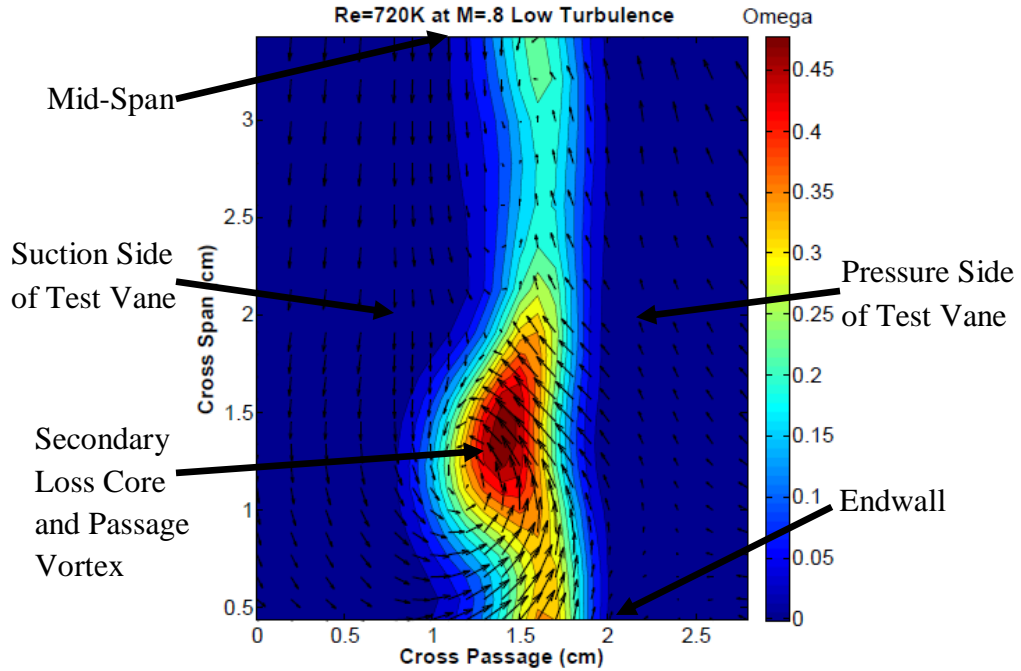
Figure 28. Example of an exit survey total pressure loss and secondary velocity contour plot.
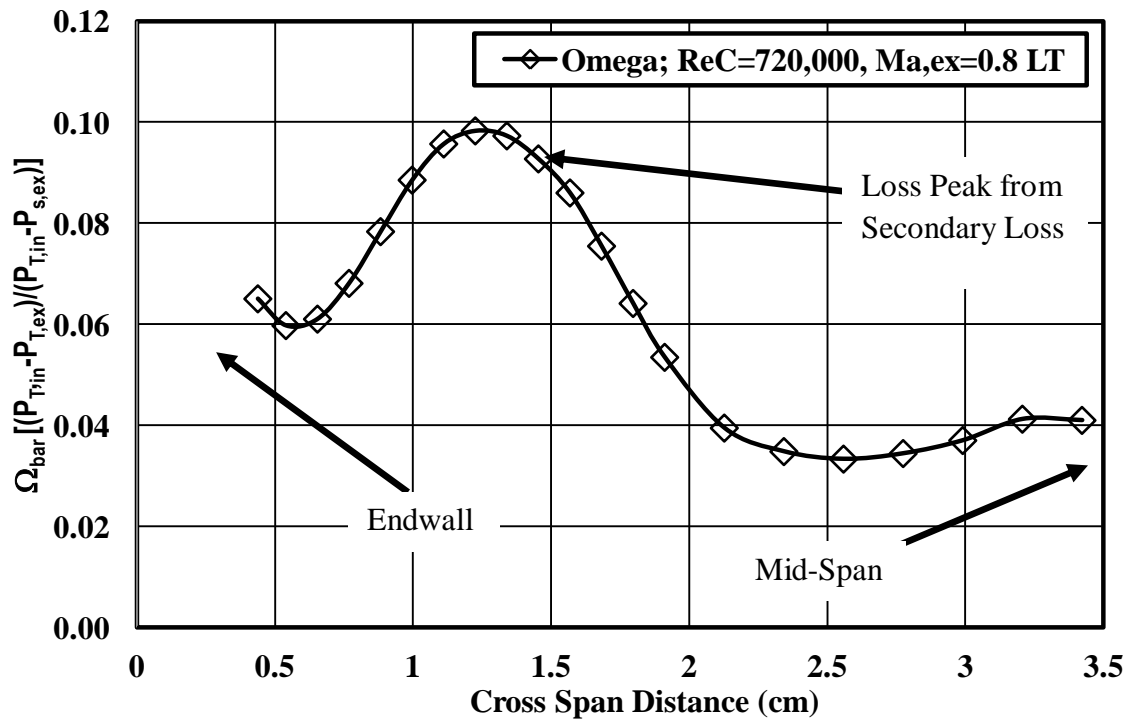
Figure 29. Example of cross-passage averaged loss coefficient Ω (Omega) as a function of cross span distance.
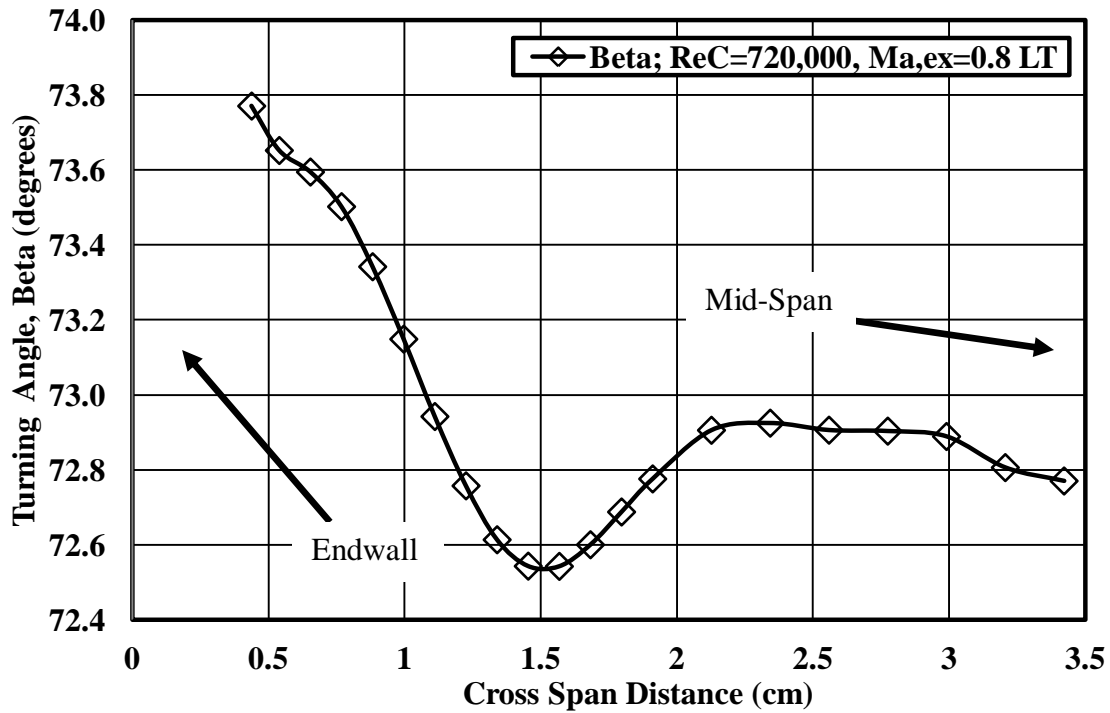
Figure 30. Example of cross-passage averaged turning angle β (Beta) as a function of cross span distance.

Data Uncertainties

Experimental data uncertainty estimates of the reported values for Mach number, total pressure loss Omega (Ω), turning angle (β) were calculated with the root sum square method described by Moffat [59]. The uncertainties of these variables are based on instrumentation error and data reduction analysis. The uncertainty for Mach number is based on one recorded inlet total and one exit static pressure. The exit static pressure measurement location is determined by averaging the exit static taps aft of the test vane and choosing the tap with the nearest pressure to the average exit static pressure. The greatest uncertainty for the Mach number measurements was found to be ± 0.019. Uncertainty in the turning angle (β) includes bias error, unsteadiness error, and installation error. The unsteadiness of the probe was most evident at higher Reynolds and Mach numbers. The maximum unsteadiness error is estimated to be $0.45°$ for the highest

53

Reynolds and Mach numbers. The installation error is estimated to be 0.25° for all tests conducted. The uncertainty for the total pressure loss Omega (Ω) is estimated to be 0.002 for all Reynolds numbers between 90,000 and 360,000 and 0.003 for Reynolds number of 720,000. All uncertainty estimates for the experimental test is based on a 95 percent confidence interval.

CHAPTER IV

PROBE CALIBRATION

The following chapter begins with a description of UND's transonic five-hole cone probe, along with a detailed explanation of the equipment, process, and results obtained for the calibration of the probe. The transonic calibration encompasses a range of Reynolds numbers of 50,000, 100,000, 200,000, 400,000, and 800,000 over a series of Mach numbers of 0.5, 0.6, 0.7, 0.8, and 0.9. The range of Reynolds and Mach numbers chosen for this calibration are desirable for the cascade exit velocity field survey test conditions.

Calibration Facility

The transonic five-hole cone probe used for exit velocity surveys in UND's compressible flow wind tunnel facility was calibrated using custom designed equipment, which was integrated into the facility for the calibration process. The calibration components integrated into the wind tunnel assembly include a flow condition unit, inlet and exit nozzle, and calibration unit seen in Figure 31.
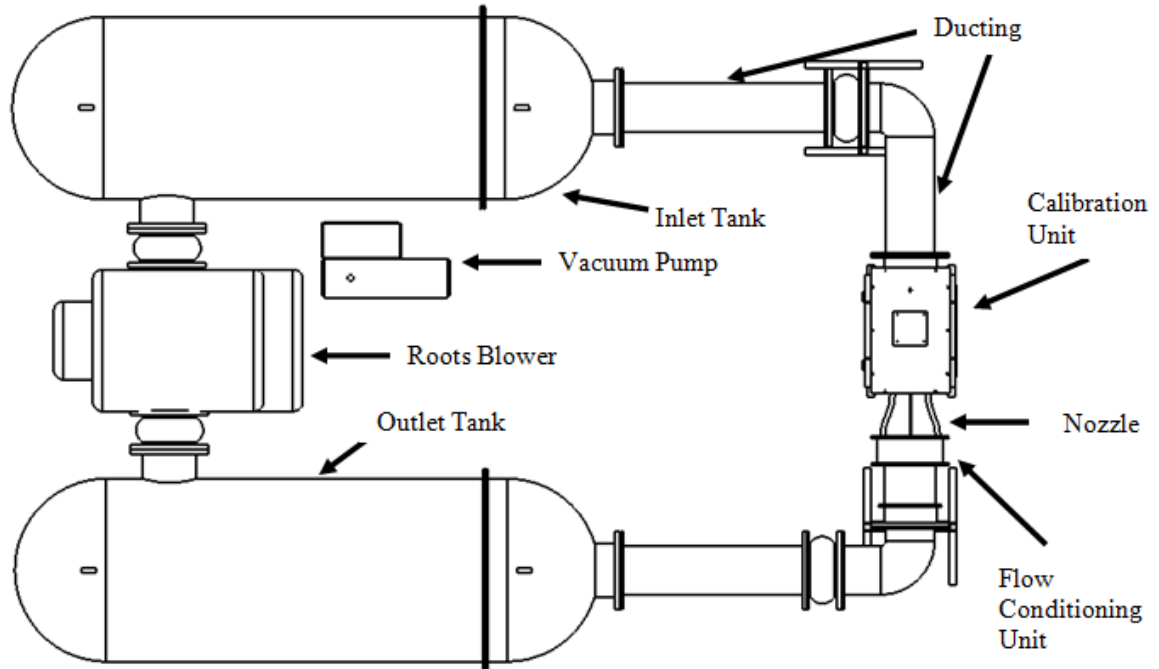
Figure 31. Overhead schematic of the compressible flow wind tunnel with the calibration equipment installed.

The compressible flow facility with the calibration equipment installed functions similarly as with the cascade installed. The relatively low velocity air flows from the outlet tank to a circular to square transition section. The flow then passes through a flow conditioning unit, which contains two perforated plates with an open area of 0.039 m^2, and also two stainless steel mesh screens. The flow accelerates through an inlet nozzle with an area ratio of 1.67, which then transitions to an outlet nozzle with an area ratio of 7.27. The outlet nozzle generates an exit air jet 15.24 by 3.5 cm, within which the five-hole cone probe is calibrated. The five-hole cone probe stinger tip is positioned perpendicular to the exit plane of the outlet nozzle. A 180° protractor with one degree increments is positioned on the top surface of the calibration unit, which provides a means for measuring the yaw angle as the probe is calibrated. The flow passes out of the calibration unit into the inlet tank, through the fin and tube heat exchanger, and back into the Roots blower.

56

The transonic calibration unit seen in Figure 32 incorporates a robust but flexible design. It is designed to withstand a complete vacuum and temperature exceeding +110 °C. The main body is comprised of standard carbon steel with a removable aluminum top plate. The removable plate allows various sizes of outlet nozzles and probes to be installed. A polycarbonate view window, positioned at the top plate's center, provides easy access or sight of the probe during calibration. Due to the necessity of removable components, butyl rubber gaskets are utilized on precision machined flanges of these components, which provide the calibration unit with minimal off-gassing and an airtight seal.
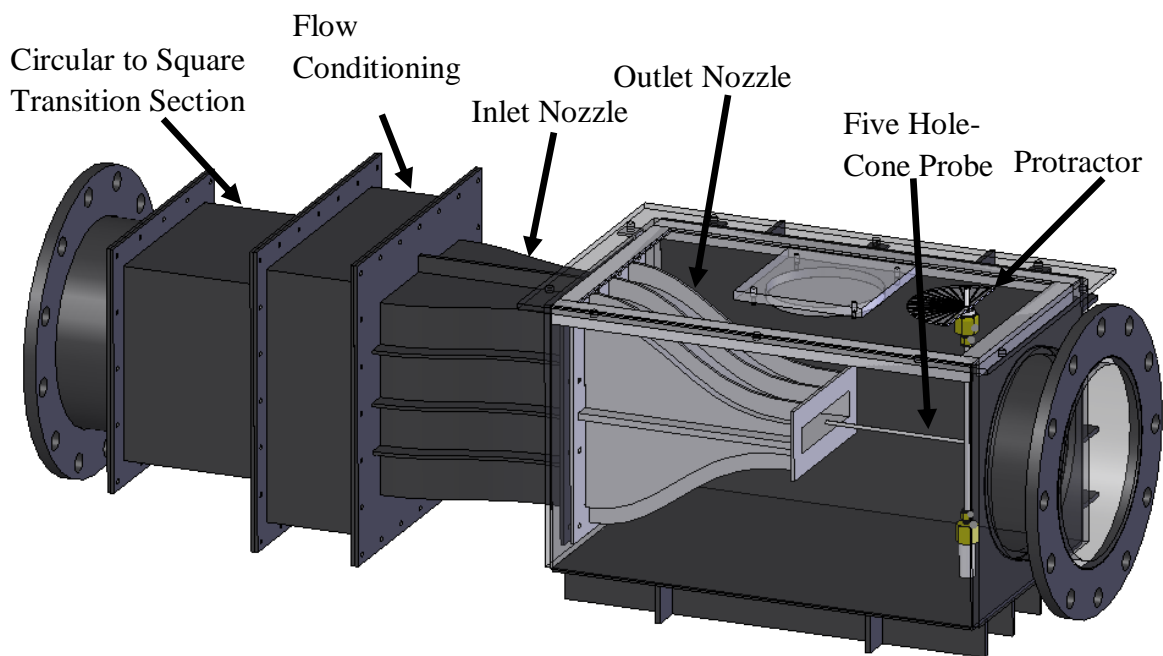
Figure 32. Assembly schematic of the calibration unit coupled with the flow conditioning unit and nozzles.

<center>Probe Geometry</center>

The pressure probe used for the calibration is of a five-hole cone probe geometry seen in Figure 33. The probe geometry was designed for high speed flows with a small profile to reduce disrupting the flow field. The probe was purchased from United Sensor Corporation, which specializes in manufacturing stainless steel pressure and temperature sensing devices. Geometrically, the probe is T-shaped, with a 0.635 cm shaft supporting a perpendicular 0.476 cm tube, which transitions to a 0.317 cm tube with a pressure stinger at the tip. The probe's stinger is comprised of a 15° cone with one 0.41 mm orifice at the tip and four orifices approximately mid-cone, positioned 90° apart, drilled normal to the surface. Pressures are conducted from the stinger orifices to one end of the 0.635 cm shaft by five, 0.635 mm stainless steel tubes.
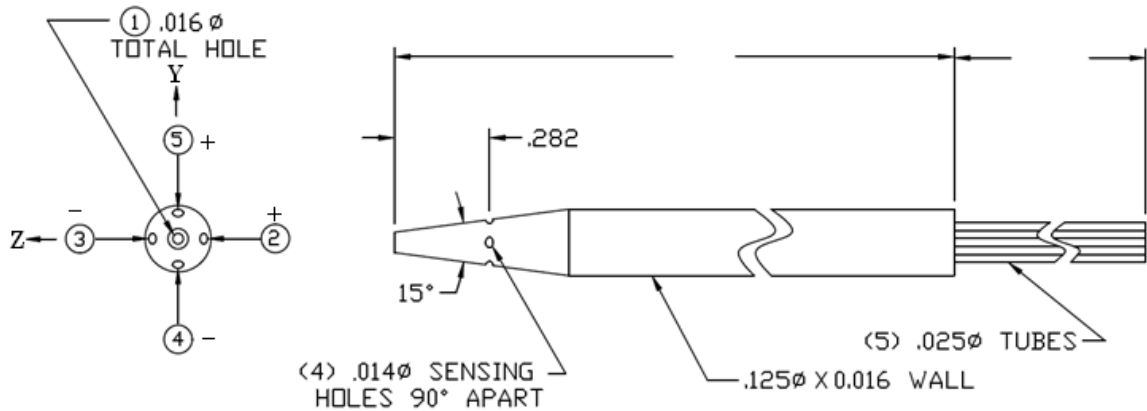
Figure 33. Schematic of the pressure sensing tip of the five-hole cone probe with the probe hole and directional orientation seen in the left of the image (units in inches).

<center>Calibration and Pressure Coefficients</center>

The probe was concentrically held between two Swagelok fittings positioned on the top and bottom of the calibration unit as seen in Figure 32. The Swagelok fittings, fitted with Teflon ferrules provided an airtight seal, while both ends of the probes 0.635 cm shaft protruded from the calibration unit. An orientation indicator clamped to the top

<center>58</center>

of the probe provides a visual reading of the yaw angle as seen on the protractor mounted to the top surface. The probe stinger was positioned in the center of the outlet jet by a custom made aluminum gage block and calipers. The gage block centered the probe in the width of the outlet nozzle exit, while the orientation indicator was aligned to the protractors 0° mark. Calipers were used to position the probe at the mid-height of the outlet nozzle exit.

A non-nulling calibration technique was utilized for calibrating the five-hole cone probe. The probe seen in Figure 22 and Figure 33 was calibrated over a range of Reynolds numbers of 50,000, 100,000, 200,000, 400,000, and 800,000, which is based on the true chord length of the vanes in the transonic cascade. Each Reynolds number was run over a series of Mach numbers of 0.5, 0.6, 0.7, 0.8, and 0.9. At each Reynolds number for a given Mach number, the probe was moved in a yaw motion over a range of angles of +22° to -22° in two degree increments. When viewed from a perspective looking down upon the protractor, a counter-clockwise angle was deemed positive, while clockwise was a negative angle. At each angle, the five probe pressures, as well as the direction and magnitude of the flow conditions, were measured with a period of two minutes between each measurement. The probe pressures were measured with five miniature differential piezo-resistive pressure sensors connected to a five volt, 20 milliamp power supply. The outlet voltages were then measured by the HP 3497A data acquisition unit and recorded by a custom Quick BASIC calibration program. Tunnel conditions were determined by measuring the total pressure and temperature in the inlet nozzle and taking an average of five static pressures at the exit of the outlet nozzle. A

59

Mach number was calculated from the total and static pressures, while density, viscosity, and static temperature were calculated from total temperature.

To mitigate sensitivity error, piezo-resistive sensors with a range of 2,488 Pascal were used for all measurements taken at a Reynolds number of 50,000. Pressures for Reynolds numbers between 100,000 to 400,000 were measured with 14,931 Pascal sensors, and a Reynolds number of 800,000 was recorded with the 34,475 Pascal sensors. The 2,488 Pascal sensors seen in Figure 34 were calibrated at atmospheric conditions with a 20 inch red gage oil micromanometer, and the 14,931 Pascal and 34,475 Pascal sensors were calibrated with a 220 inch U-tube red gage oil manometer.
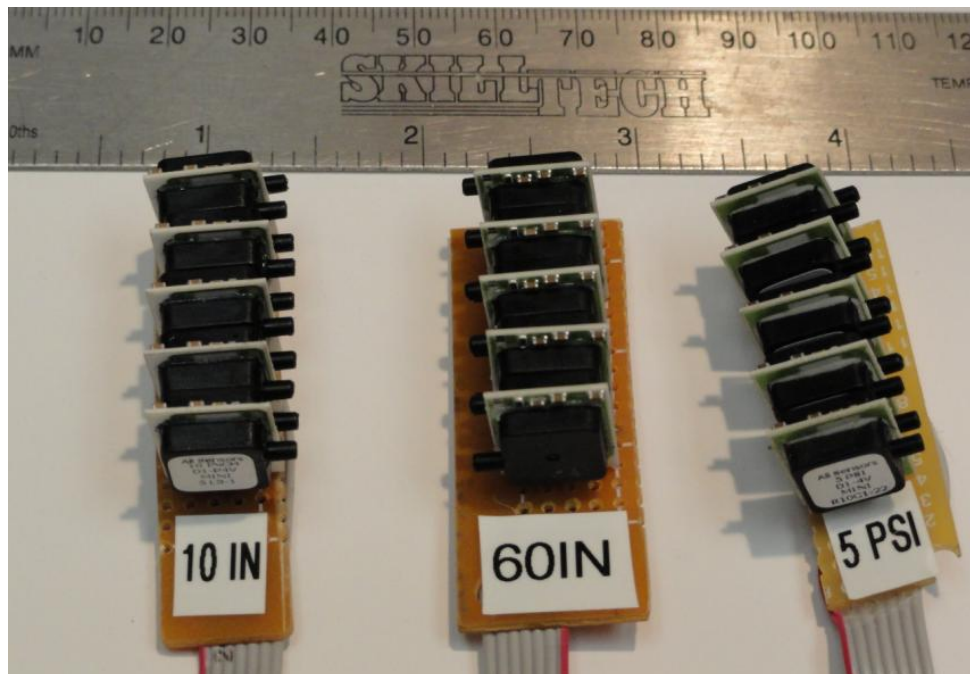
Figure 34. Miniature differential piezo-resistive pressure sensors used for calibrating the five-hole cone probe.

The calibration correlated total pressure recovery of the middle port, angle sensitivity between the opposing pitch and yaw ports, and the average port pressure compared to static pressure as a function of angle. The standard non-dimensional

60

equations for determining these values from the calibration process are in the following

equations. Total pressure recovery was calculated by the Equation 4.1.

$$Cp_{Rec} = \frac{P_T - P_1}{P_T - P_S} \tag{4.1}$$

Where P_T is the total pressure, P_1 is the stagnation pressure sensed by the probe

tip, and P_S is the local static pressure. The yaw and pitch sensitivities are determined

from Equations 4.2 and 4.3 with the hole locations depicted in Figure 33.

$$Cp_{yaw} = \frac{P_2 - P_3}{P_T - P_S} \tag{4.2}$$

$$Cp_{pitch} = \frac{P_4 - P_5}{P_T - P_S} \tag{4.3}$$

The average pressure port coefficient is calculated with Equation 4.4,

$$Cp_{Sens} = \frac{P_T - P_{ave}}{P_T - P_S} \tag{4.4}$$

where P_{ave} is the mean of the pressures measured by the side ports, that is:

$$P_{ave} = \frac{(P_2 + P_3 + P_4 + P_5)}{4} \tag{4.5}$$

The yaw and average pressure port coefficient can vary significantly depending

on the included angle of the probe. If the included angle of the probe is large, then the

yaw coefficient will be larger at a given yaw angle than a probe with a smaller included

angle. Also, if the probe included angle is small, then the averaged pressure port

coefficient will be greater than if the angle were larger.

The calibration coefficients are utilized by determining linear or polynomial

equations from the coefficients over a span of angles. The slopes of these equations are

used to calculate the angle of airflow over the probe based on sensed pressures. Once the

61

airflow angle is determined, the yaw and pitch velocities can be found by equations 4.6 and 4.7,

$$V_{yaw} = \sin(\theta)U_{\infty} \qquad (4.6)$$

$$V_{pitch} = \sin(\emptyset)U_{\infty} \qquad (4.7)$$

where θ is the calculated yaw angle, $\emptyset$ is the calculated pitch angle, and U_{∞} is the freestream velocity.

Calibration Results

The data from the calibration of the five-hole cone probe were analyzed by fitting the span of pressure coefficients over a range of angles with second and third order polynomials. Offset values of the probe data were determined though a regression analysis, which corrected for probe geometric irregularities and the possible misalignment of the probe during calibration. The offset values and polynomial coefficients were then used to analyze cascade exit survey data.

The results of the calibration process indicated the probe had adequate sensitivity over the range of Reynolds and Mach numbers, but indicated some irregularities at lower Reynolds numbers. These irregularities are thought to be a Reynolds number effect on the 0.635 mm sensing holes on the probe head. Other factors such as separation bubbles could also be responsible, but will be discussed further below.

Due to the amount of data gathered during the calibration process, data pertaining to Mach 0.9 will only be presented in this results section. Subsequently, additional data will be provided in Appendix C for the lower Mach numbers and will be referenced during the discussion of the following figures.

The yaw sensitivity of the probe over a range of Reynolds numbers of 50,000, 100,000, 200,000, 400,000, and 800,000 can be seen in Figure 35. The data sets for each Reynolds number have been adjusted with an offset angle, which was determined from a regression analysis. Qualitatively, the data points for each angle appear to have a tight grouping. There is however, better grouping on the negative angles than the positive angles. This variance could be due to probe geometry, but is likely caused by the flow conditions due to apparent improved groups at Mach 0.5, 0.6, 0.7, and 0.8. The elongated S shape contour of the yaw coefficients was fitted to a third order polynomial, but due to the lower angles of incidence expected, first order coefficients were determined between -12° and +12°.

At a Reynolds number of 50,000, the yaw sensitivity of the probe is clearly affected. The negative angled coefficients serried together with the other Reynolds number values, but the positive angled coefficients gradually fell below the trend. Interestingly, the magnitude of this deviation at a positive angle increased as the Mach number increased. Compressibility effect could explain the unexpected trend; according to Dominy and Hudson [47], the effects of compressibility may be negligible, but freestream turbulence may have a significant effect due to the influence upon low Reynolds number separation bubbles. The data supports the conclusion that compressibility does not influence the yaw sensitivity. Figure 95 to Figure 99 in Appendix C clearly show very little change in the yaw coefficient at each Reynolds number as a function of the Mach number.
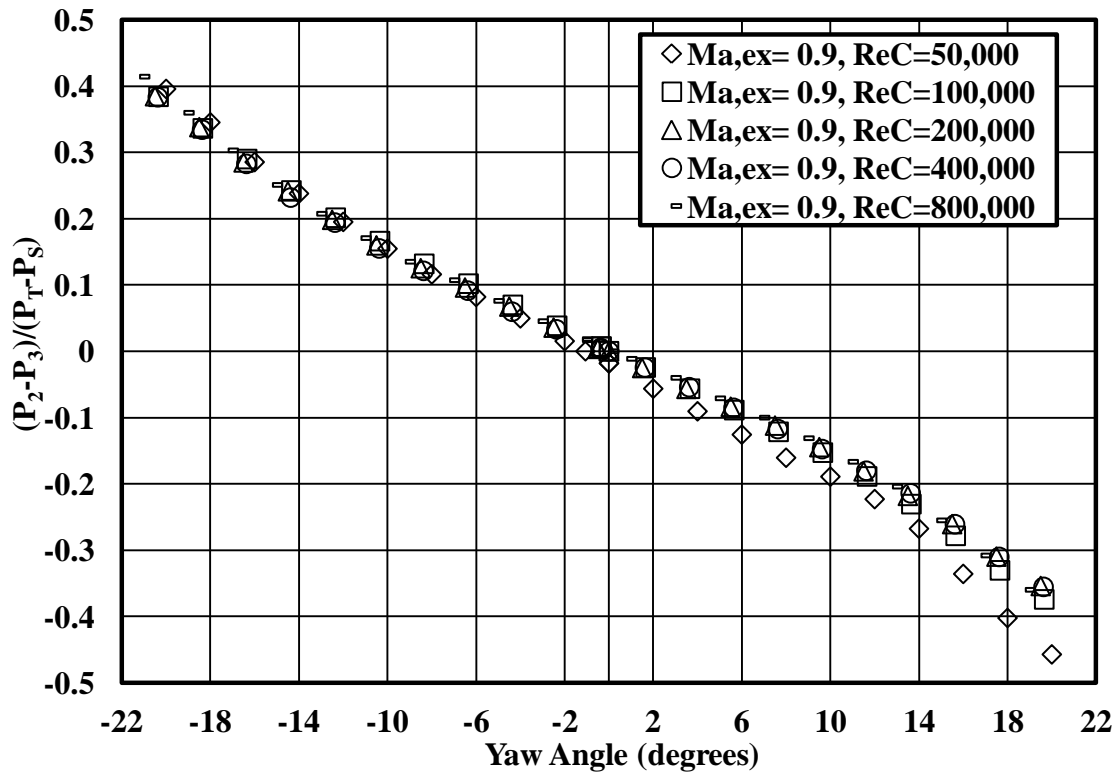
Figure 35. Yaw sensitivity coefficients of the five-hole cone probe over a span of yaw angles at Mach 0.9 as a function of Reynolds number between 50,000 and 800,000.

The total pressure recovery of the probe over a range of angles and Reynolds numbers is seen in Figure 36. Total pressure recovery was determined by comparing the inlet total pressure in the nozzle and pressure sensed by port 1 of the probe. Ideally, the inlet total pressure and pressure sensed by the forward facing pressure port should be equal when the probe is parallel to the flow. As the probe is yawed through a range of angles, the dynamic pressure sensed by the probe begins to diminish, which causes an increase in the total pressure recovery coefficient.

The total pressure recovery over the span of angles and Reynolds numbers is nearly symmetric. Total pressure recovery for all of the Reynolds numbers at each Mach number except for a Reynolds number of 50,000, begins to diminish around negative and positive 6.5°. Qualitatively, there is a precise grouping of the measured total pressure

64

recovery for smaller angles, but this grouping begins to alleviate at larger angles. The inconsistency of pressure recovery at larger angles appears to be independent of Reynolds and Mach number, but could be explained by separation turbulence.

At lower Reynolds numbers, the total pressure recovery also appears to be affected. The recovery coefficient at Reynolds numbers of 50,000 and 100,000 appear to be more sensitive to angle change. Reynolds number effect is clearly influencing these results and becomes more apparent at a 50,000 Reynolds number. This effect is persistent at each Mach number except 0.5, where perturbations of the recovery coefficient are minimal.
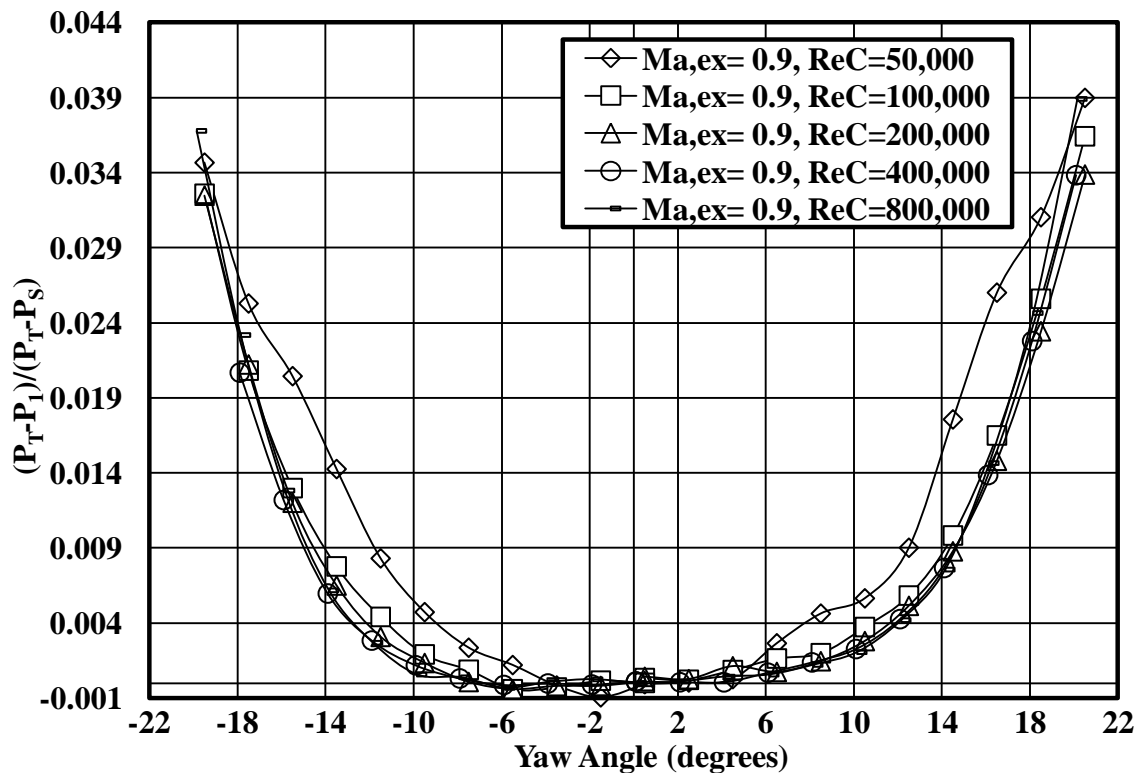
Figure 36. Total pressure recovery coefficients of the five-hole cone probe over a span of yaw angles at Mach 0.9 as a function of Reynolds number between 50,000 and 800,000.

Total pressure recovery as a function of Mach number at a Reynolds number of 800,000 is seen in Figure 37, which makes apparent the influence of compressibility on

65

total pressure recovery. By increasing the Mach number from 0.5 to 0.9, the total pressure

recovery coefficient decreases for a given angle beyond -6.5° and +6.5°. The trend of

decreasing total pressure recovery is seen through a Reynolds number of 50,000 to

800,000, which can be found in Appendix C, Figure 100 through Figure 104.
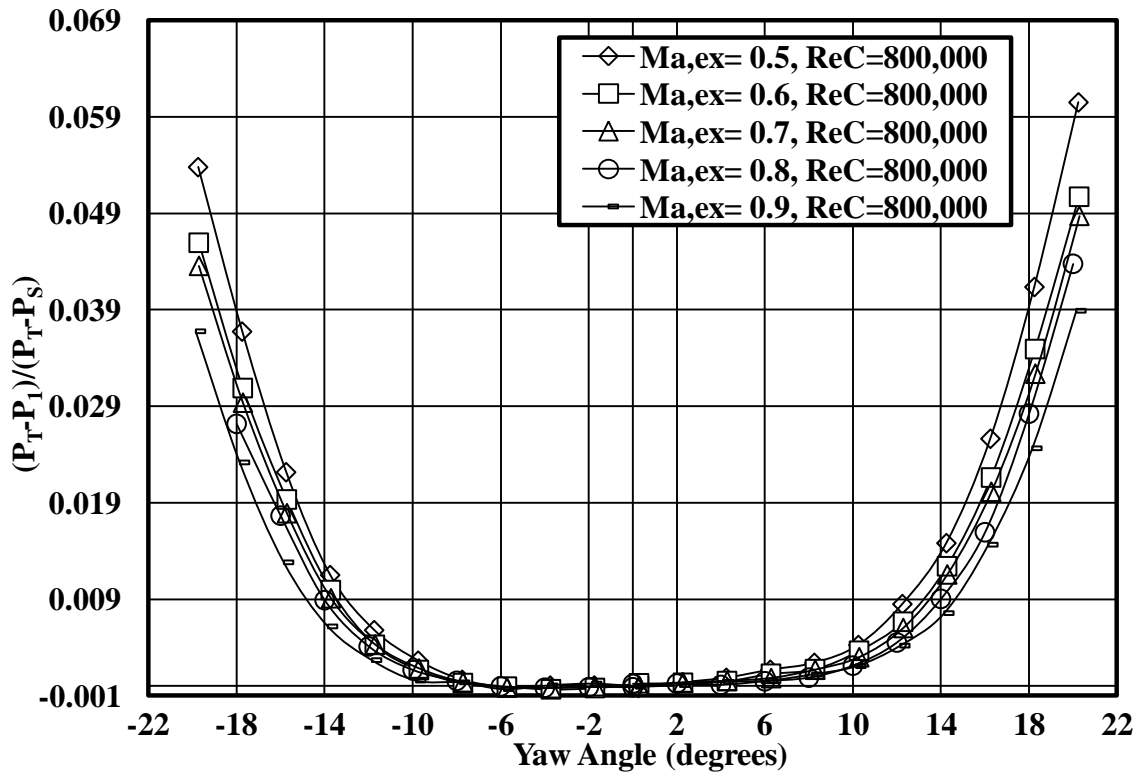
Figure 37. Total pressure recovery coefficients of the five-hole cone probe over a span of yaw angles at a Reynolds number of 800,000 as a function of Mach number between 0.5 and 0.9.

The static pressure sensitivity of the probe over a span of angles and Reynolds

numbers at Mach 0.9 is seen in Figure 38. The sensitivity of the probe over the relevant

angles of -12° and +12° varied between 0.94 and 0.96 for all Reynolds and Mach

numbers except for a Reynolds number of 50,000. The Reynolds number clearly has an

effect on the sensitivity of the probe due to the extremely skewed and sporadic sensitivity

coefficients at a Reynolds number of 50,000 for each Mach number. The effect of the

66

Reynolds number is further demonstrated, when it is increased to 800,000 and the span of

the sensitivity coefficients conform to a smooth parabolic shape as expected.
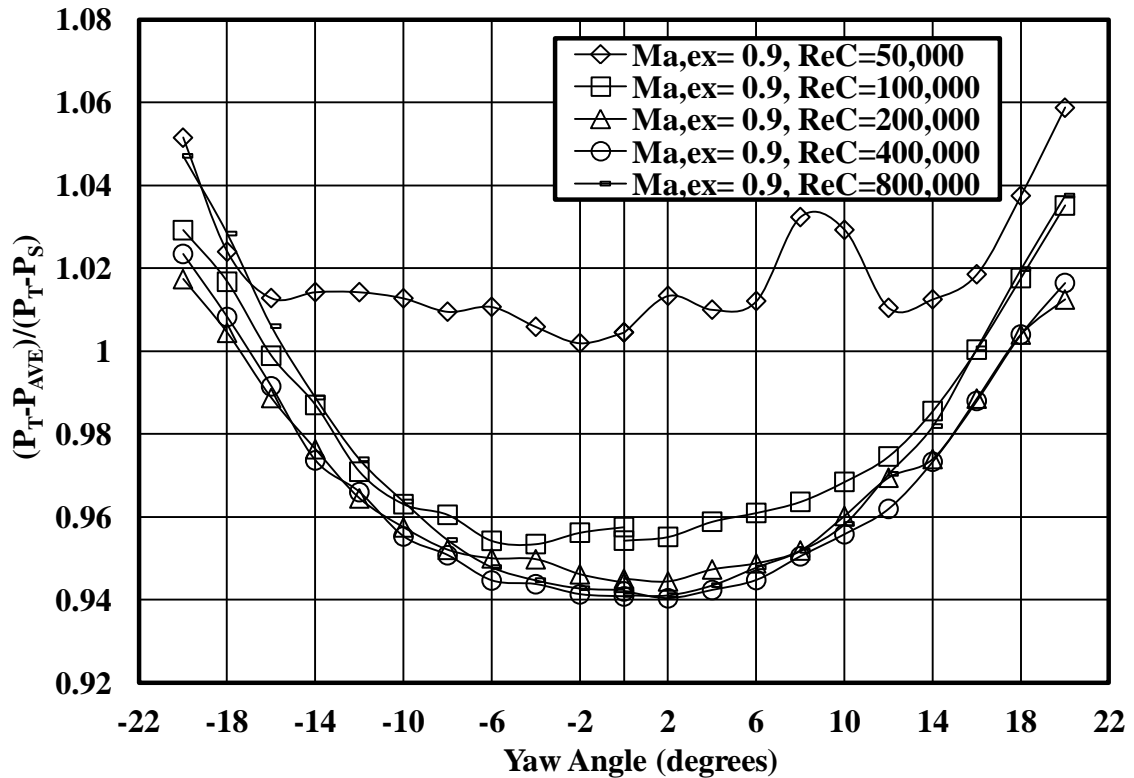
Figure 38. Pressure port sensitivity coefficients of the five-hole cone probe over a span of
yaw angles at Mach 0.9 as a function of Reynolds number between 50,000 and 800,000.

The calculated pressure sensitivity of the probe over the span of Mach numbers of

0.5 to 0.9 seen in Figure 39 indicates some influence to the change of Mach number. As

the Mach number increases, the pressure sensitivity decreases to some degree. However,

the general trend over the range of Reynolds numbers calibrated is inconsistent and a

concrete relation is hard to make with the compressibility effect. Therefore, a bow shock

might be occurring at the tip of the probe and could influence the average of pressure

ports one through four, which are located 0.71 cm aft of the tip. Fransson and Sari [51]

encountered similar discontinuities in probe calibration and also contributed it to bow

shocks, which were visually seen in Schliern photos during testing.

67
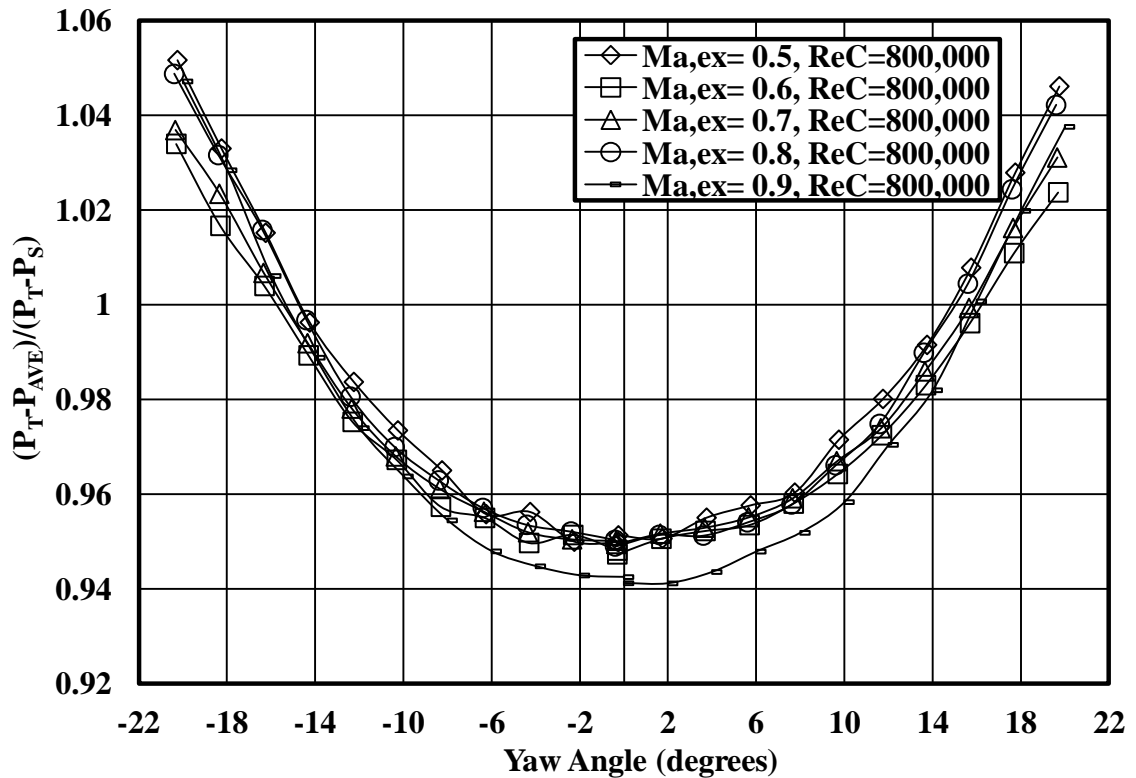
Figure 39. Pressure sensitivity coefficients of the five-hole cone probe over a span of yaw angles at a Reynolds number of 800,000 as a function of Mach number between 0.5 and 0.9.

Conclusion

The calibration facility used to calibrate a transonic five-hole cone probe over a

five different Reynolds and Mach numbers was presented. The new calibration facility at

the University of North Dakota provides adaptability, which allows numerous probe

designs to be calibrated over various conditions. The probe was calibrated with a non-

nulling technique over a span of angles between -22° to +22°. Three different ranged

miniature piezo-electric pressure sensors of 2,488, 14,931, and 34,475 Pascals were used

for the calibration over the five different Reynolds numbers to mitigate range error.

The calibration of the probe provided excellent yaw, total pressure recovery, and

average pressure sensitivity coefficients. A Reynolds number effect was evident for the

three coefficients that could be seen at each Mach number. The deviations were seen at a

68

Reynolds number of 100,000 but were most apparent at 50,000. The skewed results at these low Reynolds numbers are not thought to be a problem due to the exit survey condition being measured will be above 50,000. The calibration plots covering all of the Reynolds and Mach numbers can be found in Appendix C.

CHAPTER V

EXPERIMENTAL APPROACH—HEAT TRANSFER

The following chapter details the experimental approach for acquiring heat transfer measurements on the exterior of a test vane. The test vane is of the same geometry as the vane described in CHAPTER III, but a constant heat flux foil and thermocouples have been incorporated into its exterior surface. Testing was conducted over a range of Reynolds number of 90,000, 180,000, 360,000, 720,000, and 1,000,000 at a series of Mach numbers of 0.7, 0.8, and 0.9. Results were acquired based on true chord Reynolds number corresponding to two different flow conditions of low turbulence from a smooth nozzle and high turbulence generated by a mock aero-derivative combustor.

Heat Transfer Compressible Flow Wind Tunnel Facility

The facility used for aerodynamic testing seen in Figure 12, was also used for conducting heat transfer measurements. A detailed description of the wind tunnel operating parameters and functionality is provided in CHAPTER III. The pressure test vane was replaced by a heat transfer test vane, which will be discussed in the following section. Additional equipment was integrated into the facility to provide adequate means of conducting heat transfer tests. The additional equipment can be seen in Figure 40, which includes a 90 terminal type-K thermocouple jack panel and Hewlett-Packard 6269B DC power supply. As with the aerodynamic testing, the smooth 4 to 1 nozzle was used for low turbulence and the mock aero-derivative combustor was utilized for high turbulence conditions.

70
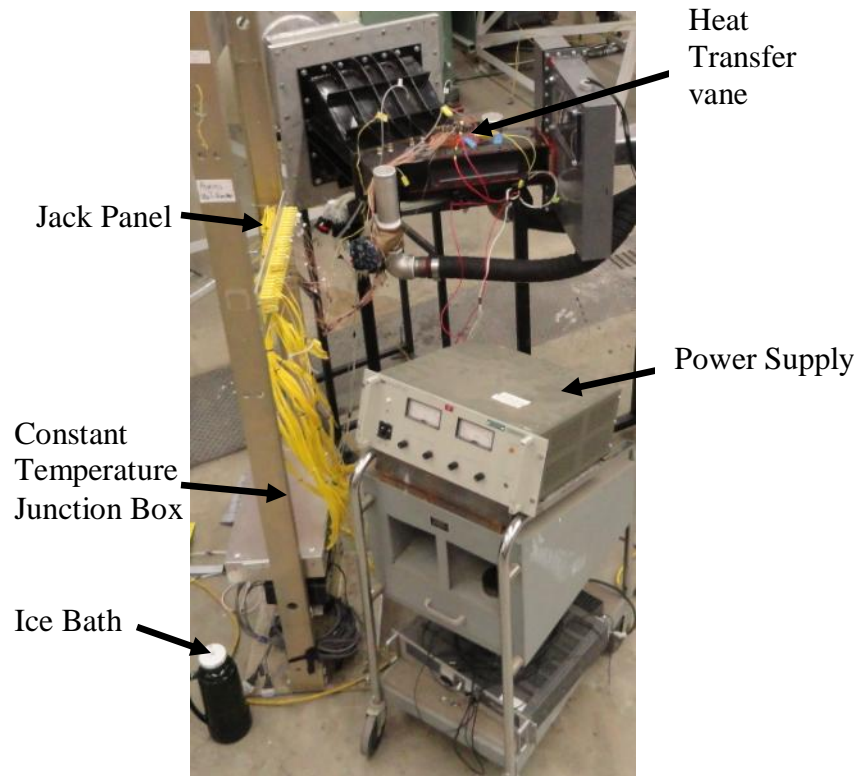
Figure 40. Instrumentation equipment used to perform heat transfer testing.

Heat Transfer Test Vane

The instrumented test vane used for heat transfer measurements can be seen in

Figure 41. The construction of the vane utilized the same methodology as the

aerodynamic vane, which is described in CHAPTER III. However, this process included

casting 40 type-K fine wire thermocouples into the vane. Before casting, the

thermocouples were fed through the 1.59 mm brass tubes positioned at the vane's mid-

span and set against the aluminum mold walls. The positioning of the thermocouples was

crucial for ensuring they were at the surface and would be directly under the Inconel foil.

After the vane had cured and was cycled thermally, channels were milled through the

flange on the trailing edge of the vane. These channels provided an unobstructed space,

where the foil's bus bars could be placed. An Inconel foil with a thickness of 0.023 mm,

backed with a 0.05 mm Kapton film with a 3M adhesive, was carefully and methodically

71

placed around the vane. The previously milled out channels in the vane's flange, were then filled with epoxy, which ensured an air tight seal around the bus bars. Kapton tape was placed around the Inconel foil edge to enhance cohesion and mitigate the possibility of the foil delaminating during testing.
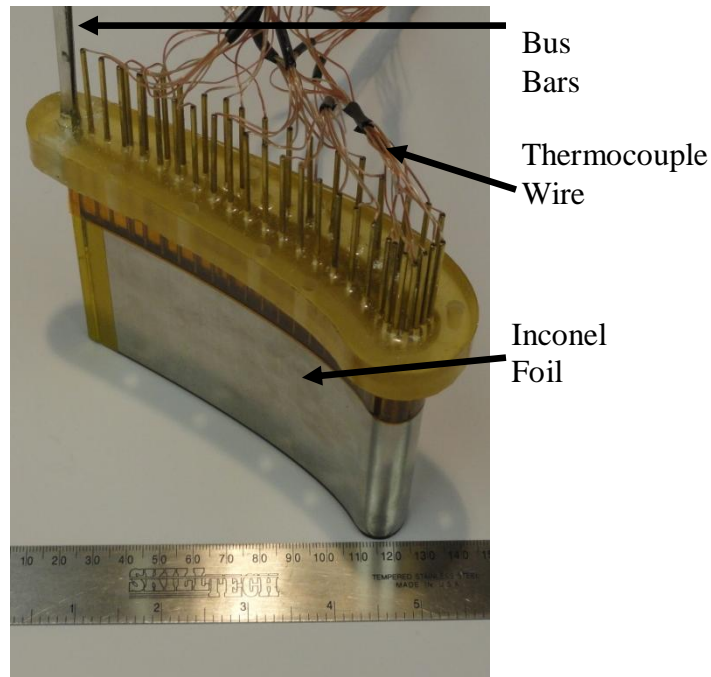
Figure 41. Heat transfer test vane.

Experimental Test Runs

Testing was conducted over a range of Reynolds number of 90,000, 180,000, 360,000, 720,000, and 1,000,000 at a series of Mach numbers of 0.7, 0.8, and 0.9. Testing was initiated by achieving a desired airflow condition inside the wind tunnel and waiting until the total temperature and vane thermocouple temperatures were at steady state. After steady state conditions were achieved, an adiabatic temperature scan was taken of each thermocouple on the vane and recorded along with tunnel conditions. The exit tunnel conditions were then used to calculate the required electrical current to produce a maximum temperature change on the vane's surface between 15 to 20 °C. A Stanton

number was first calculated with Equation 5.1, which is taken from Convective Heat and Mass Transfer by Kays, Crawford, and Weigand [60].

$$St = 0.0287Re_x^{-0.2}Pr^{-0.4} \qquad (5.1)$$

Where Re_x is the Reynolds number and Pr is the Prandtl number based on exit conditions. The global heat transfer coefficient, along with the heat flux was calculated by Equations 5.2 and 5.3.

$$h = St\rho_{ex}cp_{ex}V_{ex} \qquad (5.2)$$

$$q'' = hA_s\Delta T \qquad (5.3)$$

The exit density, specific heat and velocity are represented by ρ_{ex}, cp_{ex}, and V_{ex}. The surface area of the foil is termed A_s, while the maximum change in temperature is represented by ΔT. By estimating an electrical resistance for the foil, the voltage and current could then be calculated by Equations 5.4 and 5.5.

$$V = \sqrt{q''R} \qquad (5.4)$$

$$I = V/R \qquad (5.5)$$

The appropriate voltage and current was then supplied to the foil by using a Hewlett-Packard 6269B DC power supply, which is able to produce between 0-40 V with a current supply of 0-50 A. Once the temperature range was achieved, an hour was allowed to pass before measurements could be taken, which allowed the vane material to reach steady state conditions. After sufficient time had elapsed, the thermocouples temperatures and wind tunnel conditions were recorded and used to determine the local convection heat transfer coefficients.

Temperature Data Acquisition

The data acquisition utilized the same computing hardware as described in CHAPTER III. Where inlet total and static pressure where measured with Rosemount pressure transmitters with accuracy of 0.1%, which were used in the aerodynamic testing. However, additional components such as a passive constant temperature junction box and a 90 terminal jack-panel were integrated to aid in measuring the 40 type-K thermocouples inside the vane. The constant temperature junction box seen in Figure 40 was connected to the HP 3497A data acquisition unit, which could scan through all of the thermocouple voltages.

Additional options were included in the QUICK BASIC data acquisition program used for aerodynamic testing to aid in heat transfer measurements. The first addition provided the user with the ability to quick scan the thermocouple temperatures, which measured the thermocouples twice before reporting each temperature. This feature provided a near real time response of temperatures and aided in ensuring each thermocouple was operating correctly. The second option enabled the user to measure the power and current being supplied to the heat flux foil and measure thermocouple and wind tunnel conditions. Due to the possibility of unknown vane surface conditions, the thermocouples where measured sequentially around the vane fifteen times and then averaged. This methodology ensured local flow phenomena such as the moving locations of separation and transition would not influence results.

Data Analysis

The temperature, power, and exit flow conditions from the tests runs were analyzed to produce local Stanton numbers as a function vane position over true chord

74

length. The temperature difference between the adiabatic and heated conditions was determined by Equation 5.6,

$$\Delta T = T_{hot,v} - T_{ad,v} + \left(T_{T,ad} - T_{T,hot}\right) \tag{5.6}$$

where $T_{hot,v}$ is the individual thermocouple temperature when the foil is heated and $T_{ad,v}$ is the unheated thermocouple temperature. Inlet total temperature at an unheated condition is described by $T_{T,ad}$ and $T_{T,hot}$ represents the heated condition. The total heat flux used for determining the local Stanton number is calculated with Equations 5.7 and 5.8.

$$q''_T = q''_{gen} - q''_{rad} - q''_{cond} \tag{5.7}$$

$$q''_{rad} = \varepsilon\sigma(T_s^4 - T_\infty^4) \tag{5.8}$$

The q''_{gen} term represents the heat flux generated by the current traveling through the foil, q''_{rad} is the amount of heat flux lost to the surroundings due to radiation, and q''_{cond} is the heat flux conducted through the vane's material structure. The radiation flux is calculated by Equation 5.8, where $\varepsilon = 0.21$ is the emissivity of the foil, σ is the Stefan-Boltzmann constant, T_s is the local surface temperature, and T_∞ is the surrounding temperature. Finally, the local heat transfer and Stanton number are calculated by Equations 5.9 and 5.10, which are based on the exit conditions of the cascade.

$$h = q''_T/\Delta T \tag{5.9}$$

$$St = h/\rho_{ex}cp_{ex}V_{ex} \tag{5.10}$$

The exit flow conditions are described by its density ρ_{ex}, the specific heat cp_{ex}, and exit velocity V_{ex}. The data were then analyzed with a finite difference model to account for the conduction thickness of the Inconel foil and trailing edge cooling effect.

Vane Heat Transfer Finite Difference Conduction Model

The heat transfer coefficients found using the temperature data measured at the mid-span thermocouples will be corrected by using a finite difference conduction model of the vane seen in Figure 42. Currently, a preliminary analysis has been performed on the heat transfer data using this conduction model but further analysis is required. Therefore, the data presented in CHAPTER VII will not include corrections for conduction heat flux but only radiation heat flux.

Specifically, the model will be used to update the local surface heat flux around the vane. The uncertainties are due to the bus bars located at the trailing edge, which causes the trailing edge to act like a heat sink and cool the vane. The boundary conditions for the model at the nodes containing thermocouples are determined by the sensed temperatures beneath the foil's surface. Conditions between each node are interpolated values based on neighboring thermocouple temperatures. The model will calculate conduction heat transfer through the vane, which will either add or subtract heat flux through the surface and then will be used to correct the calculated Stanton number for each test condition.
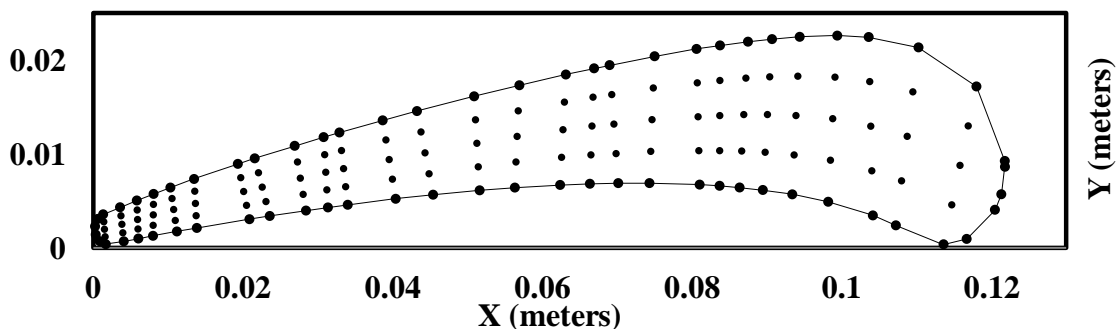
Figure 42. Finite difference model of the heat transfer vane.

Data Uncertainties

Experimental data uncertainty estimates of the reported values for thermocouple temperatures and foil power input were calculated using the root sum square method described by Moffat [59].The uncertainties of these reported test values are based on instrumentation reading error range and data reduction analysis. The foil has a nominal area of 0.0157 m^2 with an uncertainty of 1%. The maximum uncertainty for the thermocouple temperature measurements is 0.2 °C, which is based on the maximum temperatures recorded. The electrical current measurement has an uncertainty estimate of about 2% due to the uncertainty in the shunt resister resistance. The net heat flux has a 3% uncertainty due to foil thickness irregularities. The calculation of radiation loss is affected by an uncertainty of 2% in the Inconel foil emissivity and an estimated 5% in effective environment temperature the vane surfaces sees. There is also a significant uncertainty in the conduction loss or gain in both adiabatic vane temperature distribution and the surface heat flux estimate, which will be corrected for in the finite difference model when completed. All uncertainty estimates for the experimental test is based on a 95 percent confidence interval.

CHAPTER VI

EXPERIMENTAL RESULTS—AERODYNAMICS

Surface Mach Number Distribution and Exit Wake Surveys

The following chapter details results of the surface Mach number distribution and exit wake surveys for the aerodynamic test vane. The Mach number distributions are presented to show local velocity at a vane surface arc length measured from the stagnation point in relation to true axial chord length. The exit survey results include cross-passage averaged values of the total pressure loss coefficient, Ω (Omega), and the turning angle, β (Beta). Passage averaged and mid-span averaged values of Ω (Omega), and the turning angle, β (Beta) are tabulated in Table 1 and Table 2 at the end of the chapter. Resulting data are also presented in terms of cross-passage averaged Ω (Omega) and β (Beta) as a function of span and in full passage contours of local loss coefficient Ω (Omega) with secondary velocity vectors. The entirety of the surface Mach number distribution and total pressure contour results are not shown in the chapter but are presented in Appendix B and D.

Surface Mach Number Distribution

Vane surface pressure measurements were acquired at forty locations for each flow condition and used to calculate surface Mach number distributions. The data has been grouped and plotted in order to show trends as Reynolds number, turbulence level, and exit Mach numbers change. Changes in surface Mach number over these conditions can indicate boundary layer characteristics such as separation, transition, overspeed

78

regions, and shock formation. The Reynolds number can have a significant influence on boundary layer transition length on the vane's suction surface. Mach number distributions over a span of low Reynolds numbers at Mach 0.8 have been provided in Figure 43.
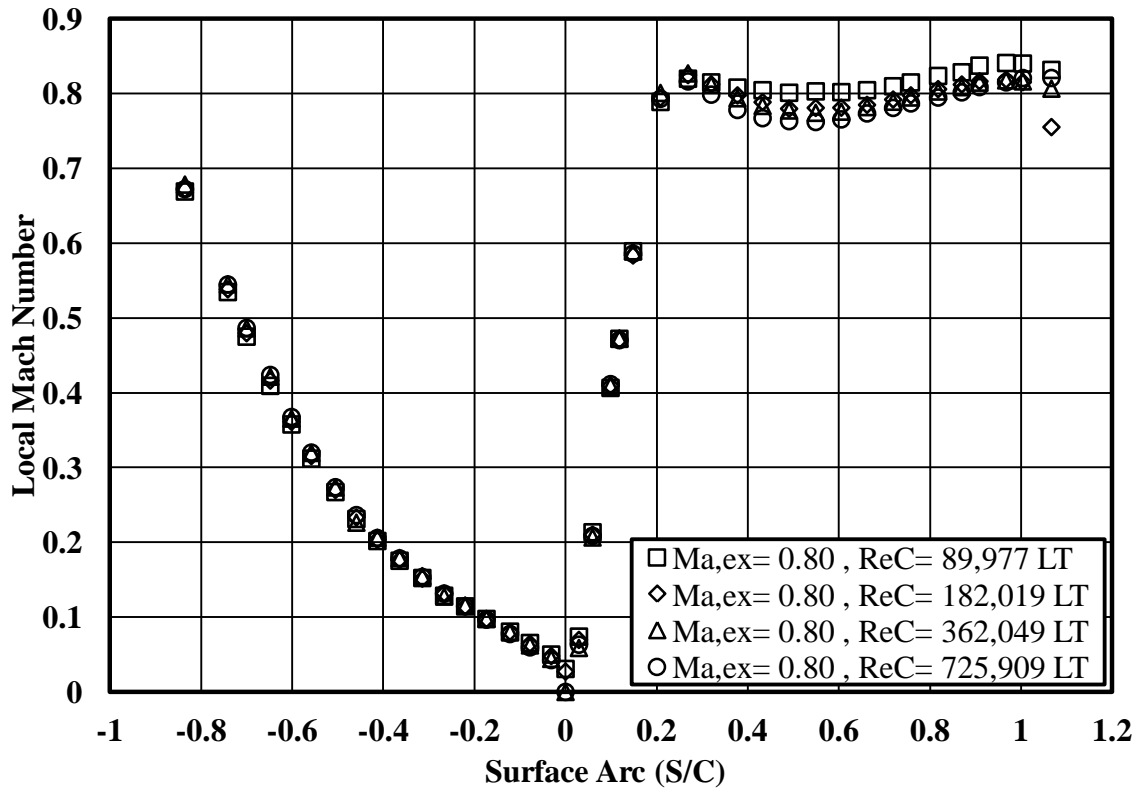
Figure 43. Surface Mach number distribution over a span of Reynolds numbers of 90,000, 180,000, 360,000, and 720,000 at an exit Mach number of 0.8 under low turbulent conditions.

The pressure surface Mach numbers, starting at the negative arc length, have not been affected by the change in Reynolds number. The suction surface Mach number, located on the positive arc length, shows a consistent trend of change as Reynolds number is varied. At the lowest Reynolds number of 90,000, a moderate overspeed region is seen just downstream from the stagnation point. The overspeed region decelerates to form a valley between arch lengths of 0.22 to 0.6 before accelerating to a maximum velocity at an arc length of 1.0, which then decelerates at the trailing edge. As the

79

Reynolds number increases, the magnitude of deceleration after the overspeed region also increases. The Mach number appears to recover to nearly the same value at the trailing edge for all Reynolds number cases. The gradual trend of diminishing Mach number after the overspeed region decreases by more than 5%, from the lowest to highest Reynolds numbers. The decrease is attributed to the change in boundary layer transition location and boundary layer thinning, which would reduce blockage in the passage.
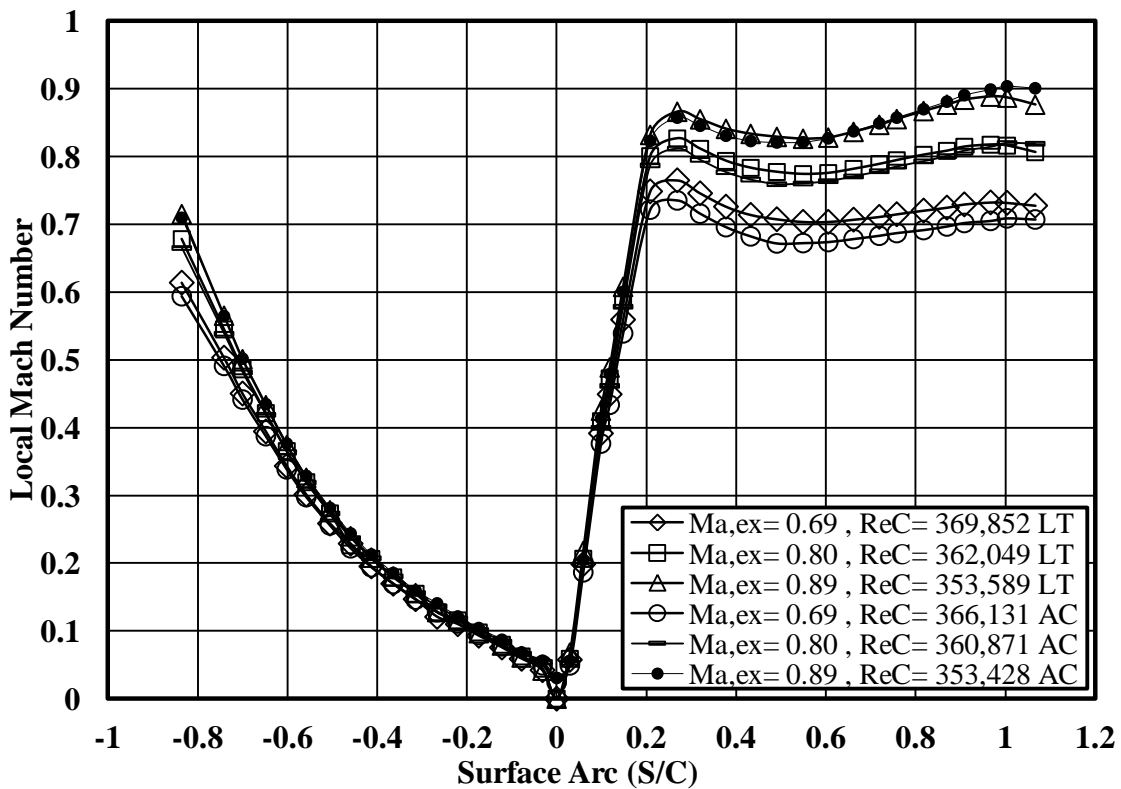
Figure 44. Surface Mach number distributions over a span of exit Mach numbers of 0.7, 0.8, and 0.9 at a Reynolds number of 360,000 under low and aero-combustor turbulence.

The changes in surface Mach number can also be influenced by freestream turbulence intensity. The elevated turbulence levels can cause a boundary layer to transition earlier than at lower turbulence levels, which could influence surface Mach number. Surface Mach numbers over a span of exit Mach numbers between 0.7, 0.8, and 0.9, at a Reynolds number of 360,000 and under low and aero-combustor turbulence has

80

been provided in Figure 44. The increased turbulence level appears to have little influence on pressure surface Mach number. This could be attributed to the turbulence unable to penetrate the laminar boundary layer and cause transition. The characteristic overspeed, decelerating, and accelerating region examined previously is still evident at each exit Mach number for the suction surface. There is a clear decrease in surface Mach number with the aero-combustor turbulence for the three exit Mach numbers. For the lowest to highest exit Mach numbers, there are an average of 3.95, 1.63, and 0.73% decrease in local Mach number. The difference on suction surface Mach number between the low and mock combustor turbulence could be attributed to flow condition changes of the two experimental tests. However, a small portion of the difference can be explained by laminar to turbulent boundary layer transition on the suction surface.
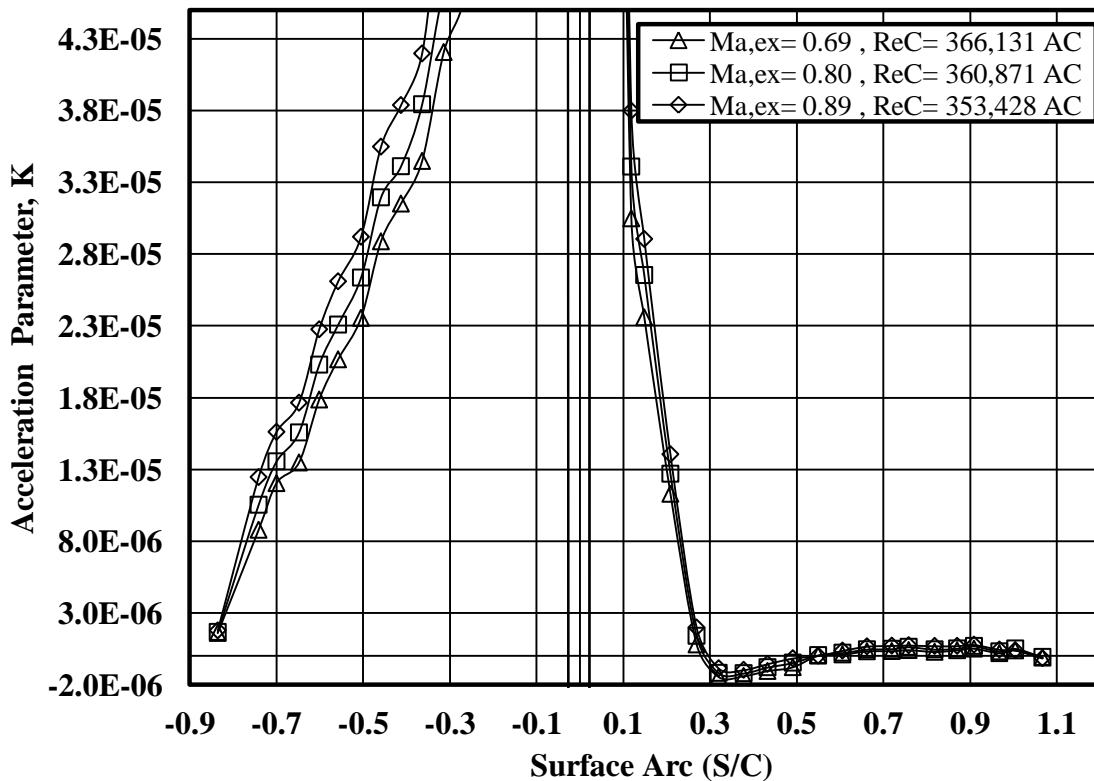
Figure 45. Acceleration parameter for a Reynolds number of 360,000 over a range of Mach numbers of 0.7, 0.8, and 0.9 under aero-combustor turbulence conditions.

81

The heat transfer results clearly show transition occurring on the suction surface for a Reynolds number of 360,000 at Mach numbers of 0.7, 0.8, and 0.9 that can be seen in Figure 72 of CHAPTER VII and Figure 126 and Figure 127 in Appendix E. Stanton number augmentation on the suction surface decreases as Mach number increases, which matches the Mach number trend in Figure 44. The decrease in transition could be related to the acceleration parameter K, which is described by Equation (6.1), which was taken from White [61],

$$K = \frac{\nu}{u_\infty^2} \frac{du_\infty}{dx} \qquad (6.1)$$

where ν is the kinematic viscosity, du_∞ is the differential change in vane surface velocity, and dx is the differential change in vane surface length. Laminarization of the turbulent boundary layer occurs when K exceeds about 3×10^{-6}. Figure 45 shows the acceleration parameter for the aero-combustor turbulence conditions presented in Figure 44. The pressure surface has a nearly equal acceleration parameter over all three Mach numbers but the acceleration parameter on the suction surface varies with Mach number. The laminarization acceleration parameter is not reached on the suction surface but it does increase as Mach number increases. The increase in acceleration parameter as Mach number increases would begin to reduce transition, which is evident in the surface Mach number and Stanton number plots previously evaluated.
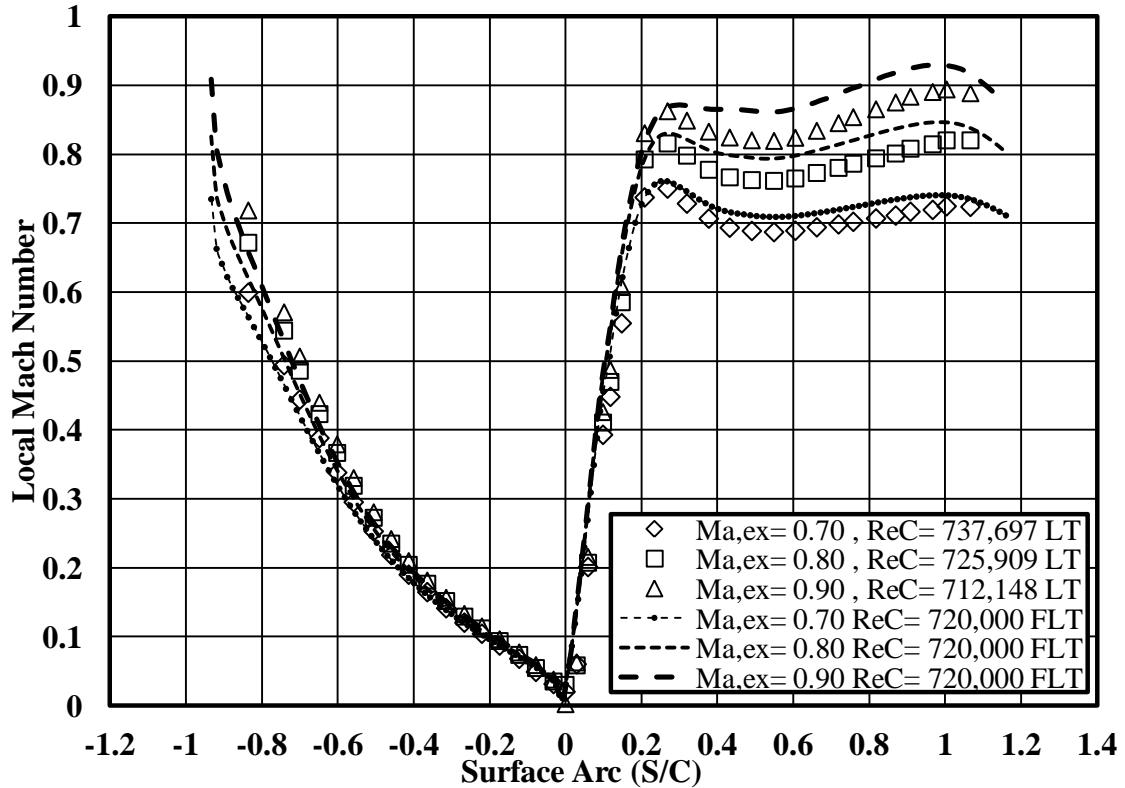
Figure 46. Surface Mach number distributions compared to FLUENT flow calculations over a span of exit Mach numbers of 0.7, 0.8, and 0.9 at a Reynolds number of 720,000, under low turbulent conditions.

Experimental results for a Reynolds number of 720,000 over a span of exit Mach numbers of 0.7, 0.8, and 0.9 have been compared to numerical calculations performed in FLUENT. The numerical prediction model utilized compressible flow parameters with inlet and outlet pressure boundary conditions taken from the experimental conditions. Inlet and outlet pressures were initialized ¼ axial chord upstream and downstream from the vane's leading and trailing edge. The vane geometry was modeled as a wall boundary condition with an inlet to exit turning angle of 73°. Periodic boundary conditions were applied to the streamlines of the mid-passages for the pressure and suction surface to simulate an infinite cascade of vanes. As seen in Figure 46, the numerical solutions provide an excellent match on the pressure surface with a slight deviation near the trailing

edge that could be attributed to the idealization of the flow equations. There is a slight deviation on the suction side for the lowest Mach number, where the numerical code over predicts the local Mach number distribution. However, the contoured shape of the suction surface is predicted well numerically, which provides confidence in the consistency of the mid-span aerodynamics produced by the cascade. Numerical prediction deviation is slightly more for the remaining exit Mach numbers but still follows the experimental data's trend. The over predictions could be explained by deviations in the experimental vane surface not accounted for in the code and flow variations.

Low Turbulence Exit Wake Surveys at ¼ Axial Chord as a Function of Reynolds Number

Total pressure loss contours, Ω (Omega), and secondary flow vectors taken at ¼ axial chord length from the aerodynamic test vane's trailing edge are shown in Figures 47, 48, 49, and 50. The contour figures characterize exit conditions for Reynolds numbers of 90,000, 180,000, 360,000, and 720,000 at a Mach number of 0.8 for low turbulence conditions. At a Reynolds number of 90,000, Figure 47 shows a significant secondary loss core at about 1.5 cm or 21% of span off the endwall. The secondary loss extends from the loss core to the mid-span due to a strong wake region. The secondary velocity vectors indicate the loss core has been strongly influenced by secondary flows from the passage vortex which has lifted the loss core away from the endwall.

Figure 47. Total pressure loss contours Ω (Omega) with secondary velocity vectors for the vane at ¼ axial chord location under low turbulence at a chord exit Reynolds number of 90,000 and Mach number of 0.8.

Due to the proximity of the probe being a spanwise distance of 0.438 cm from the endwall, the loss from the corner vortex interacting with the endwall and suction surface connection is not visible. The orientation of the secondary velocity vectors near the endwall show characteristic overturning, while turning near the loss core is minimal. Nearly two dimensional flows are indicated at the pressure side near the endwall and mid-span, due to the reduction of secondary velocity vectors and total pressure loss. Vortical flow is clearly visible in the secondary velocity vectors just above the loss core on either side. The mass averaged values for total pressure loss are presented in Table 1 for the entire passage and mid-span.

For a Reynolds number of 180,000, Figure 48 shows a significant loss core at about 1.5 cm or 22% of the span off the endwall. A second minimal loss core thought to

85

be the suction leg of the horseshoe vortex described by Goldstein and Spores [14], is also seen at about 3.1 cm or 45% of the span off the endwall. Compared to the contours at a Reynolds number of 90,000, the secondary losses appear to be slightly more concentrated around the main loss core.

Figure 48. Total pressure loss contours Ω (Omega) with secondary velocity vectors for the vane at ¼ axial chord location under low turbulence at a chord exit Reynolds number of 180,000 and Mach number of 0.8.

Secondary velocity vectors indicate the loss core has been lifted up off the endwall due to the influence by the passage vortex. The characteristic overturning of the flow is seen near the endwall, which gradually pitches up with an up-flow towards the loss core. Three dimensional flows appear to be minimal on the pressure side of the exit survey, but strong downward flows dominate the suction side near the mid-span. The combination of downward and upward flows, near the mid-passage with vortical motion, is clearly generated and seen slightly above the loss core.

86

At a Reynolds number of 360,000, the main loss core seen in Figure 49 has been lifted to about 1.4 cm or 20% of span, off the endwall. The second loss core previously seen near the mid-span has moved up to about 3.2 cm or 46% of span off the endwall. The secondary loss between these two loss contours appears to have increased, resulting in a larger overall loss area. Similar to the preceding results, secondary velocity vectors show overturning near the endwall with a strong upward pitch flow traveling to the loss core. Near the endwall, the flow is two dimensional on the pressure side and a vortical downward flow exists on the suction side resulting in two vertical vortices in series next to the main loss core.
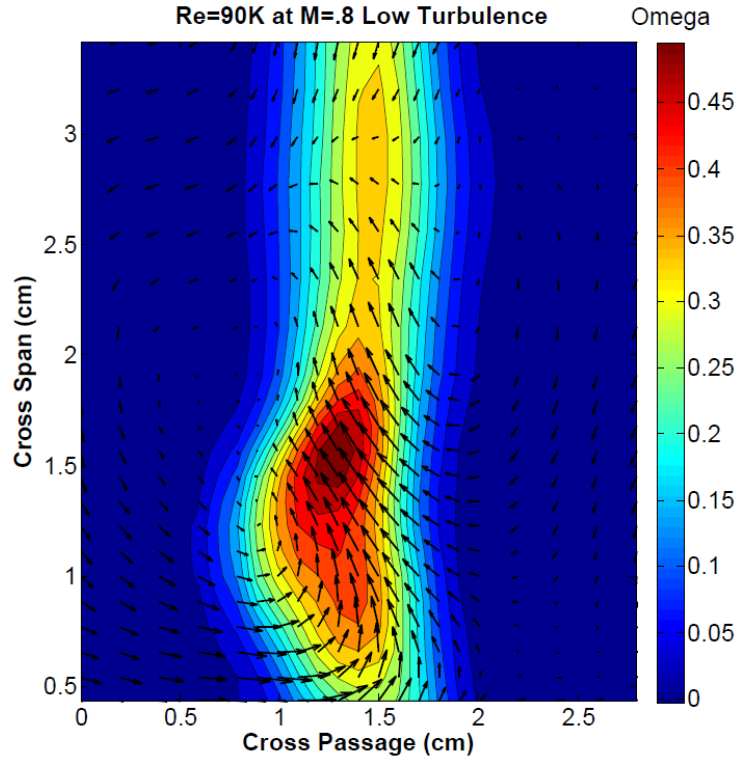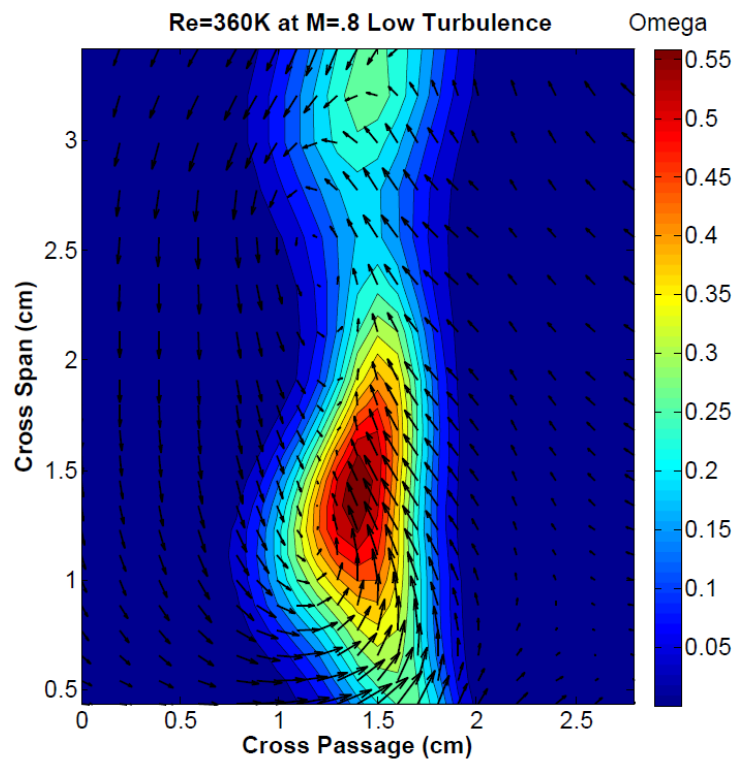

Figure 49. Total pressure loss contours Ω (Omega) with secondary velocity vectors for the vane at ¼ axial chord location under low turbulence at a chord exit Reynolds number of 360,000 and Mach number of 0.8.

At a Reynolds number of 720,000, Figure 50 shows the main loss core has maintained its position at about 1.4 cm or 20% of span off the endwall. The second loss

core moves up and centers itself at the mid-span, while its intensity has diminished compared to the lower Reynolds number cases. The loss contours across the 3.42 cm mid-span have developed an even distribution resulting in near symmetry at the mid-passage to the mid-span.
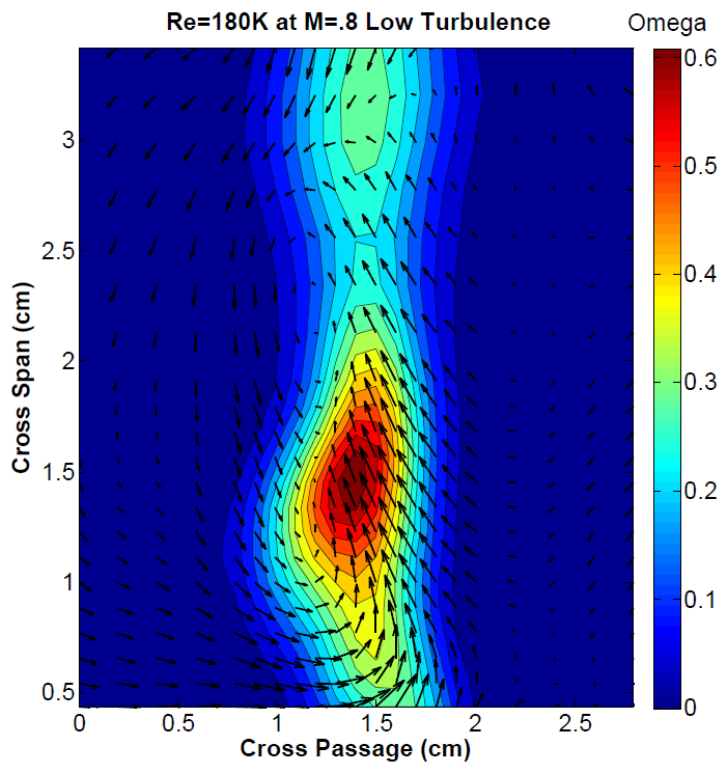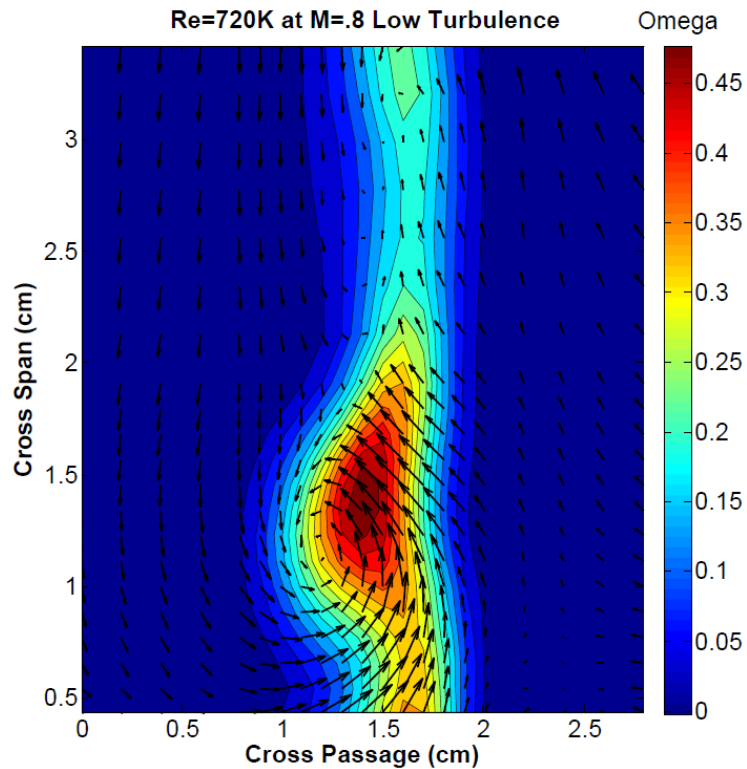

Figure 50. Total pressure loss contours Ω (Omega) with secondary velocity vectors for the vane at ¼ axial chord location under low turbulence at a chord exit Reynolds number of 720,000 and Mach number of 0.8.

The main loss core appears to be smaller and less intense than at lower Reynolds numbers. The loss near the endwall attributed to the corner vortice has grown enough to be within range of probe detection. The increase loss near the endwall can be seen in Figure 50, which is located 0.5 cm off the endwall and at the center of the cross passage. The secondary losses between the endwall and main loss core have also enhanced, compared to lower Reynolds numbers. Overturning near the endwall appears to be less evident by the secondary velocity vectors, but a vortical flow is still present, which leads

from the endwall and up into the loss core. Secondary velocity vectors show that three dimensional flows are prevalent in the exit survey with a very tight vortical formation below the loss core.

The cross-passage averaged distribution of Ω (Omega) is seen in Figure 51 for the four Reynolds numbers at Mach 0.8 under low turbulence conditions. The passage averaged total pressure losses, determined from the exit surveys, is 0.0878, 0.0784, 0.0685, and 0.0584 to Reynolds numbers of 90,000, 180,000, 360,000, and 720,000, respectively. The results indicate as Reynolds number increases, the mass averaged total pressure loss decreases.
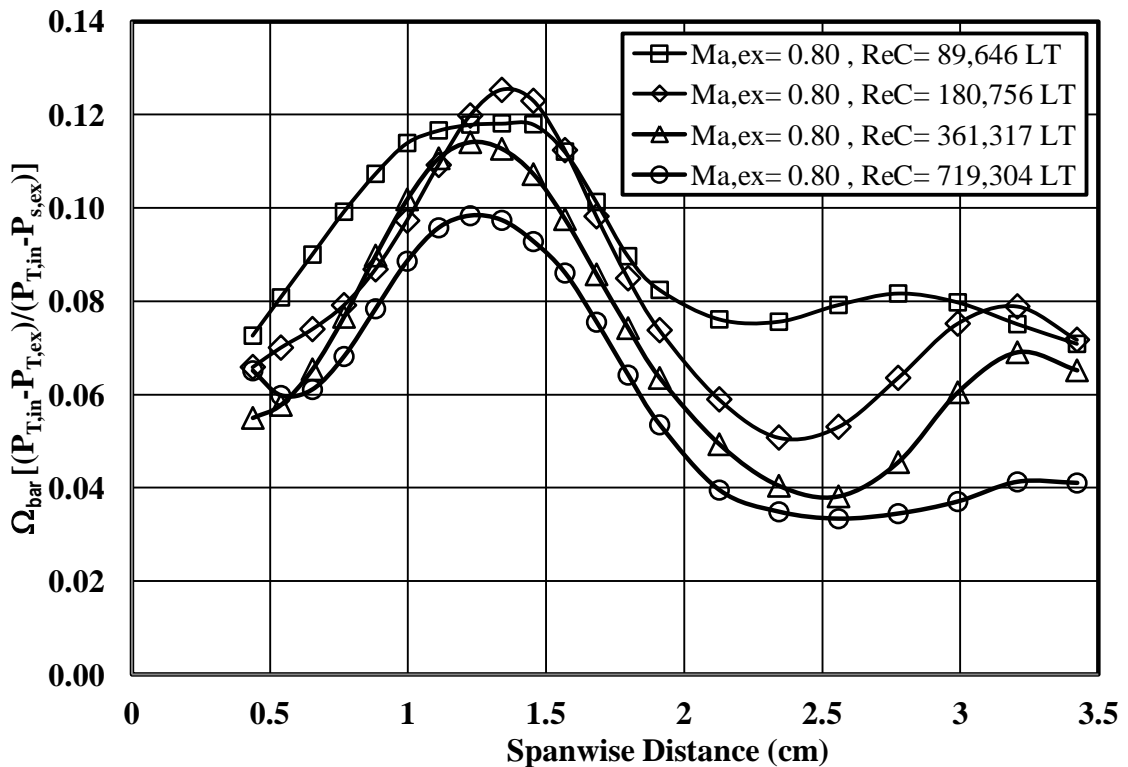
Figure 51. Cross-passage averaged total pressure loss coefficient Ω (Omega) for the vane at ¼ axial chord location under low turbulence over a range of Reynolds numbers of 90,000, 180,000, 360,000, and 720,000 at a Mach number of 0.8.

89

The spanwise loss distribution for the range of Reynolds numbers indicate the same main loss core configuration with a decreasing trend as Reynolds number increases. The peak loss core for Reynolds numbers of 90,000 and 180,000 are nearly in the same spanwise location. The peak loss core moves closer to the endwall and is in approximately the same location for Reynolds numbers of 360,000 and 720,000. A second loss core occurs near the mid-span for all Reynolds numbers, which is attributed to laminar boundary layer separation on the suction surface. The loss core peaks in the same location for all Reynolds numbers except 90,000, which is more spread out. The second loss core follows the same trend as the main core by decreasing in intensity as Reynolds number increases. The near wall mass averaged total pressure loss is not visible due to the proximity of the probe being too far from the endwall. However, based on previous results gathered by Ames, Johnson, and Fiala [19] near wall mass averaged total loss corrections have been calculated and tabulated in Table 1.

90
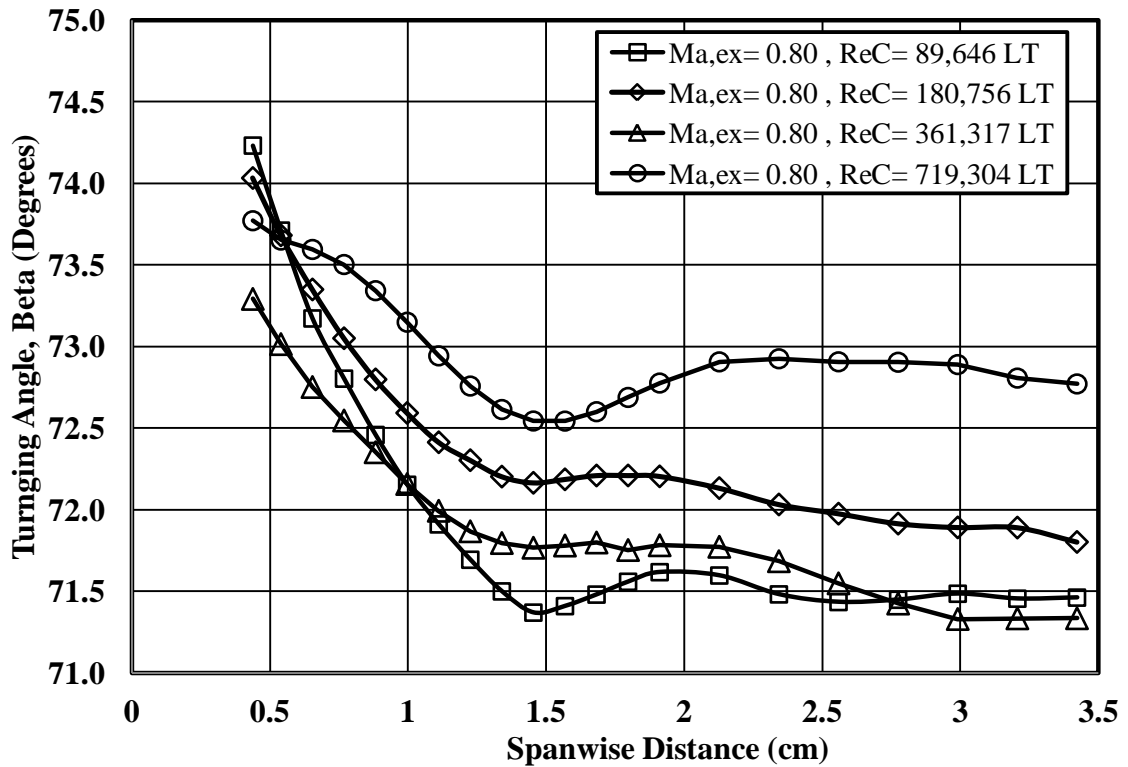
Figure 52. Cross-passage averaged turning angle β (Beta) for the vane at ¼ axial chord location under low turbulence over a range of Reynolds numbers of 90,000, 180,000, 360,000, and 720,000 at a Mach number of 0.8.

The cross-passage averaged turning angle β (Beta) is presented in Figure 52 for the previously discussed Reynolds numbers. The near wall turning angle shows significant overturning as compared to the mass averaged turning angles of 72.1, 72.5, 71.98, and 73.0 for lower to higher Reynolds numbers. The flow near the loss core produces the minimal turning angle for Reynolds numbers of 90,000 and 720,000. The minimal turning angle is apparent at the other Reynolds numbers.

Aero-Combustor Turbulence Exit Wake Surveys at ¼ Axial Chord as a Function of Reynolds Number

Exit wake surveys at ¼ axial chord show total pressure loss contours, Ω (Omega), and secondary flow vectors in Figure 53 through Figure 56 under aero-combustor turbulence conditions. The contour figures demonstrate the influence of turbulence on

91

exit conditions for previously described low turbulence Reynolds numbers of 90,000,
180,000, 360,000, and 720,000 at a Mach number of 0.8. Figure 53 shows exit survey
conditions of total pressure loss at a Reynolds number of 90,000 with a significant loss
core at 1.6 cm or 23% of span distance from the endwall. A comparison between Figure
47 and Figure 53 shows the loss core intensity has reduced and moved slightly up. The
wake region appears wider and symmetrical about the cross-passage, which Ames and
Plesniak [6] attributed to enhanced turbulent mixing.

Figure 53. Total pressure loss contours Ω (Omega) with secondary velocity vectors for
the vane at ¼ axial chord location under aero-combustor turbulence at a chord exit
Reynolds number of 90,000 and Mach number of 0.8.

The secondary velocity vectors appear to be more two dimensional near the mid-
span with a weaker vortex near the loss core, which indicates a weaker passage vortex.
Velocity vectors show secondary flows traveling up the suction surface with downward
flow on the pressure surface. The losses near the endwall have increased due to a thicker

www.manaraa.com

inlet boundary layer, which is not clearly visible due to limited probe proximity to the endwall.

At a Reynolds number of 180,000 a comparison between Figure 54 and Figure 48 clearly show enhanced mixing due to turbulence. The intensity of the loss core has slightly weakened and narrowed in the spanwise direction. The wake region between the loss core and mid-span has increased in width, while the second loss core does not appear to be present. The secondary velocities have weakened over much of the exit survey but still maintain a strong upward flow on the suction surface. The two vortices seen at lower turbulence have moved closer to the endwalls indicating a weaker passage vortex. Losses near the endwall have increased due to the corner vortex.

Figure 54. Total pressure loss contours Ω (Omega) with secondary velocity vectors for the vane at ¼ axial chord location under aero-combustor turbulence at a chord exit Reynolds number of 180,000 and Mach number of 0.8.

For a Reynolds number of 360,000 the total loss core is positioned at 1.3 cm or 19% of span off the endwall. Comparing Figure 49 and Figure 55 indicates the loss core is slightly closer to the endwall, which may result from a weaker passage vortex. Consistent uniformity is apparent in the wake region, while the second loss core has dissipated. However, the intensity of loss increases at the mid-span in the wake, which could indicate the formation of second loss core just above the mid-span. Secondary velocities have decreased while two vortical flows are visible near the endwalls on both suction and pressure sides. Overturning near the endwall is still visible but not to the extent seen at low turbulence.
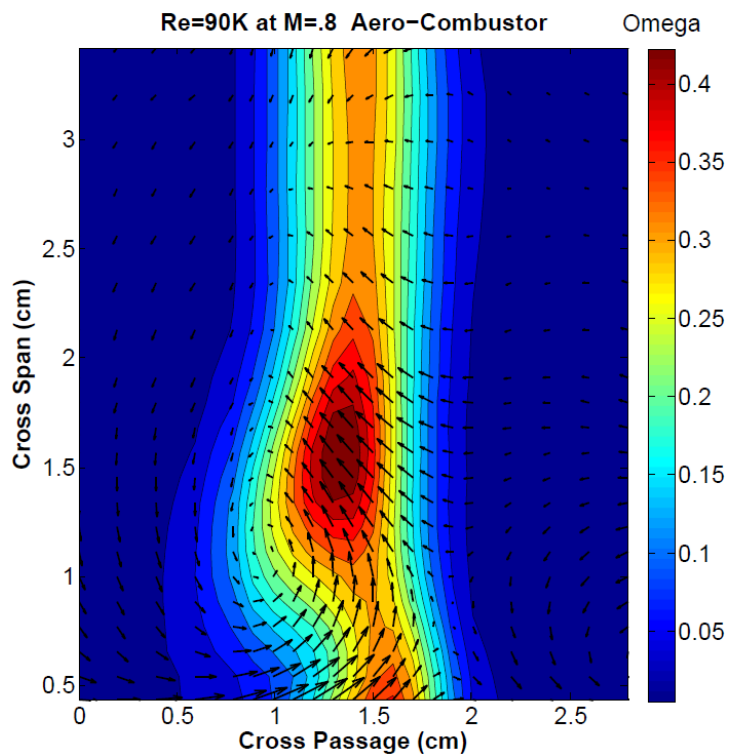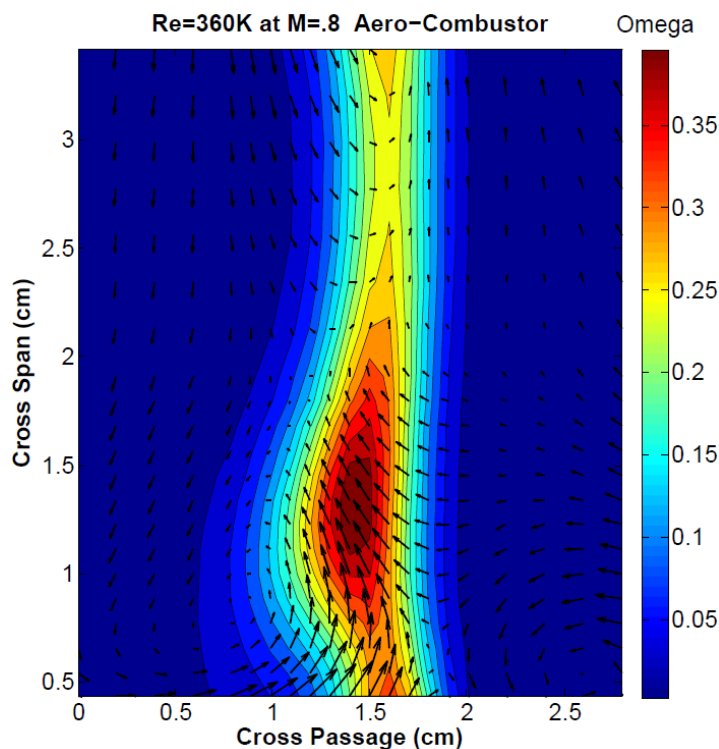

Figure 55. Total pressure loss contours Ω (Omega) with secondary velocity vectors for the vane at ¼ axial chord location under aero-combustor turbulence at a chord exit Reynolds number of 360,000 and Mach number of 0.8.

Comparing Figure 50 and Figure 56 together, a significant change in overall total pressure loss is indicated for the exit survey at a Reynolds number of 720,000. The width

of loss core has increased by 0.5 cm for the suction side. The intensity of the main loss core has decreased, but significantly increased near the endwall due to the presence of the corner vortex. The wake region above the loss core has become uniformly distributed but increased in intensity. The second loss core appears to have moved up passed the mid-passage and increased in intensity. Secondary velocity vectors appear slightly diminished but still maintain a vortex near the loss core as previously seen at low turbulence. The velocity vectors also show the corner vortex near the endwall.
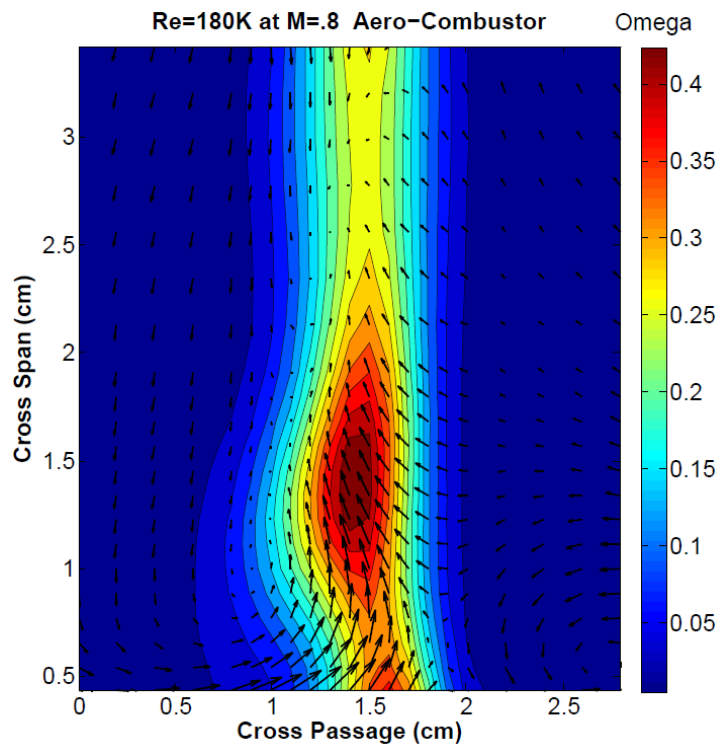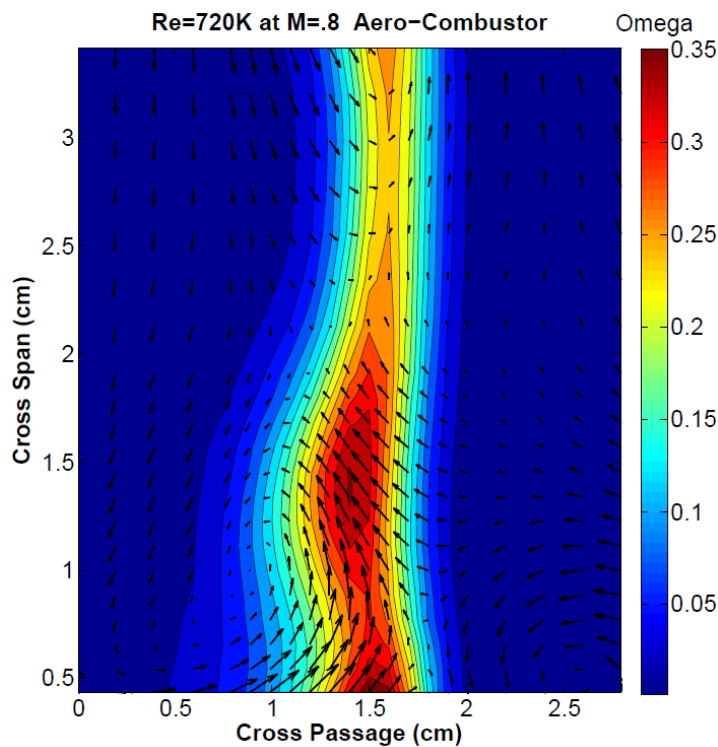

Figure 56. Total pressure loss contours Ω (Omega) with secondary velocity vectors for the vane at ¼ axial chord location under aero-combustor turbulence at a chord exit Reynolds number of 720,000 and Mach number of 0.8.

The cross-passage averaged distribution of Ω (Omega) is seen in Figure 57 for the four Reynolds numbers at Mach 0.8 under aero-combustor turbulence conditions. The passage averaged total pressure losses, determined from the exit surveys are 0.0938, 0.0796, 0.0663, and 0.0638 for the lowest to highest Reynolds number. The mass

95

averaged total pressure loss results show that as the Reynolds number increases then both profile and secondary loss decreases. These results coincide with low turbulence conditions but are slightly augmented due to turbulent mixing.
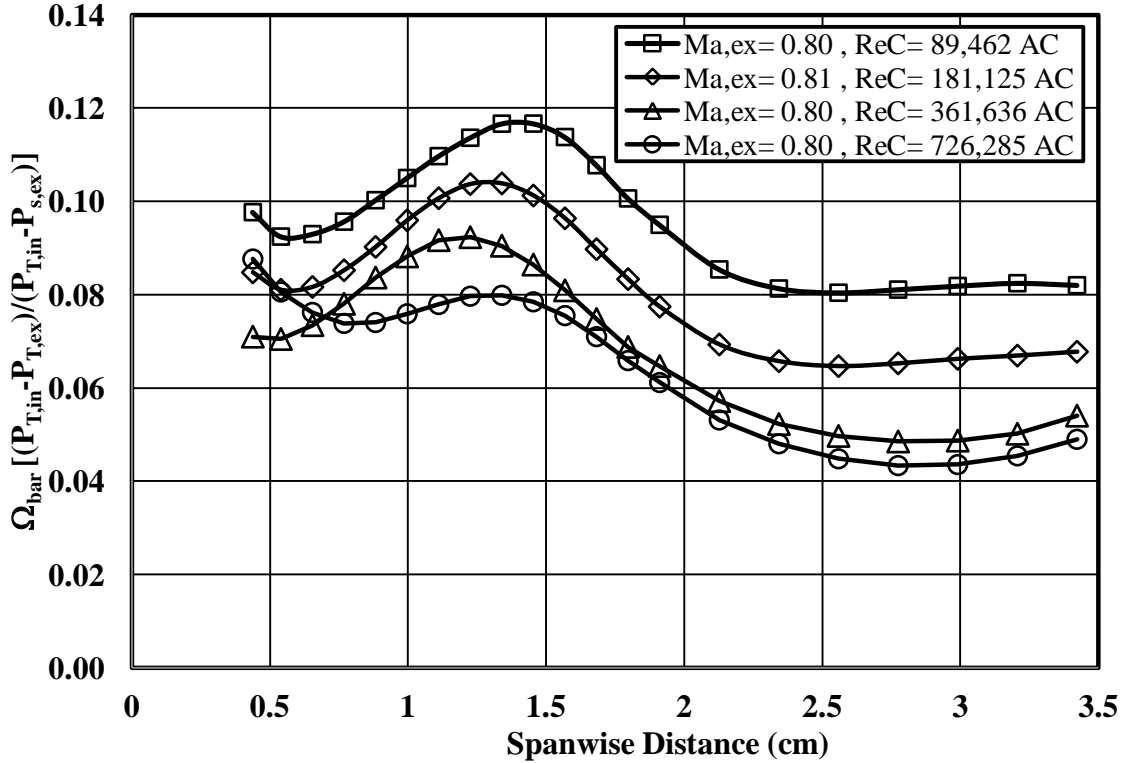
Figure 57. Cross-passage averaged total pressure loss coefficient Ω (Omega) for the vane at ¼ axial chord location under aero-combustor turbulence over a range of Reynolds numbers of 90,000, 180,000, 360,000, and 720,000 at a Mach number of 0.8.

The distribution for the span of Reynolds numbers indicate a similar secondary main loss core, as seen at lower turbulence, with a decreasing trend as Reynolds number increases. The location of the peak loss core shows a downward trend towards the endwall over all Reynolds numbers except for 720,000. Increased losses near the endwall are visible at higher turbulence conditions but are not entirely accounted for. Extrapolating from results by Ames, Johnson, and Fiala [19], adjusted values of loss have been calculated, which can be seen in Table 1.

96
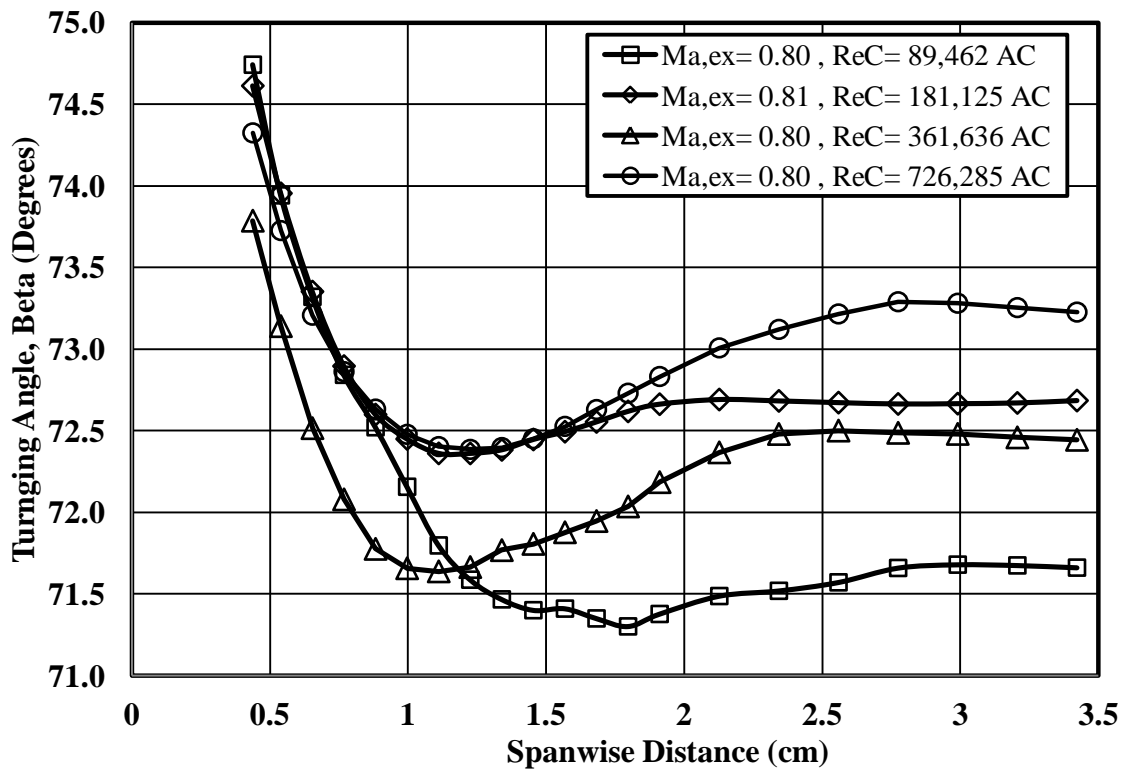
Figure 58. Cross-passage averaged turning angle β (Beta) for the vane at ¼ axial chord location under aero-combustor turbulence over a range of Reynolds numbers of 90,000, 180,000, 360,000, and 720,000 at a Mach number of 0.8.

The cross-passage averaged turning angle β (Beta) is presented in Figure 58 over the range of Reynolds numbers under aero-combustor turbulence. The trend appears similar to lower turbulence conditions, but overturning is greater near the endwall. The turning angle trend amongst the Reynolds number is also more developed, which shows gradual transition between the endwall and mid-passage. The vortex core location is identifiable as the under-turning angle reaches a minimum and recovers to a horizontal slope. The turning angle region describing the core accounts for a much larger span than at low turbulence, which indicates the loss core has weakened due to turbulent mixing.

97
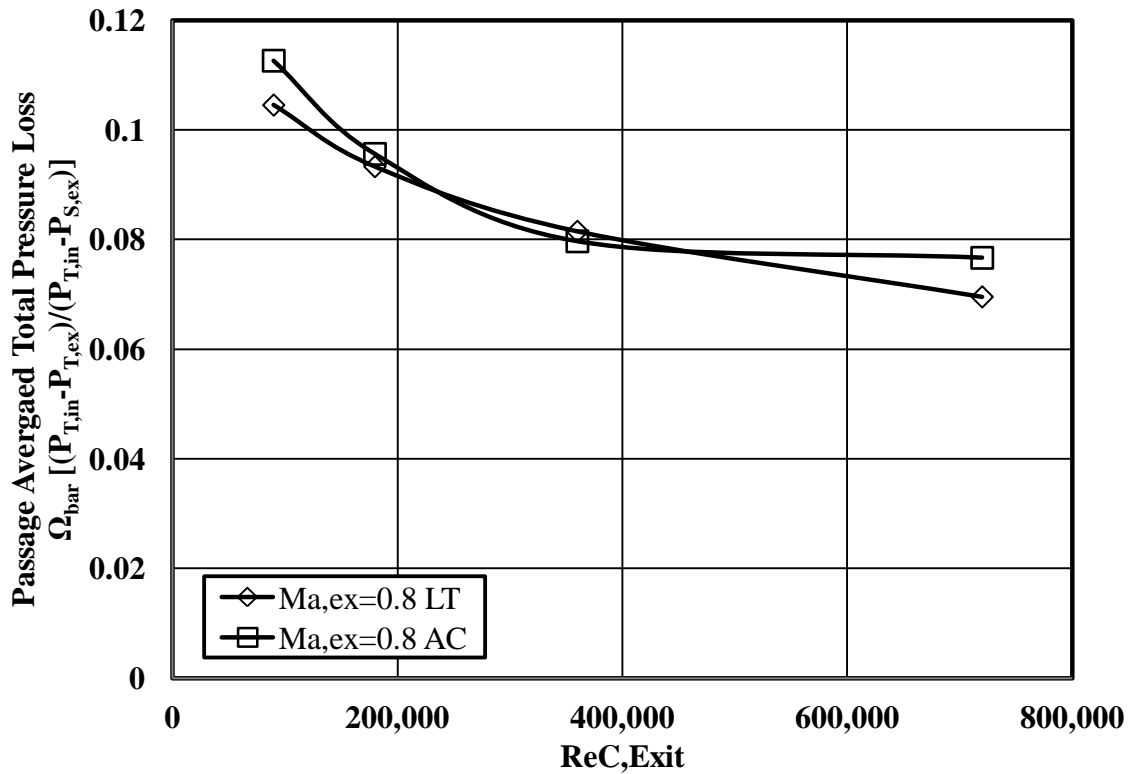
Figure 59. Comparison of passage averaged total pressure loss over a range of Reynolds numbers of 90,000, 180,000, 360,000, and 720,000 at a Mach number of 0.8 for low and aero-combustor turbulence.

A graphical comparison has been provided in Figure 59 that shows the relation of averaged total pressure loss over the span of low Reynolds numbers for low and aero-combustor turbulence. Averaged total pressure loss values have been corrected to account for near wall endwall losses, which were not measured. This correction was based on the data of Ames, Johnson, and Fiala[19] which suggested that up to 20% of the passage loss occurs in the bottom 14% of the span. The total pressure loss is clearly related to the Reynolds number, increasing as the Reynolds number decreases. However, higher turbulence appeared to weaken the passage vortex, resulting in increased total pressure loss.

98

Table 1. Wind tunnel conditions, mass averaged loss, and turning angle for ¼ axial chord exit surveys at low and aero-combustor turbulence for the aerodynamic test vane as a function of Reynolds number at Mach 0.8.

¼ Cax	Low Turbulence				Aero-Combustor Turbulence			
ReC	89,646	180,756	361,317	719,304	89,462	181,125	361,636	726,285
T_T,in (K)	320.7	322.7	331.7	337.2	327.6	326.3	328.0	326.8
P_T,in (Pa)	6,030	12,244	25,350	51,502	6,199	12,396	25,032	50,010
Vex (m/s)	270.8	272.0	275.7	278.4	272.4	275.5	273.8	273.6
Maex	0.80	0.80	0.80	0.80	0.80	0.81	0.80	0.80
Ω (Midline)	0.0708	0.0717	0.0652	0.0410	0.0820	0.0677	0.0540	0.0490
Ω (Full)	0.0878	0.0784	0.0685	0.0584	0.0938	0.0796	0.0663	0.0638
Ωcor (Full)	0.1045	0.0933	0.0815	0.0695	0.1126	0.0956	0.0797	0.0766
β (Midline)	71.46	71.80	71.33	72.77	71.66	72.68	72.44	73.23
β (Full)	72.08	72.48	71.98	73.03	72.18	72.93	72.43	73.13

Low Turbulence Exit Wake Surveys at ¼ Axial Chord as a Function of Mach Number

The exit surveys shown in Figure 60 and Figure 61 demonstrate the effects that Mach number has on secondary flows under low Reynolds number conditions. The exit surveys presented are taken at ¼ axial chord length from the vane trailing edge for a Reynolds number of 720,000 at Mach numbers of 0.7, 0.8, and 0.9 under low turbulence flow. At a Mach number of 0.7, Figure 60 shows a main loss core at around 1.5 cm or 22% of span from the endwall. The loss core gradually transitions to the mid-span and endwall with moderate wake loss.

99

Figure 60. Total pressure loss contours Ω (Omega) with secondary velocity vectors for the vane at ¼ axial chord location under low turbulence at a chord exit Reynolds number of 720,000 and Mach number of 0.7.

The secondary velocity vectors show a downdraft on the suction surface. This downdraft turns; sweeping across the endwall and rolling up to form vortical flow just below the loss core. The velocity vectors on the pressure surface show minimal turning and are nearly two-dimensional.

By increasing the Mach number to 0.9, significant total pressure-loss changes occur in the exit survey at a Reynolds number of 720,000. Figure 61 shows that the loss core has moved to 1.4 cm or 20.5% of span from the endwall. A second loss core has formed at approximately 3.2 cm or 47% of span from the endwall, which has deformed the wake loss previously seen at a Mach number of 0.7. The loss between the endwall and main loss core appears to be unaffected. Secondary velocity vectors are unchanged on the suction side and still show strong overturning near the endwall. However, velocity

100

vectors have a strong upward pitch under the main loss core, which forms a tighter vortex than previously seen at the lower Mach number. The secondary velocity vectors also show a counter-clockwise rotating flow pattern between the first and second loss cores, which could be the suction leg of the horseshoe vortex described by Goldstein and Spores [14].
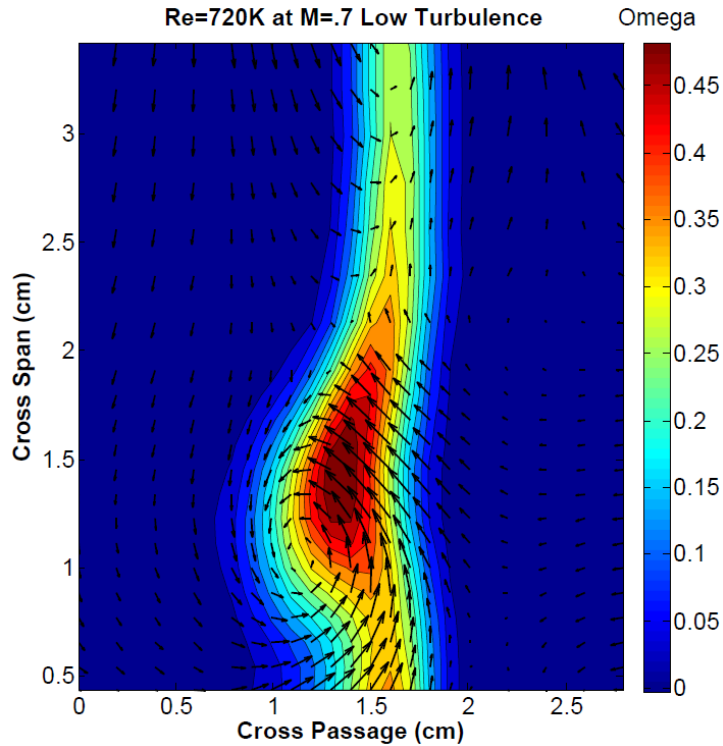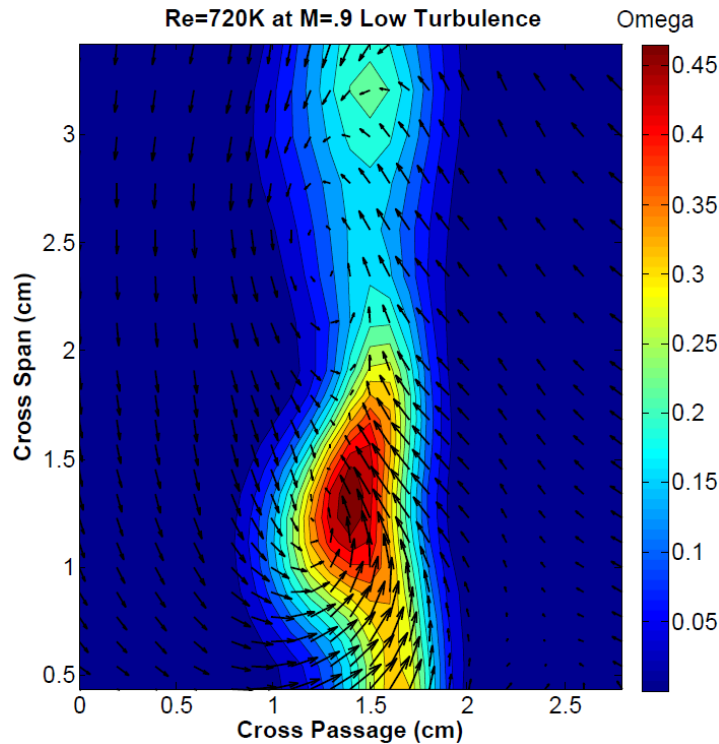

Figure 61. Total pressure loss contours Ω (Omega) with secondary velocity vectors for the vane at ¼ axial chord location under low turbulence at a chord exit Reynolds number of 720,000 and Mach number of 0.9.

The cross-averaged total pressure loss Ω (Omega), seen in Figure 62, is for a Reynolds number of 720,000 for Mach numbers of 0.7, 0.8, and 0.9 under low turbulence conditions. The trend for all three Mach numbers is essentially the same up to the maximum total pressure loss of the main loss core. The curves then separate and show an increasing mid-span loss as the Mach number increases. Near the mid-span, the second loss core begins to develop, which was seen in the contour figures. The complete loss

near the endwall is not shown due to probe proximity but an averaged corrected value can be found in Table 2.
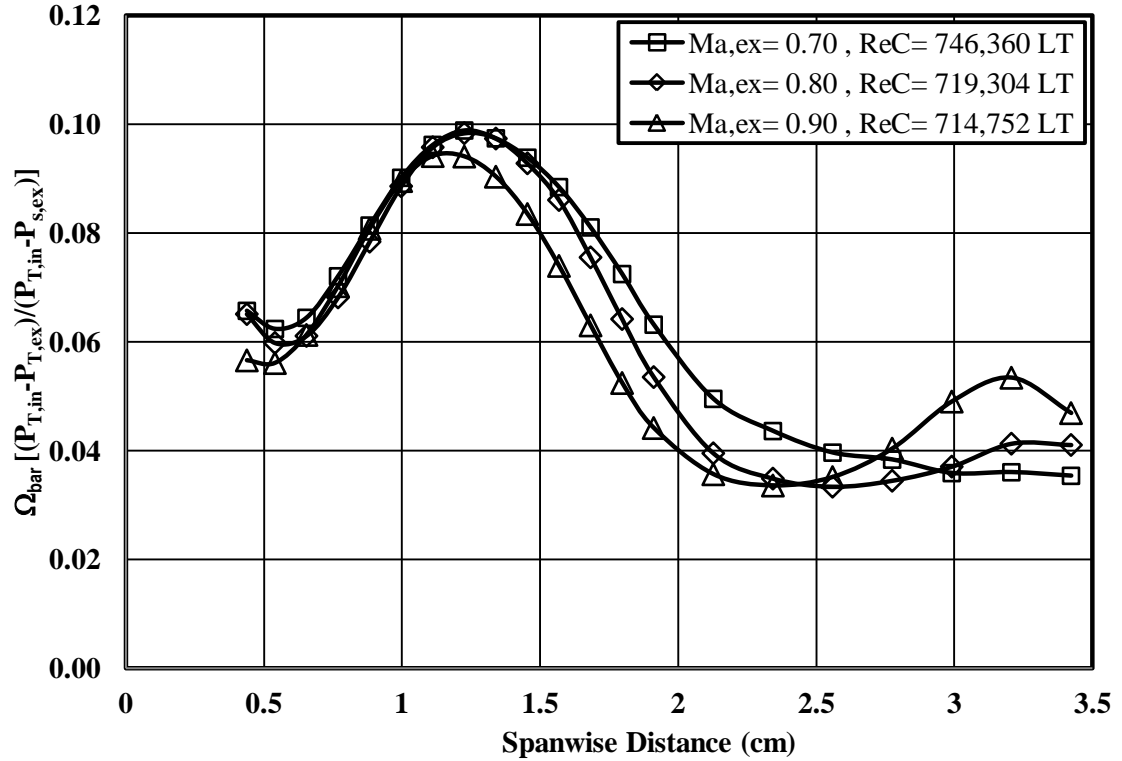
Figure 62. Cross-passage averaged total pressure loss coefficient Ω (Omega) for the vane at ¼ axial chord location under low turbulence over a range of Mach numbers of 0.7, 0.8, and 0.9 at a Reynolds number of 720,000.

The cross-passage averaged turning angle β (Beta) for the range of Mach numbers at a Reynolds number of 720,000 is seen in Figure 63 under low turbulence conditions. The characteristic overturning is present for all Mach number conditions near the endwall. The shape of the turning curve over the span is nearly the same for each Reynolds number. However, the magnitude of turning angle appears to increase between Mach 0.8 and 0.9.

102
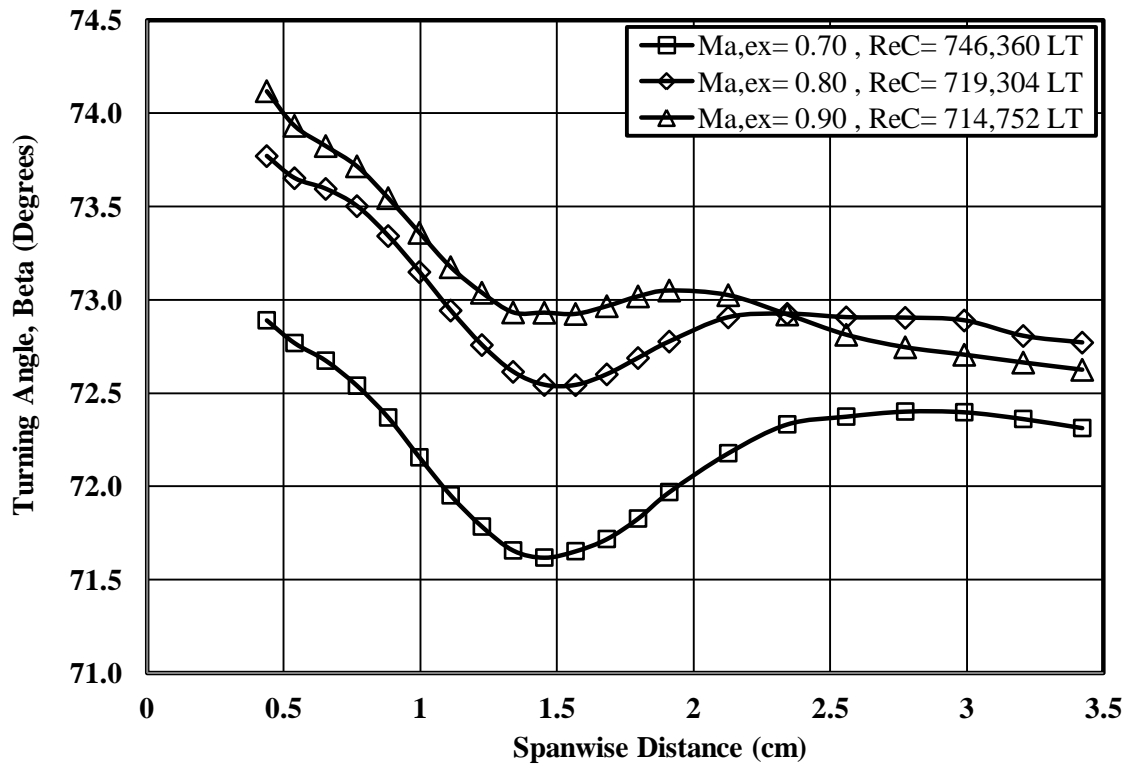
Figure 63. Cross-passage averaged turning angle β (Beta) for the vane at ¼ axial chord location under low turbulence over a range of Mach numbers of 0.7, 0.8, and 0.9 at a Reynolds number of 720,000.

Aero-Combustor Turbulence Exit Wake Surveys at ¼ Axial Chord as a Function of Mach Number

The exit survey's contour plot shown in Figure 64 and Figure 65 present the way aero-combustor turbulence has altered total pressure loss Ω (Omega) at a Reynolds number of 720,000 over Mach numbers of 0.7 and 0.9. Comparing Figure 60 and Figure 64 shows the main loss has not moved but its highest intensity area has decreased under higher turbulence conditions. The wake region between the endwall and mid-span has increased substantially, which is a result of turbulent mixing. Endwall loss intensity has clearly become more elevated, resulting from a turbulent wake and endwall corner vortex. A second loss core at the mid-span has formed, which could be the result of the

103

suction side leg of the horseshoe vortex. Secondary velocity vectors clearly show vortical

flow on the suction surface side and pressure side near the endwall.

Figure 64. Total pressure loss contours Ω (Omega) with secondary velocity vectors for the vane at ¼ axial chord location under aero-combustor turbulence at a chord exit Reynolds number of 720,000 and Mach number of 0.7.

The formation of these vortices coincide with strong downward and upward flows on the

suction and pressure surfaces, which match usual overturning near the endwall and

minimal turning near the mid-span.

At a Mach number of 0.9 under aero-combustor turbulence, the loss core has

maintained its position at approximately 1.5 cm or 22% of span off the endwall. The loss

core intensity area has increased based on Figure 65. The wake region between the

endwall and mid-span has decreased in width, indicating a reduction in turbulent mixing.

The second loss core near the mid-span and the losses near the endwall have both

decreased. Secondary velocities show a malformed corner vortex due to high overturning

104

near the endwall. The pressure side horseshoe vortex has moved closer to the endwall but is still present.

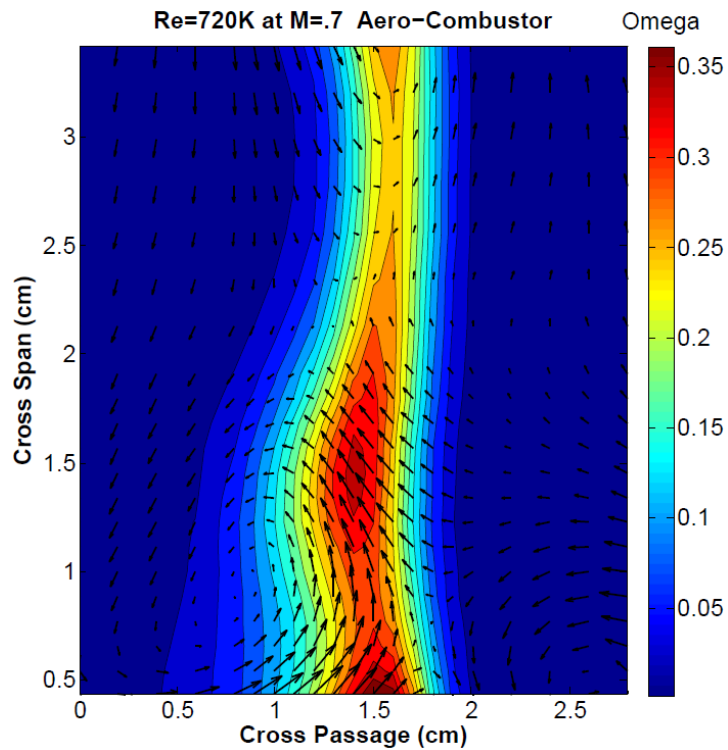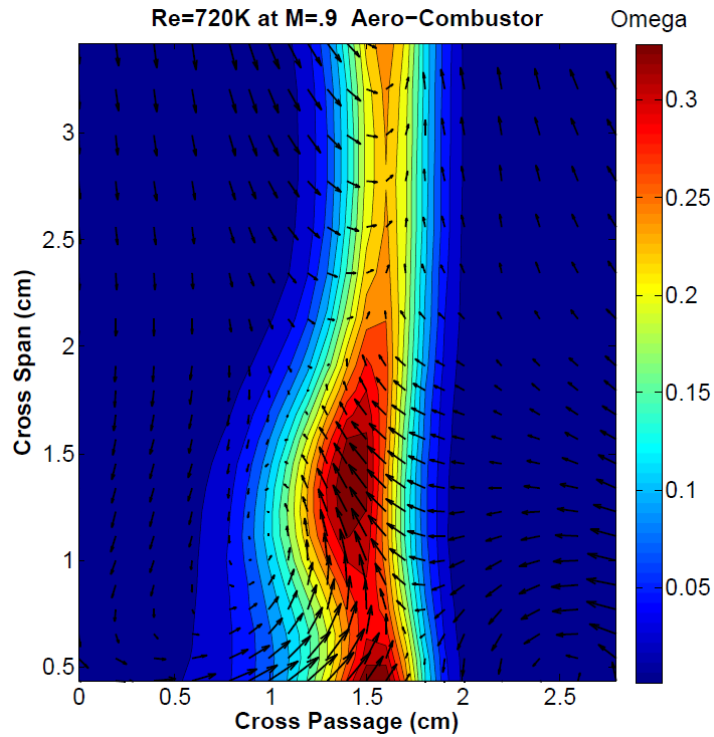Figure 65. Total pressure loss contours Ω (Omega) with secondary velocity vectors for the vane at ¼ axial chord location under aero-combustor turbulence at a chord exit Reynolds number of 720,000 and Mach number of 0.9.

The cross-passage averaged total pressure loss Ω (Omega), for the range of Mach numbers at a Reynolds number of 720,000 is seen in Figure 66 under aero-combustor turbulence conditions. Comparing Figure 62 and Figure 66 together, it is clear that averaged total pressure losses near the endwall have increased by nearly 23%, while the loss core has decreased by over 20% for each Mach number. The general trend amongst the Mach numbers is nearly identical with even periodic spacing. Losses are highest for a Mach number of 0.7 and decrease as Mach numbers increase sequentially. The averaged total pressure loss reaches a minimum at 3 cm or 43% of the span from the endwall but begins to increase as the mid-span is approached.

www.manaraa.com
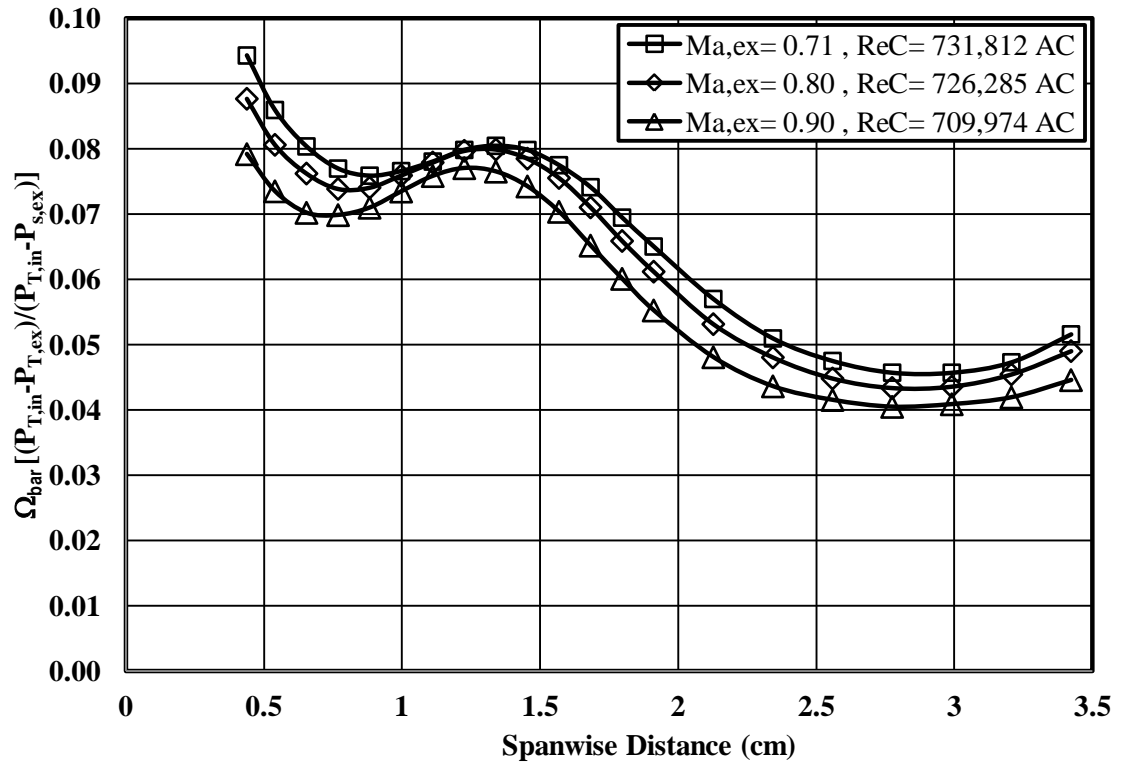
Figure 66. Cross-passage averaged total pressure loss coefficient Ω (Omega) for the vane at ¼ axial chord location under aero-combustor turbulence over a range of Mach numbers of 0.7, 0.8, and 0.9 at a Reynolds number of 720,000.

The cross-passage averaged turning angle β (Beta) for the span of Mach numbers at a Reynolds number of 720,000 is seen in Figure 67 under aero-combustor conditions. The overall turning angle distribution under higher turbulence has smoothed out considerable compared to Figure 63. The resulting large swept data trends at each Mach number indicate a dissipated loss core. There is slightly more overturning near the endwall as a result of a larger horseshoe/passage vortex on the suction surface side. Minimal turning at the loss core has only slightly changed over the span of Mach numbers. The under turning trend near the mid-span at lower turbulence is still present at higher turbulence but to a lesser degree.

106
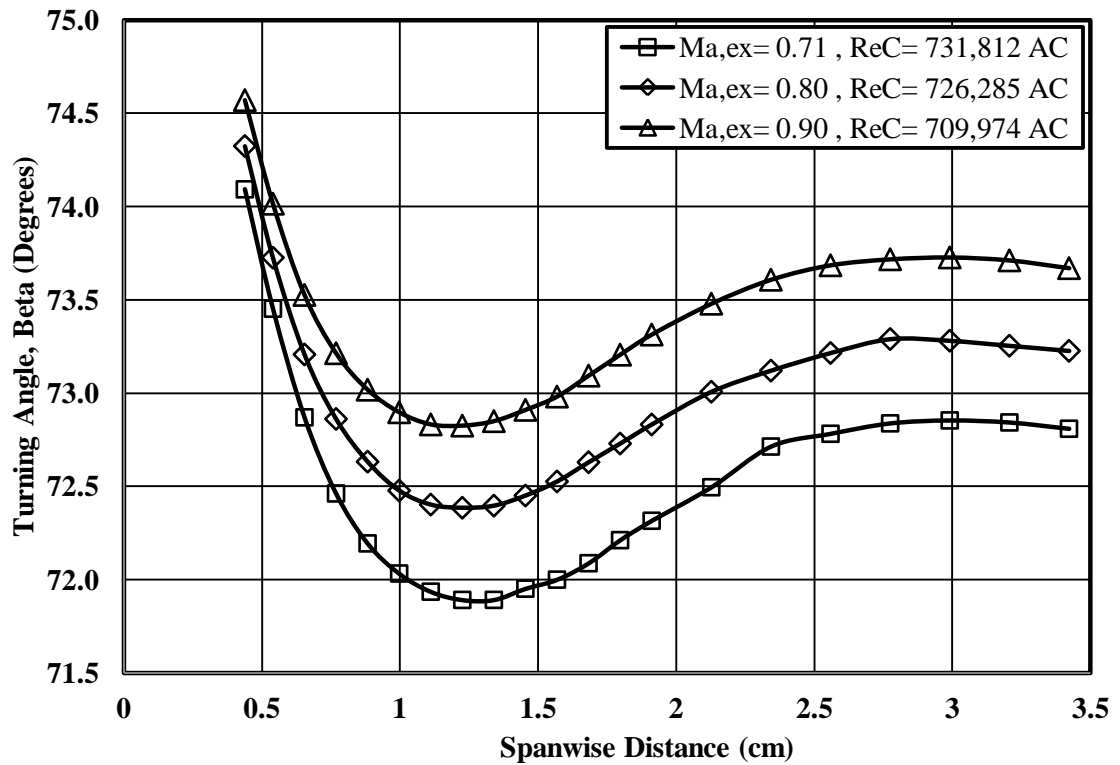
Figure 67. Cross-passage averaged turning angle β (Beta) for the vane at ¼ axial chord location under aero-combustor turbulence over a range of Mach numbers of 0.7, 0.8, and 0.9 at a Reynolds number of 720,000.

A graphical comparison relating averaged total pressure loss over a span of Mach numbers for a Reynolds number of 720,000 under low and aero-combustor turbulence is given in Figure 68. The results indicate, as Mach number increases from 0.7 to 0.9, averaged total pressure loss decreases by 6% and 11.3% for low and aero-combustor turbulence. Also, higher turbulence levels have increased losses by 3.3% and 9.5% for Mach numbers of 0.9 and 0.7.

107

Figure 68. Comparison of passage averaged total pressure loss over a range of Mach numbers of 0.7, 0.8, and 0.9 at a Reynolds number of 720,000 for low and aero-combustor turbulence.

Table 2. Wind tunnel conditions, mass averaged loss, and turning angle for ¼ axial chord exit surveys at low and aero-combustor turbulence for the aerodynamic test vane as a function of Mach number at a Reynolds number of 720,000.
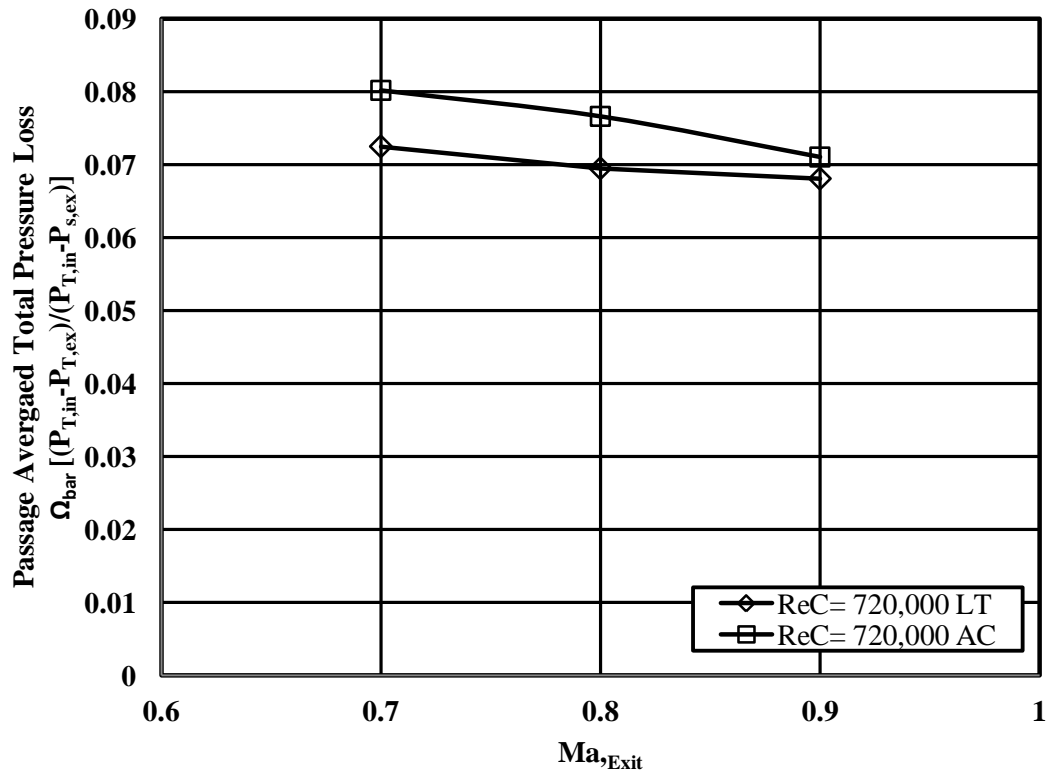
¼ Cax	Low Turbulence			Aero-Combustor Turbulence		
ReC	746,360	719,304	714,752	731,812	726,285	709,974
T_T,in (K)	317.5	337.2	345.6	319.8	326.8	352.5
P_T,in (Pa)	53286.2	51501.9	50223.1	52445.7	50009.8	51161.5
Vex (m/s)	239.2	278.4	311.7	242.1	273.6	314.7
Maex	0.70	0.80	0.90	0.71	0.80	0.90
Ω (Midline)	0.0353	0.0410	0.0469	0.0515	0.0490	0.0445
Ω (Full)	0.0609	0.0584	0.0572	0.0668	0.0638	0.0592
Ωcor (Full)	0.0725	0.0695	0.0681	0.0802	0.0766	0.0711
β (Midline)	72.31	72.77	72.62	72.81	73.23	73.67
β (Full)	72.28	73.03	73.16	72.71	73.13	73.54

CHAPTER VII

EXPERIMENTAL RESULTS—VANE SURFACE HEAT TRANSFER

This chapter discusses external vane surface heat transfer within the transonic cascade. The methodology and experimental approach have been discussed in detail in CHAPTER V. The experimental heat transfer results will be discussed on the basis of varying Mach and Reynolds number conditions. The heat transfer results will also be compared to values obtained in UND's incompressible flow wind tunnel and results found in literature. The results will be presented as vane surface Stanton number distributions over Reynolds numbers of 90,000, 180,000, 360,000, 720,000, and 1,000,000 over a range of Mach numbers of 0.7, 0.8, and 0.9 under low and aero-combustor turbulence.

Heat Transfer Vane Results

The Stanton number distribution over the previously described low to high Reynolds number conditions at an exit Mach number of 0.8 under low turbulence is presented in Figure 69. On the pressure surface, indicated by the negative surface arc, a constant trend for the Stanton number is seen for all Reynolds numbers from the trailing edge to an arc length of -0.3. The constant trend indicates a laminar boundary layer on the pressure surface. A maximum Stanton number is reached a small distance downstream of the stagnation point on the suction surface side, which is a positive surface arc distance, for each Reynolds number. As expected, the Stanton number on both the suction and pressure surfaces reduces as the acceleration in the stagnation region drops off.

109

The Nusselt number in the stagnation region of a cylinder in a cross-flow can be determined using the Falkner-Skan solution taken from White [61], which is expressed in Equation 7.1.

$$Nu_x = 0.57 Re_x^{1/2} Pr^{0.4} \tag{7.1}$$

The Nusselt number can be put in terms of diameter by using the velocity distribution around a cylinder in a cross flow defined for a relatively small x by Equation 7.2.

$$U(x)_\infty = \frac{3.63 V_\infty x}{D} \tag{7.2}$$

By substituting the freestream velocity around a cylinder, the Nu_x term can be rewritten as Nu_D. Assuming a Prandtl number of 0.71 for air, Equation 7.1 is reduced to Equation 7.3, which describes a constant solution for a ratio of Nusselt and Reynolds number at the stagnation point.

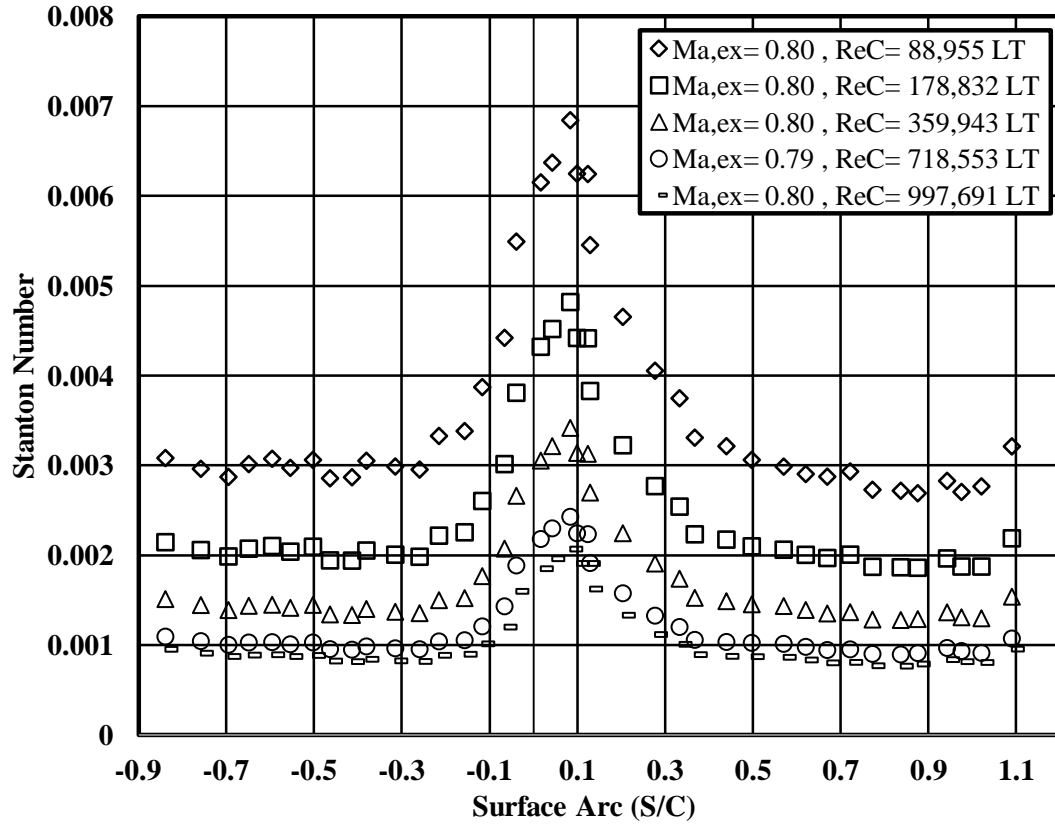$$\frac{Nu_D}{Re_D^{1/2}} = 0.945 \tag{7.3}$$

110

Figure 69. Stanton number distributions under low turbulence conditions over Reynolds numbers of 90,000, 180,000, 360,000, 720,000, and 1,000,000 at Mach 0.8 based on true chord exit conditions.

Overall, the heat transfer data shows a scaling factor to the change in Reynolds number. The scaling factor is described by Equation 7.4, which was derived by Kays, Crawford, and Weigand [60].

$$St = 0.332Re_x^{-1/2}Pr^{-2/3} \qquad (7.4)$$

Equation 7.4 shows as Reynolds number decreases, the Stanton number should increase proportionally to the inverse square root of the Reynolds number. Therefore, the Stanton number should decrease by 3.33 times going from a Reynolds number of 90,000 to 1,000,000. The experimental results presented in Figure 69 shows an average decrease by 3.4 times from a Reynolds number of 90,000 to 1,000,000, which is within acceptable error to the expected value and provides confidence in the experimental results

111

Previous work performed in UND's incompressible flow facility found similar quantitative Stanton number values to those in the transonic facility at a Reynolds number of 1,000,000 as seen in Figure 70. The stagnation Stanton number is nearly identically but the pressure side deviates by around 10%, with the greatest variation occurring on the suction surface. The incompressible suction surface Stanton number has a steady decreasing slope towards the trailing edge that is not present in the compressible flow data. The difference in heat transfer trend between the results presented for this study and the incompressible facilities is the Reynolds number is not coupled with Mach number. Coupled conditions require an increase in freestream velocity to elevate Reynolds number, which could affect boundary layer transition and turbulence influence.
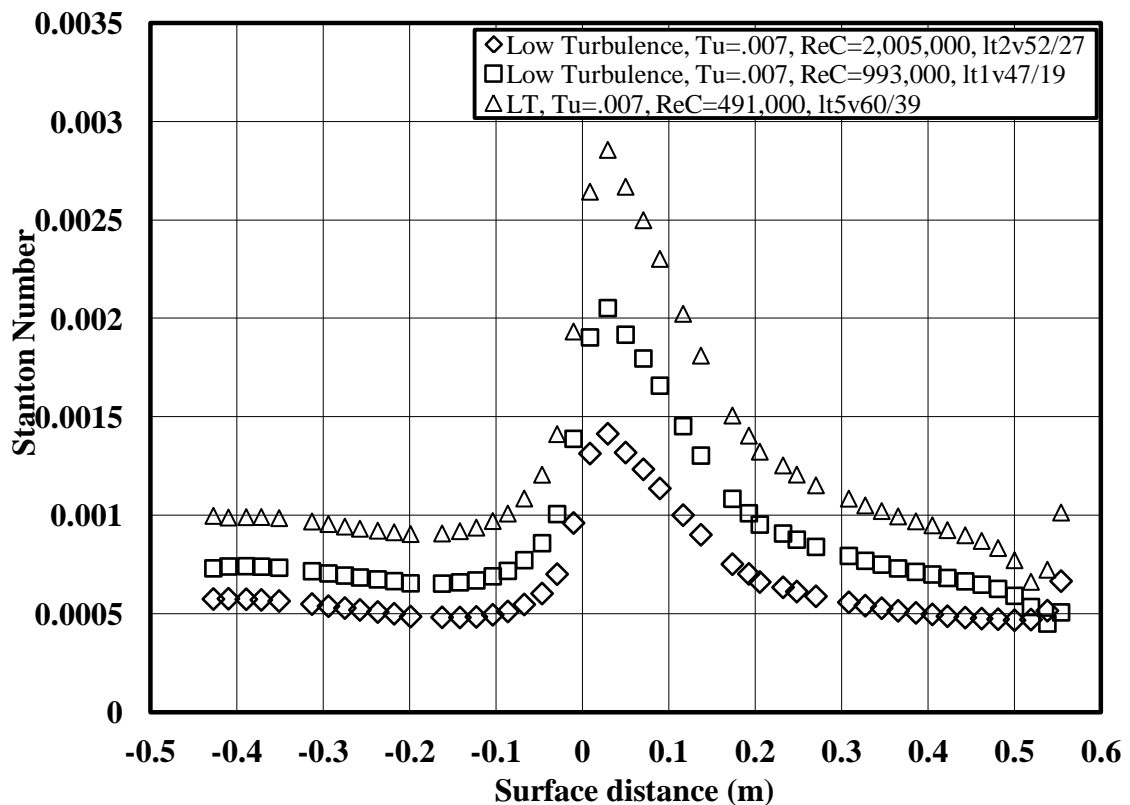

Figure 70. Heat transfer data taken at UND's incompressible flow wind tunnel over three different Reynolds numbers under low turbulence conditions.

The heat transfer flow conditions similar to those conducted at low turbulence levels were also performed with a mock aero-derivative combustor, which enhanced freestream turbulence levels. Figure 71 shows Stanton number distributions over a range of Reynolds numbers at Mach 0.8 under aero-derivative combustor turbulence. The elevated freestream turbulence level has significantly augmented laminar heat transfer on pressure surface and stagnation region and leads to transition on the suction surface. Augmented heat transfer results were also found by Ames [41] under elevated turbulence. Ames explains the main effect of the turbulence on the suction surface is to cause the boundary layer to transition at an earlier location. Early boundary layer transition is indicated by a gradual increase in Stanton number over the suction surface, which is seen at Reynolds numbers of 360,000, 720,000 and 1,000,000.
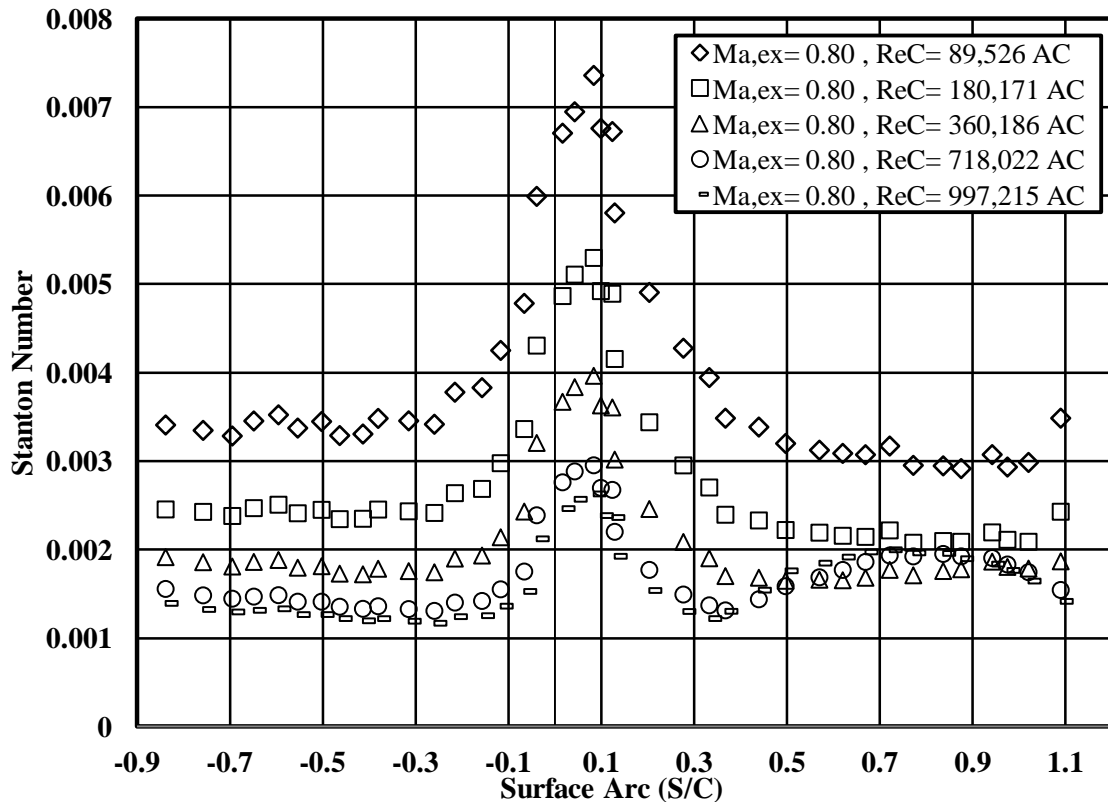

Figure 71. Stanton number distributions under aero-combustor turbulence conditions over Reynolds numbers of 90,000, 180,000, 360,000, 720,000, and 1,000,000 at Mach 0.8 based on true chord exit conditions.

113

Heat transfer augmentation over the pressure, suction, and stagnation surfaces is presented as $(St - St_0)/St_0$ versus the ratio of surface arc length to the true chord in Figure 72. The pressure surface indicated by the negative surface arc shows a rising increase past the stagnation region and with a moderately steady value further downstream past a surface arc (S/C) of -0.4. This trend indicates laminar augmentation due to the increase of freestream turbulence. The augmentation levels have been averaged between the surface arc length of -0.3 to the trailing edge of the blade, for the pressure surface and are presented in Table 3. Laminar augmentation levels on the pressure surface were found to be 14%, 19%, 28%, 40%, and 46% for Reynolds number of 90,000 to 1,000,000. Ames, Wang, and Barbot[62] postulated that heat transfer augmentation to laminar boundary layer should scale on the turbulence intensity (Tu), Reynolds number to the $1/3^{rd}$ power and energy scale (Lu) to the negative $1/3^{rd}$ power. This can be stated as $(St - St_0)/St_0 \propto TuRe_C^{1/3}(C/Lu)^{1/3}$. Ames, states the dissipation of the turbulence adjacent to the pressure surface boundary layer is unaltered by the boundary layer velocity gradient or the streamwise acceleration. Ames, Kwon, and Moffat [63], indicate the $Tu * Lu^{-1/3}$ dependency implies that the relatively large turbulence eddies in the v' spectrum are blocked by the presence of the wall leaving only the smaller eddies to penetrate into the thin pressure surface boundary layer and increase mixing.

The augmented heat transfer at the stagnation region for elevated freestream turbulence is related to the strain rate of small and large scale turbulent eddies in the stagnation region of a cylinder which was first predicted by Hunt [64]. Using rapid distortion theory, Hunt determined the relatively small scale eddies are amplified as they are stretched around the stagnation region of a cylinder by the approaching flow, and the

114

large scale eddies are adherently deflected by the cylinder's presence. Ames and Moffat[42] later developed a model from Hunt's conclusions, which correlated stagnation region heat transfer as a function of turbulence intensity, Reynolds number to the $5/12^{th}$ power, and diameter to energy scale to the $1/3^{rd}$ power. This relation is described as $(Nu-Nu_0)/Nu_0 \propto Tu Re_D^{5/12}(D/Lu)^{1/3}$.
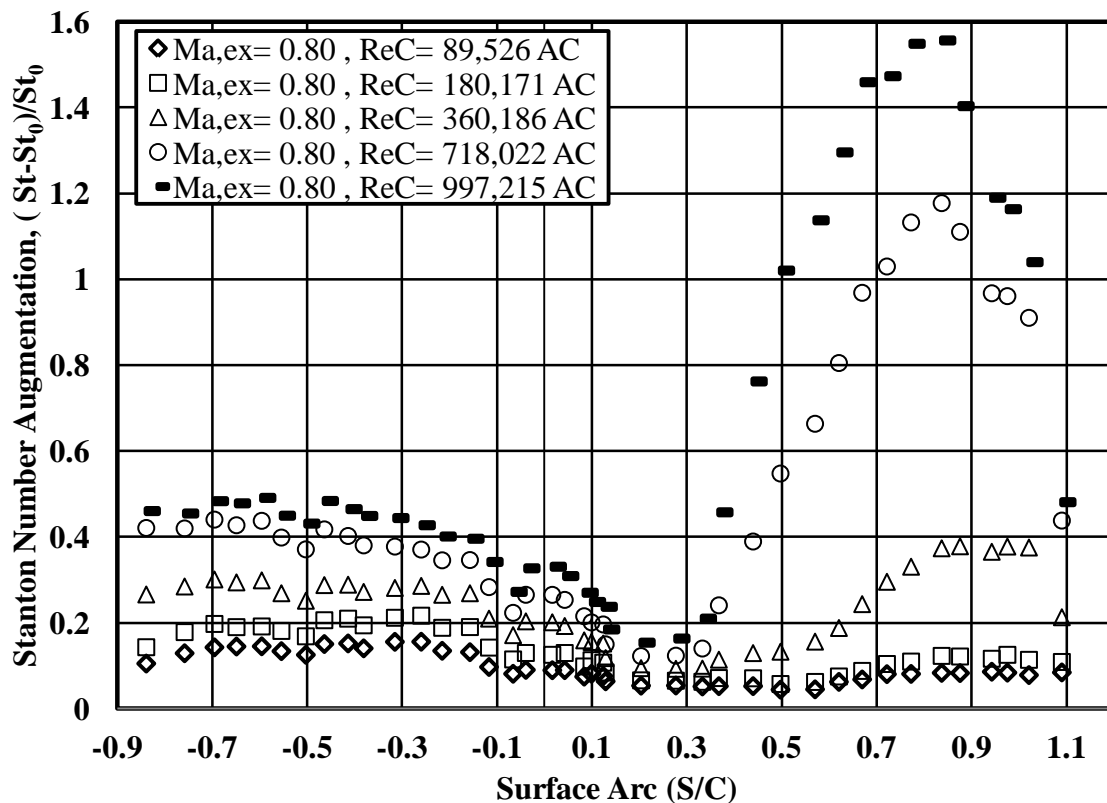

Figure 72. Effects of mock aero-derivative combustor turbulence characteristics on Stanton number augmentation and location of transition over Reynolds numbers of 90,000, 180,000, 360,000, and 720,000 at an exit Mach number of 0.8.

Transitional augmentation levels on the suction surface were averaged from a surface arc of 0.4 to the vanes trailing edge. Transition augmentation levels on the suction surface were found to be 7%, 10%, 29%, 89%, and 126% for Reynolds number of 90,000 to 1,000,000. The scale of heat transfer augmentation is clearly a factor of Reynolds number, which increases as Reynolds number increases.

115

Table 3 shows the percentage increase of averaged surface Stanton number values for the pressure, suction, and stagnation surfaces. The percentage of increase for the pressure and stagnation surfaces still follow the Reynolds number scaling between the lowest and highest Reynolds number. However, the suction surface for Reynolds numbers of 360,000, 720,000, and 1,000,000 vary from the scaling trend significantly. Transition on the suction surface from a laminar to turbulent boundary layer for these three Reynolds numbers is not only evident in Table 3 but can be clearly seen in Figure 71 by the gradual increase of Stanton number.

Table 3. Averaged Percentage of Stanton number increase from low to aero-combustor turbulence for the pressure and suction surface and stagnation region of the heat transfer vane over a range of Reynolds numbers at vane exit Mach number of 0.8

Reynolds Number	Averaged Increase		
	Pressure Surface, 0.4 to 1 (S/C) %	Stagnation Region, 0 (S/C) %	Suction Surface, -0.3 to -0.9 (S/C) %
90,000	14	9	7
180,000	19	13	10
360,000	28	20	29
720,000	40	27	89
1,000,000	46	33	123

A comparison of low turbulence and aero-combustor turbulence Stanton number distribution is provided in Figure 73 for a Reynolds number of 1,000,000 over a span of Mach numbers of 0.7, 0.8, and 0.9. Under low turbulence conditions, the variation of Mach number does not affect heat transfer, but does on the suction surface for a Mach number of 0.7. Other than the aforementioned suction surface transition, the variation in Mach number did not alter heat transfer at any Reynolds number case under low turbulence conditions. However, under aero-combustor conditions at Reynolds numbers of 720,000 and 1,000,000, the Mach number augmented suction surface heat transfer.

116

Figure 73 shows that as the Mach number increases, the Stanton number distribution on the suction surface decreases. The decrease in Stanton number shows that the elevating Mach exit number inhibits the transition to some degree. Based on the conclusions from the acceleration parameter plot seen in Figure 45, Stanton number variation with a change in Mach number could be related to a small degree with the acceleration parameter. Therefore, as exit Mach number increases the acceleration parameter on the suction surface also increases.
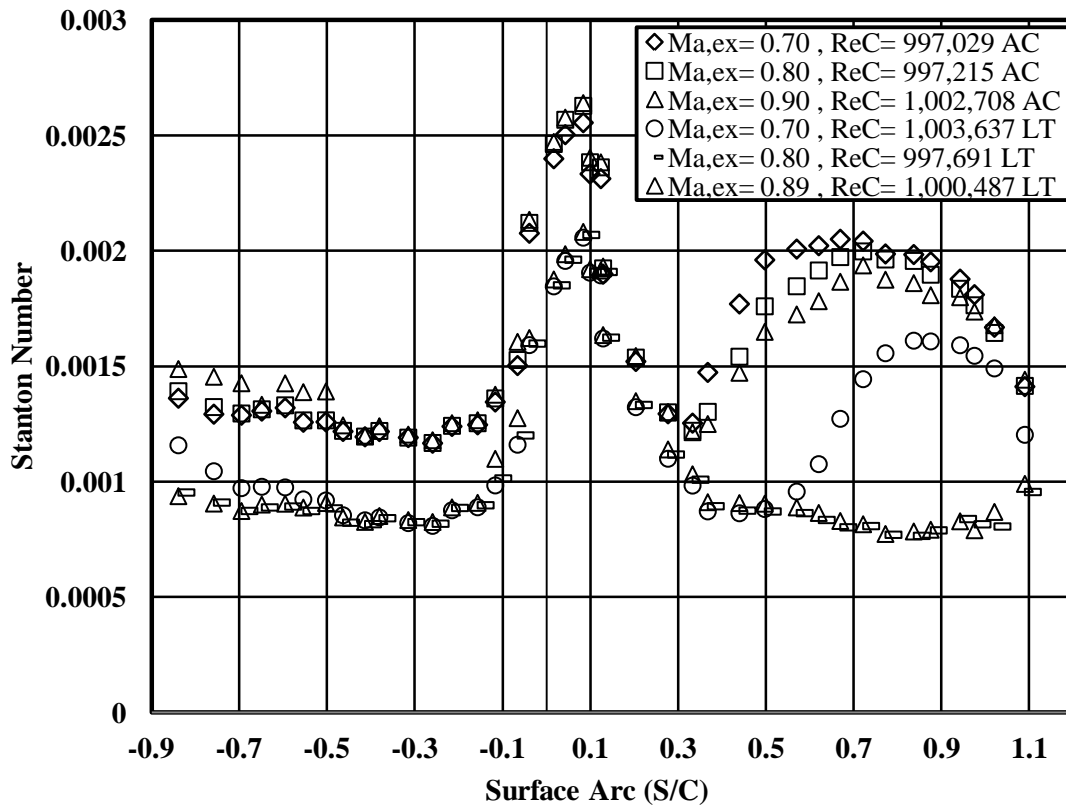
Figure 73. Stanton number distributions under low and aero-combustor turbulence conditions over Mach numbers of 0.7, 0.8, and 0.9 at a Reynolds number of 1,000,000 based on true chord exit conditions.

The boundary layer transition on the suction surface at a 1,000,000 Reynolds number under high freestream turbulence has also been found by Ames, Wang, and Barbot[62] .The results found by the authors are seen in Figure 74, which follows a

117

similar trend to the results shown in Figure 73. Under low turbulence, both sets of data show similar values of Stanton number for the pressure and suction surface, with nearly identical stagnation values. Under aero-combustor turbulence conditions, heat transfer augmentation values are nearly identical over the suction and stagnation region, but a slight difference is seen on the suction surface. The deviation in suction surface heat transfer could be attributed to the Mach number difference between the two sets of data, the acceleration parameter, or conduction not being accounted for through the vane.
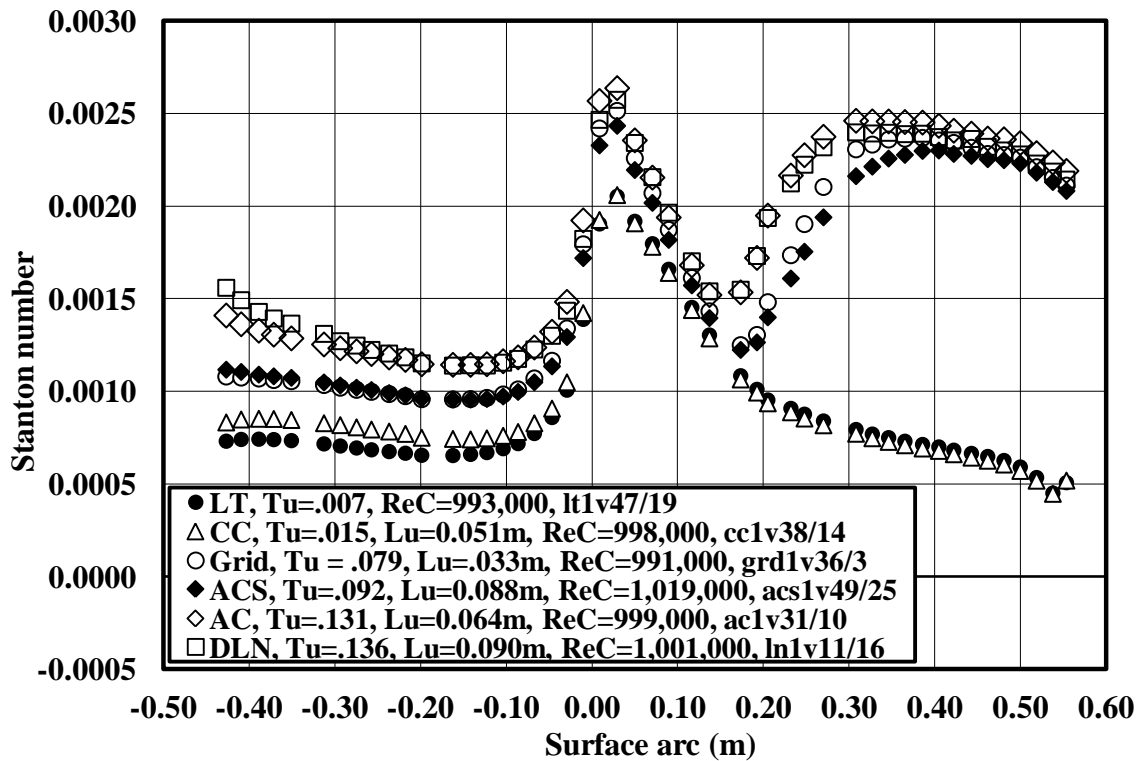
Figure 74. Comparison of Stanton number distributions at low, grid generated, and aero-combustor turbulence conditions with an exit Reynolds number of 1,000,000 [62].

Ames' tests were conducted in an incompressible wind tunnel, with an exit Mach number of 0.2. The conclusions from Figure 73 demonstrated that as Mach number decreases, the location of suction surface transition moves forward due to enhanced

118

transition at lower Mach numbers. The difference found with Ames' data on the suction

surface could be due to a Tu or Re_c effect.

CHAPTER VIII

CONCLUSIONS

The construction of a new closed loop, steady state, transonic, low Reynolds number facility has been completed. The construction of this project was undertaken by the Mechanical Engineering Department at UND and completed through the hard work of faculty members, undergraduate, and graduate students. The facility encompasses the ability to calibrate flow field probes and conduct linear vane cascade aerodynamic and heat transfer research over Reynolds numbers of 50,000 to 1,000,000 at Mach numbers up to 0.9. Research was conducted on vane surface heat transfer and pressure distributions along with exit surveys measuring total pressure loss under low and aero-combustor turbulence conditions.

Aerodynamic Losses

The aerodynamic testing results encompassed vane surface pressure distributions and exit surveys documenting total pressure losses, secondary velocity vectors, and turning angles at four low Reynolds numbers over three transonic Mach numbers for low and aero-combustor turbulence at ¼ axial chord downstream from the test vane's trailing edge. Results were compared systematically by a function of Reynolds and Mach number to show the influence each variation had on flow characteristics.

The vane surface Mach number analysis compared results as a function of Reynolds and Mach number under low and aero-derivative combustor turbulence conditions. Under low turbulence conditions, the pressure surface Mach number was not

120

affected by varying the Reynolds number. However, a decrease in Mach number over the suction surface was observed as Reynolds number increased, indicating a thinner boundary layer resulting from a reduction of blockage in the passage. Aero-combustor turbulence had no effect on the pressure surface but decreased the suction surface Mach number distribution. The adverse effect to surface Mach number was mitigated as the exit Mach number increased. Predictions of the surface Mach number were generated using FLUENT, which closely matched experimental trends and deviated slightly as exit Mach number increased. The deviation was possibly due to surface irregularities not accounted for in the numerical model.

Under low turbulence conditions, overall total pressure loss and secondary velocity vectors show a clear concentration where the passage/horseshoe vortex has elevated losses off the endwall. The results indicate secondary losses increase as Reynolds number decreases; this decrease also produces the growth of a second loss core near the mid-span. The second loss core increased while Reynolds number was held constant and the Mach number was increased, which could be explained by the strengthening of the suction leg of the horseshoe vortex. The wake region loss also increases as Reynolds number decreases. The enhanced mixing due to the high aero-combustor turbulence produced much broader and uniform wakes than seen at lower turbulence. The higher turbulences levels have weakened the main loss core and dissipated the second loss core. Due to the laminar boundary layer formation on the vanes surfaces, the lower turbulence condition has significantly less mass averaged losses than higher turbulence. The higher turbulence case indicates increased wake losses and background mixing resulting in a redistribution of loss, which are also more apparent in

121

the near wall region. The turning angle (β) near the endwall shows an increase in overturning at higher turbulence levels and has a consistent trend of decreasing as Reynolds number decreases.

External Heat Transfer

Heat transfer test results encompassed Stanton number distributions on the vane's surface over a range of low Reynolds number spanning three transonic Mach numbers under low and high aero-derivative combustor turbulence conditions. Comparisons spanning the range of Reynolds number at Mach 0.8 were provided, which showed a scaling factor to Stanton number distribution as Reynolds number increased. At each Reynolds and Mach number test performed, peak heat transfer developed a small distance downstream of the stagnation region on the suction surface side. As expected, there is a reduction of heat transfer on both the suction and pressure surfaces as the acceleration in the stagnation region drops off. Aero-combustor turbulence conditions augmented heat transfer over the range of tests performed. The enhanced turbulence levels acted to increase mixing and cause the laminar boundary layer to transition earlier on the suction surface. Transitional affects were seen at Reynolds numbers of 360,000, 720,000 and 1,000,000, which elevated heat transfer on the suction surface significantly.

A Stanton number plot at a Reynolds number of 1,000,000 as a function of Mach number under low and aero-combustor turbulence was compared to data gathered from an incompressible flow facility by Ames, Wang, and Barbot. The two comparisons showed excellent quantitative relation on the pressure, and stagnation surfaces with a slight deviation on the suction surface.

122

The compressible flow data showed sensitivity to a change in Mach number, that is, as Mach number increased, the suction surface Stanton number decreased. The decrease is thought to be influenced to a small degree by the acceleration parameter, which increases over the suction surface as exit Mach number increases.

123

APPENDICES

Appendix A

Total Pressure Loss, Turning Angle, and Wind Tunnel Conditions during Exit Surveys

Table 4. Wind tunnel conditions, mass averaged loss, and turning angle for ¼ axial chord exit surveys at low and aero-combustor turbulence for the aerodynamic test vane as a function of Reynolds number at Mach 0.7.

¼ Cax	Low Turbulence				Aero-Combustor Turbulence			
ReC	94,955	186,587	372,088	746,360	93,770	184,249	369,114	731,812
T_T,in (K)	310.0	313.6	315.3	317.5	317.5	322.1	322.7	319.8
P_T,in (Pa)	6,585	13,063	26,326	53,286	6,723	13,474	26,919	52,446
Vex (m/s)	235.8	239.2	238.6	239.2	237.8	238.9	241.1	242.1
Maex	0.70	0.71	0.70	0.70	0.70	0.70	0.70	0.71
Ω (Midline)	0.0732	0.0682	0.0533	0.0353	0.0893	0.0677	0.0576	0.0515
Ω (Full)	0.0875	0.0767	0.0677	0.0609	0.0966	0.0792	0.0696	0.0668
Ωcor (Full)	0.1041	0.0913	0.0806	0.0725	0.1160	0.0952	0.0836	0.0802
β (Midline)	71.48	72.09	72.01	72.31	71.56	72.70	72.21	72.81
β (Full)	72.36	72.94	72.51	72.28	72.08	72.84	72.18	72.71

Table 5. Wind tunnel conditions, mass averaged loss, and turning angle for ¼ axial chord exit surveys at low and aero-combustor turbulence for the aerodynamic test vane as a function of Reynolds number at Mach 0.9.

¼ Cax	Low Turbulence				Aero-Combustor Turbulence			
ReC	88,875	179,627	353,882	714,752	90,002	178,175	357,081	709,974
T_T,in (K)	354.7	377.4	360.7	345.6	355.2	381.0	371.6	352.5
P_T,in (Pa)	6,544	14,213	26,294	50,223	6,649	14,245	27,546	51,161
Vex (m/s)	306.0	320.0	317.2	311.7	305.4	322.8	321.8	314.7
Maex	0.87	0.88	0.90	0.90	0.87	0.89	0.90	0.90
Ω (Midline)	0.0633	0.0648	0.0584	0.0469	0.0776	0.0669	0.0503	0.0445
Ω (Full)	0.0847	0.0727	0.0643	0.0572	0.0922	0.0755	0.0631	0.0592
Ωcor (Full)	0.1008	0.0866	0.0766	0.0681	0.1107	0.0907	0.0757	0.0711
β (Midline)	73.61	72.66	72.72	72.62	72.98	73.62	73.28	73.67
β (Full)	73.77	73.36	73.37	73.16	73.35	73.74	73.41	73.54

Table 6. Methodology used for thermal-cycling aerodynamic and heat transfer vane after epoxy cured in the mold for 24 hours.

Vane Thermal Cycle					
Time (min.)	Temp. (K)	Heater	Time (min.)	Temp. (K)	Heater
0	296	on	101	415	
11	334	off	111	408	on
21	335		118	418	off
31	334	on	128	427	
41	373	off	138	424	on
51	388		153	450	off
61	389		163	456	
71	384	on	173	449	on
81	406	off	180	450	off
91	419		Cool to Room Temperature		

126

Appendix B

Aerodynamic Vane Surface Mach Number Plots Not Reported in Results
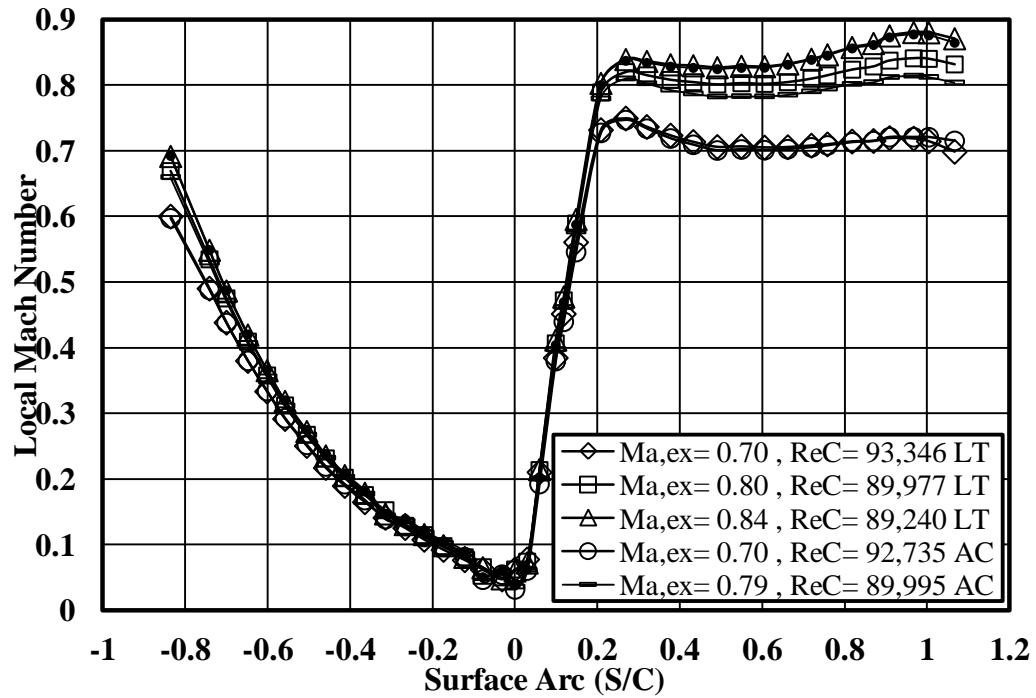
Figure 75. Surface Mach number distributions over a range of exit Mach numbers of 0.7, 0.8, and 0.9 at a Reynolds number of 90,000, under low and aero-combustor turbulence.

127
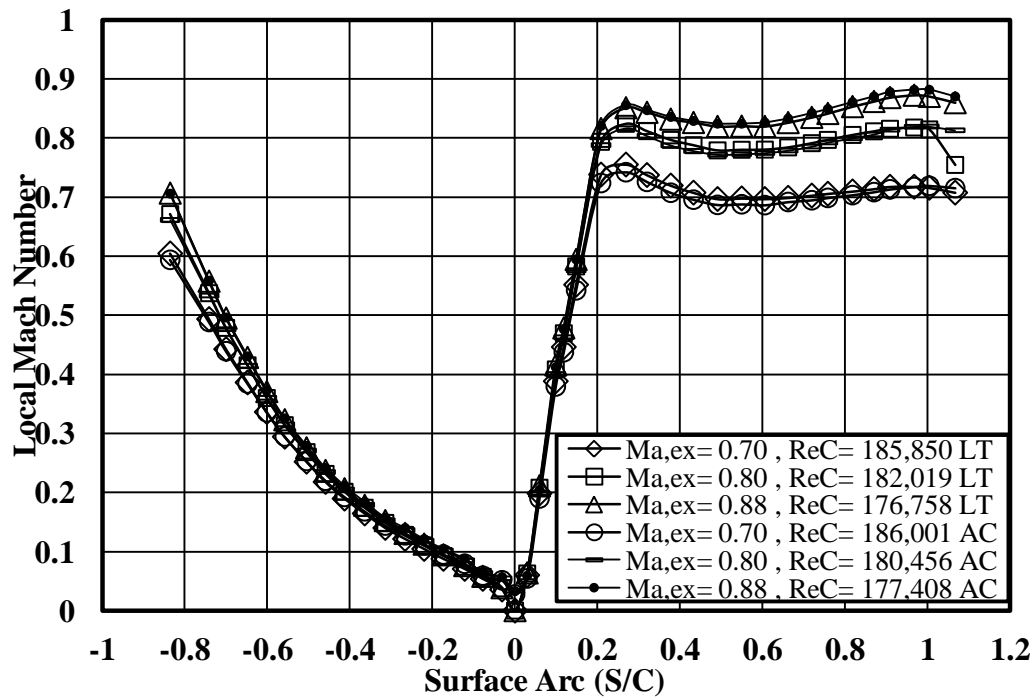
Figure 76. Surface Mach number distributions over a span of exit Mach numbers of 0.7, 0.8, and 0.9 at a Reynolds number of 180,000, under low and aero-combustor turbulence.
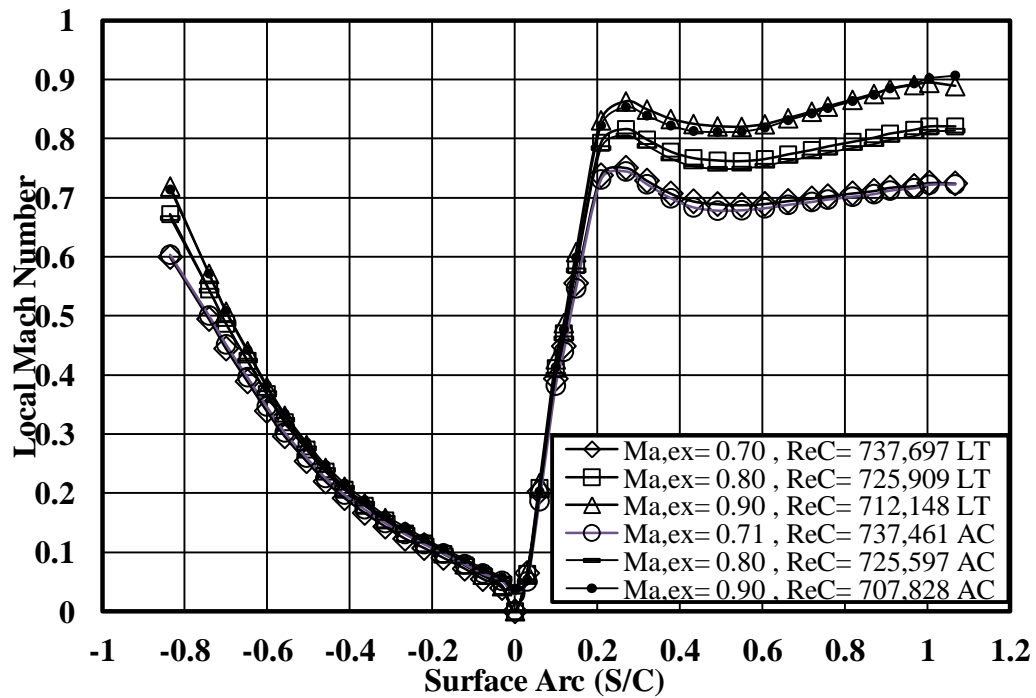
Figure 77. Surface Mach number distributions over a range of exit Mach numbers of 0.7, 0.8, and 0.9 at a Reynolds number of 720,000, under low and aero-combustor turbulence.
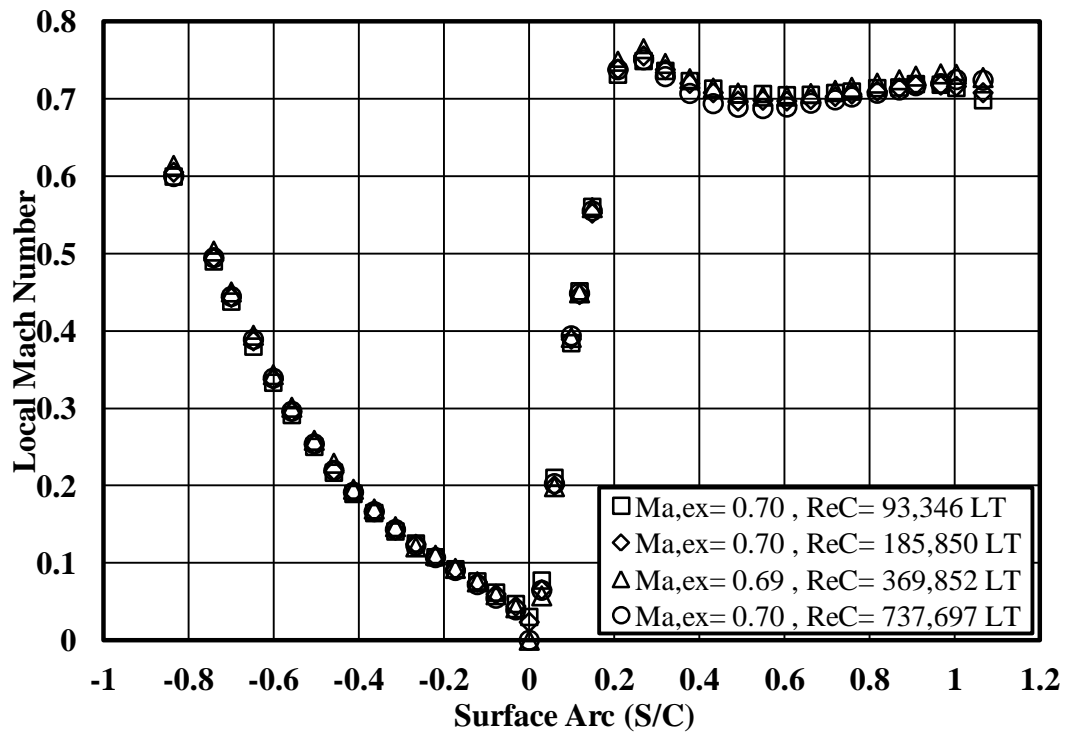
Figure 78. Surface Mach number distribution over a range of Reynolds numbers of 90,000, 180,000, 360,000, and 720,000 at an exit Mach number of 0.7 under low turbulent conditions.
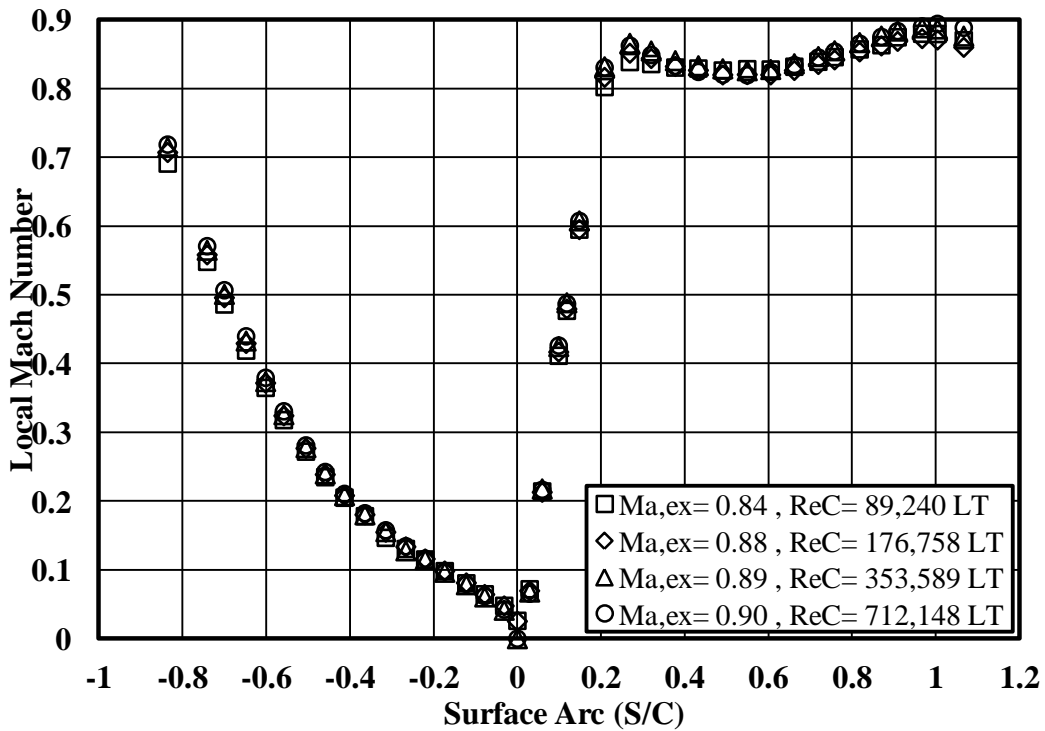
Figure 79. Surface Mach number distribution over a range of Reynolds numbers of 90,000, 180,000, 360,000, and 720,000 at an exit Mach number of 0.9 under low turbulent conditions.

129

Appendix C

Five-Hole Cone Probe Calibration Plots Not Reported in Results
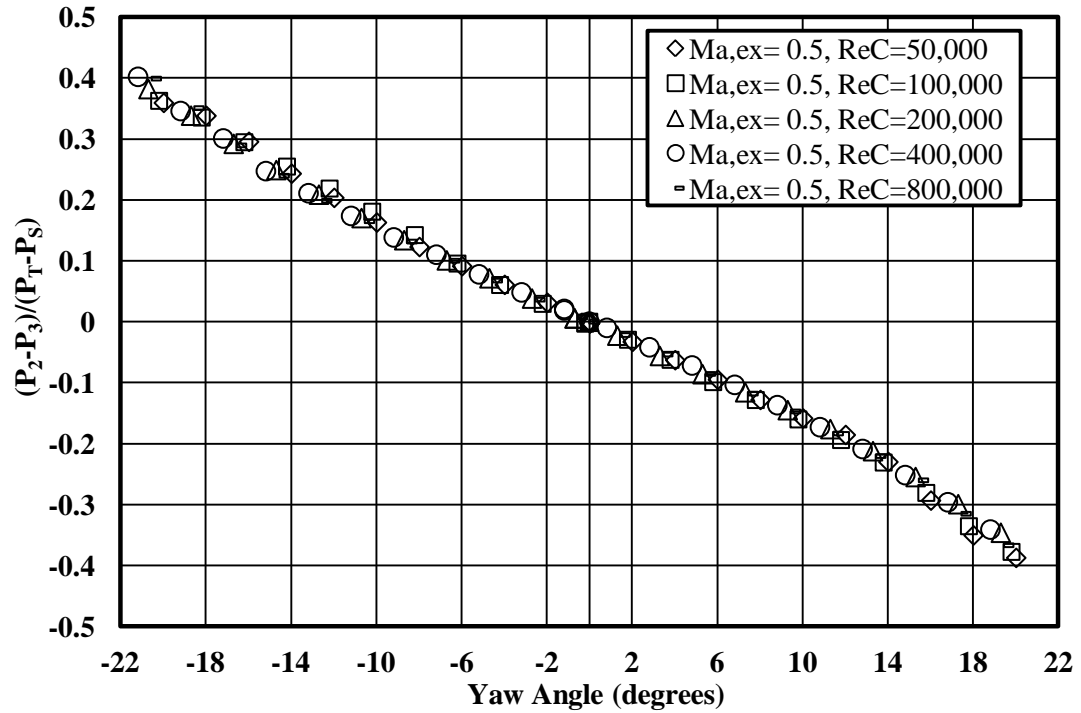
Figure 80. Yaw sensitivity coefficients of the five-hole cone probe over a span of yaw angles at Mach 0.5 as a function of Reynolds number between 50,000 and 800,000.
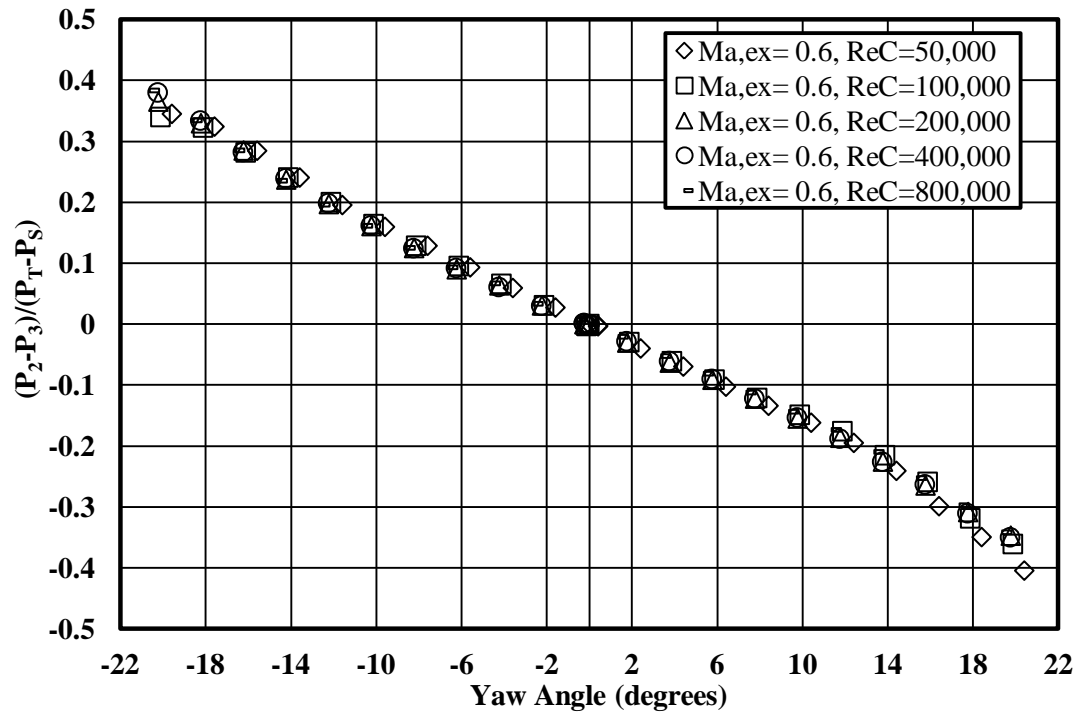
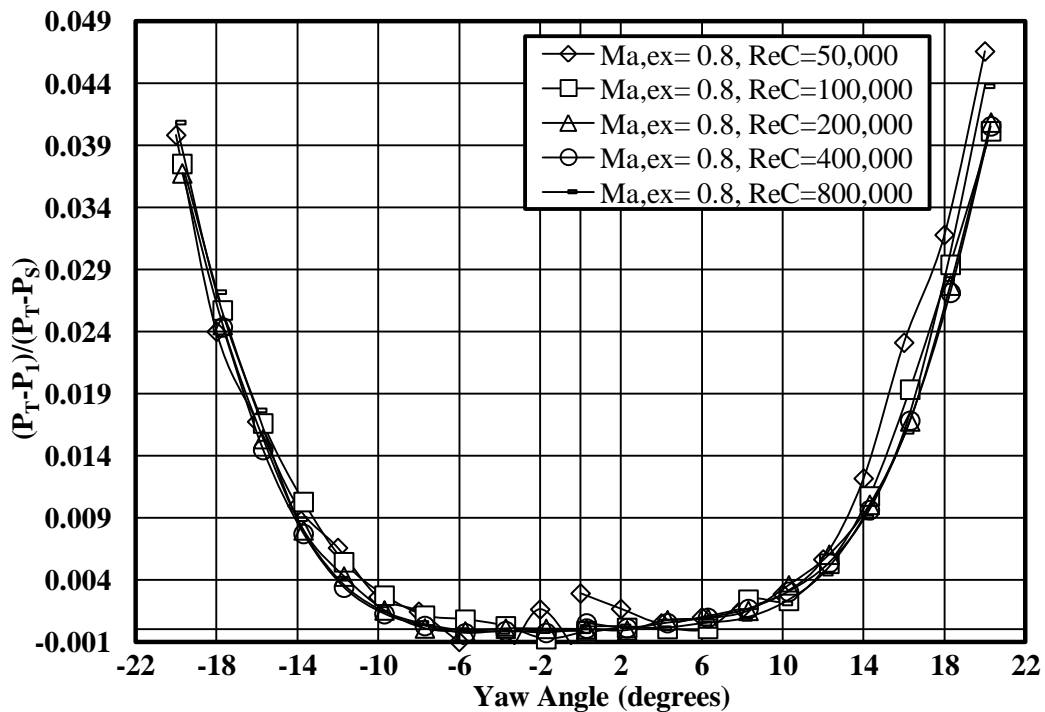Figure 81. Yaw sensitivity coefficients of the five-hole cone probe over a span of yaw angles at Mach 0.6 as a function of Reynolds number between 50,000 and 800,000.
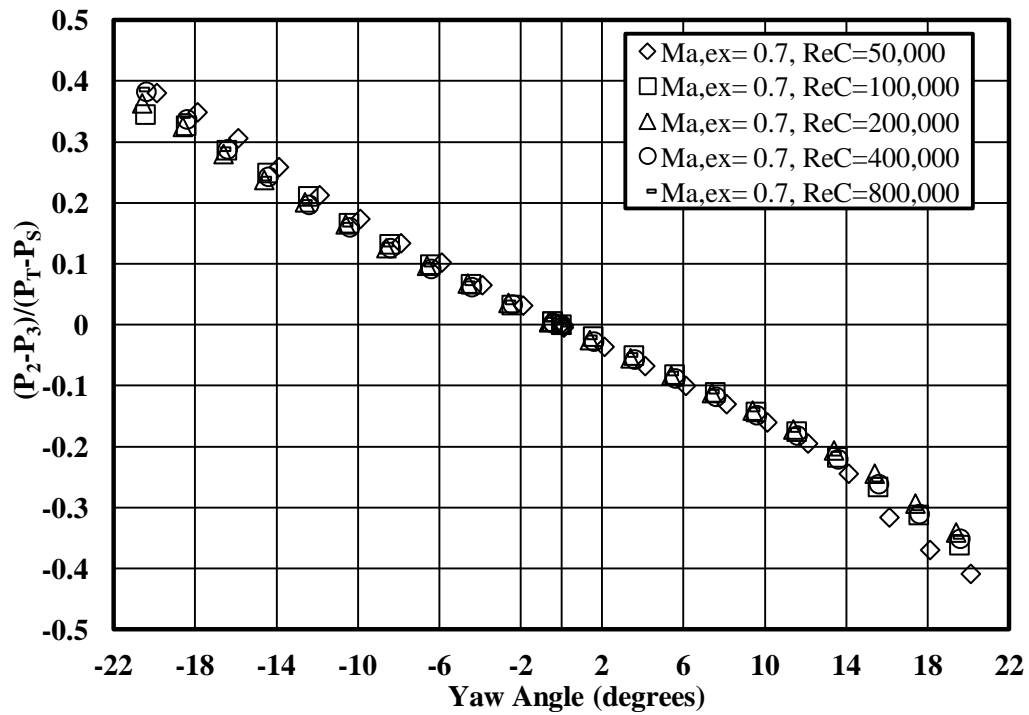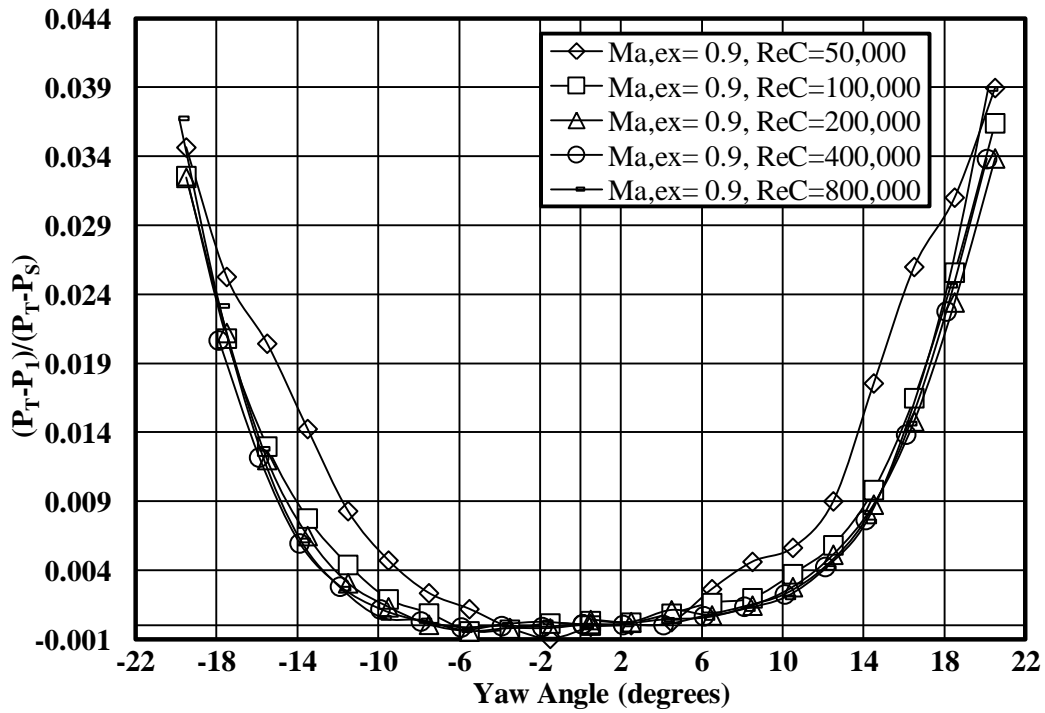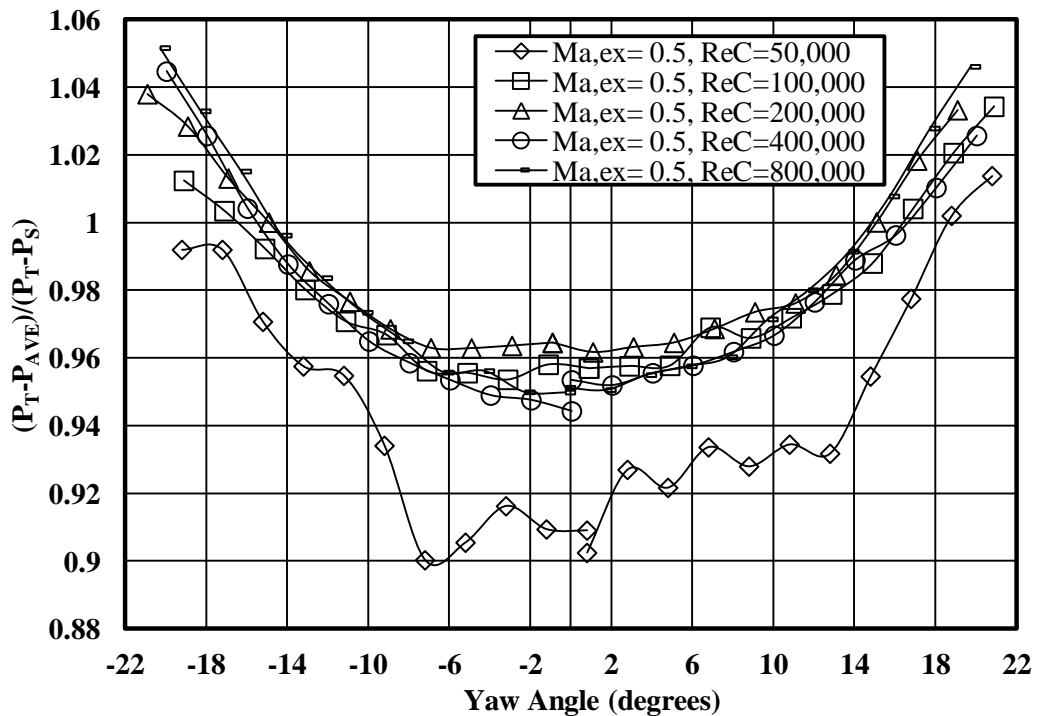

Figure 82. Yaw sensitivity coefficients of the five-hole cone probe over a span of yaw angles at Mach 0.7 as a function of Reynolds number between 50,000 and 800,000.

131
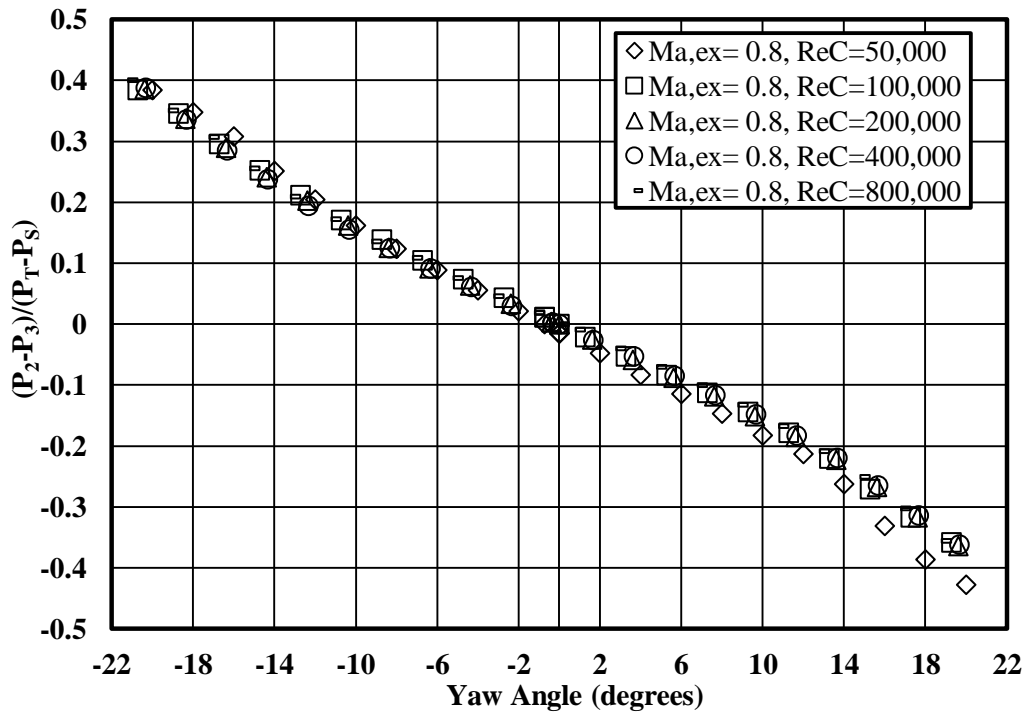
Figure 83. Yaw sensitivity coefficients of the five-hole cone probe over a span of yaw angles at Mach 0.8 as a function of Reynolds number between 50,000 and 800,000.
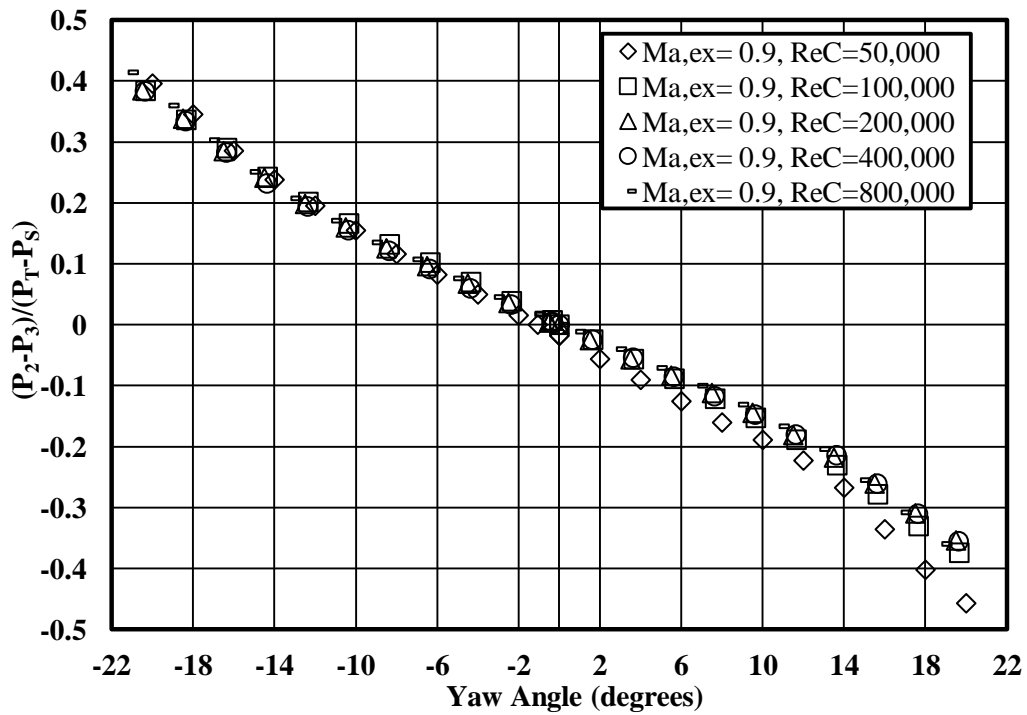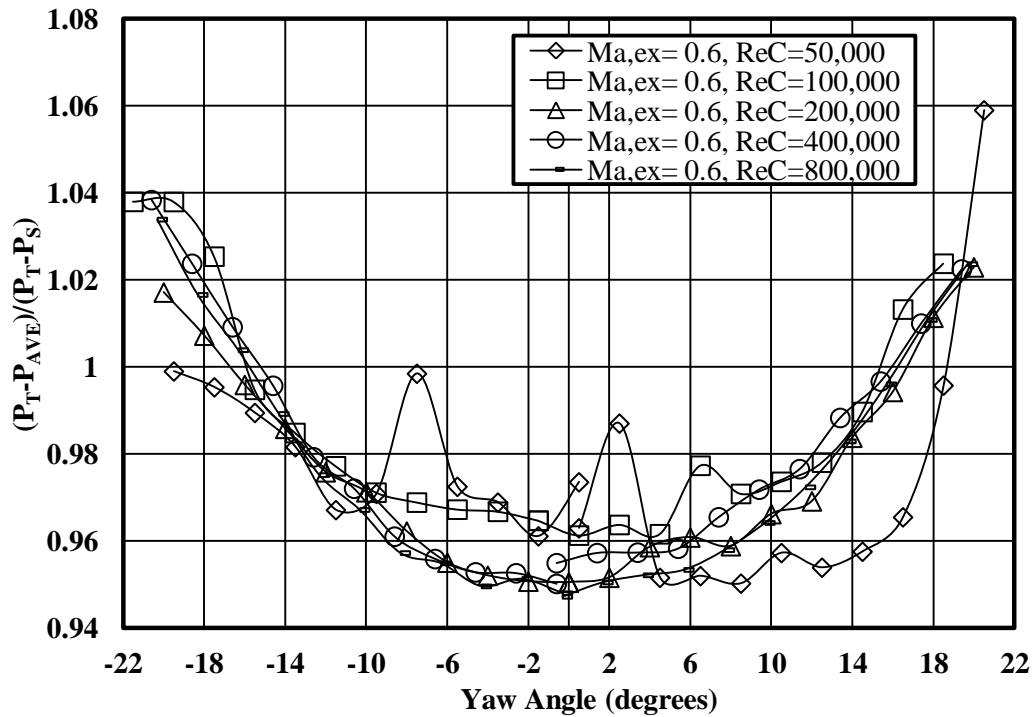

Figure 84. Yaw sensitivity coefficients of the five-hole cone probe over a span of yaw angles at Mach 0.9 as a function of Reynolds number between 50,000 and 800,000.
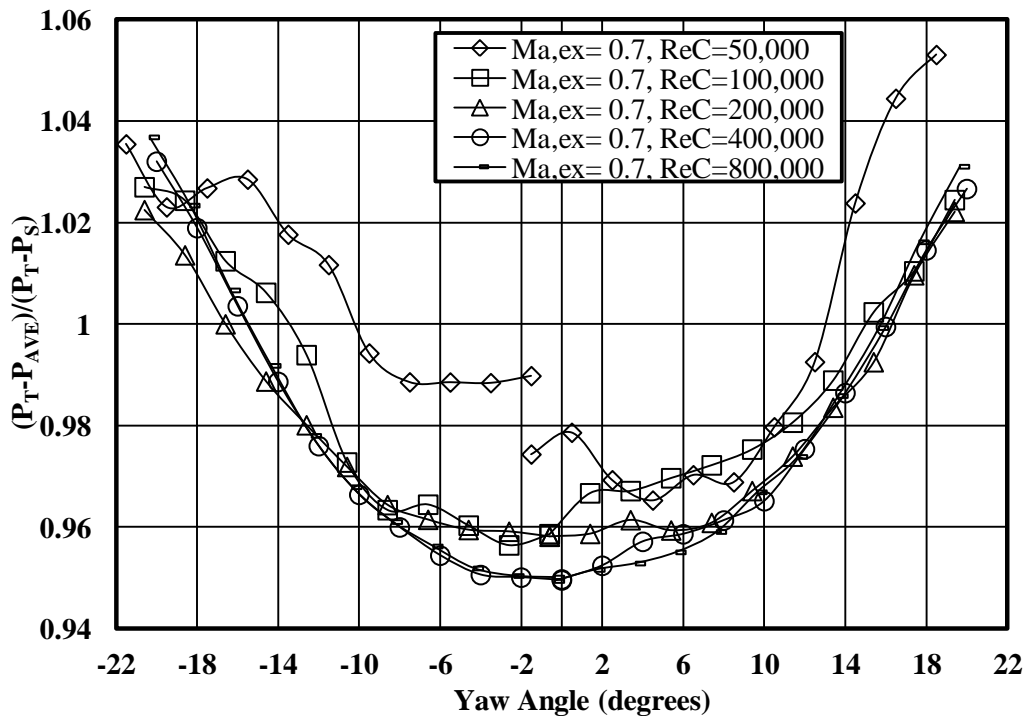
132
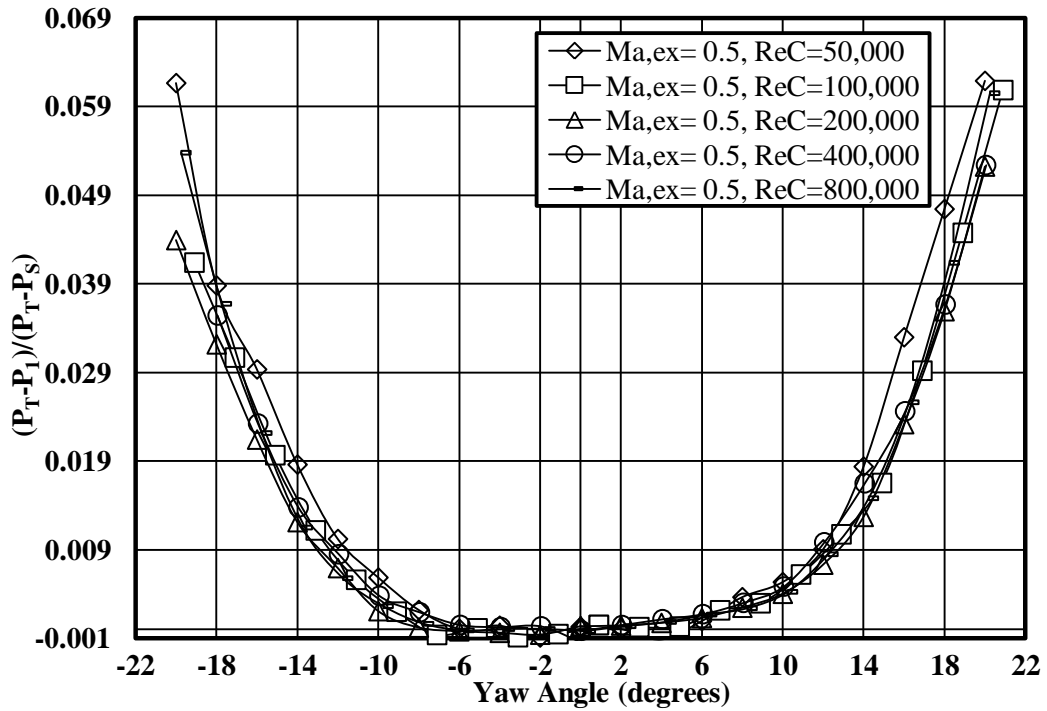
Figure 85. Total pressure recovery coefficients of the five-hole cone probe over a span of yaw angles at Mach 0.5 as a function of Reynolds number between 50,000 and 800,000.
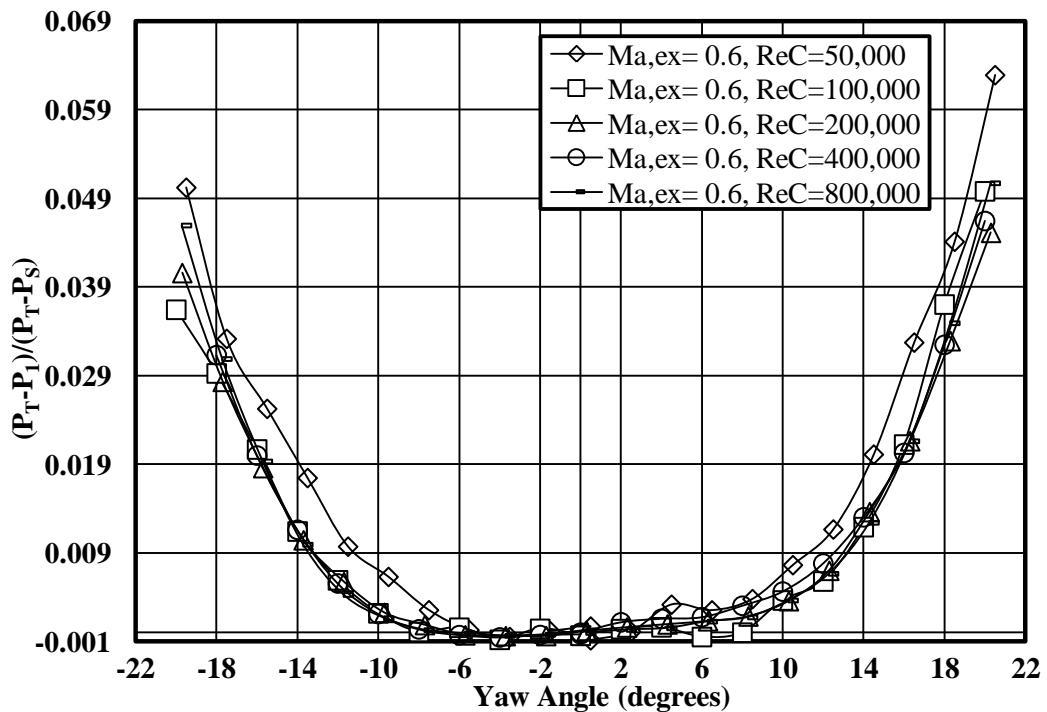
Figure 86. Total pressure recovery coefficients of the five-hole cone probe over a span of yaw angles at Mach 0.6 as a function of Reynolds number between 50,000 and 800,000.

133
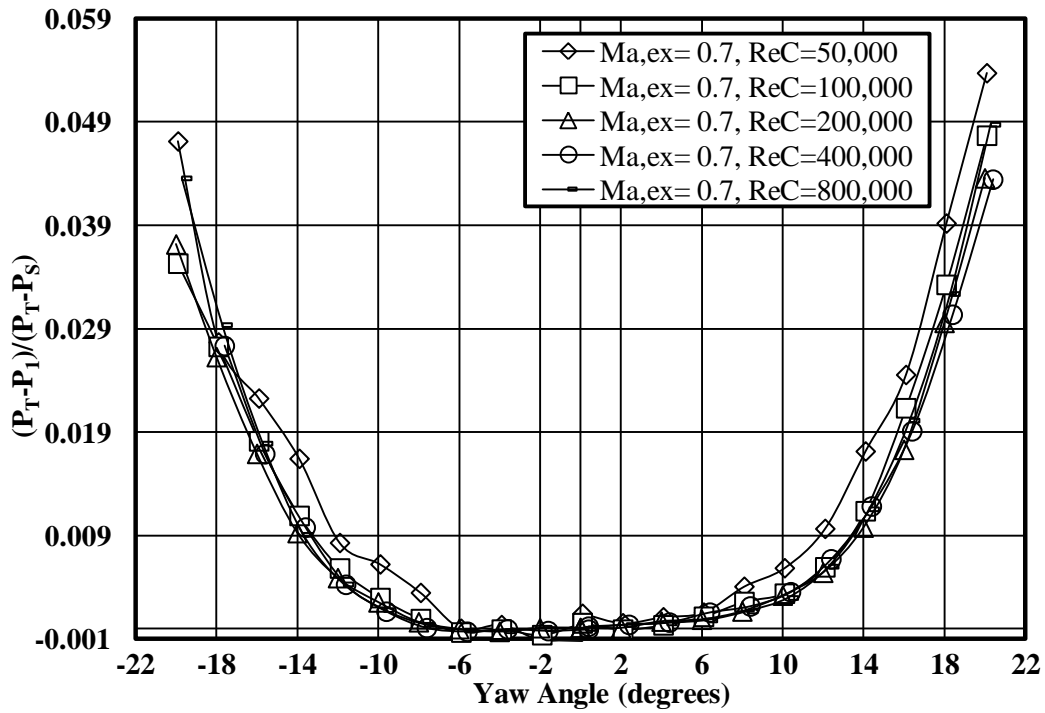
Figure 87. Total pressure recovery coefficients of the five-hole cone probe over a span of yaw angles at Mach 0.7 as a function of Reynolds number between 50,000 and 800,000.

Figure 88. Total pressure recovery coefficients of the five-hole cone probe over a span of yaw angles at Mach 0.8 as a function of Reynolds number between 50,000 and 800,000.
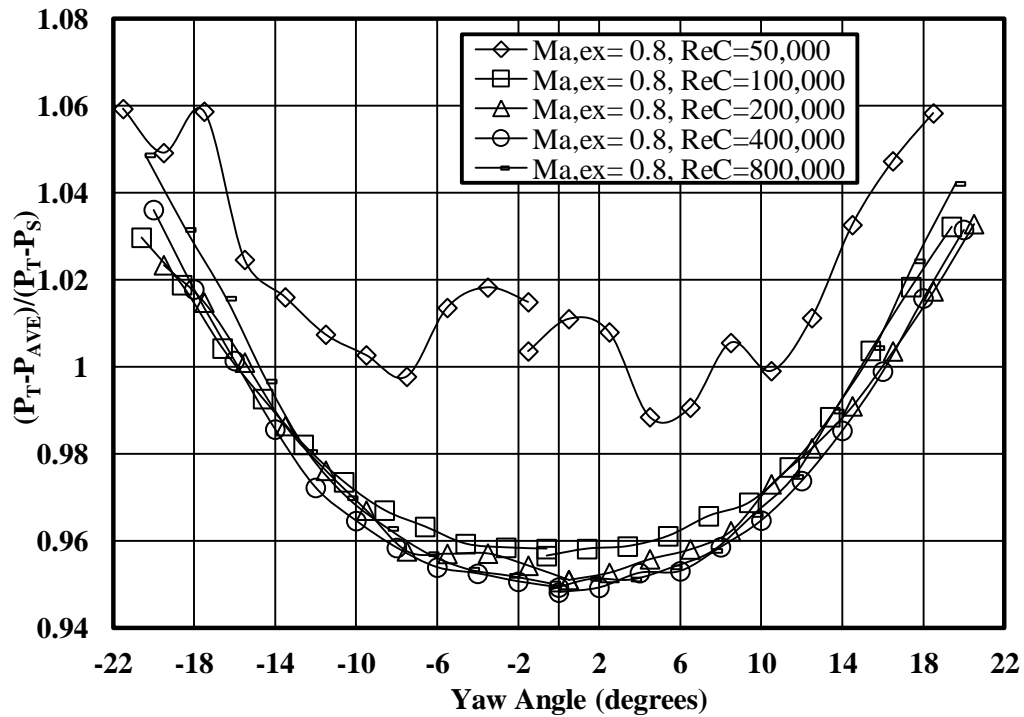
134

Figure 89. Total pressure recovery coefficients of the five-hole cone probe over a span of yaw angles at Mach 0.9 as a function of Reynolds number between 50,000 and 800,000.
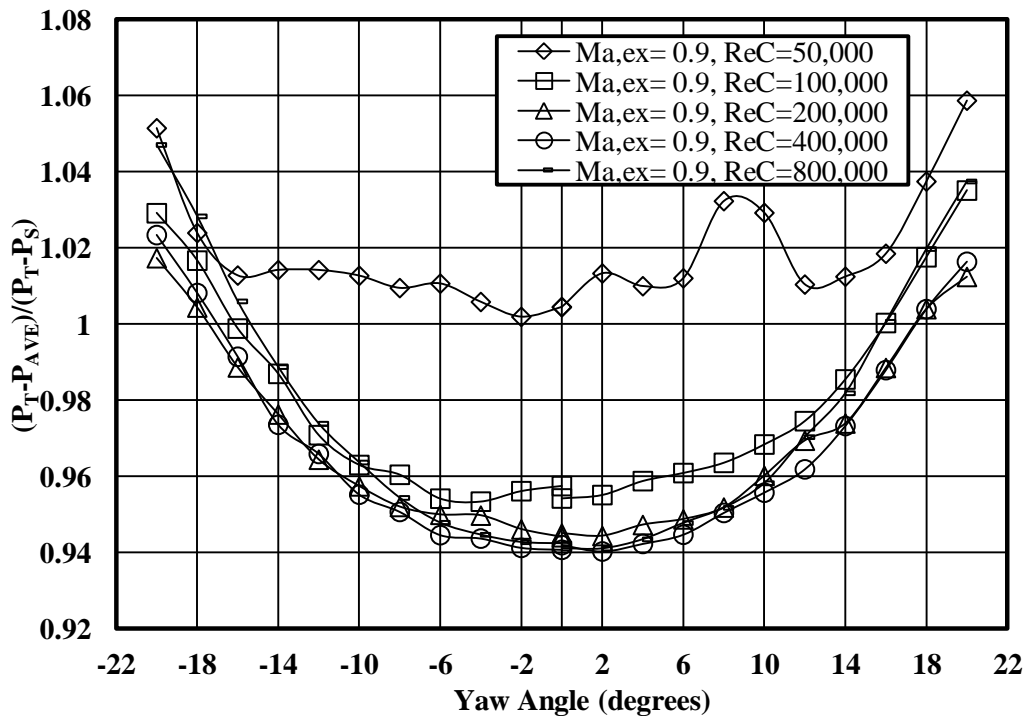

Figure 90. Pressure port sensitivity coefficients of the five-hole cone probe over a span of yaw angles at Mach 0.5 as a function of Reynolds number between 50,000 and 800,000.
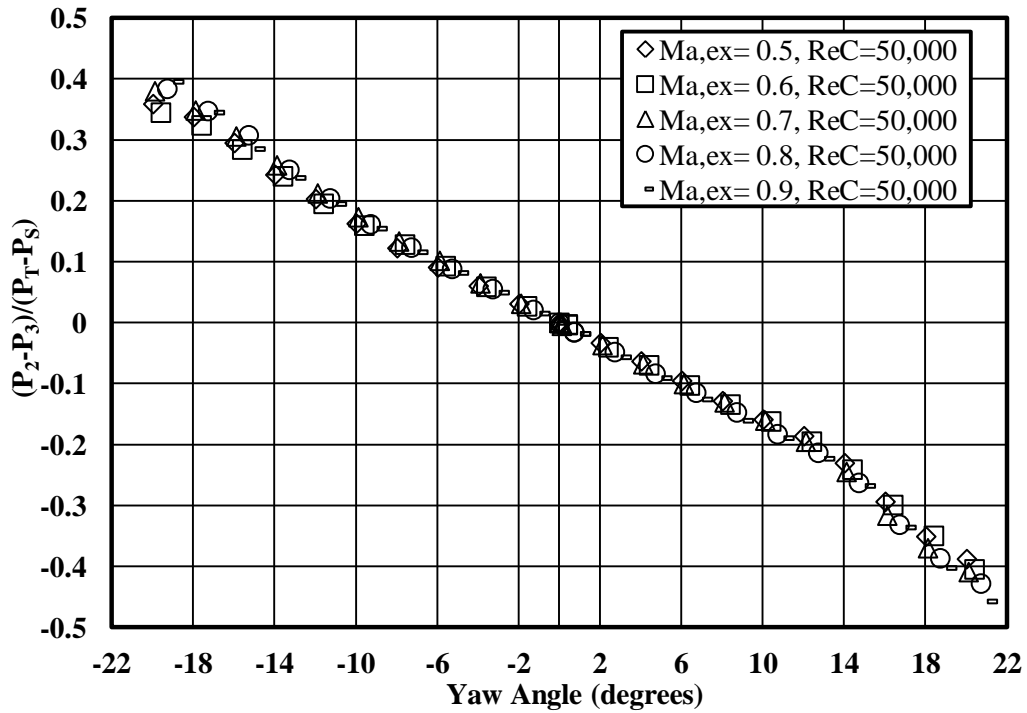
135

Figure 91. Pressure port sensitivity coefficients of the five-hole cone probe over a span of yaw angles at Mach 0.6 as a function of Reynolds number between 50,000 and 800,000.

Figure 92. Pressure port sensitivity coefficients of the five-hole cone probe over a span of yaw angles at Mach 0.7 as a function of Reynolds number between 50,000 and 800,000.

136

Figure 93. Pressure port sensitivity coefficients of the five-hole cone probe over a span of yaw angles at Mach 0.8 as a function of Reynolds number between 50,000 and 800,000.

Figure 94. Pressure port sensitivity coefficients of the five-hole cone probe over a span of yaw angles at Mach 0.9 as a function of Reynolds number between 50,000 and 800,000.

137

Figure 95. Yaw sensitivity coefficients of the five-hole cone probe over a span of yaw angles at a Reynolds number of 50,000 as a function of Mach number between 0.5 and 0.9.
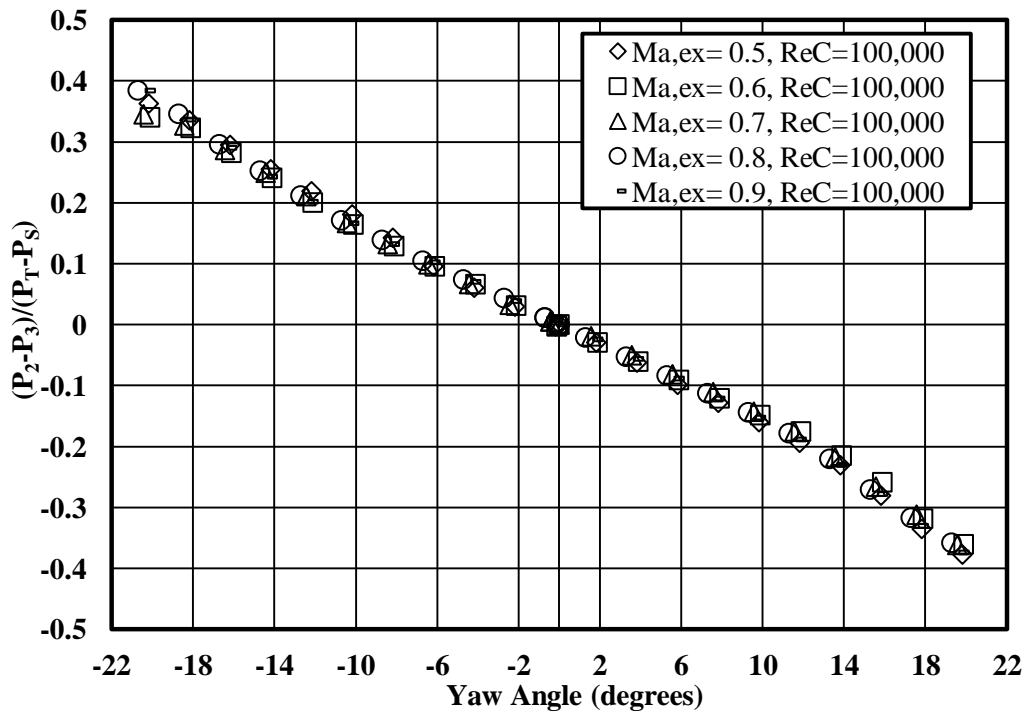
Figure 96. Yaw sensitivity coefficients of the five-hole cone probe over a span of yaw angles at a Reynolds number of 100,000 as a function of Mach number between 0.5 and 0.9.
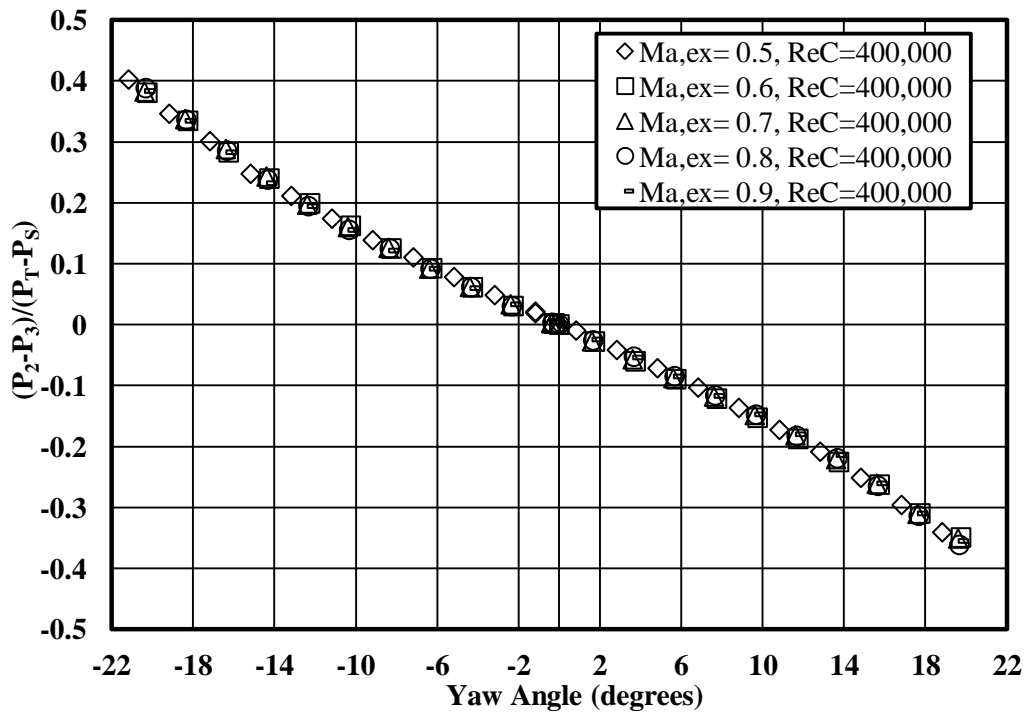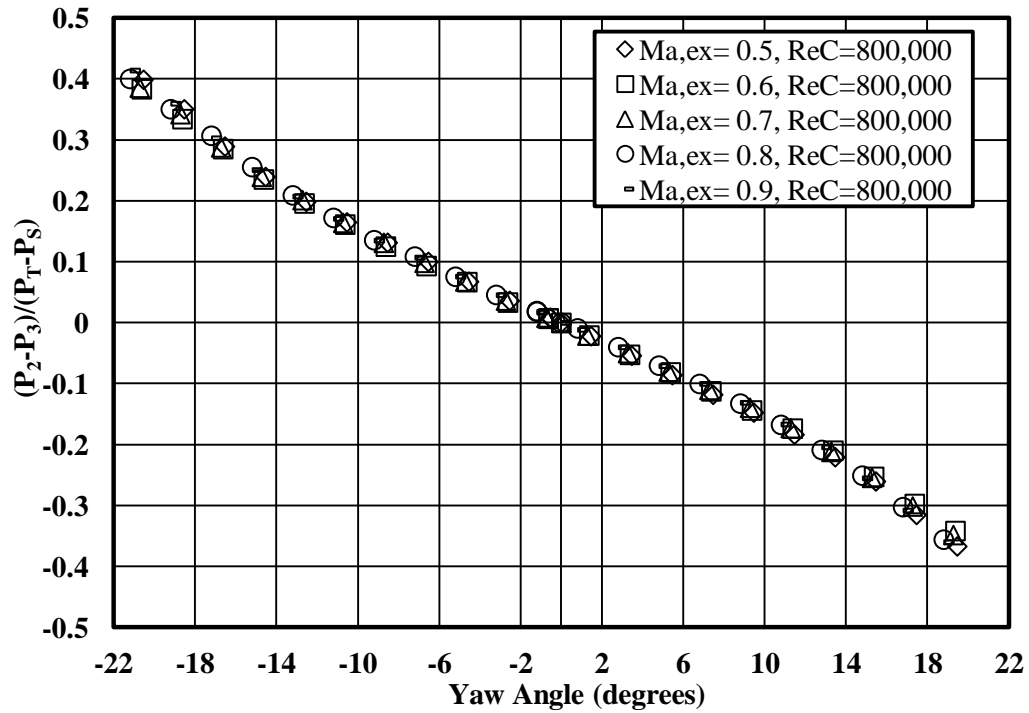
138
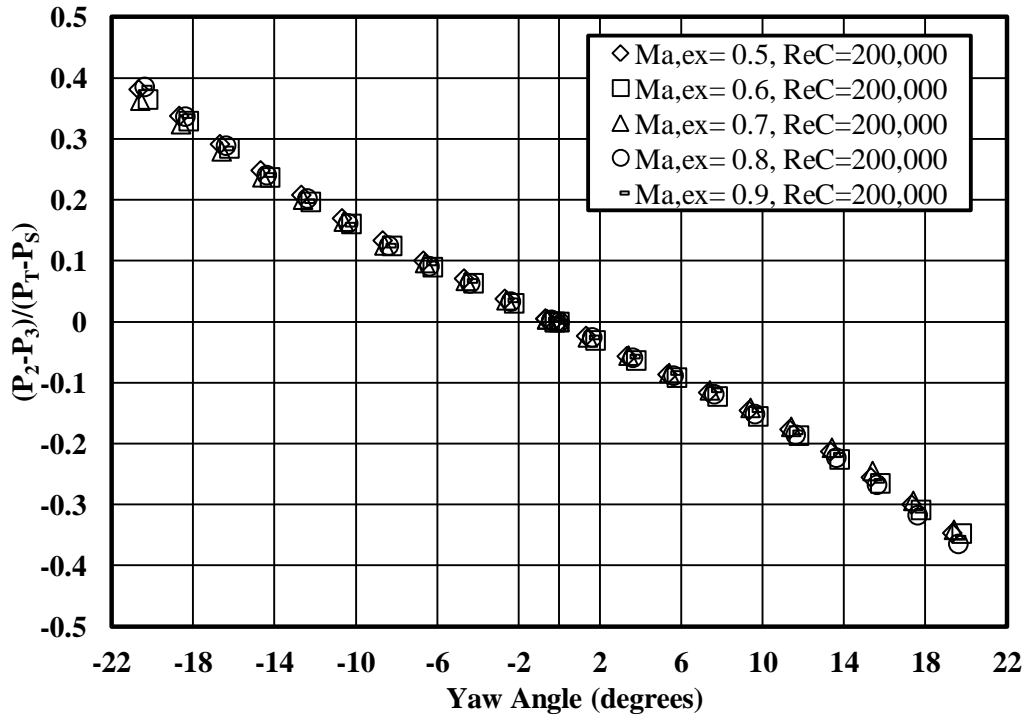
Figure 97. Yaw sensitivity coefficients of the five-hole cone probe over a span of yaw angles at a Reynolds number of 200,000 as a function of Mach number between 0.5 and 0.9.

Figure 98. Yaw sensitivity coefficients of the five-hole cone probe over a span of yaw angles at a Reynolds number of 400,000 as a function of Mach number between 0.5 and 0.9.

139

Figure 99. Yaw sensitivity coefficients of the five-hole cone probe over a span of yaw angles at a Reynolds number of 800,000 as a function of Mach number between 0.5 and 0.9.
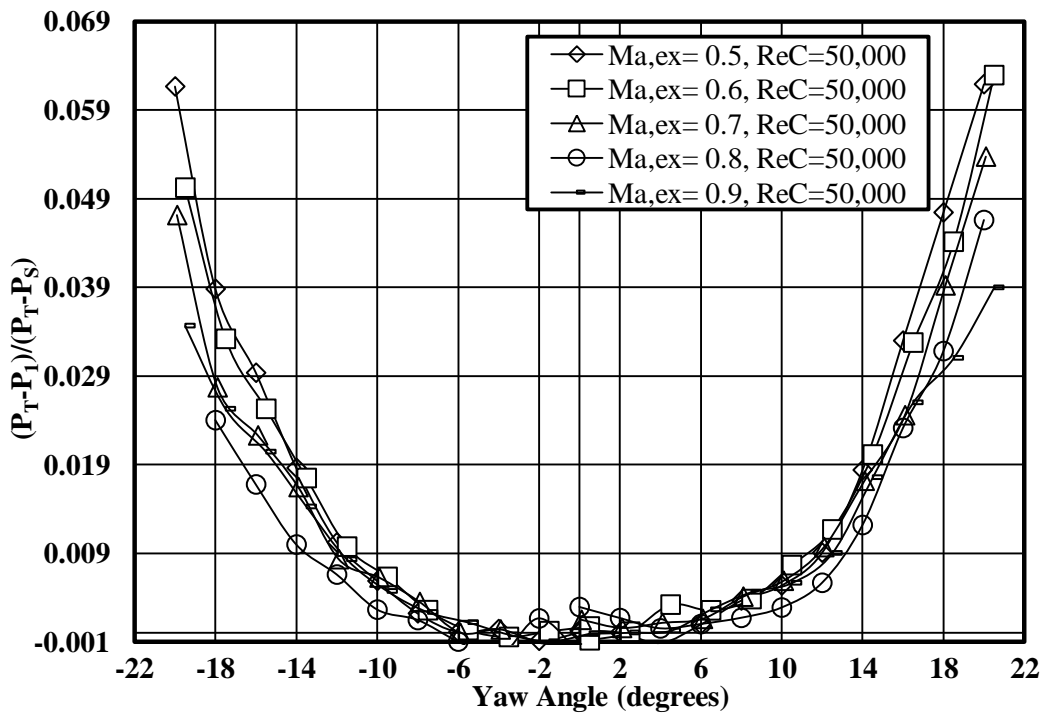

Figure 100. Total pressure recovery coefficients of the five-hole cone probe over a span of yaw angles at a Reynolds number of 50,000 as a function of Mach number between 0.5 and 0.9.
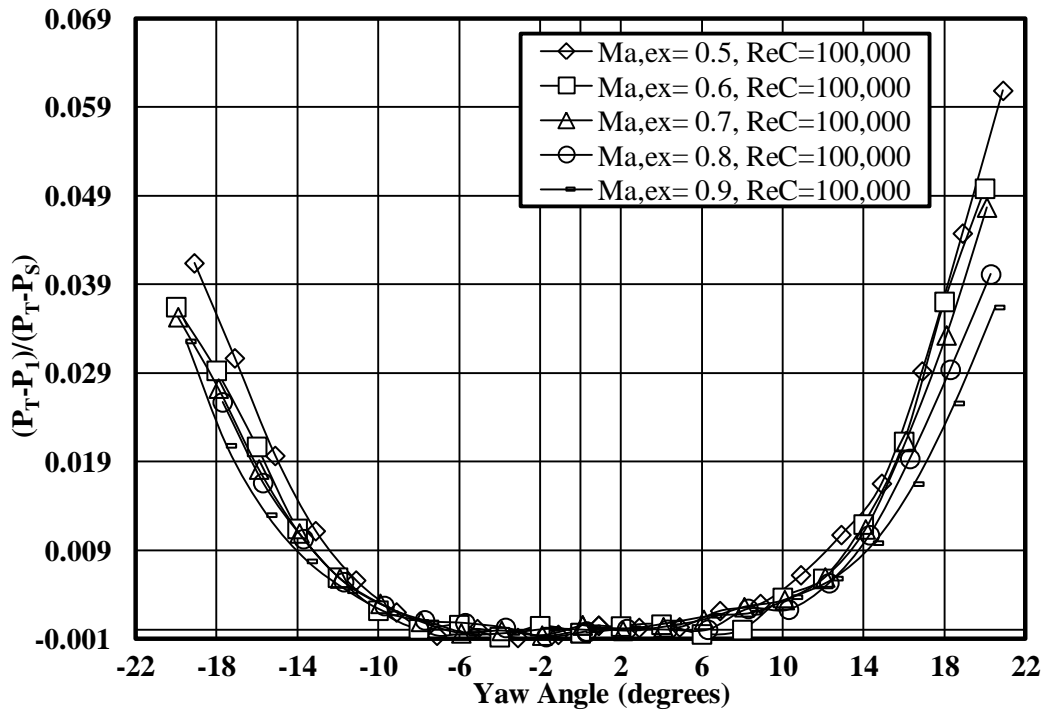
140

Figure 101. Total pressure recovery coefficients of the five-hole cone probe over a span of yaw angles at a Reynolds number of 100,000 as a function of Mach number between 0.5 and 0.9.
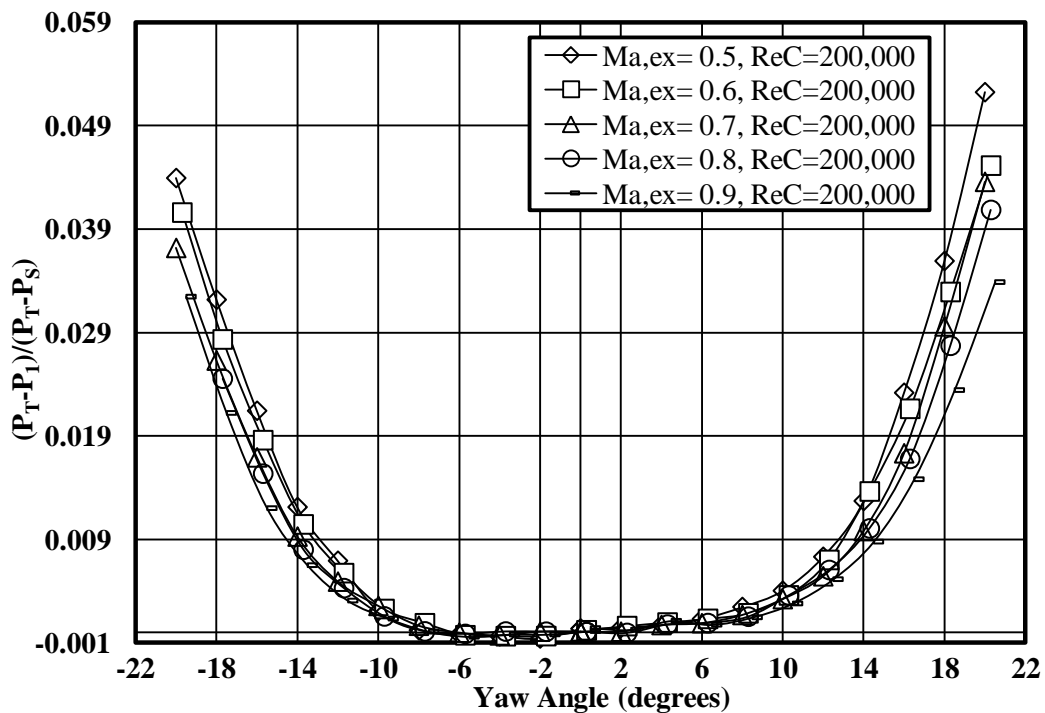

Figure 102. Total pressure recovery coefficients of the five-hole cone probe over a span of yaw angles at a Reynolds number of 200,000 as a function of Mach number between 0.5 and 0.9.
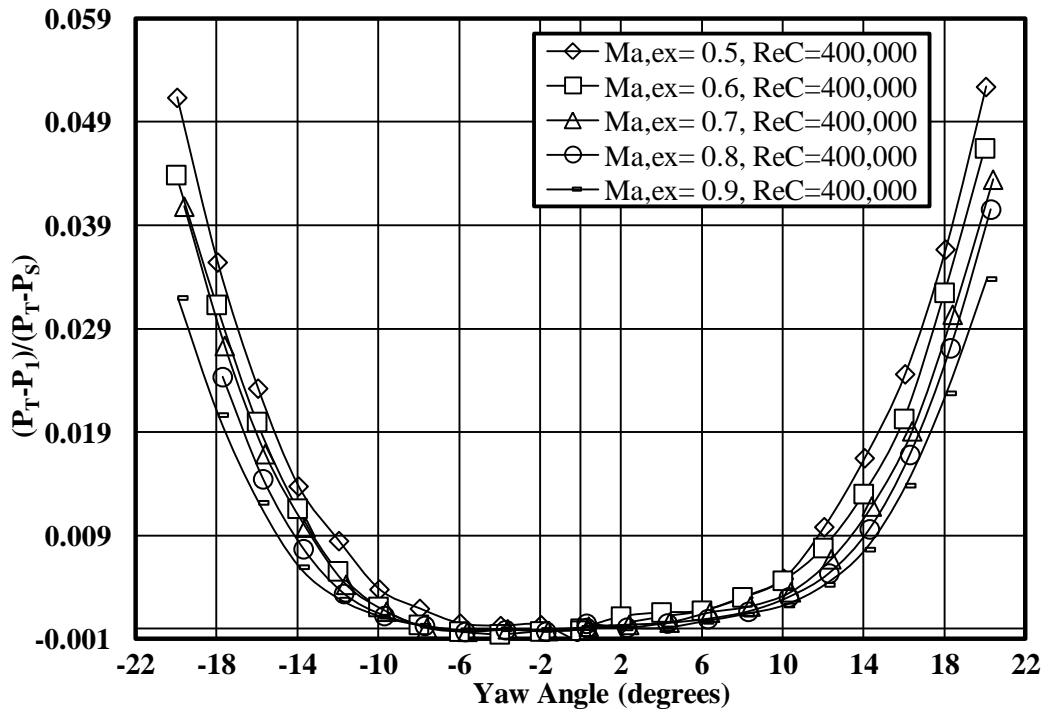
141

Figure 103. Total pressure recovery coefficients of the five-hole cone probe over a span of yaw angles at a Reynolds number of 400,000 as a function of Mach number between 0.5 and 0.9.
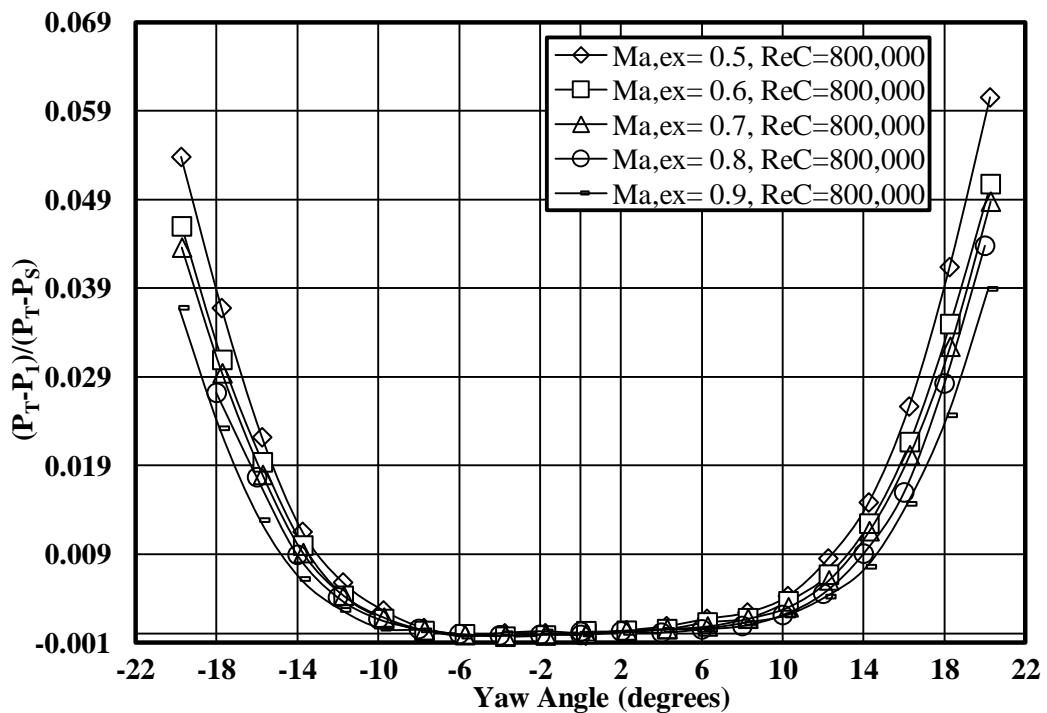

Figure 104. Total pressure recovery coefficients of the five-hole cone probe over a span of yaw angles at a Reynolds number of 800,000 as a function of Mach number between 0.5 and 0.9.
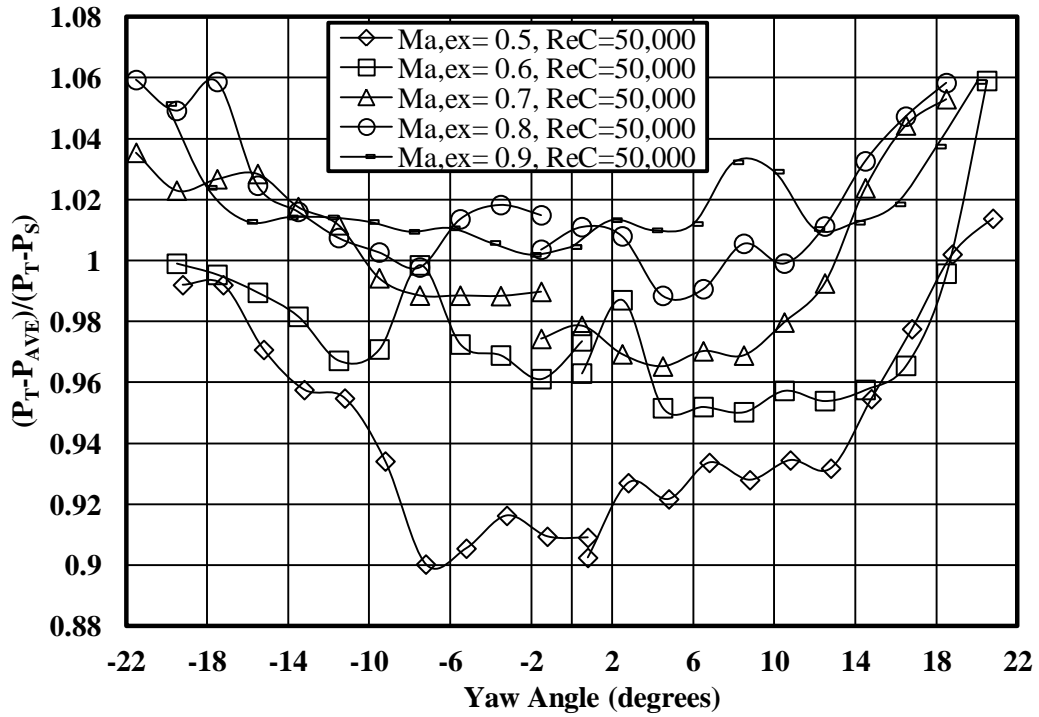
142

Figure 105. Pressure sensitivity coefficients of the five-hole cone probe over a span of yaw angles at a Reynolds number of 50,000 as a function of Mach number between 0.5 and 0.9.

Figure 106. Pressure sensitivity coefficients of the five-hole cone probe over a span of yaw angles at a Reynolds number of 100,000 as a function of Mach number between 0.5 and 0.9.
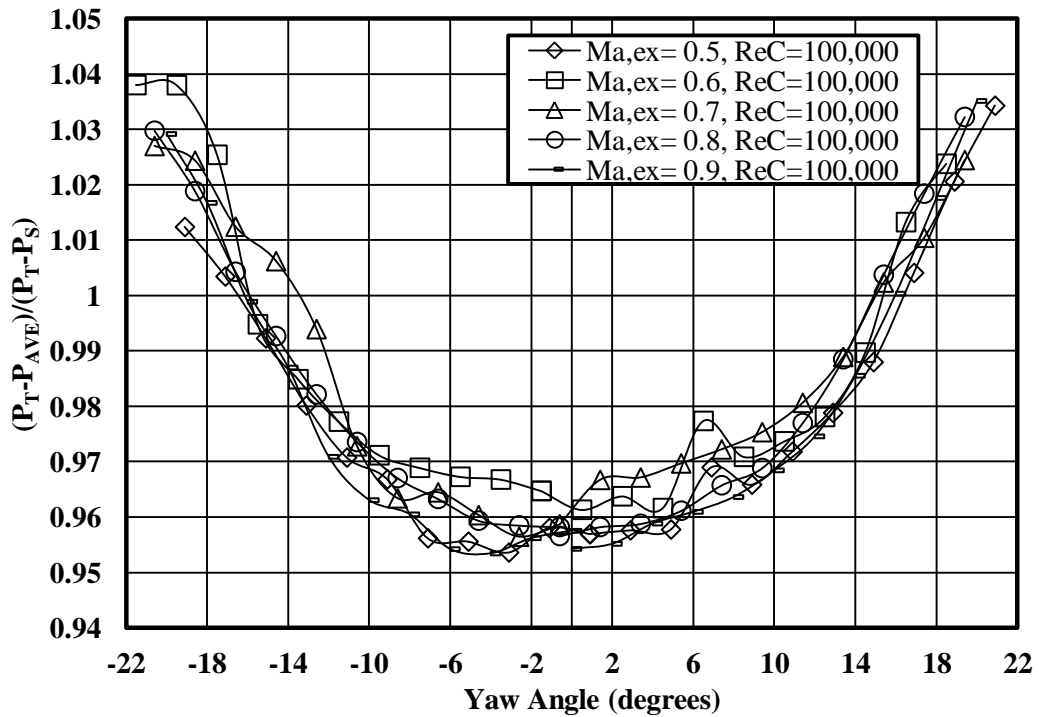
143

Figure 107. Pressure sensitivity coefficients of the five-hole cone probe over a span of yaw angles at a Reynolds number of 200,000 as a function of Mach number between 0.5 and 0.9.

Figure 108. Pressure sensitivity coefficients of the five-hole cone probe over a span of yaw angles at a Reynolds number of 400,000 as a function of Mach number between 0.5 and 0.9.

144

Figure 109. Pressure sensitivity coefficients of the five-hole cone probe over a span of yaw angles at a Reynolds number of 800,000 as a function of Mach number between 0.5 and 0.9.
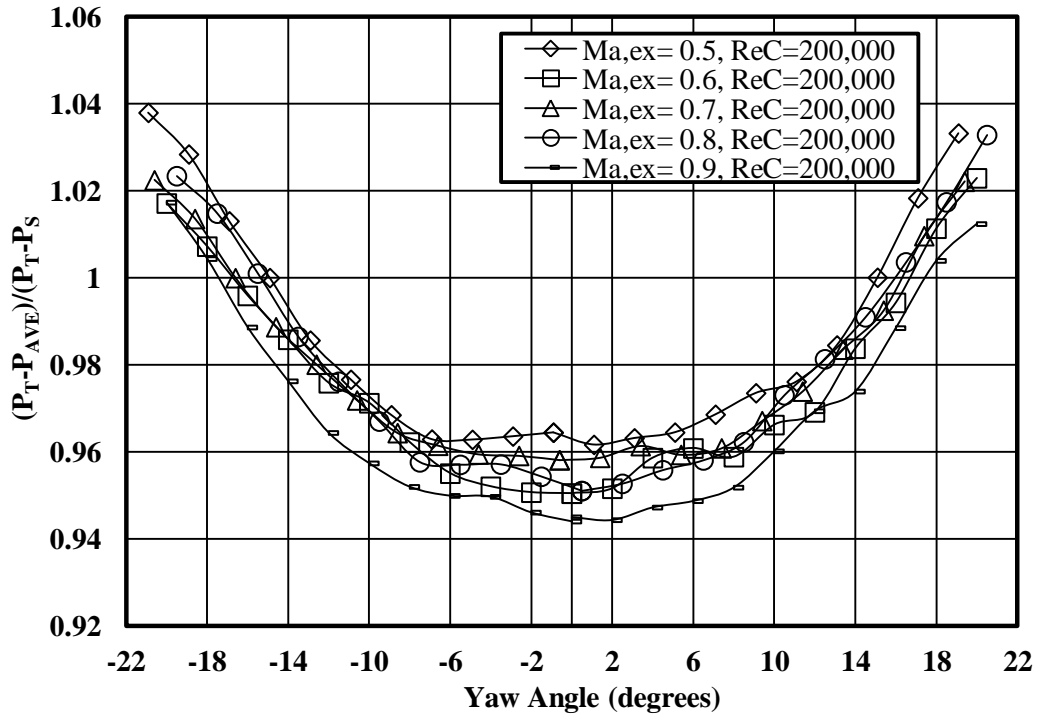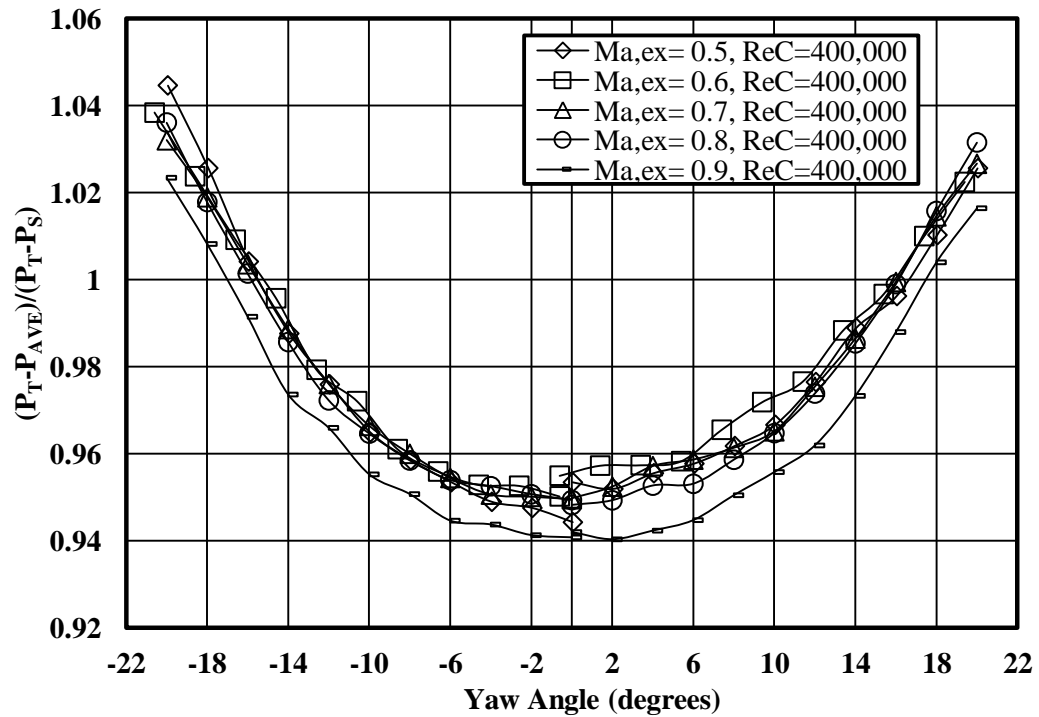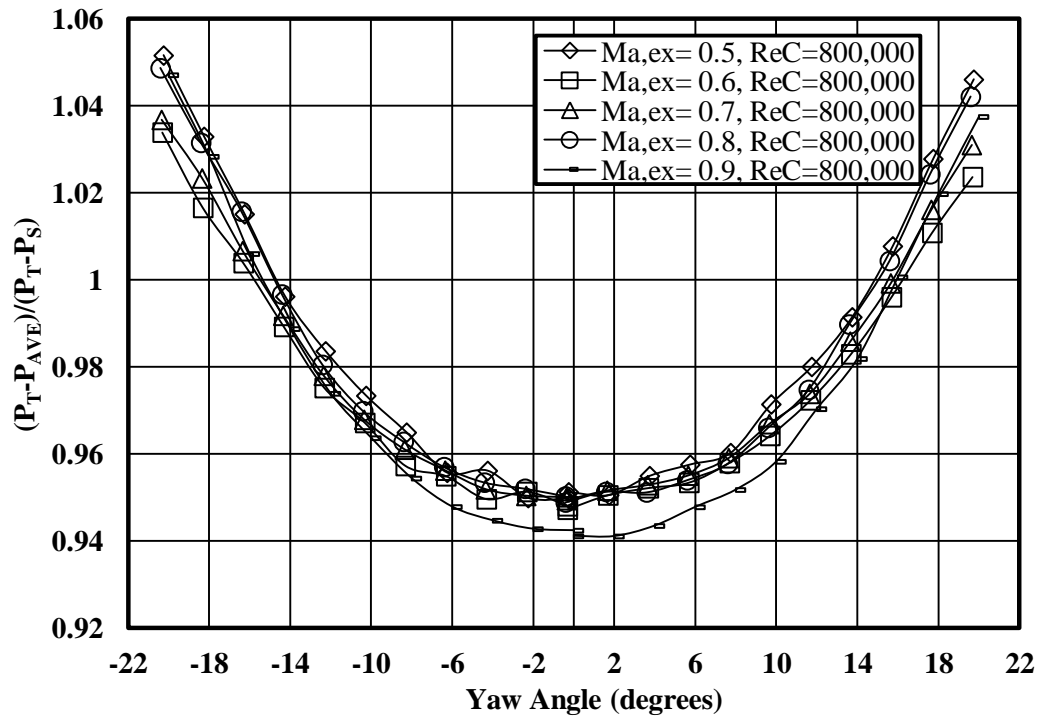
Appendix D

Baseline Vane Exit Survey Contour Plots Not Reported in Results

¼ Axial Chord – Low Turbulence

Figure 110. Total pressure loss contours Ω (Omega) with secondary velocity vectors for the vane at ¼ axial chord location under low turbulence at a chord exit Reynolds number of 90,000 and Mach number of 0.7.

Figure 111. Total pressure loss contours Ω (Omega) with secondary velocity vectors for the vane at ¼ axial chord location under low turbulence at a chord exit Reynolds number of 90,000 and Mach number of 0.87.

Figure 112. Total pressure loss contours Ω (Omega) with secondary velocity vectors for the vane at ¼ axial chord location under low turbulence at a chord exit Reynolds number of 180,000 and Mach number of 0.7.
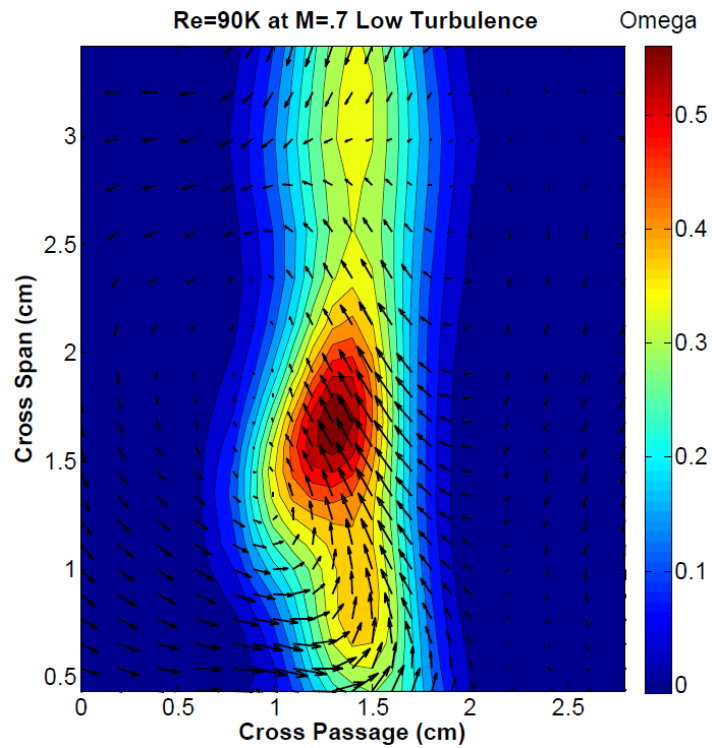
147

Figure 113. Total pressure loss contours Ω (Omega) with secondary velocity vectors for the vane at ¼ axial chord location under low turbulence at a chord exit Reynolds number of 180,000 and Mach number of 0.88.

Figure 114. Total pressure loss contours Ω (Omega) with secondary velocity vectors for the vane at ¼ axial chord location under low turbulence at a chord exit Reynolds number of 360,000 and Mach number of 0.7.
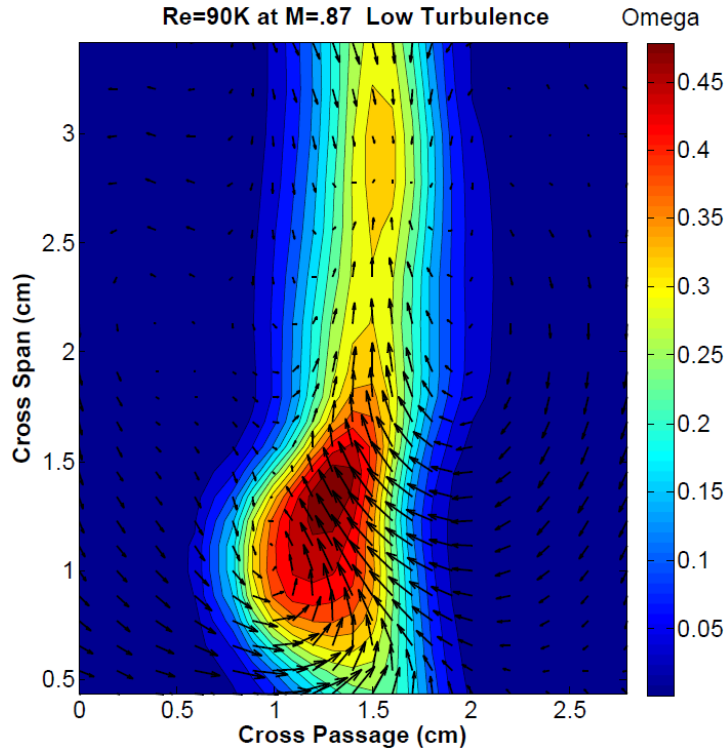
148
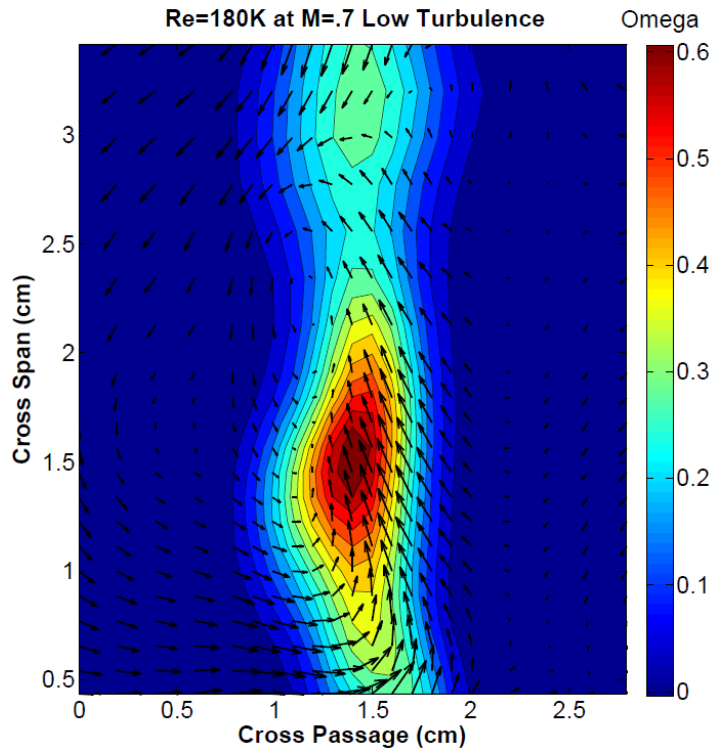
Figure 115. Total pressure loss contours Ω (Omega) with secondary velocity vectors for the vane at ¼ axial chord location under low turbulence at a chord exit Reynolds number of 360,000 and Mach number of 0.9.

Figure 116. Total pressure loss contours Ω (Omega) with secondary velocity vectors for the vane at ¼ axial chord location under aero-combustor turbulence at a chord exit Reynolds number of 90,000 and Mach number of 0.7.
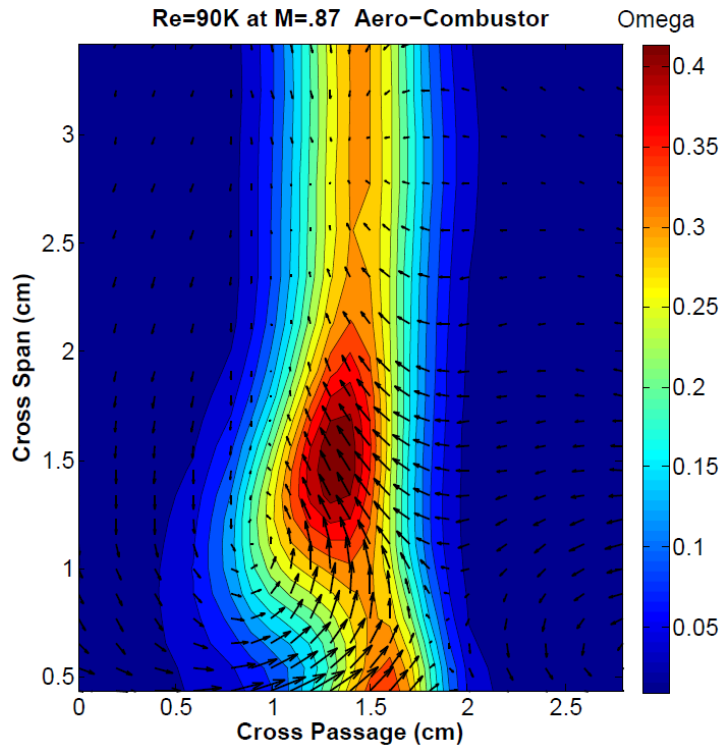
Figure 117. Total pressure loss contours Ω (Omega) with secondary velocity vectors for the vane at ¼ axial chord location under aero-combustor turbulence at a chord exit Reynolds number of 90,000 and Mach number of 0.87.
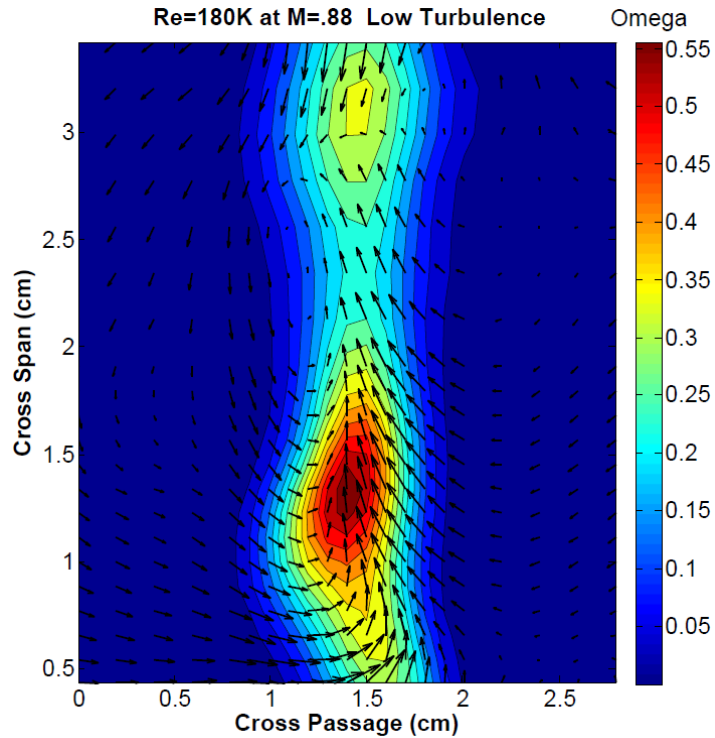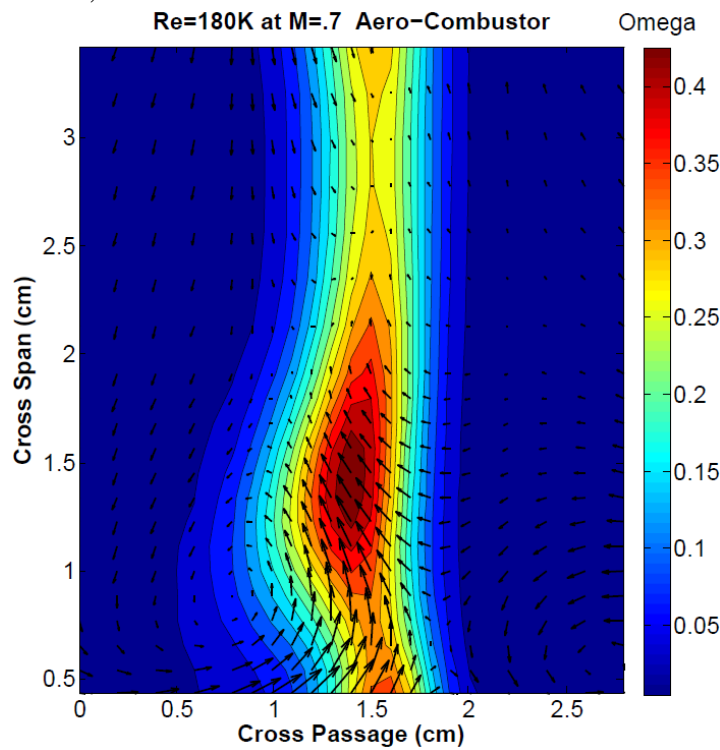

Figure 118. Total pressure loss contours Ω (Omega) with secondary velocity vectors for the vane at ¼ axial chord location under aero-combustor turbulence at a chord exit Reynolds number of 180,000 and Mach number of 0.7.
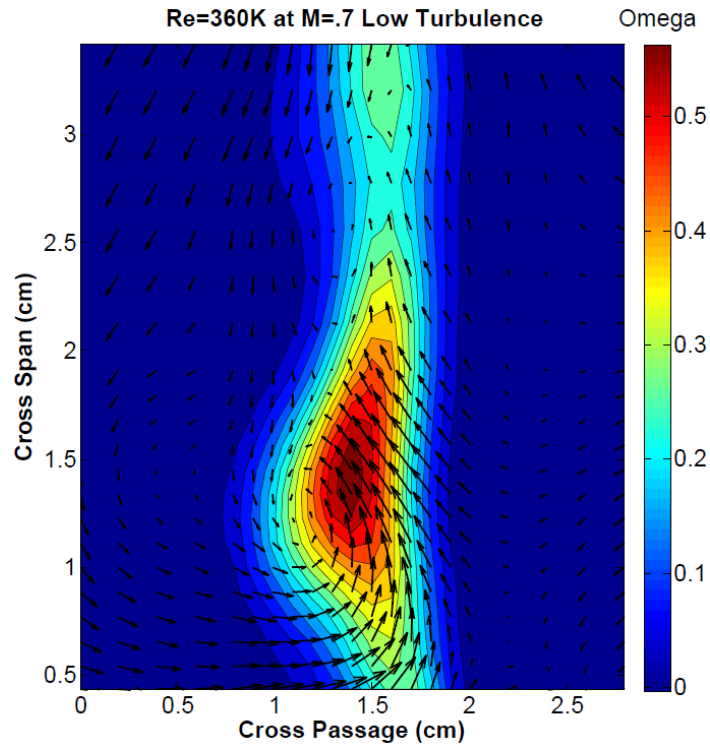
151
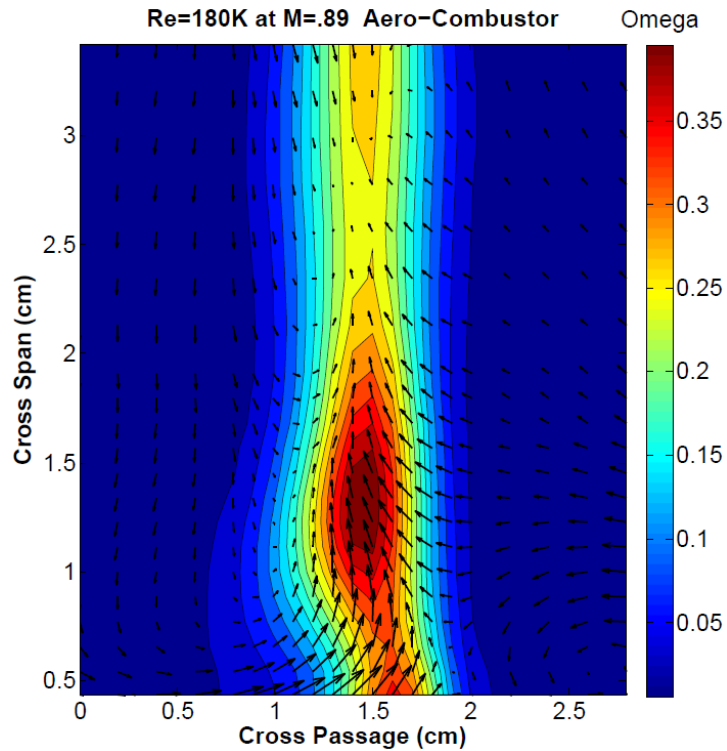
Figure 119. Total pressure loss contours Ω (Omega) with secondary velocity vectors for the vane at ¼ axial chord location under aero-combustor turbulence at a chord exit Reynolds number of 180,000 and Mach number of 0.89.
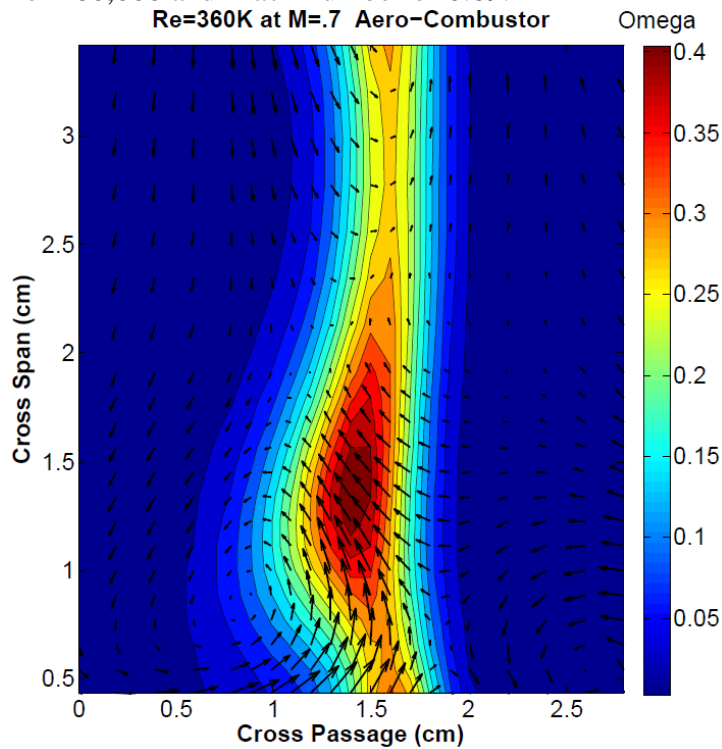
Figure 120. Total pressure loss contours Ω (Omega) with secondary velocity vectors for the vane at ¼ axial chord location under aero-combustor turbulence at a chord exit Reynolds number of 360,000 and Mach number of 0.7.
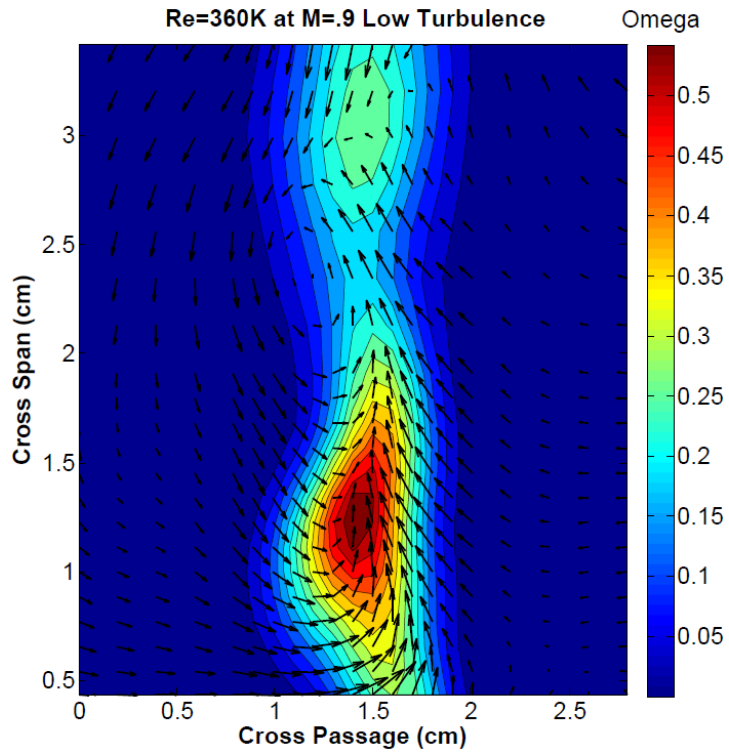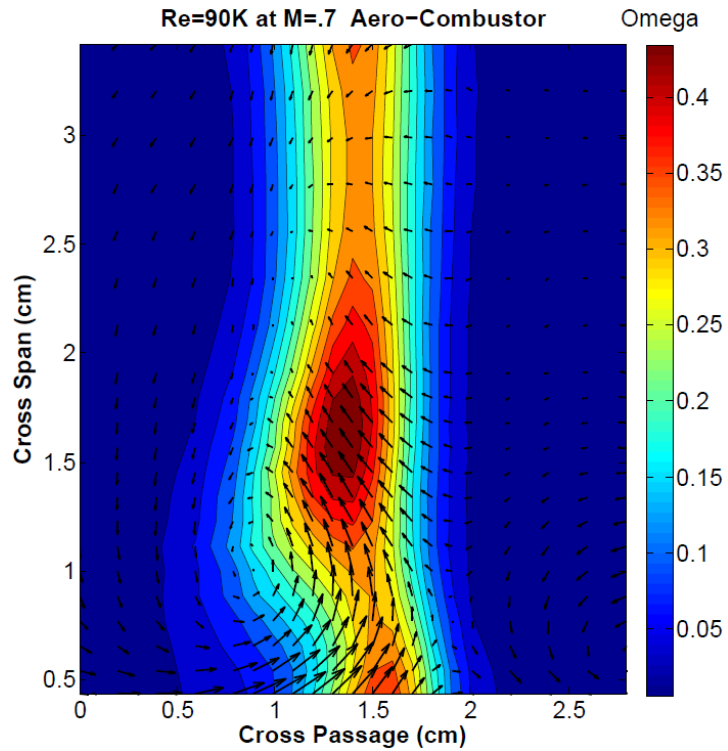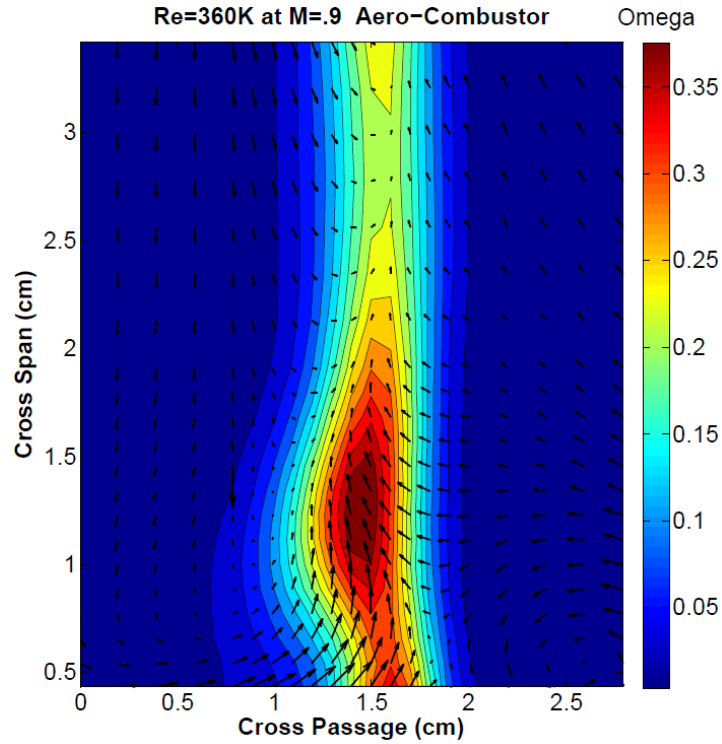
Figure 121. Total pressure loss contours Ω (Omega) with secondary velocity vectors for the vane at ¼ axial chord location under aero-combustor turbulence at a chord exit Reynolds number of 360,000 and Mach number of 0.9.

Vane Surface Heat Transfer Measurements
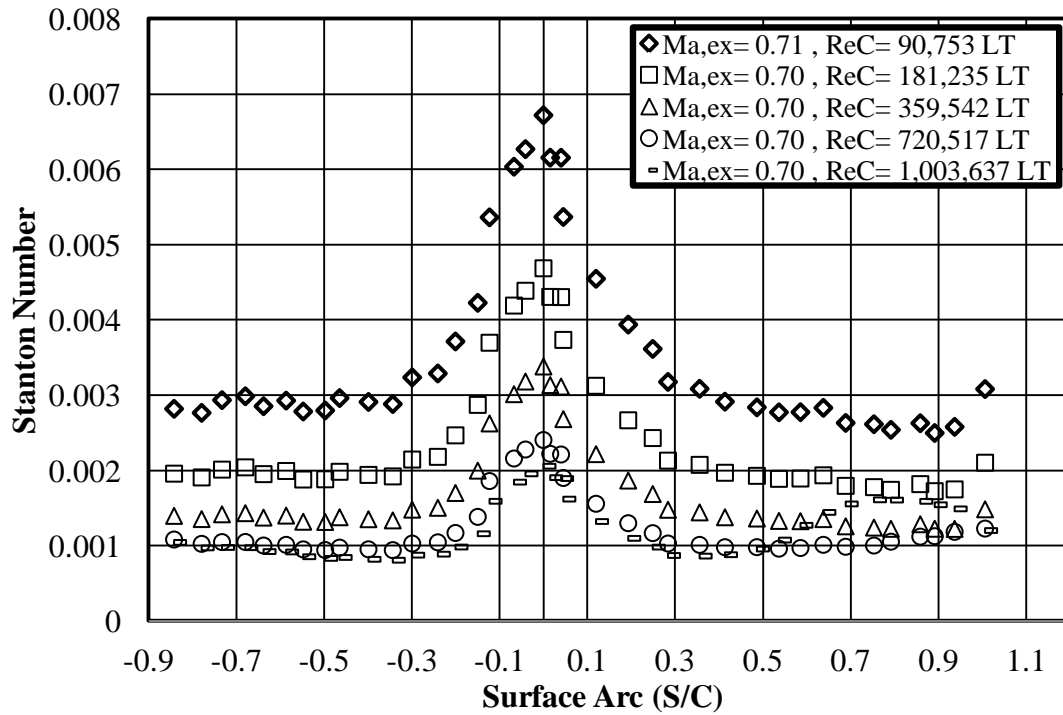
Figure 122. Stanton number distributions under low turbulence conditions over Reynolds numbers of 90,000, 180,000, 360,000, 720,000, and 1,000,000 at Mach 0.7 based on true chord exit conditions.
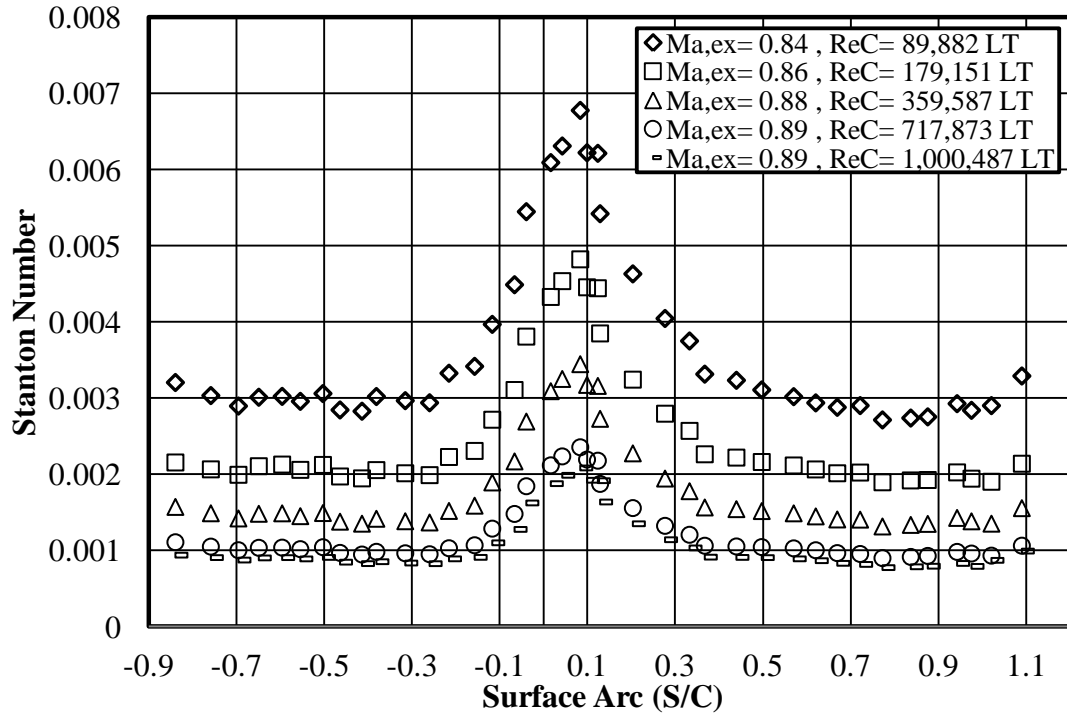
Figure 123. Stanton number distributions under low turbulence conditions over Reynolds numbers of 90,000, 180,000, 360,000, 720,000, and 1,000,000 at Mach 0.9 based on true chord exit conditions.
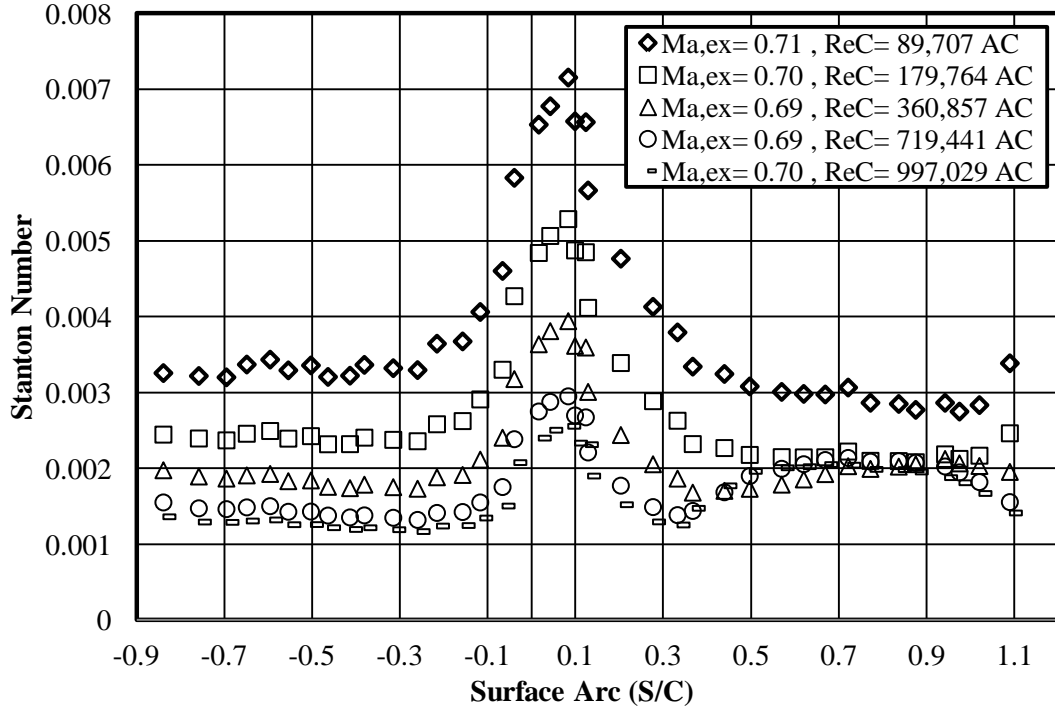
Figure 124. Stanton number distributions under aero-combustor turbulence conditions over Reynolds numbers of 90,000, 180,000, 360,000, 720,000, and 1,000,000 at Mach 0.7 based on true chord exit conditions.

155
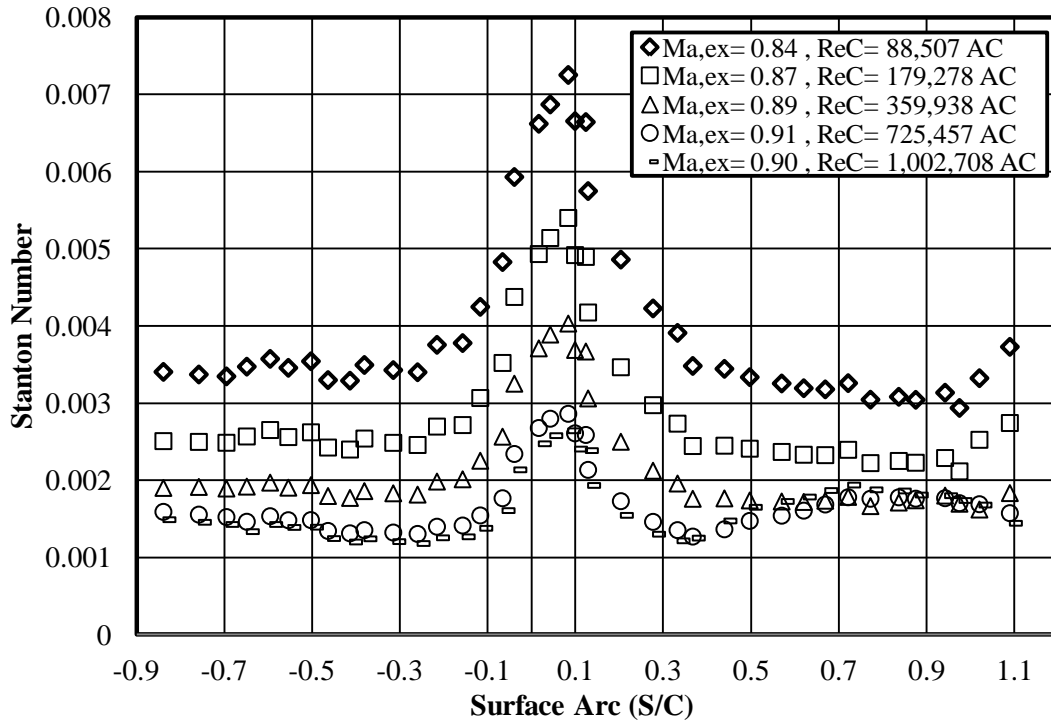
Figure 125. Stanton number distributions under aero-combustor turbulence conditions over Reynolds numbers of 90,000, 180,000, 360,000, 720,000, and 1,000,000 at Mach 0.9 based on true chord exit conditions.
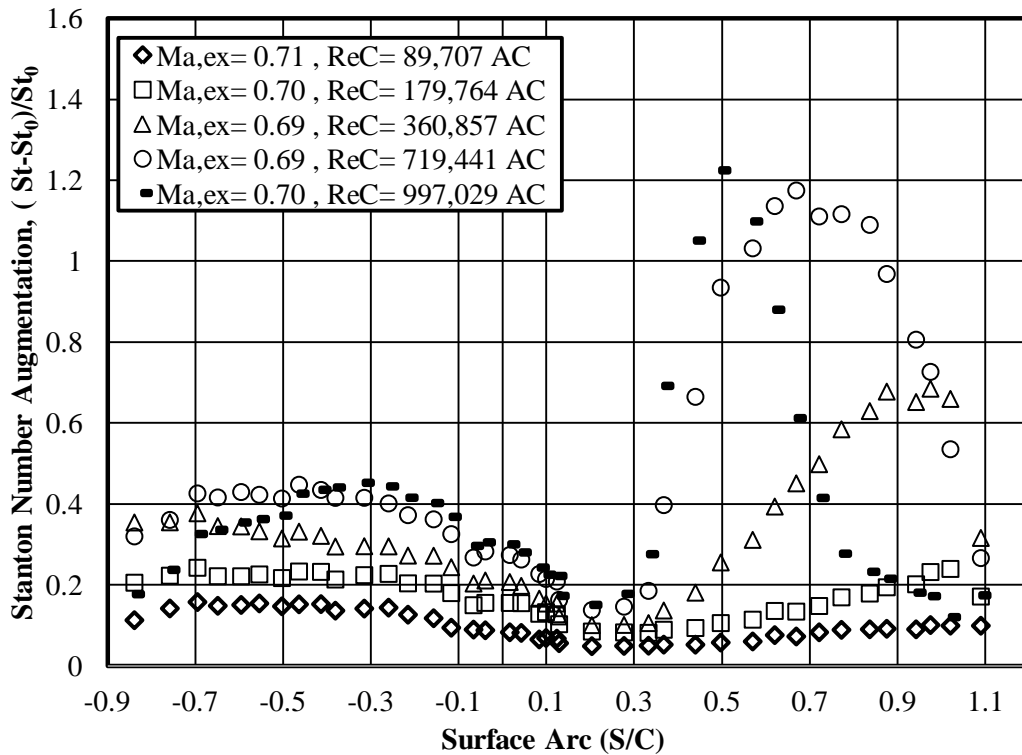
Figure 126. Effects of mock aero-derivative combustor turbulence characteristics on Stanton number augmentation and location of transition over Reynolds numbers of 90,000, 180,000, 360,000, and 720,000 at an exit Mach number of 0.7.

156
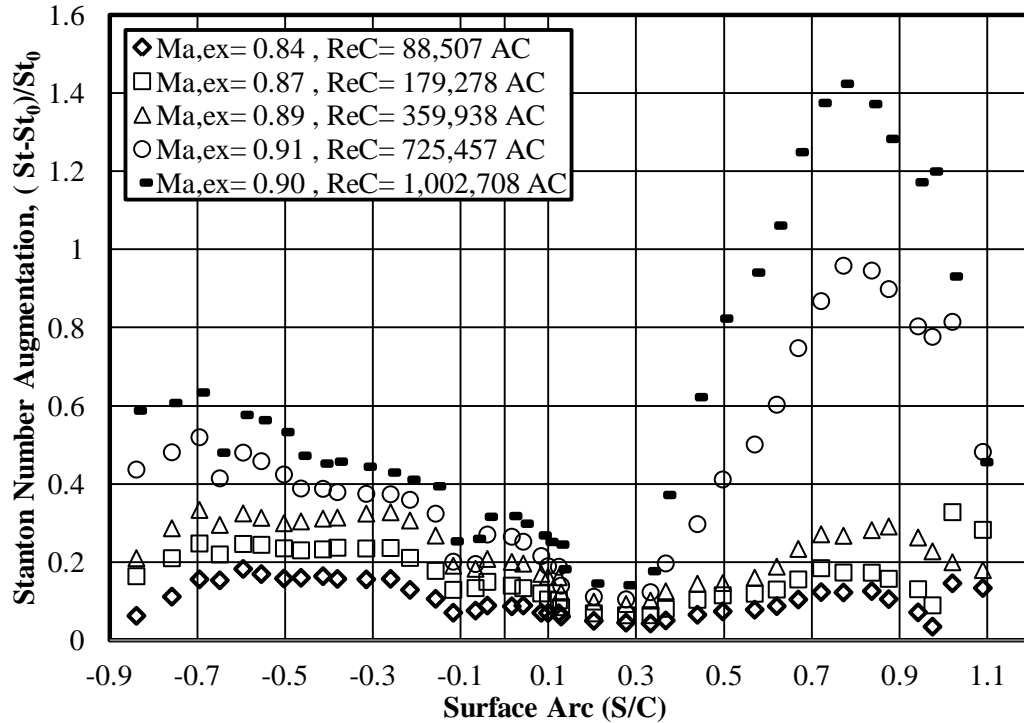
Figure 127. Effects of mock aero-derivative combustor turbulence characteristics on Stanton number augmentation and location of transition over Reynolds numbers of 90,000, 180,000, 360,000, and 720,000 at an exit Mach number of 0.9.

Finite Difference Methodology

The finite difference methodology consists of modeling the heat transfer vane material makeup in order to accurately calculate conduction heat transfer. Accounting for heat conduction through the vane is required due to the possibility that heat generated on the foil surface would not all be dissipated by convection but be conducted into the vane. The finite difference model is used to determine the Inconel foil surface temperatures, based on the energy transfer through the vane nodal network seen in Figure 42. The specific finite difference models used for calculating energy exchange near the surface, between different materials, and through the vane are seen in Figure 128 and Figure 129. The equations that describe the energy exchange between each node are also provided below each model. These equations are utilized to describe the entire vane model in an

157

excel sheet, which calculates a temperature distribution through the vane and used to calculate surface Stanton number.
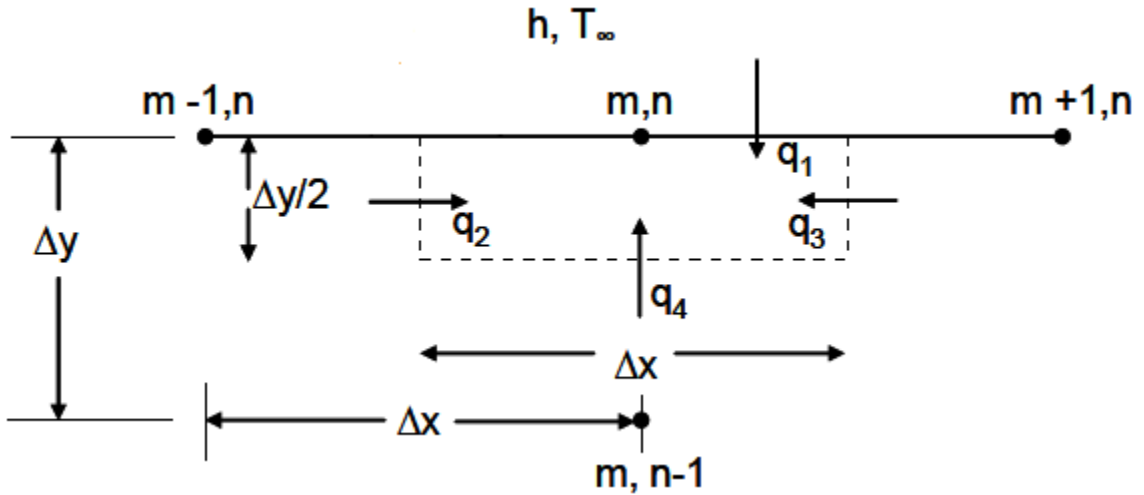
Figure 128. A finite difference diagram that shows heat exchange at surface nodes, which was used to calculate heat flow due to conduction in the heat transfer vane.

The following equations were used to describe the energy transfer between nodes at the vanes surface. The convective heat transfer term q_1 was only used for the trailing edge of the vane, which was not in contact with the foil. The q_1 term was then neglected for surface vane nodes that were in contact with the constant heat flux foil.

$$E_{in} - E_{out} = 0$$

$$q_1 + q_2 + q_3 + q_4 = 0$$

$$\frac{h(T_S - T_\infty)}{\Delta x} + \frac{k(T_{m-1,n} - T_{m,n})}{\Delta x}\frac{\Delta y}{2}1 + \frac{k(T_{m+1,n} - T_{m,n})}{\Delta x}\frac{\Delta y}{2}1 + \frac{k(T_{m,n-1} - T_{m,n})}{\Delta y}\Delta x1 = 0$$

Figure 129. Finite difference diagram for nodal conduction heat exchange in a homogeneous material.

The following equations describe the energy transfer between nodes throughout the vane epoxy.

$$E_{in} - E_{out} = 0$$

$$q_1 + q_2 + q_3 + q_4 = 0$$

$$\frac{k(T_{m-1,n} - T_{m,n})}{\Delta x}\frac{\Delta y}{2}1 + \frac{k(T_{m,n+1} - T_{m,n})}{\Delta y}\Delta x 1 + \frac{k(T_{m+1,n} - T_{m,n})}{\Delta x}\frac{\Delta y}{2}1$$

$$+ \frac{k(T_{m,n-1} - T_{m,n})}{\Delta x}\frac{\Delta y}{2}1 = 0$$

159

REFERENCES

[1] Schobeiri, M.T., Ozturk, B., and Ashpis, D.E., "On the Physics of the Flow Separation Along a Low Pressure Turbine Blade Under Unsteady Flow Conditions," *ASME Conference Proceedings,* Vol. 2003, No. 36894, 2003, pp. 1063-1079.

[2] Van Treuren, K.W., Simon, T., von Koller, M., "Measurements in a Turbine Cascade Flow Under Ultra Low Reynolds Number Conditions," *Journal of Turbomachinery,* Vol. 124, No. 1, 2002, pp. 100-106.

[3] Rivir, R.B., and Wright Lab Wright-Patterson AFB OH, "Transition on Turbine Blades and Cascades at Low Reynolds Numbers," 1996, pp. 1-12.

[4] Denton, J.D., "The 1993 IGTI Scholar Lecture: Loss Mechanisms in Turbomachines," *Journal of Turbomachinery,* Vol. 115, No. 4, 1993, pp. 621-656.

[5] Glassman, A.J., and United States, "Turbine Design and Application," *Nasa Sp,* Vol. 290, Scientific and Technical Information Program, National Aeronautics and Space Administration ; Linthicum Heights, MD, Washington, DC, 1994, pp. 389.

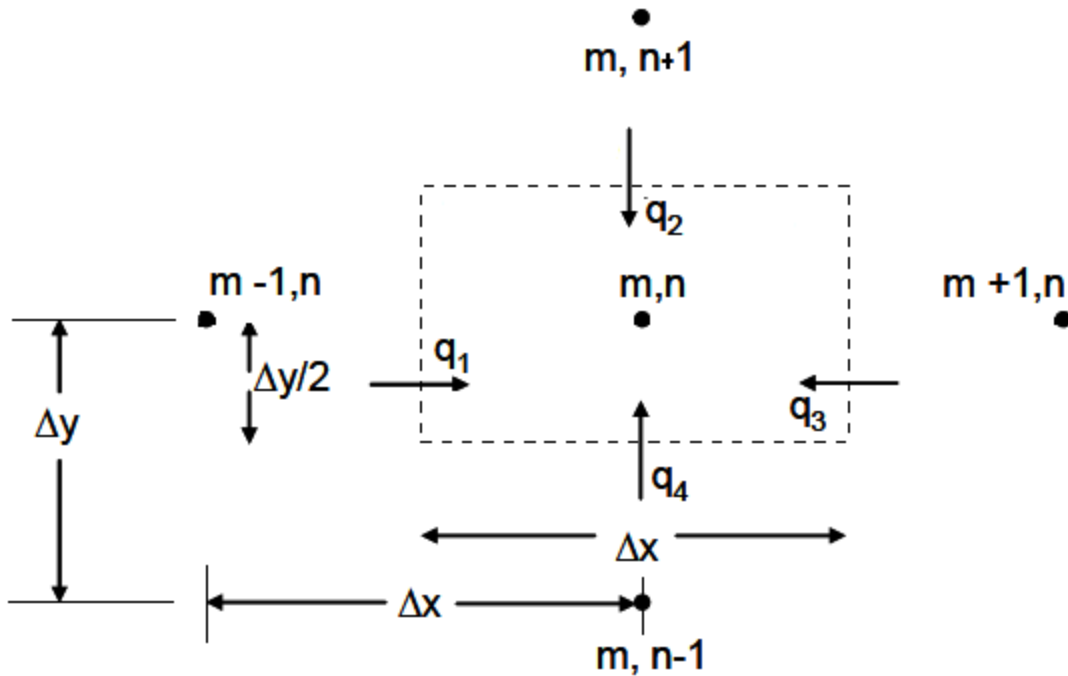[6] Ames, F.E., and Plesniak, M.W., "The Influence of Large-Scale, High-Intensity Turbulence on Vane Aerodynamic Losses, Wake Growth, and the Exit Turbulence Parameters," *Journal of Turbomachinery,* Vol. 119, No. 2, 1997, pp. 182-192.

[7] Gregory-Smith, D.G., and Cleak, J.G.E., "Secondary Flow Measurements in a Turbine Cascade With High Inlet Turbulence," *Journal of Turbomachinery,* Vol. 114, No. 1, 1992, pp. 173-183.

[8] Gregory-Smith, D.G., and Von Karman Institute for Fluid Dynamics., "Secondary and Tip-Clearance Flows in Axial Turbines, Physics of Secondary Flows," Von Karman Institute for Fluid Dynamics, Rhode St. Genèse, Belgium, 1997.

[9] Sieverding, C.H., "Recent Progress in the Understanding of Basic Aspects of Secondary Flows in Turbine Blade Passages," *Journal of Engineering for Gas Turbines and Power,* Vol. 107, No. 2, 1985, pp. 248-257.

[10] Eckerle, W.A., and Langston, L.S., "Horseshoe Vortex Formation Around a Cylinder," *Journal of Turbomachinery,* Vol. 109, No. 2, 1987, pp. 278-285.

[11] Klein, A., "Investigation of the entry boundary layer on the secondary flows in the blading of axial turbines," 1966.

160

[12] Langston, L.S., Volino, R.J., and Hooper, R.M., "Three-dimensional flow within a turbine cascade passage," *Journal of Engineering for Power,* Vol. 99, No. 1, 1977, pp. 21-28.

[13] Marchal, P., and Sieverding, C.H., "Secondary flows within turbomachinery bladings," *Secondary Flows in Turbomachines,* 1977, pp. 214.

[14] Goldstein, R.J., and Spores, R.A., "Turbulent Transport on the Endwall in the Region Between Adjacent Turbine Blades," *Journal of Heat Transfer,* Vol. 110, No. 4a, 1988, pp. 862-869.

[15] Chung, J.T., and Simon, T.W., "Three-Dimensional Flow near the Blade/Endwall Junction of a Gas Turbine: Visualization in a Large-Scale Cascade Simulator," *American Society of Mechanical Engineers,* 1990.

[16] Sharma, O.P., and Butler, T.L., "Predictions of Endwall Losses and Secondary Flows in Axial Flow Turbine Cascades," *Journal of Turbomachinery,* Vol. 109, No. 2, 1987, pp. 229-236.

[17] Sharma, O.P., Ni, R.H., and Tanrikut, S., "Unsteady flows in turbines: Impact on design procedure," 1994, pp. 1-27.

[18] Wang, H.P., Olson, S.J., Goldstein, R.J., "Flow Visualization in a Linear Turbine Cascade of High Performance Turbine Blades," *Journal of Turbomachinery,* Vol. 119, No. 1, 1997, pp. 1-8.

[19] Ames, F.E., Johnson, J.D., and Fiala, N.J., "The Influence of Aero-Derivative Combustor Turbulence and Reynolds Number on Vane Aerodynamics Losses, Secondary Flows, and Wake Growth," *ASME Conference Proceedings,* Vol. 2006, No. 4238X, 2006, pp. 139-148.

[20] Shih, T.I., and Lin, Y.-., "Controlling Secondary-Flow Structure by Leading-Edge Airfoil Fillet and Inlet Swirl to Reduce Aerodynamic Loss and Surface Heat Transfer," *Journal of Turbomachinery,* Vol. 125, No. 1, 2003, pp. 48-56.

[21] Zess, G.A., and Thole, K.A., "Computational Design and Experimental Evaluation of Using a Leading Edge Fillet on a Gas Turbine Vane," *Journal of Turbomachinery,* Vol. 124, No. 2, 2002, pp. 167-175.

[22] Han, S., and Goldstein, R.J., "Influence of Blade Leading Edge Geometry on Turbine Endwall Heat (Mass) Transfer," *Journal of Turbomachinery,* Vol. 128, No. 4, 2006, pp. 798-813.

[23] Sauer, H., Muller, R., and Vogeler, K., "Reduction of Secondary Flow Losses in Turbine Cascades by Leading Edge Modifications at the Endwall," *Journal of Turbomachinery,* Vol. 123, No. 2, 2001, pp. 207-213.

161

[24] Knezevici, D.C., Sjolander, S.A., Praisner, T.J., "Measurements of Secondary Losses in a Turbine Cascade With the Implementation of Nonaxisymmetric Endwall Contouring," *Journal of Turbomachinery,* Vol. 132, No. 1, 2010, pp. 011013.

[25] Burd, S.W., and Simon, T.W., "Flow Measurements in a Nozzle Guide Vane Passage With a Low Aspect Ratio and Endwall Contouring," *Journal of Turbomachinery,* Vol. 122, No. 4, 2000, pp. 659-666.

[26] Shyne, R.J., Sohn, K., and De Witt, K.J., "Experimental Investigation of Boundary Layer Behavior in a Simulated Low Pressure Turbine," *Journal of Fluids Engineering,* Vol. 122, No. 1, 2000, pp. 84-89.

[27] Simon, T.W., and Kaszeta, R.W., "Transition to Turbulence Under Low-Pressure Turbine Conditions," *Annals of the New York Academy of Sciences,* Vol. 934, No. 1, 2001, pp. 37-51.

[28] Schobeiri, M.T., Ozturk, B., and Ashpis, D.E., "On the Physics of Flow Separation Along a Low Pressure Turbine Blade Under Unsteady Flow Conditions," *Journal of Fluids Engineering,* Vol. 127, No. 3, 2005, pp. 503-513.

[29] Satta, F., Simoni, D., Ubaldi, M., "Experimental Investigation of Separation and Transition Processes on a High-Lift Low-Pressure Turbine Profile Under Steady and Unsteady Inflow at Low Reynolds Number," *Journal of Thermal Science,* Vol. 19, No. 1, 2010, pp. 26-33.

[30] McAuliffe, B.R., and Sjolander, S.A., "Active Flow Control Using Steady Blowing for a Low-Pressure Turbine Cascade," *Journal of Turbomachinery,* Vol. 126, No. 4, 2004, pp. 560-569.

[31] Volino, R.J., and Hultgren, L.S., "Measurements in Separated and Transitional Boundary Layers Under Low-Pressure Turbine Airfoil Conditions," *Journal of Turbomachinery,* Vol. 123, No. 2, 2001, pp. 189-197.

[32] Jouini, D.B.M., Sjolander, S.A., and Moustapha, S.H., "Aerodynamic Performance of a Transonic Turbine Cascade at Off-Design Conditions," *Journal of Turbomachinery,* Vol. 123, No. 3, 2001, pp. 510-518.

[33] Mee, D.J., Baines, N.C., Oldfield, M.L.G., "An Examination of the Contributions to Loss on a Transonic Turbine Blade in Cascade," *Journal of Turbomachinery,* Vol. 114, No. 1, 1992, pp. 155-162.

[34] Rona, A., Paciorri, R., and Geron, M., "Design and Testing of a Transonic Linear Cascade Tunnel With Optimized Slotted Walls," *Journal of Turbomachinery,* Vol. 128, No. 1, 2006, pp. 23-34.

[35] Woodason, R., Asghar, A., and Allan, W.D.E., "Assessment of the Flow Quality of a Transonic Turbine Cascade," *ASME Conference Proceedings,* Vol. 2009, No. 48883, 2009, pp. 1131-1141.

[36] Verhoff, V., G., Camperchioli, W., P., and Lopez, I., "Transonic turbine blade cascade testing facility," *American Institute of Aeronautics and Astronautics,* 1992, pp. 1-11.

[37] Povey, T., Oldfield, M.L.G., and Haselbach, F., "Transonic turbine vane tests in a new miniature cascade facility," *Proceedings of the Institution of Mechanical Engineers, Part A: Journal of Power and Energy,* Vol. 222, No. 5, 2008, pp. 529-539.

[38] Gostelow, J.P., and Watson, P.J., "A Closed Circuit Variable Density Air Supply for Turbomachinery Research " *American Society of Mechanical Engineers,* 1976, pp. 1-8.

[39] Hodson, H.P., "Boundary-Layer Transition and Separation Near the Leading Edge of a High-Speed Turbine Blade," *Journal of Engineering for Gas Turbines and Power,* Vol. 107, No. 1, 1985, pp. 127-134.

[40] Bathie, W.W., "Fundamentals of Gas Turbines," J. Wiley, New York, 1996, pp. 453.

[41] Ames, F.E., "The Influence of Large-Scale High-Intensity Turbulence on Vane Heat Transfer," *Journal of Turbomachinery,* Vol. 119, No. 1, 1997, pp. 23-30.

[42] Ames, F.E., and Moffat, R.J., "Heat Transfer With High Intensity, Large Scale Turbulence: The Flat Plate Turbulent Boundary Layer and the Cylindrical Stagnation Point," 1990.

[43] Ames, F.E., Zhang, L., Smart, R., "Turbine vane surface heat transfer measurements in a compressible linear cascade," *34th National Heat Transfer Conference,* 2000, pp. 1-8.

[44] Nasir, S., Carullo, J.S., Ng, W., "Effects of Large Scale High Freestream Turbulence and Exit Reynolds Number on Turbine Vane Heat Transfer in a Transonic Cascade," *Journal of Turbomachinery,* Vol. 131, No. 2, 2009, pp. 021021.

[45] Boyle, R.J., Ames, F.E., and Giel, P.W., "Predictions for the Effects of Freestream Turbulence on Turbine Blade Heat Transfer," *ASME Conference Proceedings,* Vol. 2004, No. 41685, 2004, pp. 1029-1044.

[46] Ames, F.E., Barbot, P.A., and Wang, C., "Effects of Aeroderivative Combustor Turbulence on Endwall Heat Transfer Distributions Acquired in a Linear Vane Cascade," *Journal of Turbomachinery,* Vol. 125, No. 2, 2003, pp. 210-220.

163

[47] Dominy, R.G., and Hodson, H.P., "An Investigation of Factors Influencing the Calibration of Five-Hole Probes for Three-Dimensional Flow Measurements," *Journal of Turbomachinery,* Vol. 115, No. 3, 1993, pp. 513-519.

[48] Adcock, J.B., and Smith, L.A., "Effect of Reynolds Number and Mach Number on Flow Angularity Probe Sensitivity," *NASA Technical Memorandum 8775,* 1986, pp. 1-26.

[49] Wallen, G., "Reynolds Number Effects of a Cone and a Wedge Type Pressure Probe," *Proceedings of the 7th Symposium on Measuring Techniques in Transonic and Supersonic Flows in Cascades and Turbomachines,* 1983.

[50] Schoenenberger, M., Greber, I., and Davis, D.O., "Flow Measurements Downstream of a Single Bleed Hole in a Subsonic, Turbulent Boundary Layer Using a New 5-Hole Pressure Probe," *American Institute of Aeronautics and Astronautics,* 1999, pp. 1-16.

[51] Fransson, T., and and Sari, I., "Characteristics of Aerodynamic Five-Hole-Probes in Transonic and SuperSonic Flow Regimes," *Proceedings of the 6h Symposium on Measuring Techniques for Transonic and Supersonic Flows in Cascades and Turbomachines,* 1981.

[52] Bryer, D.W., and Pankhurst, R.C., "Pressure-probe methods for determining wind speed and flow direction," H.M.S.O., London, 1971.

[53] Morrison, G.L., Pappu, K.R., and Schobeiri, M.T., "Five-hole pressure probe analysis technique," *Flow Measurements and Instrumentation,* 1998, pp. 153-158.

[54] Campbell, J.F., and Brandon, J.M., "Calibration and Flight Results for the Ares I-X 5-Hole Probe," *Acta Astronautica,* Vol. 68, No. 7-8, 2010, pp. 1219-1227.

[55] Huffman, G.D., Poti, N.D., and Rabe, D.C., "Flow direction probes from a theoretical and experimental point of view," *Journal of Physics E: Scientific Instruments,* Vol. 13, No. 7, pp. 751-760.

[56] Gonsalez, J.C., and Arrington, E.A., "Five–Hole Flow Angle Probe Calibration for the NASA Glenn Icing Research Tunnel," *American Institute of Aeronautics and Astronautics,* No. 96-2201, 1999, pp. 1-23.

[57] Ames, F.E., "Lecture 16-An Approximate Solution to the Momentum Boundary Layer," *Computational Fluid Dynamics,* 2011.

[58] John, J.E.A., and Keith, T.G., "Gas Dynamics," Pearson Prentice Hall, New Jersey, 2006, pp. 672.

[59] Moffat, R.J., "Describing the Uncertainties in Experimental Results," *Experimental Thermal and Fluid Science,* Vol. 1, 1988, pp. 3-17.

164

[60] Kays, W.M., Weigand, B., and Crawford, M.E., "Convective Heat and Mass Transfer," *McGraw-Hill series in mechanical engineering,* McGraw-Hill Higher Education, Boston, 2005, pp. 546.

[61] White, F.M., "Viscous Fluid Flow," *McGraw-Hill series in mechanical engineering,* McGraw-Hill Higher Education, New York, NY, 2006, pp. 629.

[62] Ames, F.E., Wang, C., and Barbot, P.A., "Measurement and Prediction of the Influence of Catalytic and Dry Low NO[sub x] Combustor Turbulence on Vane Surface Heat Transfer," *ASME Conference Proceedings,* Vol. 2002, No. 36088, 2002, pp. 969-980.

[63] Ames, F.E., Kwon, K., and Moffat, R.J., "An Algebraic Model for High Intensity Large Scale Turbulence," *American Society of Mechanical Engineers,* 1999.

[64] Hunt, J.C.R., "A Theory of Turbulent Flow Round Two-Dimensional Bluff Bodies," *Journal of Fluid Mechanics,* Vol. 61, No. 04, 1973, pp. 625.